DISSERTATION

NMR INVESTIGATION OF THE BEHAVIOR OF CHLORPYRIFOS AND METHYL PARATHION SORBED ON CLAYS, AND QUANTITATIVE ^{13}C NMR ANALYSIS OF SEQUENCE DISTRIBUTIONS IN POLY(ETHYLENE-CO-1-HEXENE).

Submitted by

Mark R. Seger

Department of Chemistry

In partial fulfillment of the requirements

for the Degree of Doctor of Philosophy

Colorado State University

Fort Collins, Colorado

Spring 2008

COLORADO STATE UNIVERSITY

May 19, 2003

WE HEREBY RECOMMEND THAT THE DISSERTATION PREPARED UNDER OUR SUPERVISION BY MARK SEGER ENTITLTED NMR INVESTIGATION OF THE BEHAVIOR OF CHLORPYRIFOS AND METHYL PARATHION SORBED ON CLAYS, AND QUANTITATIVE ^{13}C NMR ANALYSIS OF SEQUENCE DISTRIBUTIONS IN POLY(ETHYLENE-CO-1-HEXENE) BE ACCEPTED AS FULFILLING IN PART REQUIREMENTS FOR THE DEGREE OF DOCTOR OF PHILOSOPHY.

Committee on Graduate Work

Adviser

Department Head

ABSTRACT OF DISSERTATION

NMR Investigation of the Behavior of Chlorpyrifos and Methyl Parathion Sorbed on Clays, and Quantitative ^{13}C NMR Analysis of Sequence Distributions in Poly(ethylene-co-1-hexene).

Chapters 1 and 2 (and Appendix): Decomposition of chlorpyrifos and methyl parathion on kaolinite and various cation-exchanged montmorillonites (at room temperature, in the dark) was monitored by ^{31}P NMR. Decomposition products included the results of hydrolysis reactions, isomerization reactions and oxidation reactions; mineralization also appears to occur in some cases. Assignments of ^{31}P peaks was based mostly on literature values of chemical shifts of similar structures and ^{31}P NMR experiments on DMSO-d_6 extracts of the pesticide/clay samples. When initially sorbed onto the clay, both pesticides appear by solid-state ^{31}P NMR to exhibit significant motion on the molecular level, resulting in almost liquid-like spectra. Over a period of days or weeks, the signal due to unreacted pesticide diminishes and was replaced by new ^{31}P NMR signals arising from various decomposition products. The rate of pesticide decomposition was found to vary greatly, depending on the cation present in montmorillonite. The fastest initial decomposition (disappearance of unreacted pesticide) occurred with the Cu^{2+}-exchanged montmorillonites. Higher hydration levels of Al-

exchanged montmorillonite were found to reduce the decomposition rate of methyl parathion; similarly, chlorpyrifos decomposed more quickly when sorbed on Zn-montmorillonite with lower hydration levels.

Chapter 3: Different ^{13}C NMR methods of determining triad distributions in two poly(ethylene-co-1-hexene) copolymers are examined using high signal-to-noise 126 MHz ^{13}C spectra of the copolymers dissolved in deuterated 1,2,4-trichlorobenzene at 398K. This examination includes three integration techniques, the experimental impact of decoupler sidebands and significantly non-equal ^{13}C nOe values. A least-squares regression analysis technique for solving for triad mole fractions is tested and appears to be more reliable than two published algebraic expressions. The resultant triad mole fractions are compared to sequence distribution parameters expected by Bernoullian and first-order Markovian statistical models. On the basis of ^{13}C NMR-determined average reactivity ratios, the copolymer designated sample H (5.3 mol % 1-hexene) appears to be a Bernoullian copolymer resulting from a single-site catalytic system. The copolymer designated sample L (3.6 mol % 1-hexene overall) is better described as a mixture of polyethylene and a Bernoullian copolymer with 6.4 mol % 1-hexene content.

Mark Raymond Seger
Chemistry Department
Colorado State University
Fort Collins, CO 80523
Spring 2008

Table of Contents

Chapter 1: NMR Investigation of the Behavior of Chlorpyrifos Sorbed on Clays

INTRODUCTION

Millions of metric tons of organothiophosphate pesticides are used annually worldwide (*1-1*). Although there have been hundreds of studies detailing the disappearance of many commercial organothiophosphate pesticides from a wide variety of agricultural and natural environments, not much is known of the detailed chemistry of decomposition, especially the interaction of pesticides and their decomposition residues with soil components. This paper describes the investigation, primarily by solid-state NMR, of the effect of some soil components on the *chemical* (non-biological) decomposition of an organothiophosphate pesticide, chlorpyrifos (**I**, see Scheme 1-1), a commonly used agricultural agent. Photochemical reactions were not studied.

Scheme 1-1

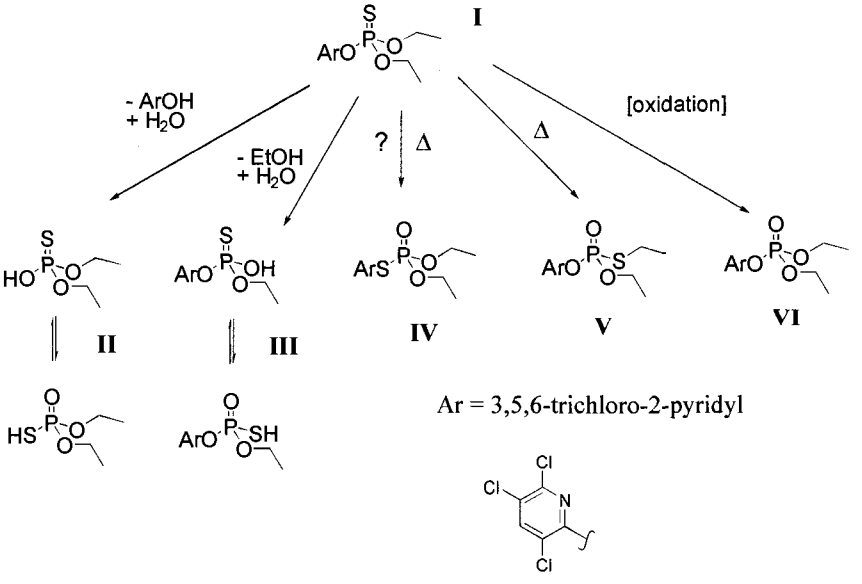

Soils are complex systems, a complicated mixture of organic compounds (e.g., humic acids, fulvic acids and humins) and a variety of minerals (e.g., silica, silicates, clays). Some clay minerals are reported to be catalytically active for many chemical transformations, including the decomposition of organophosphate pesticides (*1-2*). Humic acids are also reported to catalyze organothiophosphate decomposition (*1-3*).

NMR is rather well suited for the analysis of chemical and physical interactions and transformations in complex systems. Organophosphate pesticides contain the ^{31}P nuclide (100 % natural abundance) and ^{31}P NMR chemical shifts have large sensitivity to structural variation (*1-4*). Since most soil components have low natural phosphorus contents, information on the chemical microstructure and interactions of the organophosphate pesticide and its phosphorus-containing residues can be obtained without substantial interference. However, compared to many other analytical techniques, NMR is relatively insensitive and requires relatively large sample concentrations for detection. Therefore, no attempt was made in the study reported here to simulate actual pesticide or residue concentrations (e.g., ppm level) found in the environment; instead, the focus of this study is to characterize the *chemistry* of interactions and decompositions of chlorpyrifos on clays, which should carry over from one concentration to another.

Chemical reactions that have been reported or suggested for the initial step in the chemical decomposition of organothiophosphate pesticides (not including photo-assisted processes) are summarized in Scheme 1-1. Isomerization is known to occur during synthesis or storage at elevated temperatures, but is usually not described as a major decomposition process in the environment. Isomerization to the S-alkyl isomer (**V** in

Scheme 1-1) is known (*1-5*), but no reports were found for isomerization to the S-aryl analogue (**IV**). Oxidation to the oxon form (**VI**) is of special concern, since this form has much greater mammalian toxicity than does the starting organothiophosphate (*1-6, 1-7*). Hydrolysis reactions are usually reported to predominate initial decomposition in the environment (*1-8, 1-9*). The hydrolysis products in Scheme 1-1 are shown in their conjugate acid form; thiophosphoric acids of this type typically have pK_a values below 2 (*1-10*), and thus may be significantly dissociated when sorbed on clay.

Chlorpyrifos has two different initial hydrolysis products, resulting from a) removal of ethanol or ethoxide (structure **III** in Scheme 1-1), or b) removal of the substituted pyridol (**II**), depending on chemical conditions. Investigation of the montmorillonite-catalyzed decomposition of quinalphos (O,O-diethyl O-quinoxalin-2-yl phosphorothioate) has been reported for a variety of exchangeable metal cations (*1-11*). It was suggested that, in presence of Cu(II)-, Fe(III)- or Al-montmorillonite, the decomposition mechanism involves initial bidentate coordination of quinalphos to the metal cation, as shown in Structure A. Other studies report that

Structure A

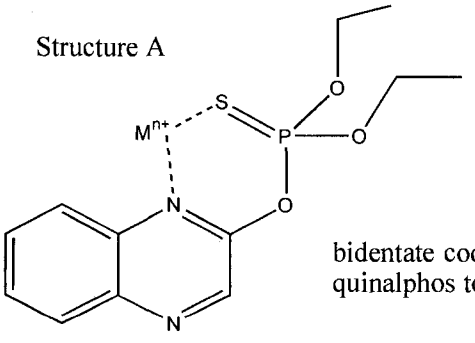

bidentate coordination of quinalphos to a metal cation

Cu(II) is especially efficient, whether present as an aqueous cation or as Cu(II)-exchanged clay, in catalyzing this hydrolysis reaction, presumably because Cu(II) forms strong bidentate complexes of this type (*1-12, 1-13*). Aqueous base hydrolysis of chlorpyrifos is

reported to remove the aryl moiety preferentially, whereas neutral or acidic water tends to hydrolyze the alkoxide portion (*1-14*). Full hydrolysis to an unsubstituted aqueous phosphate ion or "mineralization" (*i.e.*, incorporation into the clay mineral structure) may be the ultimate fate of the phosphorus atom after pesticide decomposition. Formation of a soluble mineral phase has been reported when triethylphosphate reacted with kaolin (*1-15*). Na- and K-montmorillonites exhibit the tendency to hydrolyze adsorbed water to form hydroxide anions (*1-16*) and were not included in the study reported here, which focused on the effects of kaolinite and the Ca-, Al-, Zn- and Cu(II)-forms of montmorillonite.

Previous reports of the decomposition of organothiophosphates have tended to focus only on the disappearance of the starting pesticide and its initial decomposition reactions. Several reports indicate that not all of the decomposition products are extractable from clays, and thus may not be accounted for by the analytical techniques used, which, unlike solid-state NMR, mostly require extraction of the pesticide and its transformation products from the soil substrate. However, pesticide residues and their groundwater transportability are of concern, since some of the potential residues (e.g., the oxon) are known to be much more toxic to mammals than the starting pesticide (*1-17*).

EXPERIMENTAL

Materials. Calcium montmorillonite, designated STx-1, was obtained from the Source Clay Mineral Repository (located at the University of Missouri-Columbia). X-ray powder diffraction indicated the material to be predominately montmorillonite, with traces of quartz. Information provided by the supplier: traces of quartz, silica and carbonate present (IR analysis); low iron and phosphorus content (0.65 % Fe_2O_3, 0.15 %

FeO, and 0.026 % P as P_2O_5, by weight; elemental analysis). (No phosphorus signals were detectable by solid-state ^{31}P NMR after three days of signal averaging). Dehydration of the 'as received' material at 100 °C and 3 x 10^{-3} Torr achieved constant weight after two days, indicating 2.1% water content by weight.

The Zn(II)-, Al(III)- , and Cu(II)-exchanged montmorillonites were prepared by utilizing several washes of the 'as received' Ca-montmorillonite with 1 M aqueous solutions of the corresponding metal chloride, followed by multiple washes with water until the wash solution no longer precipitated silver chloride when added to 1 M $AgNO_3$(aq) solution. Dehydration of the ion-exchanged clays was carried out at 100 °C and 3 x 10^{-3} Torr until constant weight was achieved.

Kaolinite, designated KGa-1b and identified as "Kaolin, well crystallized", was also obtained from the Source Clay Mineral Repository. Information provided by the supplier: no traces of silica and carbonate present (IR analysis); low iron and phosphorus content (0.12 % Fe and <0.0005 % P, by weight as elements; elemental analysis). Dehydration of the 'as received' KGa-1b kaolinite at 100°C and 3 x 10^{-3} Torr indicated a 1.1 % water content by weight.

Weighed samples of both 'as received' STx-1 and 'as received' KGa-1b clay samples were placed in a humidifying chamber (a sealed chamber containing liquid water and no desiccant) at room temperature for five months. The clay minerals adsorbed water until constant weights were obtained (after about 3 months): STx-1, 19.5 % water (w/w); KGa-1b, 6.2 % water (w/w).

Moisture in Chlorpyrifos-Loaded Clays. Gravimetric trials showed that, when exposed to air as a shallow layer in an open vessel, two grams of anhydrous Ca- or Zn-

montmorillonite gained about 1 mg water per minute of air exposure; for clay samples containing added water, the weight change due to air exposure was judged to be insignificant, as air exposure was usually only a few minutes.

Chlorpyrifos. Analytical grade chlorpyrifos, **I** (IUPAC name O,O-diethyl O-3,5,6-trichloro-2-pyridyl phosphorothioate, CAS Registry No. [2921-88-2]) was donated by DowElanco of Indianapolis, IN. Mp 42 – 43 °C; lit. 42 - 43.5 °C (*1-18*). Liquid-solution NMR analysis (^{1}H, ^{13}C and ^{31}P) of the chlorpyrifos dissolved in DMSO-d_6 and $CDCl_3$ showed no indications of impurities, with detection limits estimated to be less than 0.1 % (by ^{1}H NMR analysis). Recrystallization from hot ethanol did not change the melting point or ^{1}H liquid-solution NMR spectrum, so the analytical grade material was used as received.

The *in-vitro* hydrolysis product, **II**, was prepared by the slow addition (over 20 minutes) of ethanolic KOH (1.2 M) to a solution of chlorpyrifos in ethanol at room temperature, followed by stirring for one hour. The precipitate that formed was found to be predominately the potassium salt of diethylthiophosphoric acid, while the substituted pyridinyl moiety remained in ethanol solution.

Chlorpyrifos-Loaded Clays. Unless otherwise noted, a weighed amount (typically 2 g) of anhydrous clay was transferred to a round bottom flask in a dry box. Two methods were used to adsorb water onto the clay minerals. Method 1(initial samples): a known quantity of water was added to the clay by pipet (usually about 5 % water by weight), and the clay was stirred for at least two hr. Method 2 (later preparations): water was loaded onto the clay in a humidifying chamber for about one hour, following the water adsorption gravimetrically, and then stirred for at least 15 min in a sealed round

bottom flask The weighed pesticide (or pesticide residue) was dissolved in about 30 ml of hexane or anhydrous ethanol, and stirred at room temperature with the clay for at least one hour. Solvent was removed by either evaporation or filtration. Typically, the pesticide or residue were loaded at about 1 % to 10 % by weight to facilitate detection of the NMR signals.

NMR Spectroscopy. Most of the liquid-solution ^{1}H, ^{13}C and ^{31}P NMR spectra were collected using a modified Bruker AM-500 NMR spectrometer (operating at 500.1 MHz, 125.7 MHz and 202.4 MHz, respectively), and a Chemagnetics Infinity-600 NMR spectrometer (operating at 600.1 MHz for ^{1}H and 242.9 MHz for ^{31}P).

Solid-state 60.7 MHz ^{31}P NMR spectra were obtained on 400 – 700 mg samples, using a home-built 150 MHz (^{1}H) spectrometer based on a Chemagnetics CMX-II data system. Two different solid-state magic-angle spinning (MAS) NMR probes were employed: a home-built 8 mm Gay-style probe (*19*), with a 1.8 kHz MAS speed; and a home-built probe utilizing a 9 mm Chemagnetics Pencil spinning system, with a 4-5 kHz MAS speed.

Solid-state ^{13}C CP-MAS NMR spectra were obtained at 25.3 MHz using a Chemagnetics CMX-II-100 NMR spectrometer. ^{27}Al MAS spectra were obtained using a Bruker AM-600 NMR spectrometer, operating at 156.3 MHz, with a home-built probe incorporating a 4 mm Chemagnetics Pencil spinning system, up to 17 kHz MAS speed.

Packed Powder X-Ray Diffraction. All packed powder X-ray diffraction analyses were performed at a wavelength of 0.154 nm (Cu-α line).

RESULTS

*^{31}P, ^{13}C and ^{1}H NMR of Pure Chlorpyrifos (**I**) and Its Aryl Hydrolysis Product (**II**).* Table 1-1 lists twenty different phosphorus-containing structures that might possibly be observed in solid-state ^{31}P NMR spectra of chlorpyrifos decomposed on clay in the presence of water. ^{31}P chemical shifts are also reported for those structures for which values are available in the literature. For some structures, ^{31}P chemical shifts were available for only analogous compounds, as indicated in the Table 1-1 caption.

Based on the ^{31}P chemical shifts given in Table 1-1, the following chemical shift ranges were established to assign ^{31}P chemical shifts observed during chlorpyrifos decomposition (*vide infra*): peaks within the 58 to 48 ppm range represent initial hydrolysis products containing the P=S moiety; the 31 to 23 ppm range represents S,O-isomerized residues; the 3 to -5 ppm range represents phosphate and alkyl phosphates; and the -4 to -10 ppm range represents oxidized chlorpyrifos (chlorpyrifos oxon). Peaks might be also observed for reportedly common pesticide synthesis contaminants: bis aryl alkyl thiophosphates in the 56 to 59 ppm range and trialkyl thiophosphates in the 68 to 74 ppm range.

Figure 1-1 shows the 60.7 MHz ^{31}P MAS spectra of pure crystalline chlorpyrifos, observed with magic-angle spinning, using both cross polarization (CP-MAS) and direct polarization (DP-MAS, *via* ^{31}P spin-lattice relaxation). Except for the largest peak in each spectrum, the peaks observed in these MAS spectra are spinning sidebands, which are marked with asterisks in Figure 1-1, but not in subsequent figures. The observed isotropic ^{31}P chemical shift is 61 ppm (*vs.* 85 % H_3PO_4 external standard). Figure 1-1C

shows the 242.9 MHz ^{31}P spectrum of chlorpyrifos dissolved in DMSO-d_6.

Figure 1-2 compares the ^{31}P CP-MAS spectra of pure chlorpyrifos and the recrystallized hydrolysis product **II**, involving the removal of the pyridyl moiety, and the corresponding spectrum obtained for a DMSO-d_6 solution. The observed chemical shift values for chlorpyrifos (**I**) and the hydrolysis product (**II**) are comparable to literature values (*1-20*). When dissolved in DMSO-d_6, **II** has a ^{31}P chemical shift of 55.2 ppm. Figure 1-2 shows the spinning sideband arrays observed for **I** with 4 kHz MAS (Figure 1-2A) and **II** during slow spinning (about 1 kHz, in the Gay-style probe, Figure 1-2B). The spectrum of the partially-purified sample of **II** in Figure 1-2B indicates the presence of two species. The major component at about 55 ppm represents **II**, the phosphorothiolate anion. The minor component has an isotropic ^{31}P shift of about 60 ppm and is unreacted chlorpyrifos.

The similar spinning sideband arrays seen for the two components in Figure 1-2B suggest that chlorpyrifos (**I**) and its hydrolysis product (**II**) have similar values of the principal elements of the ^{31}P chemical shift tensor. Examination of the spectra at various spinning speeds (*1-21,1-22*) yielded principal elements of approximately 160 ppm, 110 ppm and -90 ppm for both **I** and **II**. These elements correspond to a chemical shift tensor consistent with a structure that lacks a C_3 or higher rotation symmetry element passing through the phosphorus atom, consistent with the structures shown for **I** and **II**.

Measurement (by inversion recovery) of the ^{31}P T_1 value of pure crystalline chlorpyrifos (**I**), data not shown here, gave a value of 381 s, not an unexpected value for a pure crystalline compound with apparently little molecular motion. Values of the $^{1}H \rightarrow {}^{31}P$ cross polarization (CP) time constant, T_{HP} , and the proton $T_{1\rho}$ values of chlorpyrifos

were determined by a variable contact-time ^{31}P CP-MAS experiment to be 490 μs and 2.6 s, respectively. The corresponding ^{1}H T_1 value is 4.3 s, again consistent with expectations for a pure crystalline compound exhibiting little or no atomic-level motion. These results and other relaxation data are collected in Table 1-2.

The solid-state CP-MAS ^{13}C NMR spectrum of pure chlorpyrifos is shown in Figure 1-3B. Only three peaks are resolved: two relatively sharp peaks due to the ethoxy carbons, plus broad resonance intensity in the aromatic region. The CP-MAS ^{13}C spectrum of the recrystallized hydrolysis fraction that contains the 3,4,6-trichloropyridinyl moiety, obtained from hydrolytic splitting off of the aryl functionality in chlorpyrifos, is shown in Figure 1-3A. It lacks (as expected) the ethoxy carbon signals, and has a better resolved aromatic region than does the corresponding spectrum of chlorpyrifos. Apparently, upon hydrolysis the oxygen-bearing aromatic carbon is shifted to lower shielding. This behavior can also be seen in the ^{13}C liquid-solution DMSO-d_6 spectra of these two compounds (not shown), which display a 14 ppm shift of the oxygen-bearing aromatic carbon resonances to lower shielding upon hydrolysis. The phenolic oxygen is expected to be predominantly protonated (i.e., in the –OH form), considering the relative pK_a values of diethyl thiophosphoric acid and 3,4,6-trichloropyridinol (1.49 and 4.55, respectively) (*1-10*), and hydrolysis stoichiometry. The ^{13}C resonances of the other aromatic carbons are also shifted upon hydrolysis, but to a lesser degree. These results suggest that ^{13}C CP-MAS experiments should be able to distinguish chlorpyrifos from the aryl hydrolysis product by detection or absence of the aromatic peak at about 164 ppm. ^{13}C CP-MAS experiments were not pursued in depth, as they suffer from substantially lower sensitivity than corresponding ^{31}P experiments (*1-23*), mostly because of the low

natural abundance of ^{13}C (1.1 % *vs.* 100 % for ^{31}P). ^{31}P NMR also has the advantage that phosphorus chemical shifts are more sensitive to the anticipated structural changes during pesticide decomposition than are carbon chemical shifts. For example, the ethoxy carbon chemical shifts in organothiophosphates show very little structural dependence as compared to phosphorus chemical shifts (*1-24*). Another problem with solid-state ^{13}C NMR is the large ^{13}C background signal that must be present if soil or humic acid is the adsorbent instead of clay. For example, Figure 1-3 also compares the ^{13}C DP-MAS (Figure 1-3E) and CP-MAS (Figure 1-3D) spectra of chlorpyrifos loaded (10 %) onto Uncomphagre soil with the ^{13}C CP-MAS spectrum of unloaded soil (Figure 1-3C). The presence of chlorpyrifos is almost unnoticed in Figure 1-3D because of the background carbon signal of the soil's organic content.

The aromatic proton chemical shift of chlorpyrifos (in DMSO-d_6 solution) also changes upon aryl hydrolysis, as indicated in Table 1-3. The observed ^{1}H chemical shift difference (1.1 ppm) suggests that solid-state ^{1}H NMR techniques such as CRAMPS (*1-25*) or fast MAS (*1-26*) may be marginally suitable, at best, for monitoring chlorpyrifos hydrolysis in clay because of anticipated peak overlaps. The ethoxy protons exhibit only minor changes in ^{1}H chemical shift upon hydrolysis.

^{31}P NMR of Chlorpyrifos Loaded onto Soil, Humic Acid, and 'as Received' Kaolinite and Calcium Montmorillonite. Initial solid-state ^{31}P NMR efforts employed slow-speed (1.2 kHz) magic-angle spinning. The CP-MAS and DP-MAS ^{31}P spectra, shown in Figure 1-4, indicate the presence of two phosphorus-containing components in the samples of chlorpyrifos loaded onto whole soil, humic acid and kaolinite. The CP experiment in each case detects a component for which the isotropic ^{31}P chemical shift

and spinning sideband envelop appear to be the same as those of crystalline chlorpyrifos (see Figure 1-1A), to within experimental uncertainty. The ^{31}P T_1 relaxation time constant determined for this component (360 s) is not significantly different than the value for crystalline chlorpyrifos (381 s). This component was removed by a n-hexane wash (spectrum not shown).

The largest peak in the ^{31}P DP-MAS spectrum in Figure 1-4F appears to represent chlorpyrifos adsorbed onto the outer surfaces of the kaolinite microcrystallites. It has an isotropic ^{31}P chemical shift of 60 ppm (not substantially different from the 61 ppm shift value measured for pure chlorpyrifos), but has a much smaller spinning sideband array than does crystalline chlorpyrifos. Furthermore, the ^{31}P T_1 value determined by an inversion-recovery experiment (T_1 = 76 ms) is much reduced compared to that measured for crystalline chlorpyrifos (381 s).

Extraction of the sample of chlorpyrifos adsorbed onto kaolinite into DMSO-d_6 solution gave liquid-solution ^{31}P, ^{13}C and ^{1}H spectra that are identical to those of chlorpyrifos, confirmed by the addition of an authentic aliquot of chlorpyrifos. Thus, the phosphorus-containing species observed in Figure 1-4F appears to be kaolin-sorbed chlorpyrifos. Figure 1-4F indicates that, because of a lack of signal intensity near 58 to 48 ppm, no hydrolysis reaction had yet occurred (within about three days) on kaolinite under the mild conditions to which the sample was subjected.

Figures 1-4A and 1-4B show CP-MAS and DP-MAS ^{31}P NMR spectra of chlorpyrifos adsorbed (10 wt. %) onto a whole soil sample obtained from the Uncomphagre National Forest in southwestern Colorado (*1-27, 1-28*). Powder X-ray diffraction indicates that the principal mineral phase in this whole soil is kaolinite.

Figures 1-4C and 1-4D show the CP-MAS and DP-MAS ^{31}P spectra of 10 % chlorpyrifos (by wt.) added to a humic acid sample obtained from the whole soil represented in Figures 4A and 4B (*1-29*). The only ^{31}P signals seen are due to pure crystalline chlorpyrifos; apparently little or no adsorption of the applied chlorpyrifos has occurred, at least during the time period (about 5 days) when the humic acid was exposed to the pesticide. When the sample was washed with n-hexane to remove non-adsorbed chlorpyrifos, no ^{31}P NMR signals were detected overnight from the washed soil by either CP-MAS or DP-MAS methods.

The ^{13}C MAS spectra of chlorpyrifos 10 % w/w on 'as received' kaolinite, shown in Figure 1-5, display results that parallel the ^{31}P results given in Figures 1-4E and 1-4F. The ^{13}C DP-MAS spectrum (Figure 1-5A) is consistent with the presence of an adsorbed chlorpyrifos phase, albeit with a more highly resolved aromatic region compared to the crystalline phase shown in Figure 1-3B. The least-shielded aromatic carbon resonances in Figure 1-5A has a chemical shift (152 ppm) that is comparable to that of crystalline chlorpyrifos (150 ppm), but not comparable to that of the aryl-hydrolyzed material (164 ppm). The lack of appearance of the hydrolyzed species in the ^{13}C CP-MAS spectrum of Figure 1-5, the apparent lack of spinning sidebands in the spectrum, and the almost liquid-like peak linewidths are all consistent with the assignment of this peak to adsorbed but unhydrolyzed chlorpyrifos that undergoes significant atomic-level motion. The ^{13}C signals in the ^{13}C CP-MAS spectrum (Figure 1-5B) are presumably due to chlorpyrifos in excess of the kaolinite adsorption capacity, appearing as an unadsorbed, crystalline chlorpyrifos phase.

Figures 1-4G and 1-4H show the CP-MAS and DP-MAS ^{31}P spectra obtained for

10 % w/w chlorpyrifos on 'as received' (2.1 wt. % water content) calcium montmorillonite. The T_1 value of the ^{31}P signal in the DP-MAS spectrum in Figure 1-4H was determined to be 35 ms. The lack of a ^{31}P CP-MAS signal in Figure 1-4G and the appearance of the DP-MAS spectrum in Figure 1-4H suggest the following tentative conclusions: (1) No crystalline (unadsorbed) chlorpyrifos phase is present. (2) The adsorption capacity of chlorpyrifos on Ca-montmorillonite was not exceeded by 10 % w/w chlorpyrifos, and is thus larger than for the kaolinite case. (*1-3*) The DP-MAS signal appears to be almost identical to the DP-MAS ^{31}P signal for chlorpyrifos adsorbed on kaolinite (both at about 60 ppm), except for the ^{31}P T_1 values determined (shorter in the case of calcium montmorillonite). (4) Chlorpyrifos adsorbed on Ca-montmorillonite appears to undergo substantial atomic-level motion. The apparently larger capacity for chlorpyrifos adsorption by Ca-montmorillonite, relative to that by kaolinite, is consistent with Ca-montmorillonite's propensity to intercalate guest molecules between the sheets of the clay structure (*1-30*). X-ray powder results (Table 1-4), indicate a small but significant increase in the interlayer spacing of the calcium montmorillonite clay upon loading with chlorpyrifos (10 % by wt.).

Figure 1-5 also shows the ^{13}C CP-MAS and DP-MAS spectra of the sample represented in Figures 1-4G and 1-4H (10 % by weight chlorpyrifos on 'as received' Ca-montmorillonite). No ^{13}C CP-MAS signal was observed (Figure 1-5D), consistent with an adsorbed phase undergoing substantial motion on the relevant NMR timescale; i.e., motional averaging of the ^{1}H- ^{13}C heteronuclear dipolar interaction has reduced cross polarization efficiency to near zero. The ^{13}C DP-MAS spectrum is less well resolved than for kaolinite-adsorbed chlorpyrifos, suggesting greater variety of adsorption sites in

the Ca-montmorillonite case, resulting in an unresolved distribution of isotropic chemical shifts. The least-shielded ^{13}C DP-MAS peak in Figure 1-5C has a chemical shift (169 ppm) that is more suggestive of the aromatic-containing fraction of aryl-hydrolyzed chlorpyrifos than of the unhydrolyzed material, although the other aromatic chemical shifts are not consistent with either compound's ^{13}C spectrum in DMSO-d_6 solution. The ^{31}P results discussed above (Figure 1-4) strongly indicate that chlorpyrifos is adsorbed but not hydrolyzed on Ca-montmorillonite.

Figure 1-6A shows the nonspinning ^{31}P DP NMR spectrum of chlorpyrifos (10 %) on Ca-montmorillonite ('as received'). Figure 1-6B shows the ^{31}P DP-MAS spectrum obtained with 1.5 kHz spinning without ^{1}H decoupling, and Figure 1-6C shows the corresponding ^{31}P DP-MAS spectrum obtained with decoupling. The peak observed in Figure 1-6A is much narrower than for the same technique applied to pure crystalline chlorpyrifos (not shown), consistent with the notion that the adsorbed phase is highly mobile on the relevant NMR time scale, i.e., motions with frequencies of at least kHz-to-MHz ranges, which could, for example, average isotropic chemical shift heterogeneities.

Decomposition of Chlorpyrifos Adsorbed onto Various Clays

Figure 1-7 compares the ^{31}P CP-MAS and DP-MAS spectra of chlorpyrifos (1.3 % w/w) adsorbed on *partially-hydrated KGa-1b kaolinite* ('as received', i.e., with a 1.1 % w/w water content), after one day and after 108 days. After one day, there is apparently no statistically significant CP-MAS signal observed after 14926 scans (Figure 1-7B). Figure 1-7A shows the DP-MAS ^{31}P spectrum of this sample after one day. This spectrum was obtained in only 4338 scans, involving 2.4 hours of signal averaging. The only ^{31}P NMR signal observed (at 61 ppm) is apparently due to mobile adsorbed

chlorpyrifos, as discussed above for the chlorpyrifos/Ca-montmorillonite sample. Quantitative comparisons of the total signal integral in Figures 1-7A with the DP-MAS spectrum of pure crystalline chlorpyrifos shown in Figure 1-1A indicate that about 99 % of the initially-loaded phosphorus atoms (as chlorpyrifos) are detected by ^{31}P DP-MAS NMR in Figure 1-7A, essentially all as the highly-mobile, adsorbed chlorpyrifos phase. Figure 1-7D indicates that after 108 days of storage (at room temperature in the dark), a small but statistically significant ^{31}P CP-MAS signal is seen. Because of the slow sample spinning speed (< 2 kHz) obtainable with the Gay-style probe utilized to obtain Figure 1-7, the number and identity of decomposition products is not clear. Quantitative comparisons to the ^{31}P DP-MAS spectrum of pure crystalline chlorpyrifos (Figure 1-1A) indicate that about 95 % of the initially-loaded phosphorus atoms are detected in Figure 1-7C.

Liquid-solution ^{31}P NMR analysis of the DMSO-d_6 extract of the sample represented in Figures 7C and 7D was carried out, as shown in Figure 1-8A. The extract apparently consists mostly of unreacted chlorpyrifos (62 ppm), although at least three other peaks are seen: a substantial peak at 28 ppm probably represents S,O-isomerized chlorpyrifos (either structure **IV** or **V**), the small peak at 53 ppm is probably hydrolyzed chlorpyrifos (**II**; diethylthiophosphoric acid), and the small peak at about 49 ppm may represent a product resulting from two hydrolysis reactions, such as O-ethyl thiophosphoric acid (**VII**). This last assignment is very tentative, and is based only on chemical shift comparisons with data from structurally related species. Phosphorus chemical shifts in the 40 ppm to 100 ppm range are seen (Table 1-1) for structures of the type $S=P(OR')_3$, where R' is an alkyl or aryl group, whereas structures containing O=P

give rise to shifts in the 35 ppm to -25 ppm range (*1-19, 1-23*).

Figure 1-9 shows the ^{31}P MAS spectra of the 136 day-old version of the sample represented in Figure 1-7, but with substantially faster MAS (4.5 kHz *vs.* 1 kHz in Figure 1-7). The largest peak (61 ppm) in the ^{31}P DP-MAS spectrum (Figure 1-9C) after 136 days is due to unreacted chlorpyrifos; again, it is not observed convincingly by cross polarization. There is some intensity near this region of the corresponding CP-MAS ^{31}P spectrum (Figure 1-9D) that may be due to the apparently small amount of hydrolyzed chlorpyrifos (**II**) seen at about 53 ppm in the ^{31}P spectrum of the DMSO-d_6 extract (Figure 1-8A). In both the DP-MAS and CP-MAS spectra, a small peak is seen at about 27 ppm, which probably represents the S,O-isomerized pesticide (**V**). Spectral intensity also appears at about -5 to -10 ppm in Figure 1-9D; this may represent oxon (**VI**), or other O=P structures, such as organic phosphates or phosphates incorporated into the kaolinite structure. In the DMSO-d_6 extract no peaks were seen in this spectral region by liquid-solution ^{31}P NMR (Figure 1-8A). Apparently the phosphorus species giving rise to the intensity near –10 ppm in the solid-state ^{31}P MAS spectra are not readily extracted in two hours by DMSO-d_6. Clearly, decomposition occurs in chlorpyrifos adsorbed on kaolinite (with 1.1 % w/w water), albeit quite slowly.

The slow decomposition of chlorpyrifos (9.6 % w/w) sorbed on *partially-hydrated Ca-montmorillonite* (STx-1 with 5 % water by weight) was investigated over a period of almost four years. Figure 1-10 shows ^{31}P DP-MAS and CP-MAS spectra obtained after 1 day and 3.7 years. No decomposition products are apparent after one day storage at room temperature in the dark; no CP-MAS signals are observed even with about 20 hours of signal averaging. However, it is clear from Figures 1-10C and 1-10D that after 3.7 years

of storage some chlorpyrifos decomposition has occurred. The tallest peak (61 ppm) seen in the DP-MAS spectrum (Figure 1-10C), not seen by CP-MAS (Figure 1-10D), is due to the highly mobile, adsorbed chlorpyrifos phase noted above with chlorpyrifos/kaolinite. This apparently physisorbed-chlorpyrifos peak contributes less than half of the total integrated intensity of the DP-MAS spectrum; thus more than half of the chlorpyrifos (not lost through volatilization) has decomposed to at least three different phosphorus-containing species. In addition to a small amount of aryl-hydrolyzed product (**II**), represented by the peak around 55 ppm (mostly easily seen by CP-MAS), peaks are seen at 30 ppm, 20 ppm and 4 ppm, and a broad intensity is noted between zero and –10 ppm. The peak at 30 ppm is probably due to one of the S,O-exchanged isomers (**IV** and/or **V**); the other S,O-exchanged isomer may be responsible for the peak at 20 ppm in the ^{31}P MAS spectra after 3.7 years.

When the sample represented in Figures 1-10C and 1-10D was extracted by acetone-d_6 for two hours at room temperature, only three peaks were seen (at 61, 27 and 24 ppm) in the extract (Figure 1-8B). DMSO-d_6 extraction gave the same results. The 61 ppm peak is due to unreacted chlorpyrifos, while the latter two are thought to be due to **IV** and **V**, the S,O-exchanged isomers. It appears that these peaks are shifted to 30 and 20 ppm, respectively, when chlorpyrifos is adsorbed on Ca-montmorillonite (5 % w/w water content).

The phosphorus-containing species remaining adsorbed on Ca-montmorillonite after acetone-d_6 extraction (and ten minutes drying in air) were examined by DP-MAS and CP-MAS ^{31}P NMR (Figure 1-11). From these experiments, it is clear that much of the phosphorus-containing material was not extracted. About 80 % of the unreacted

chlorpyrifos (61 ppm in the DP-MAS spectrum) was extracted, but only about 50 % of the species responsible for the 30 ppm peak. It appears that less than 10 % of the species giving rise to the 20 ppm peak was extracted. The intensity at 4, -5 and -10 ppm in the spectra of the solid samples appears to be unaffected by the acetone-d_6 extraction; no peaks were observed in this region of the extract's spectrum (Figure 1-8B). The post-extraction solid-state spectra (Figure 1-11) indicate that the small amount of intensity near 55 ppm in the spectrum of the extraction residue, attributed to the aryl-hydrolysis product (**II**), is also unaffected by the acetone-d_6 extraction.

To investigate further the appearance and fate of aryl-hydrolyzed chlorpyrifos (**II**) on Ca-montmorillonite, compound **II** (as the potassium salt) was loaded (9.6 % by wt.) onto partially-hydrated (5 % w/w water) Ca-montmorillonite. The DP-MAS and CP-MAS ^{31}P NMR spectra obtained after 1 day and 102 days are shown in Figure 1-12. After 1 day, only a single peak at about 45 ppm is observed by both DP and CP techniques. This is the same chemical shift observed for pure solid **II** (as the potassium salt). Apparently, adsorbed aryl-hydrolyzed chlorpyrifos is much more 'solid-like' than the highly-mobile, adsorbed phase of unreacted chlorpyrifos. After 102 days, about 10 % of the adsorbed **II** has decomposed, giving rise to small peaks at –4 ppm and –11 ppm, similar to peaks seen in the long-term decomposition of chlorpyrifos on Ca-montmorillonite (Figure 1-10). When the 102 day old sample of **II** adsorbed on Ca-montmorillonite was extracted by DMSO-d_6 and by acetone-d_6, only unreacted **II** was observed at about 52 ppm by liquid-solution ^{31}P NMR; the species responsible for peaks near zero ppm were not extracted significantly by DMSO-d_6 or acetone-d_6.

Solid-state ^{31}P MAS NMR spectra of chlorpyrifos (10.2 % by weight) adsorbed on

partially-hydrated Zn-montmorillonite (4.2 % water by weight) show that detectable decomposition occurs within one day, as seen in Figure 1-13. After one day, the largest peak in the DP-MAS spectrum is due to adsorbed, but unreacted, chlorpyrifos, at a chemical shift of 60 ppm; this peak is missing in the corresponding CP-MAS spectrum. Physisorbed chlorpyrifos appears to exhibit sufficiently rapid atomic-level motion that $^{1}H \rightarrow ^{31}P$ cross polarization is extremely inefficient and essentially eliminated.

The DP-MAS and CP-MAS ^{31}P spectra of chlorpyrifos adsorbed on Zn-montmorillonite in Figure 1-13 show the presence of two chlorpyrifos decomposition products after only one day, i.e., a peak at 45 ppm and a broader peak at 27 ppm. The 45 ppm peak is thought to be due to hydrolyzed chlorpyrifos (**II**, resulting from aryl hydrolysis), while the broader 27 ppm resonance is probably due to S,O-isomerized chlorpyrifos (structures **IV** and/or **V**). These peaks (45 and 27 ppm) are detected by both DP-MAS and CP-MAS experiments, indicating that a least a portion of the responsible decomposition products exhibit less molecular motion than does physisorbed chlorpyrifos (60 ppm). Quantitative analysis (based on spectral deconvolution) of the DP-MAS spectrum after one day indicates that the 45 ppm peak represents about 15 % of the detected ^{31}P nuclei, whereas the 27 ppm peak accounts for about 9 % of the total spectral integral.

Figure 1-13 also includes DP-MAS and CP-MAS ^{31}P NMR spectra of a chlorpyrifos/Zn-montmorillonite sample prepared similarly to the one-day sample, but after aging 166 days at room temperature in the dark. In addition to a large reduction in the intensity of the 60 ppm peak due to physisorbed chlorpyrifos (as compared to the one day results in Figure 13), the 45 ppm peak due to hydrolysis product (**II** or **III**) is

substantially larger after 166 days. S,O-isomerization (structure **IV** and/or **V**) also apparently increased in time in this chlorpyrifos/Zn-montmorillonite sample, as indicated by the growth of the signal intensity near 25 ppm in Figures 1-13C and 1-13D.

Figure 1-13 shows the presence in the chlorpyrifos/Zn-montmorillonite sample, after 166 days of adsorption, of apparently two additional phosphorus-containing species that are not seen after only one day, with ^{31}P resonance intensity at about 3 ppm and –7 ppm. The chemical shift region near zero ppm is typical of inorganic and organic phosphates; thiophosphates have chemical shifts above 15 ppm (see Table 1-1), whether sulfur is present as P=S or P-SR or P-SAr (R = alkyl, Ar = aryl). Table 1-1 shows five different possible phosphate structures that lack sulfur and may be expected, on the basis of reported chemical shifts for similar compounds, to have a ^{31}P resonance near zero ppm. One of these five is the oxon form (**VI**), resulting from oxidation of chlorpyrifos. The other structures (**IX**, **X**, **XI** and **XV**) are the result of subsequent hydrolysis of the oxon form or hydrolysis of an S,O isomer of chlorpyrifos. Not included in Table 1-1 are the possible structures resulting from reaction with the clay, such as those involving Al–O–P linkages, or possible reaction with the Zn^{2+} cation.

Liquid-solution ^{31}P NMR was helpful for clarifying some of the problematic assignments mentioned above. Unreacted pesticide and its extractable residues were extracted from roughly 0.1 g of the 166 day old pesticide-loaded clay of Figures 1-13C and 1-13D, using 2.0 g of DMSO-d_6, followed by filtration. The liquid-solution ^{31}P NMR spectrum of the DMSO-d_6 extract (Figure 1-8C) shows four signals: unreacted chlorpyrifos at 61.6 ppm (confirmed by the addition of pure chlorpyrifos), hydrolyzed chlorpyrifos at 56.6 ppm (confirmed by addition of known material), an isomerization

product at 28.1 ppm (structures **IV** or **V**), and the hydrolysis product resulting from the isomerization product (17.1 ppm). The latter two assignments are tentative, as no authentic samples of these structures were available to add to the sample to confirm these assignments.

In Figure 1-8C the peaks at 56.6 ppm and 17.1 ppm appear broader than the other two peaks. This observation is consistent with the reported tautomerization of thiophosphoric acids, assuming that the increased linewidth is due to such a chemical exchange process. Two possibilities exist: either these peaks represent the two species that are interconverting and the chemical exchange is slow compared to the frequency separation of their resonances, or the chemical exchange is fairly rapid on the NMR timescale (a rate much faster than frequency separation of their resonances) and each of the peaks observed represents the exchange-averaged signal arising from tautomerization reactions (of each primary chlorpyrifos hydrolysis product, as shown for structures **II** and **III** in Table 1). The latter explanation seems more likely, since a solution of hydrolyzed chlorpyrifos (potassium salt of diethylthiophosphoric acid, **II**, prepared *in vitro* using ethanolic KOH) in DMSO-d_6 produces a single ^{31}P resonance at about 55 ppm (not shown), again with a larger than normal linewidth.

An attempt was made to prepare the S,O-isomerized products **IV** and **V** by thermally isomerizing chlorpyrifos. Refluxing a toluene solution of chlorpyrifos (at 105 ^{o}C) for 24 hours produced no decomposition products detectable by liquid-solution ^{31}P NMR, whereas 4 days at reflux produced a solution that yielded a spectrum (Figure 1-8D) with three small peaks: 26.4 ppm, 24.9 ppm and 23.7 ppm. The species represented by these peaks may include the two expected S,O-isomerized products, one of which is

apparently seen at 28.1 ppm when extracted into DMSO-d_6 from Zn-montmorillonite (Figure 1-8C). Other peaks seen in the ^{31}P spectrum of the heated toluene solution of chlorpyrifos include chlorpyrifos oxon (**VI**) at –6.7 ppm, a peak at 53.7 ppm that may be the aryl hydrolysis product (**II**) and a previously unseen peak at 69.3 ppm.

The 69.3 ppm peak is apparently not due to the bis aryl variation of chlorpyrifos (**XIX**), $S=P(OR)(OAr)_2$, which is expected to have a chemical shift of about 56 ppm. Instead, the 69.3 ppm peak is tentatively assigned as the O,O,O-triethyl phosphorothioate (**XX**), which is reported to have a chemical shift of 68.6 ppm in benzene-d_6 (*1-4*). Both the bis aryl and tris ethyl phosphorothioate structures are reported to be side products occurring during chlorpyrifos synthesis, though the ^{31}P spectrum (in DMSO-d_6; Figure 1-1) of the pure, crystalline chlorpyrifos showed no traces of these or any other impurities.

To test the assignment of species **II** for chlorpyrifos decomposition on Zn-montmorillonite, hydrolyzed chlorpyrifos (**II**) was adsorbed (10 % by weight) from ethanol solution onto Zn-montmorillonite (with 5 % water content by weight). The DP-MAS and CP-MAS ^{31}P NMR spectra of the resultant sample after 200 days at room temperature in the dark are shown in Figures 1-14A and 1-14B. These spectra confirm that the shift of hydrolyzed chlorpyrifos on partially-hydrated Zn-montmorillonite is 45 ppm (*vs.* 55 ppm in DMSO). In addition to this product, there may be a minor constituent responsible for small signals at -4 ppm in Figure 1-14A and 1-14B, a region associated in Table 1-1 with phosphate structures that lack sulfur. These spectra appear very similar to those for the 8-day old material (spectra not shown), except the peak at about 6 ppm is apparently larger after 200 days. No sign of S,O-isomerized structures are detected around 25 ppm; evidently **II** decomposes on this partially-hydrated Zn-montmorillonite

by slow hydrolysis to a sulfur-free phosphate structure, perhaps monoethylphosphoric acid (**X**; $O=P(OEt)(OH)_2$) or inorganic phosphates, or **II** may be oxidizing to a hydrolyzed oxon form.

Figures 1-14C and 1-14D also show ^{31}P NMR spectra of a sample of chlorpyrifos adsorbed on partially-hydrated Zn-montmorillonite (10 % chlorpyrifos and 5 % water by weight) that was stored in a vial for 3.7 years at room temperature in the dark. Most of the physisorbed chlorpyrifos has decomposed, as seen by the small size of the peak at 61 ppm in the DP-MAS spectrum. Quantitative comparison of the total integral in the DP-MAS spectrum in Figure 1-14C with the integral of a corresponding spectrum of a reference (pure chlorpyrifos, Figure 1-1A), and taking into account quantitative factors such sample mass, number of scans, etc., leads to the conclusion that not more than 5 % - 15 % of the expected ^{31}P DP-MAS signal is missing after 3.7 years.

In Figures 1-14C and 1-14D one sees that after 3.7 years adsorption on partially-hydrated Zn-montmorillonite, the major chlorpyrifos decomposition products include the aryl hydrolysis product (**II**) at 45 ppm, one or more of the S,O-isomerized structures (**IV** and/or **V**) with a peak maximum at 22.9 ppm, and a species responsible for a peak at 2.5 ppm that may be inorganic phosphate or ethyl phosphate structures. Some other small peaks also appear to be present at 32.0 ppm (tentatively assigned to another S,O-isomerized structure) and at about –10 ppm, although the latter is partially overlapped with a spinning sideband at about –17 ppm. The –10 ppm chemical shift is assigned to **VI**, the oxon form of chlorpyrifos.

The 3.7 year old chlorpyrifos/Zn-montmorillonite sample represented in Figure 1-14C was chosen to measure the $^{1}H \rightarrow {}^{31}P$ cross polarization time constants for the major

CP-MAS detected species, because the decomposition products have stronger CP-MAS signals than those in the less-aged samples. Accordingly, variable-contact-time experiments were carried out on this sample. The peak intensities $M(\tau)$ as a function of CP contact time τ were fitted to equation (1-1), where T_{HP} is the time constant that characterizes $^{1}H \rightarrow {}^{31}P$ polarization transfer and $T_{1\rho}$ is the proton spin-lattice relaxation time in the rotating frame, which characterizes the

$$M(\tau) = M^{*} [\exp(-\tau/T_{1\rho}) - \exp(-\tau/T_{HP})] \quad (1)$$

process that is responsible for the disappearance of CP-MAS signal at longer contact times (*1-31*). M^{*} is the quantity of prime interest for quantitative analysis by CP-MAS, and is the CP signal that one would achieve if $^{1}H \rightarrow {}^{31}P$ polarization transfer were infinitely fast and ^{1}H rotating-frame spin-lattice relaxation were infinitely slow. The results are included in Table 1-2, where it is seen that all four measured peaks show similar proton $T_{1\rho}$ values, suggesting that all the phosphorus atoms receive polarization from the same proton spin bath. Although an accurate fitting of the variable-contact-time data to Equation 1 yields M^{*} values with quantitative significance, a simpler approach to quantitation is available *via* DP-MAS experiments in which sufficiently long relaxation (repetition) delays are used during data collection so that all signal integrals are proportional to concentration. In interpreting the results summarized in Table 1-2, one can recall that the T_{HP} value is related to the strength of the heteronuclear dipolar coupling between ^{1}H and ^{31}P, reflecting ^{1}H-^{31}P internuclear distances and possibly partial averaging by atomic-level motions, if present. The greater the value of T_{HP}, the stronger the dipolar interaction and the faster the growth of ^{31}P magnetization during cross polarization with short contact times. ^{1}H $T_{1\rho}$ is the rotating-frame spin lattice relaxation

time constant for the ^{1}H nuclei involved in CP to a given ^{31}P spin set and typically determines the rate at which CP intensities diminish as the contact time τ is increased.

Although ^{31}P T_1 values were not directly determined, the DP-MAS ^{31}P signal intensities were measured as a function of relaxation delay (for both aged and freshly prepared chlorpyrifos/Ca-montmorillonite and chlorpyrifos/Zn-montmorillonite; spectra not shown), from which it is apparent that the signal intensities do not change if the experimental relaxation delay is one second or longer. Thus, a two-second relaxation delay is sufficient for obtaining quantitative results (while keeping the amplifier duty cycle well under 5 %).

A freshly prepared sample of chlorpyrifos adsorbed onto partially-hydrated Zn-montmorillonite (10.2 % by weight chlorpyrifos, and 4.2 % by weight water) was used to follow the kinetics of initial disappearance of physisorbed chlorpyrifos. Figure 1-15 shows the DP-MAS ^{31}P NMR spectra obtained. Analogous CP-MAS results are given in the Figure 1-16. Figure 1-17 shows a plot of DP-MAS peak heights of the three major peaks observed as a function of time expired since sample preparation, during the first 130 hours of chlorpyrifos decomposition. These three peaks are assigned as physisorbed chlorpyrifos (61 ppm), the aryl hydrolysis product (**II**, 45 ppm) and one or more of the S,O-isomerized structures (**IV** and/or **V**, 28 ppm). The unreacted-chlorpyrifos peak at 61 ppm decreases monotonically during the reaction, while the product peaks increase in intensity. At short decomposition times, the product peaks (45 and 28 ppm) are quite small (after 20 hours about 5 % and 1 %, respectively, of the height of the unreacted chlorpyrifos peak), and thus are much more susceptible to random errors associated with signal-to-noise considerations.

The disappearance of chlorpyrifos from various clay samples is shown graphically in Figure 1-18; corresponding plots of log peak heights *vs.* time, and inverse peak heights *vs.* time are shown in Figures 1-19 and 1-20. The kinetics of disappearance of chlorpyrifos when sorbed on clay samples will be discussed in Chapter 2, along with kinetic results for the disappearance of methyl parathion from clay samples.

Figure 1-21 shows DP-MAS and CP-MAS ^{31}P NMR spectra of chlorpyrifos loaded (9.3 % by weight) onto *partially-hydrated Al-montmorillonite* (3.6 % water by weight) after one day and 87 days. After one day, only about 2 % of the adsorbed chlorpyrifos appears to have reacted. Products include small (or overlapping) peaks at about 45 ppm and 28 ppm, which may be assigned as the aryl hydrolysis product (**II**) and one of the S,O-isomerized structures (**IV** and **V**). By comparing the DP-MAS and CP-MAS spectra after one day, one again sees that the 61 ppm peak due to physisorbed (i.e., adsorbed but unreacted) chlorpyrifos is mostly missing in the CP experiment. Again, it is presumed that atomic-level motions interfere with CP dynamics. One difference may be noted in the CP-MAS spectrum of Figure 1-21B from those seen in Figures 1-10 and 1-13: there is resonance intensity observed at 59 ppm, close to but different from the ^{31}P chemical shift of 61 ppm observed by DP-MAS for physisorbed chlorpyrifos.

The largest peak (5 ppm) in both the DP-MAS and CP-MAS spectra (Figure 1-21C and D) of the chlorpyrifos/Al-montmorillonite sample after 87 days (in the dark at room temperature) is attributed to sulfur-free and partially hydrolyzed organophosphate esters (such as **IX**, **X** and **XV**). Additional peaks are tentatively assigned as follows: the peak at 24 ppm (with a possible shoulder at 31 ppm) may be due to S,O-isomerization products (**IV** and **V**), and the broad resonance at about –7 ppm is assigned to the oxon

form of chlorpyrifos (**VI**). The largest difference between the DP-MAS and CP-MAS spectra in Figure 1-21 is seen in the 60 ppm peak due to physisorbed but unreacted chlorpyrifos, which is large in the DP-MAS spectrum, but small or insignificant in the CP-MAS counterpart. The CP-MAS spectrum (Figure 1-21D) shows some unresolved intensity in the 65 to 55 ppm region; this may be due to different forms of physisorbed chlorpyrifos.

DP-MAS and CP-MAS ^{31}P NMR spectra (Figures 1-22 and 1-23) were obtained as a function of time during the first 74 (and 452) hours of reaction of chlorpyrifos adsorbed (10.0 % by wt.) on partially-hydrated Al-montmorillonite (4.3 % H_2O by wt.) stored at room temperature in the dark. As expected, the 25 ppm and 5 ppm product peaks grow with time in both the DP and CP spectra as the 61 ppm peak of physisorbed chlorpyrifos disappears from the DP-MAS spectrum. The results indicate that hydrolysis is not the predominant initial step when chlorpyrifos decomposes on partially-hydrated Al-montmorillonite, judging by the limited spectral intensity detected near 50 ppm. Figure 1-18 shows a plot of the unreacted-chlorpyrifos peak height *vs.* sample-storage time, shown as data points, and analogous results for other samples (*vide infra*).

The $^{1}H \rightarrow {}^{31}P$ dynamics of the chlorpyrifos/Al-montmorillonite sample after 11 days of storage/reaction investigated by variable-contact-time experiments, yielded results summarized in Table 1-2. In most organic solids, the number density of proton spins is sufficiently large, and thus the proton-proton internuclear distances sufficiently small, that all the protons in the material act as a homogeneous ^{1}H spin bath in typical multinuclear NMR experiments. In such a case only a single ^{1}H $T_{1\rho}$ value would be observed for all ^{31}P or ^{13}C peaks in a CP-MAS spectrum. In the chlorpyrifos/Al-montmorillonite sample

at least two distinct proton populations appear to be present, based on the observation of what appears to be significantly different ^{1}H $T_{1\rho}$ values associated with different ^{31}P resonances. These different proton populations may be a) clay protons (as framework hydroxyls, or the hydration sphere of the Al^{3+} cations), and b) hydrogens in the pesticide residues (aryl or ethoxy protons).

T_{HP} results shown on Table 1-2 for the variable-contact-time experiment for the 11-day chlorpyrifos/Al-montmorillonite sample are: 0.27 ms for the 59 ppm peak, 0.30 ms for the 25 ppm peak, and 0.31 ms for the 5 ppm peak. The standard errors associated with these values (about 10 %) are greater than the differences between the values, and thus, to within experimental uncertainty, all three peaks have the same T_{HP} value of about 0.30 ms. Also, the proton $T_{1\rho}$ values obtained for the 59 ppm and 25 ppm peaks are not significantly different (11.9 ms and 11.6 ms, respectively) from each other, but the 5 ppm peak has a significantly shorter ^{1}H $T_{1\rho}$ value of 8.2 ms. Since these two relaxation parameters, T_{HP} and $T_{1\rho}$, have different functional dependences on motion and geometry, it is not surprising that one of them is uniform over the sample while the other shows peak-to-peak variation. For all of the other samples studied by variable contact-time experiments, there are substantial peak-to-peak variations among *both* T_{HP} and $T_{1\rho}$.

DP-MAS and CP-MAS ^{31}P NMR spectra (Figure 1-24) of a similar sample of chlorpyrifos loaded (8.6 % by weight) onto partially-hydrated Al-montmorillonite (4.6 % water by weight) were also obtained after 3.8 years of storage/reaction in the dark at room temperature. In the DP-MAS spectrum the 60 ppm peak due to unreacted chlorpyrifos was found to represent only about 5 - 10 % of the total DP-MAS signal intensity after 3.8 years. The largest peak in both the DP-MAS and CP-MAS spectra in the 3.8-year sample

is a 5 ppm peak, with approximately 75 % of the DP-MAS signal area. The broad intensity in the region from 15 to 35 ppm appears to be due to two or more overlapping resonances, with apparent peaks at 31 and 24 ppm. Again, these peaks are thought to be due to S,O-isomerization products, but with greater linewidth and reduced intensity after 3.8 years relative to the 87-day sample. The –6 ppm peak (about 3 % of the total DP-MAS signal intensity), is assigned to the oxon, and is not much larger after 3.8 years than after 87 days. We conclude that the sulfur-free, partially-hydrolyzed phosphate species (5 ppm) appears to be the major long-term product for this sample of chlorpyrifos on partially-hydrated Al-montmorillonite.

A liquid-solution ^{31}P spectrum (Figure 1-25A) of the DMSO-d_6 extract of a chlorpyrifos/Al-montmorillonite sample shows only the 60.8 ppm peak of unreacted chlorpyrifos, after only one day of storage/reaction. (Evidently the small amounts of decomposition products shown in the solid-state spectra of Figures 1-24A and 1-24B were not extractable in detectable quantities.) For the 3.8 year-old sample, two phosphorus peaks are detected at 31 and 27 ppm (Figure 1-25B), assigned to the two S,O-isomerized products (**V** and **IV**). Not detected are the peaks at 5 ppm and –6 ppm that are seen in the MAS spectra of the parent solid sample (Figure 1-24). Apparently, the sulfur-free, partially-hydrolyzed or totally-hydrolyzed phosphates and the oxon form are not extracted by DMSO-d_6.

Figure 1-26 shows changes in the DP-MAS ^{31}P NMR spectrum of chlorpyrifos (9.8 % by weight) adsorbed on *partially-hydrated Cu(II)-montmorillonite* (5.1 % water by weight) during the first 43 hours of reaction in the dark at room temperature. As the 60 ppm peak assigned to physisorbed (unreacted) chlorpyrifos decreases in intensity, broad

peaks at about 21 ppm and –8 ppm grow over the 43 hour period. The peak at 21 ppm is tentatively assigned as an S,O-isomerized product (probably structure **IV**, based on model-compound chemical shifts), while the –8 ppm peak is typical for the oxon form (**VI**). Unresolved intensity at about 48 ppm and 32 ppm seems to increase with time, and the chemical shifts suggest the presence of a hydrolysis product (**II** or **III**) and another S,O-isomerized product (probably structure **V**), respectively. These species are represented by small, broad peaks that are partially or mostly overlapped with the more intense peaks at 60 ppm and about 21 ppm. Analogous CP-MAS ^{31}P spectra of the chlorpyrifos/Cu-montmorillonite sample during the first 43 hours of reaction (Figure 1-27) display qualitatively the disappearance of physisorbed chlorpyrifos and the growth of the decomposition product peaks during the reaction. The liquid-solution ^{31}P NMR spectrum of the DMSO-d_6 extract of the chlorpyrifos/Cu-montmorillonite sample after 13 hours (Figure 1-25C) shows only two detectable signals, which are attributed to unreacted chlorpyrifos (61 ppm) and one of the S,O-isomerized structures (20 ppm), probably structure **V**, corresponding to the assignments in the DP-MAS spectra of the chlorpyrifos/Al-montmorillonite samples. As noted above with the DMSO-d_6 extracts of chlorpyrifos adsorbed on Al-montmorillonite, no peaks are detected near 5 ppm or in the –5 to –10 ppm region. The sulfur-free hydrolyzed phosphates and oxon species that appear in these regions of the solid-sample spectra appear, to the detection level of the NMR experiment, to be unextractable by DMSO-d_6.

Figure 1-28 shows the DP-MAS and CP-MAS ^{31}P NMR spectra of a similar chlorpyrifos/Cu-montmorillonite sample (10.5 % by wt. adsorbed chlorpyrifos; 5.3 % by wt. water) after 3.8 years in the dark at room temperature. For comparison purposes,

Figure 1-28 also includes the spectrum of the sample represented in Figure 1-26 (9.8 % by wt. adsorbed chlorpyrifos; 5.1 % by wt. water on Cu-montmorillonite) after only one day. After 3.8 years, apparently no unreacted physisorbed chlorpyrifos is present; the signal intensity seen in the 50 to 70 ppm region of the DP and CP spectra is due to spinning sidebands of the peaks between zero and –25 ppm. Figure 1-28 shows that, after 3.8 years, most of the intensity in the ^{31}P spectrum is at –6 ppm and in a broader peak with a maximum at about –19 ppm. The former is probably due to the oxon of chlorpyrifos (**VI**), while the identity of the latter is unknown (maybe a mineralized form of phosphate). Extraction of the 3.8 year old sample by DMSO-d_6 yielded no detectable liquid-state phosphorus signals after 19 hours of signal averaging (8160 scans).

^{27}Al MAS NMR. ^{27}Al MAS spectra were obtained on several samples of loaded and unloaded kaolinite and montmorillonite clays (Figure 1-29). ^{27}Al is a relatively sensitive nucleus for NMR observation, although its quadrupolar behavior in the solid state usually gives rise to extensive line broadening and arrays of spinning sidebands (*1-32,1-33*). In order to minimize the overlap of centerbands with spinning sidebands, solid state ^{27}Al NMR usually requires high magnetic fields and very rapid spinning (> 15 kHz). Octahedral aluminum atoms buried within the clay layer structure yield peaks at about zero ppm (relative to aqueous $Al(NO_3)_3$ reference), as seen in Figure 1-29, which presents the ^{27}Al MAS spectra of the 'as received' kaolinite (Figure 1-29A) and the same 'as received' kaolinite with sorbed chlorpyrifos (2 % by wt.; Figure 1-29B). The small amount of aluminum in tetrahedral substitution sites appears as intensity between 50 and 80 ppm. These tetrahedral sites are thought to be more accessible to adsorbed organophosphate pesticides (*1-34*). There appears to be no significant change in the ^{27}Al

spectrum upon loading chlorpyrifos on 'as received' kaolinite.

Figure 1-29 also compares the ^{27}Al MAS spectrum of 'as received' Ca-montmorillonite (5.0 % water by wt.; Figure 1-29C) with the ^{27}Al MAS spectra of the same Ca-montmorillonite clay with sorbed chlorpyrifos (9.6 % by wt.; Figure 1-29D) or sorbed aryl-hydrolyzed chlorpyrifos, **II** (10 % by wt.; Figure 1-29E). There seems to be a significant effect on the ^{27}Al NMR lineshape in the tetrahedral aluminum region when chlorpyrifos is sorbed on this partially-hydrated Ca-montmorillonite; sorption of **II** appears to have less effect on the tetrahedral aluminum region of the spectrum. The origin of this effect was not explored.

Figure 1-29 also shows the ^{27}Al MAS spectra of Al-montmorillonite, Cu(II)-montmorillonite and Zn-montmorillonite, without chlorpyrifos sorption (Figures 1-29F through 1-29H). Note that although the dominant octahedral aluminum peak appears to be invariant in this series, there are some differences in the lineshape in the region between 50 and 80 ppm (the tetrahedral aluminum region).

Since the ^{27}Al MAS spectra shown in Figure 1-29 were rather similar, detailed studies were not pursued.

Discussion

The ^{31}P MAS spectra displayed above show a variety of chemical and physical states of phosphorus-containing species deposited on the substrates studied. The spectra shown in Figure 1-4 suggest that the spectral component with an extensive MAS sideband pattern represents chlorpyrifos that is not adsorbed by the samples, existing as a crystalline chlorpyrifos phase. Apparently, a loading level of about 10 % w/w

chlorpyrifos exceeds the adsorption capacity of the kaolinite, humic acid and whole soil substrates. In the case of kaolinite, this seems reasonable, considering the limited water adsorption capacity (6.2 % w/w) observed for this kaolinite sample humidified for over four months. Kaolinite is known (*1-31, 1-32*) to resist intercalation of adsorbed molecules during mild experimental conditions, and thus any adsorption is limited to the exterior surfaces of the kaolinite structure, which has an adsorption capacity for chlorpyrifos that is apparently exceeded by a 10 % loading level. That fraction of chlorpyrifos that is adsorbed on kaolinite undergoes some type of rapid atomic-level motion (or chemical exchange) that efficiently averages to zero both the ^{31}P chemical shift anisotropy (CSA) and the heteronuclear dipolar interaction between protons and phosphorus (Figure 1-4).

Hexane washing of the samples of chlorpyrifos adsorbed on kaolinite, humic acid and whole soil removed from the CP-MAS ^{31}P spectra the extensive spinning sideband arrays due to unadsorbed crystalline chlorpyrifos. In fact, after the hexane wash, none of these three materials exhibited any CP-MAS ^{31}P signals, and the humic acid material also showed no DP-MAS ^{31}P signals. The chlorpyrifos/whole soil sample and the chlorpyrifos/kaolinite sample, on the other hand, produce sharp DP-MAS ^{31}P signals at about 61 ppm that persist even after hexane washing. Thus, chlorpyrifos is not adsorbed substantially on this humic acid, but is apparently adsorbed onto the clay portion of the whole soil, but again in the highly motional state seen for chlorpyrifos adsorbed onto kaolinite (or Ca-montmorillonite). The Uncomphagre whole soil appears to have chlorpyrifos adsorption characteristics determined primarily by its clay content.

The extensive MAS sideband patterns seen in Figures 1-1C, 1-4A, 1-4C, 1-4D and 1-4E exemplify the consequences of insufficiently rapid spinning, which may also be

responsible for the poorly defined spectrum of Figure 1-7D. Spinning sidebands in the MAS spectrum arise if the spinning speed is less than the frequency range determined by the chemical shift anisotropy (CSA), the range of values of the principal elements of the chemical shift tensor.

The isotropic chemical shift is the average of the three principal elements of this tensor. Because of rapid atomic-level motion, only the isotropic chemical shift value is observed in liquid samples (or in solid samples with sufficiently rapid atomic-level motion. This is the situation for the adsorbed, but unreacted chlorpyrifos seen in the DP-MAS ^{31}P spectra (Figures 1-7A and 1-7C). In these spectra, the spinning sidebands are small or non-existent. Note that the same atomic-level motions that average out the chemical shift orientation dependence will also serve to attenuate or average to zero the ^{1}H-^{31}P heteronuclear dipolar interactions necessary for cross polarization – hence, the absence of CP-MAS ^{31}P peaks in Figure 1-4G.

The decomposition products seen by CP-MAS ^{31}P NMR for the 108-day chlorpyrifos/kaolinite sample in Figure 1-7D apparently manifest much more limited atomic-level motions than does adsorbed, but unreacted chlorpyrifos. As with crystalline chlorpyrifos in CP-MAS experiments (see Figures 1-1D and 1-2A), the CSA gives rise to spinning sideband arrays spanning more than 100 ppm, resulting in unresolved intensity in Figure 1-7D. The faster the spinning rate (which is the frequency separation between MAS sidebands), the fewer the spinning sidebands, and the more intensity is present in the centerband at the isotropic chemical shift, as seen in a comparison of Figures 1-7, 1-9 and 1-10.

The peak maximum in Figure 1-13 is at 23 ppm after 166 days, whereas after only

one day the peak maximum was at 27 ppm. The entire 15 to 35 ppm region in the ^{31}P spectra after 166 days is complex in lineshape. The observed signals probably involve isotropic chemical shift heterogeneity (a range of isotropic chemical shifts for a single compound), reflecting a range of chemical environments possible when the phosphorus-containing species is adsorbed by the clay. Two or more different decomposition products may contribute signal intensity in the 15 to 35 ppm region, such as the two expected S,O-isomerization products (structures **IV** and/or **V**). The apparent shift in the position of the peak maximum after 166 days may be due to a change in the relative amounts of these isomers.

It was suggested in the *Results* section that the 69.3 ppm peak in the ^{31}P NMR spectrum of the toluene solution of chlorpyrifos that had been refluxed four days (Figure 1-8) is due to O,O,O-triethyl phosphorothioate. If this is true, this species may have formed by a thermally activated transesterification reaction between two chlorpyrifos molecules, which would produce the bis aryl structure as the other product:

$$\underset{\mathbf{I}}{2\ S{=}P(OEt)_2(OAr)} \rightarrow \underset{\mathbf{XX}}{S{=}P(OEt)_3} + \underset{\mathbf{XIX}}{S{=}P(OEt)(OAr)_2} \qquad (2)$$

In this interpretation, the 53.7 ppm peak could be assigned to either bis aryl (**XIX**) or aryl hydrolyzed chlorpyrifos (**II**), as both are expected to exhibit ^{31}P chemical shifts in toluene near 55 to 56 ppm. The 53.7 ppm peak is rather narrow; however, compound **II** exhibits increased linewidth in DMSO-d_6 solution due to the following tautomerization reaction (*1-10*):

$$(EtO)_2P(=S)OH \leftrightarrows (EtO)_2P(=O)SH \qquad (3)$$

No oxon, for which a ^{31}P chemical shift is expected at about -5 ppm, appears to be

present in the DMSO-d_6 extract of the 166-day sample of chlorpyrifos/Zn-montmorillonite, although there are at least two peaks near zero ppm in the spectrum of the solid precursor sample (Figures 1-13C and 1-13D). Evidently, the phosphorus-containing compounds contributing resonance intensity near zero ppm in Figure 1-13 are not extractable by DMSO-d_6; the phosphorus atoms involved may be incorporated into the clay framework, or may in some other way be strongly chemisorbed.

Considering the spectra shown in Figures 1-13 through 1-16, it appears that decomposition of chlorpyrifos adsorbed on partially-hydrated Zn-montmorillonite (5 % water by weight) starts within hours, with the aryl hydrolysis product (**II**) and one or more of the S,O-isomerized structures (**IV** and/or **V**) as the initial products. Within 166 days detectable amounts of sulfur-free phosphates are seen, tentatively identified as inorganic phosphates and oxon (**VI**). After 3.7 years, more of each of these products is present, except the amount of **II** has decreased. It is not clear whether the decomposition reactions are still continuing slowly after almost four years, or whether the sample will remain unchanged hereafter. The molar ratio of adsorbed water to adsorbed chlorpyrifos in the original sample was 9.7 to 1, whereas complete hydrolysis of each adsorbed chlorpyrifos molecule would require 4 molecules of water. Thus, stoichiometrically the initial sample contained sufficient water to completely hydrolyze all the chlorpyrifos to inorganic phosphates, assuming that all the adsorbed water is available for hydrolysis reactions; however, adsorption onto the clay (by intercalation) may be so strong that much of the water may be effectively unavailable for taking part in hydrolysis reactions.

The spectra in Figures 1-21 through 1-24, suggest that the major mode of decomposition of chlorpyrifos on partially-hydrated Al-montmorillonite is S,O-

isomerization (24-31 ppm intensity) followed by hydrolysis to a sulfur-free partially-hydrolyzed phosphate (5 ppm). Little or no aryl hydrolysis product (**II**) is detected, suggesting that either aryl hydrolysis is not an important initial decomposition reaction, or any **II** formed is immediately hydrolyzed further.

Several reports in the literature indicate that chlorpyrifos and similar organothiophosphate pesticides exhibit pseudo-first order hydrolysis kinetics, based on the disappearance of extractable unreacted pesticide (*1-14*). Alkaline hydrolysis of organophosphate esters (OPE) is generally accepted as being described by second-order overall rate expressions that are first-order in both OPE and hydroxide concentrations (*1-33*). Acid and neutral hydrolysis of chlorpyrifos typically occurs more slowly, but frequently also exhibits pseudo-first order kinetics (*1-14*).

The results shown in Figures 1-17 through 1-20 for a chlorpyrifos/Zn-montmorillonite sample, and analogous results obtained for other samples, do not clearly identify the kinetic orders relevant to these systems. Some regions of each plot can be described as zero-order, first-order, or second-order kinetics, and the data are not sufficiently numerous or precise to permit a clear kinetics interpretation. Nevertheless, it is useful to compare these systems relative to each other. This is accomplished by estimating the ratio of the initial rate to the initial concentration for each sample that was studied as a function of time, by calculating the slope, dC/dt, at the extrapolated point of zero time. The results of this analysis are summarized in Table 1-2.

Several conclusions are immediately obvious from Table 1-2 and Figure 1-18. First, the cation identity can strongly affect the initial pesticide decomposition rates. Among the partially-hydrated clays studied as a function of time, chlorpyrifos

decomposition on Al-montmorillonite and Cu(II)-montmorillonite is significantly faster than when sorbed on three partially-hydrated Zn-montmorillonite samples. Second, the water content can also affect the decomposition rate. For chlorpyrifos adsorbed on Zn-montmorillonite (the system studied for which samples were prepared with three different water contents), the disappearance of the physisorbed pesticide was initially fastest at lower water content, but apparently nearly the same for the higher water contents. Similar observations have been reported (albeit at much lower pesticide loading levels) for the decomposition of other organothiophosphate pesticides on clays, as determined by extraction followed by GC/MS analysis (*1-34*). One possible explanation for the slowing of decomposition with increasing water content is based on the competition between water and unreacted chlorpyrifos for the adsorption sites which catalyze the decomposition reactions observed. Third, the predominant mode of decomposition of chlorpyrifos is quite different for the different clay samples. This situation can be summarized as follows:

partially-hydrated clay	*predominant chlorpyrifos decomposition mode*	*secondary chlorpyrifos decomposition mode*
kaolinite	oxidation	hydrolysis, mineralization
Ca-montmorillonite	isomerization	mineralization
Zn-montmorillonite	hydrolysis	all
Al-montmorillonite	mineralization	isomerization
Cu(II)-montmorillonite	oxidation	isomerization, mineralization

The Al^{3+}-exchanged montmorillonite appears to favor mineralization, i.e., the incorporation of phosphorus into the mineral framework. This may reflect the favorable energetics of P-O-Al bond formation; aluminum phosphate species such as ALPO-5 are

well known and very stable microporous solids (*1-35*). The Cu(II)-montmorillonite, on the other hand, appears to catalyze oxidation of chlorpyrifos to the oxon form. Among the exchangeable metal cations involved in this study, only copper exhibits more than one stable cation form. Aqueous Cu^{2+} cations are known to be oxidizing agents and catalysts for oxidation reactions (*1-9, 1-36*).

Summary and Conclusions

The solid-state ^{31}P MAS NMR techniques (CP-MAS and DP-MAS) used in this study show applicability to the detection and characterization of organophosphate pesticides and their residues in kaolinite and cation-exchanged montmorillonites. Solid-state ^{13}C CP-MAS and ^{27}Al MAS NMR were found to be less informative and solid-state ^{1}H NMR techniques also appear to be much less promising.

Pesticide loading levels (1 – 10 % w/w) that are very much higher than typically found in the environment were used to facilitate ^{31}P NMR detection of less-than-dominant decomposition species. Although no claim is made here that the empirical rate constants or decomposition product distributions determined in this study are directly indicative of the behavior at lower concentrations, these high loading-level results should still be of value in that they provide fundamental information on the types of decomposition reactions and physico-chemical states that may occur at any loading level.

Solid-state ^{31}P NMR results indicate that a loading level of ten percent by weight chlorpyrifos exceeds the adsorption capacity of the soil, humic acid and kaolinite tested, but not the various cation-exchanged montmorillonites. This pattern is consistent with intercalation into the montmorillonites, but only surface adsorption on kaolinite.

Chlorpyrifos was found to physisorb initially on kaolinite and various cation-exchanged montmorillonites in a state with rapid liquid-like molecular-level motion, as evidenced by the sharp DP-MAS ^{31}P NMR signal and lack of CP-MAS ^{31}P signal. Subsequent decomposition led to a variety of decomposition products, including the products of hydrolysis reactions, isomerization reactions and oxidation reactions; mineralization also appears to occur in some cases. The predominant mode of decomposition of chlorpyrifos sorbed on partially-hydrated clays varies with the clay, the cation form, and the water content. On kaolinite, decomposition appears to be mostly oxidation, whereas on Ca-montmorillonite, decomposition is mostly isomerization. On Zn-montmorillonite, Al-montmorillonite and Cu(II)-montmorillonite, decomposition was predominately hydrolysis, mineralization and oxidation, respectively. Of the clays used in this study, initial chlorpyrifos decomposition was the slowest on kaolinite and Ca-montmorillonite. The fastest initial decomposition of chlorpyrifos occurred on Al-montmorillonite and Cu(II)-montmorillonite, but was slower on various Zn-montmorillonite samples.

Chapter 1 Literature Cited

(1-1) Brown, A. E., Ed. *Pesticide Notes*: *Maryland Cooperative Extension Newsletter* **2000**, *19*, 1.

(1-2) Yaron, B. *Soil Sci.* **1978**, *125*, 210.

(1-3) Kamiya, M.; Mitsuhashi, S.; Makino, M. *Chemosphere* **1992**, *25*, 1783.

(1-4) Mingelgrin, U.; Saltzman, S.; Yaron, B. *Soil Sci. Soc. Am. J.* **1977**, *41*, 519.

(1-5) Fukuto, T. R.; Hornig, E. O.; Metcalf, R. L. *J. Agric. Food Chem.* **1964**, *12*, 169.

(1-6) Greenhalgh, R.; Blackwell, B. A.; Preston, C. M.; Murray, W. J. *J. Agric. Food Chem.* **1983**, *31*, 10.

(1-7) Brzak, K. A.; Harms, D. W.; Bartels, M. J.; Nolan, R. J. *J. Anal. Toxicol.* **1998**, *22*, 203.

(1-8) Racke, K. D.; Steele, K. P.; Yoder, R. N.; Dick, W. A.; Avidov, E. *J. Agric. Food Chem.* **1996**, *44*, 1582.

(1-9) Awasthi, M. D.; Prakash, N. B. *Pestic. Sci.* **1997**, *50*, 1.

(1-10) Kabachnik, M. I.; Mastrukova, T. A.; Shipov, A. E.; Melentyeva, T. A. *Tetrahedron* **1960**, *9*, 10.

(1-11) Pusino, A.; Gessa, C.; Kozlowski, H. *Pestic. Sci.* **1988**, *24*, 1.

(1-12) Mortland, M. M.; Raman, K. W. *J. Agric. Food Chem.* **1967**, *15* , 163.

(1-13) Blanchet, P. F.; St-George, A. *A. Pestic. Sci.* **1982**, *13*, 85.

(1-14) Macalady, D. L.; Wolfe, N. L. *J. Agric. Food Chem.* **1983**, *31*, 1139.

(1-15) Sanchez-Camazano, M.; Sanchez-Martin, M. J. *Clay and Clay Miner.* **1994**, *42*, 221.

(1-16) Shainberg, I. *Soil Sci. Soc. Am. Proc.* **1973**, *37*, 689.

(1-17) Coats, J. R. *ACS Symposium Series*, No. 459, **1991**, 10.

(1-18) Worthing, C. R.; Walker, S. B., Eds. *The Pesticide Manual*, 8th Ed., British Crop Protection Council, UK, 1987.

(1-19) Gay, I. D. *J. Magn. Reson.* **1984**, *58*, 413.

(1-20) Bielawski, J.; Casida, J. E. *J. Agric. Food Chem.* **1988**, *36*, 610.

(1-21) Herzfeld, J.; Berger, A. E. *J. Chem. Phys.* **1980**, *73*, 6021.

(1-22) Herzfeld, J.; Berger, A. E. *Phil. Trans. R. Soc. London* **1980**, *B289*, 459.

(1-23) Mortimer, R. D.; Dawson, B. A. *J. Agric. Food Chem.* **1991**, *39*, 911.

(1-24) Krolski, M. E.; Bosnak, L. L.; Murphy, J. J. *J. Agric. Food Chem.* **1992**, *40*, 458.

(1-25) Maciel, G. E.; Bronnimann, C. E.; Hawkins, B. L. *Adv. Magn. Reson.* **1990**, *14*, 125.

(1-26) Dec, S. F.; Bronnimann, C. E.; Wind, R. A.; Maciel, G. E. *J. Magn. Reson.* **1989**, *82*, 454.

(1-27) Keeler, C. Ph.D. Dissertation, Colo. State Univ., 2001.

(1-28) Keeler, C.; Maciel, G. E. *Anal. Chem.* submitted.

(1-29) Keeler, C.; Maciel, G. E. *J. Molec. Struct.* **2000**, *550-551*, 297.

(1-30) Sanchez-Camazano, M.; Sanchez-Martin, M. J. *Soil Sci.* **1983**, *136*, 89.

(1-31) Kowalska, M.; Güler, H.; Cocke, D. *Sci. Total Environ.* **1994**, *141*, 223.

(1-32) Duer, M. J.; Rocha, J.; Klinowski, J.; *J. Am. Chem. Soc.* **1992**, *114*, 6867.

(1-33) Cox, J. R., Jr.; Ramsey, B. *Chem. Rev.* **1964**, *64*, 317.

(1-34) Saltzman, S.; Mingelgrin, U.; Yaron, B. *J. Agric. Food Chem.* **1976**, *24*, 739.
(1-35) Klinowski, J. *Encyclopedia of Nuclear Magnetic Resonance* Grant, D. M.; Harris, R. K. Eds., Wiley and Sons, Chichester, U. K., 1996, Vol. 5, p. 3098.
(1-36) Soma, Y.; Soma, M. *Environ. Health Perspectives* **1989**, *83*, 205.

Table 1-1. Some possible chlorpyrifos decomposition products and relevant ^{13}P chemical shifts from the literature.

	Structure (R = Et, Ar = 3,5,6-trichloro-2-pyridyl)	**^{31}P Chemical Shifts** [a]
I chlorpyrifos	$S=P(OR)_2(OAr)$	60.8 ppm
II	$S=P(OR)_2(OH) \leftrightarrows O=P(OR)_2(SH)$	55.2 (this study; as K^+ salt) 57 ppm (ref.; as Na^+ salt)
III	$S=P(OR)(OAr)(OH) \leftrightarrows O=P(OR)(OAr)(SH)$	48 ppm, estimate
IV	$O=P(OR)_2(SAr)$	22 ppm (if Ar = phenyl; also 22 ppm if SEt vs. SAr)
V	$O=P(OR)(SR)(OAr)$	24.6 ppm (for ethyl parathion; i.e., if R = Et and Ar = 4-nitrophenyl) 24.0 ppm (for ethyl parathion) 31.4 ppm if SR = S-n-propyl and Ar = -C_6H_4-SMe)
VI oxon	$O=P(OR)_2(OAr)$	- 6.5 ppm (for ethyl parathion)
VII	$S=P(OR)(OH)_2 \leftrightarrows O=P(OR)(OH)(SH)$	
VIII	$S=P(OH)_3 \leftrightarrows O=P(OH)_2(SH)$	32 to 34 ppm
IX	$O=P(OR)_2(OH)$	-1.3 ppm (+3.8 ppm as Na^+ salt)
X	$O=P(OR)(OH)_2$	
XI	$O=P(OH)_3$	0 ppm
XII	$O=P(OR)(SAr)(OH)$	
XIII	$O=P(SAr)(OH)_2$	
XIV	$O=P(OR)(OAr)(OH)$	
XV	$O=P(OAr)(OH)_2$	-5 ppm (if Ar = phenyl; 0 ppm if Na^+ salt and Ar = phenyl)
XVI	$O=P(SR)(OAr)(OH)$	24.9 ppm (if R = n-Pr and Ar = -C6H4-SMe)
XVII	$O=P(SR)(OH)_2$	
XVIII	$S=P(OAr)(OH)_2 \leftrightarrows O=P(OAr)(OH)(SH)$	
XIX bis	$S=P(OR)(OAr)_2$	56.2 ppm (for ethyl parathion) 56.3 ppm (for diazinon)
XX	$S=P(OR)_3$	68.6 ppm

[a] ppm relative to 85 % H_3PO_4

Table 1-2. NMR relaxation times of chlorpyrifos and its decomposition products adsorbed on partially-hydrated clays.

clay	chlorpyrifos % by wt.	H_2O % by wt.	peak (ppm)[a]	^{31}P T_1 (s)	^{1}H T_1 (s)	T_{HP} (ms)	^{1}H $T_{1\rho}$ (ms)
none	100 %	0	61	381	4.3	0.49	2.6×10^3
kaolin	10 % (exceeds adsorption capacity)	1.4 %	61	360 (unadsorbed) 0.76 (adsorbed)			
Ca-mont.	10 %	2.1 %	31	0.35	< 1	0.32 (+.21/-.12)	3.8 (+3.3/-1.8)
			20		< 1	0.38 (+.23/-.13)	3.5 (+2.4/-1.6)
			3		< 1	0.29 (+.08/-.06)	6.7 (+2.7/-1.8)
Zn-mont.	10.8 %	7.4 %		< 2	< 1		
Zn-mont.	10.2 %	4.2 %	47	< 2	< 1	0.27 (+.10/-.07)	21 (+49/-10)
			25			0.29 (+.21/-.13)	7 (+7/-3)
			4			0.4 (+.8/-.2)	5 (+8/-3)
Zn-mont.	10.3 %	2.3 %	47	< 2	< 1	0.52 (+.07/-.06)	8.9 (+0.4/-0.3)
			25			0.56 (+.39/-.23)	8.6 (+7/-3.4)
			4			0.37 (+.05/-.05)	6.4 (+1.3/-0.6)
Zn-mont.	10 %	5 %	62	< 2	< 1	0.6	4
			46			0.41 (+.07/-.07)	9.5 (+1.8/-1.4)
			23			0.35 (+.15/-.11)	8.2 (+3.8/-2.4)
			2			0.28 (+.07/-.07)	6.3 (+1.3/-1.1)
			- 13			0.25 (+.12/-.08)	6.9 (+2.9/-1.9)
Al-mont.	9.3 %	3.6 %	59	< 2	< 1	0.27	11.9
			25			0.30	11.6
			5			0.31	8.2
Cu-mont.	9.8 %	5.1 %		< 2	< 1		

[a] relative to 85 % H_3PO_4

Table 1-3. ^{1}H chemical shifts in DMSO-d_6 (ppm *vs.* TMS).

sample	**aromatic H**	**-CH_2-**	**-CH_3**
chlorpyrifos	8.7	4.4	1.4
hydrolyzed chlorpyrifos	7.6	3.7	1.1
extract of hydrolyzed chlorpyrifos on Ca-montmorillonite	7.5	3.7	1.1
extract of chlorpyrifos on hydrated kaolin (after 110 days)	8.7	4.3	1.4
extract of chlorpyrifos on hydrated Zn-montmorillonite after 27 days)	8.6, 7.8 (weak)	4.3, 3.7	1.3, 1.1
extract of chlorpyrifos on 'dry' Zn-montmorillonite (after 27 days)	8.7, 8.0	4.3, 3.7	1.3, 1.1

Table 1-4 . Packed powder X-ray diffraction results.

sample	**(001) spacing (Å)**
'as received' Ca-montmorillonite	15.17
chlorpyrifos on 'as received' Ca-montmorillonite	15.33
hydrolyzed chlorpyrifos on 'as received' Ca-montmorillonite	12.51
chlorpyrifos on 'dry' Zn-montmorillonite	15.02
chlorpyrifos on hydrated (10 % by wt.) Zn-montmorillonite	15.33
'dry' Zn-montmorillonite, sample (a)[a]	14.57
'dry' Zn-montmorillonite, sample (b)[a]	13.29
'dry' Cu-montmorillonite	12.20
'as received' kaolinite	7.11
sifted clay material from Uncomphagre soil	9.81, 7.11

[a] Prior to XRD analysis, sample (a) was exposed to atmospheric moisture several hours longer than sample (b).

Fig. 1-1

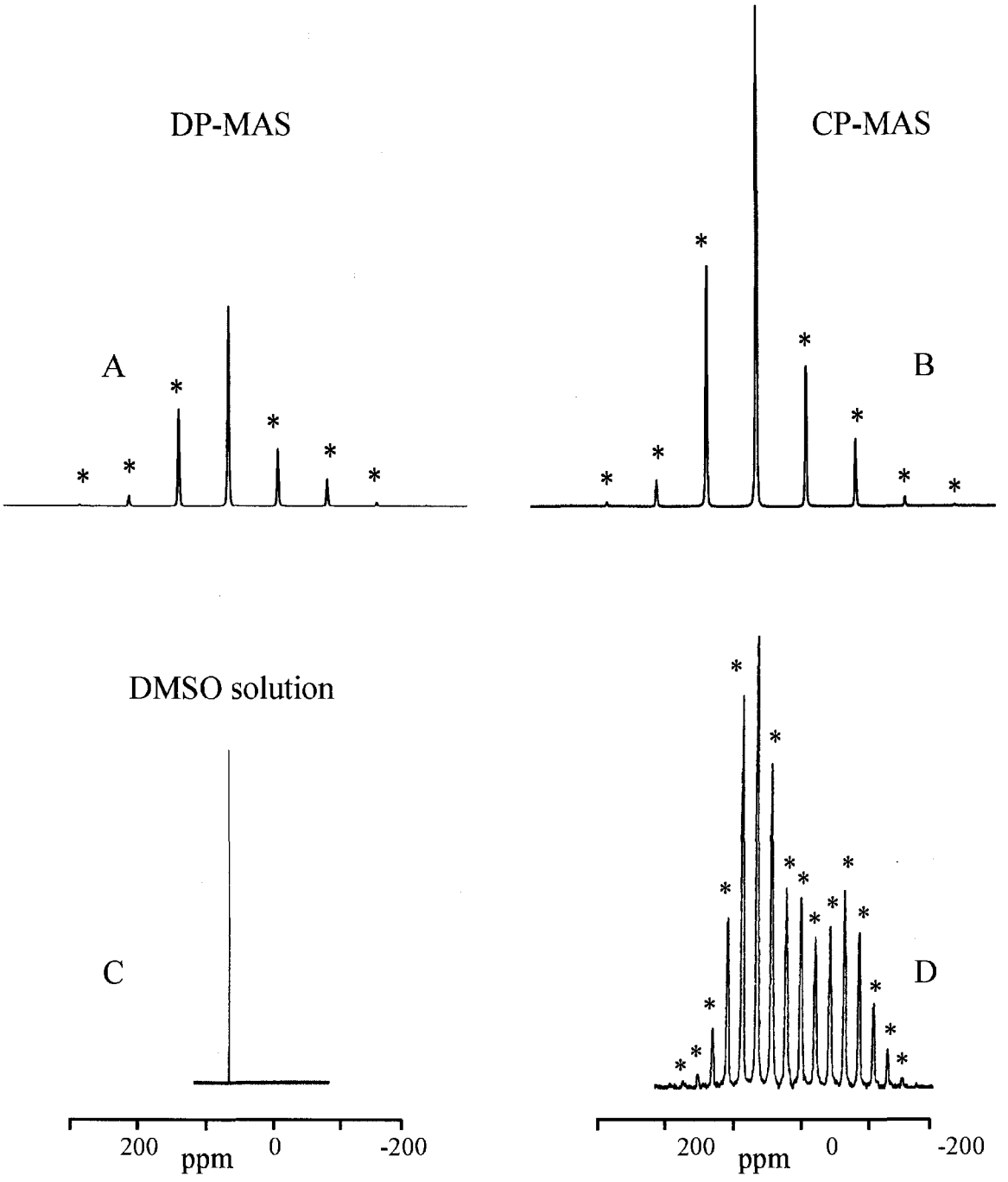

Figure 1-1. ^{31}P NMR spectra of pure chlorpyrifos: A) 60.7 MHz ^{31}P DP-MAS spectrum (4.1 kHz MAS). B) 60.7 MHz ^{31}P CP-MAS spectrum (4.1 kHz MAS). C) 242.9 MHz ^{31}P liquid-sample spectrum (with proton decoupling) of chlorpyrifos dissolved in DMSO-d_6. D) 60.7 MHz ^{31}P DP-MAS spectrum (1.0 kHz MAS).

Fig. 1-2

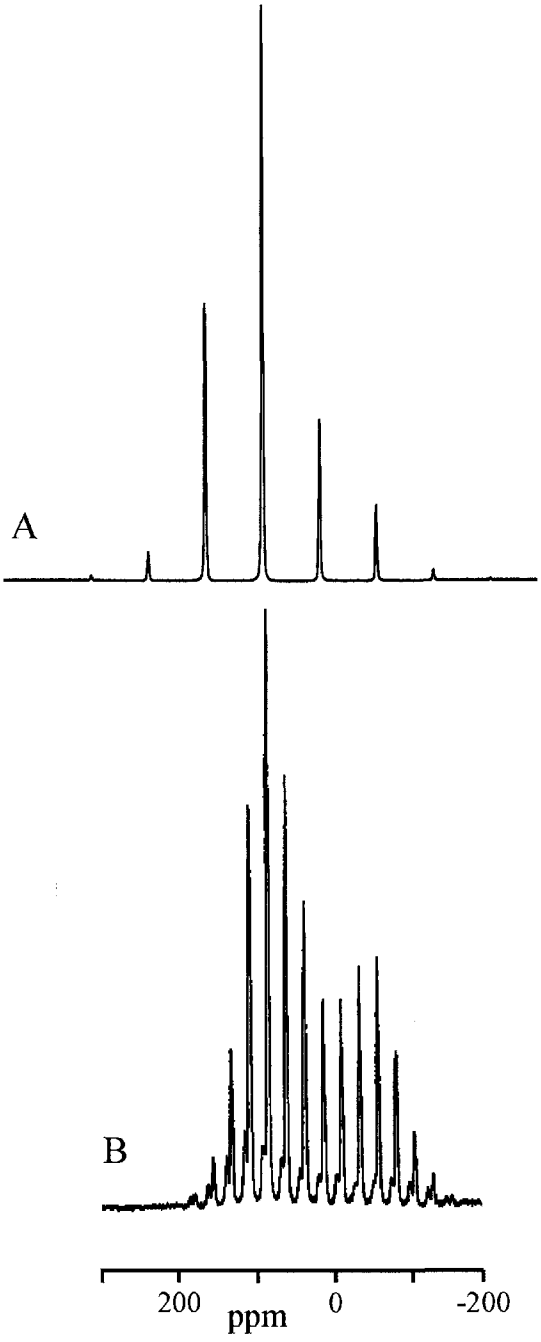

Figure 1-2. Comparison of the 60.7 MHz ^{31}P CP-MAS spinning sideband arrays observed during MAS: A) pure chlorpyrifos, **I** (4.1 kHz MAS). B) partially-purified aryl-hydrolyzed chlorpyrifos, **II** (1.0 kHz MAS).

Fig. 1-3

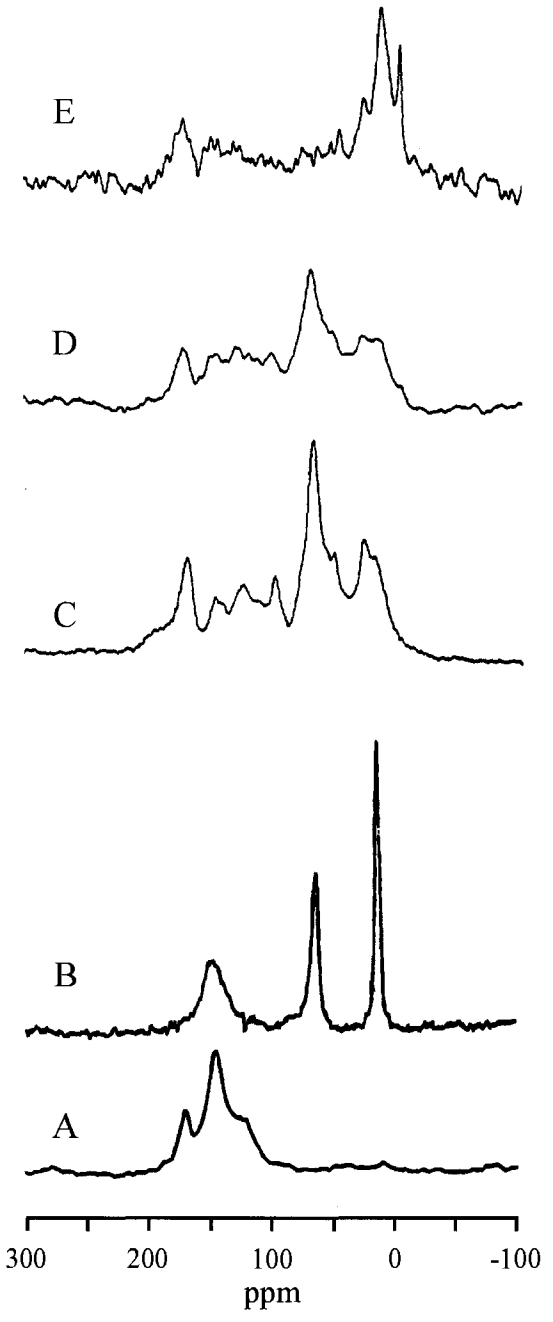

Figure 1-3. Comparison of the 25.3 MHz ^{13}C spectra obtained during MAS: A) CP-MAS spectrum of aryl-hydrolyzed chlorpyrifos (**II**). B) CP-MAS spectrum of pure chlorpyrifos (**I**). C) CP-MAS spectrum of unloaded Uncomphagre soil. D) CP-MAS spectrum of Uncomphagre soil loaded (10 % by wt.) with chlorpyrifos. E) DP-MAS spectrum of Uncomphagre soil loaded (10 %) with chlorpyrifos.

Fig. 1-4

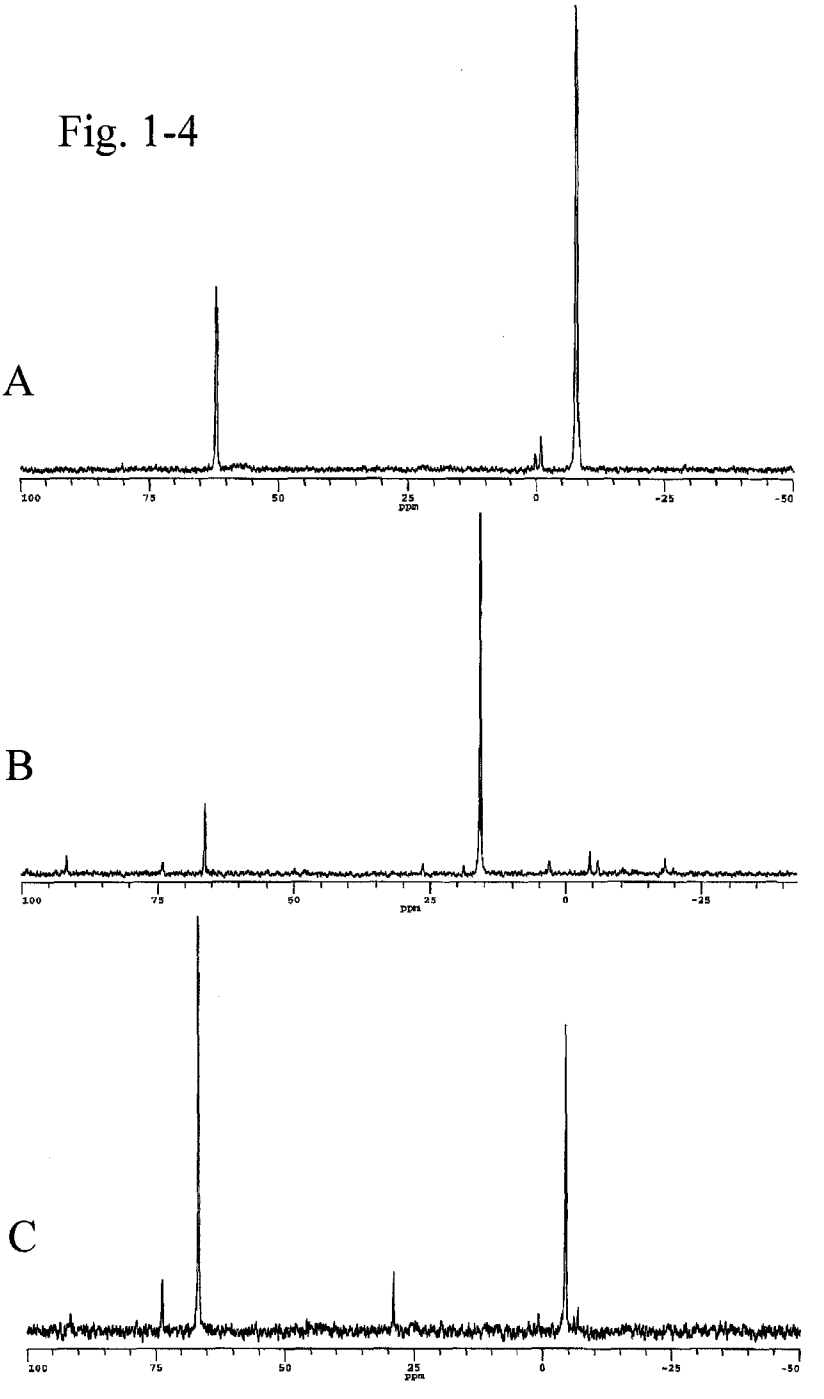

Figure 1-4. 60.7 MHz solid-state ^{31}P NMR spectra of chlorpyrifos at a 10 % by weight loading level on various substrates, obtained with 1.2 kHz MAS: A) On soil, using CP-MAS. B) On soil, using DP-MAS. C) On humic acid, using CP-MAS. D) On humic acid, using DP-MAS. E) On kaolinite, using CP-MAS. F) On kaolinite, using DP-MAS. G) On Ca-montmorillonite, using CP-MAS. H. On Ca-montmorillonite, using DP-MAS.

Fig. 1-5

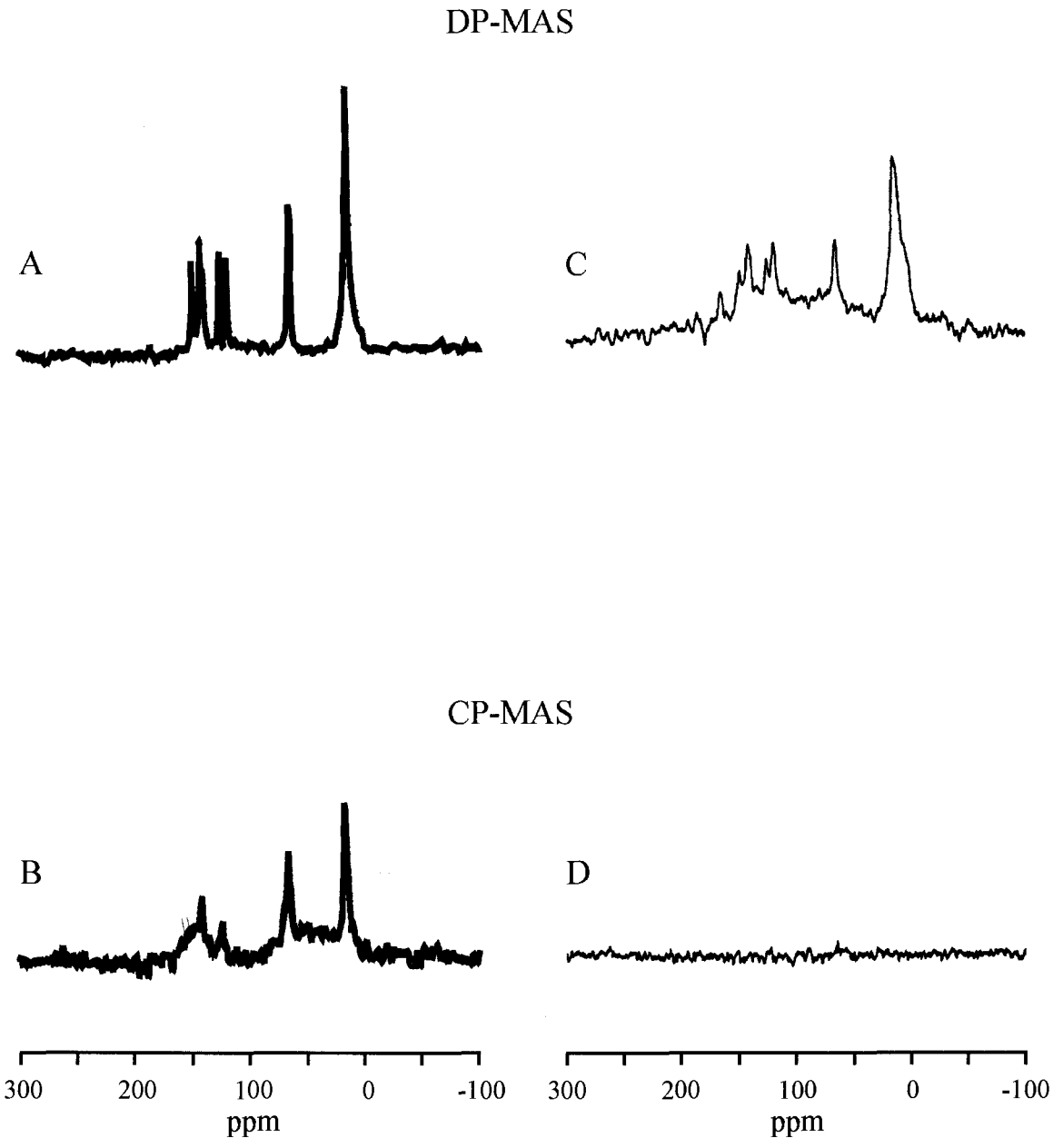

Figure 1-5. 25.3 MHz ^{13}C MAS spectra of chlorpyrifos 10 % w/w sorbed on 'as received' clays. A) DP-MAS, on 'as received' kaolinite. B) CP-MAS, on 'as received' kaolinite. C) DP-MAS, on 'as received' Ca-montmorillonite. D) CP-MAS, on 'as received' Ca-montmorillonite.

Fig. 1-6

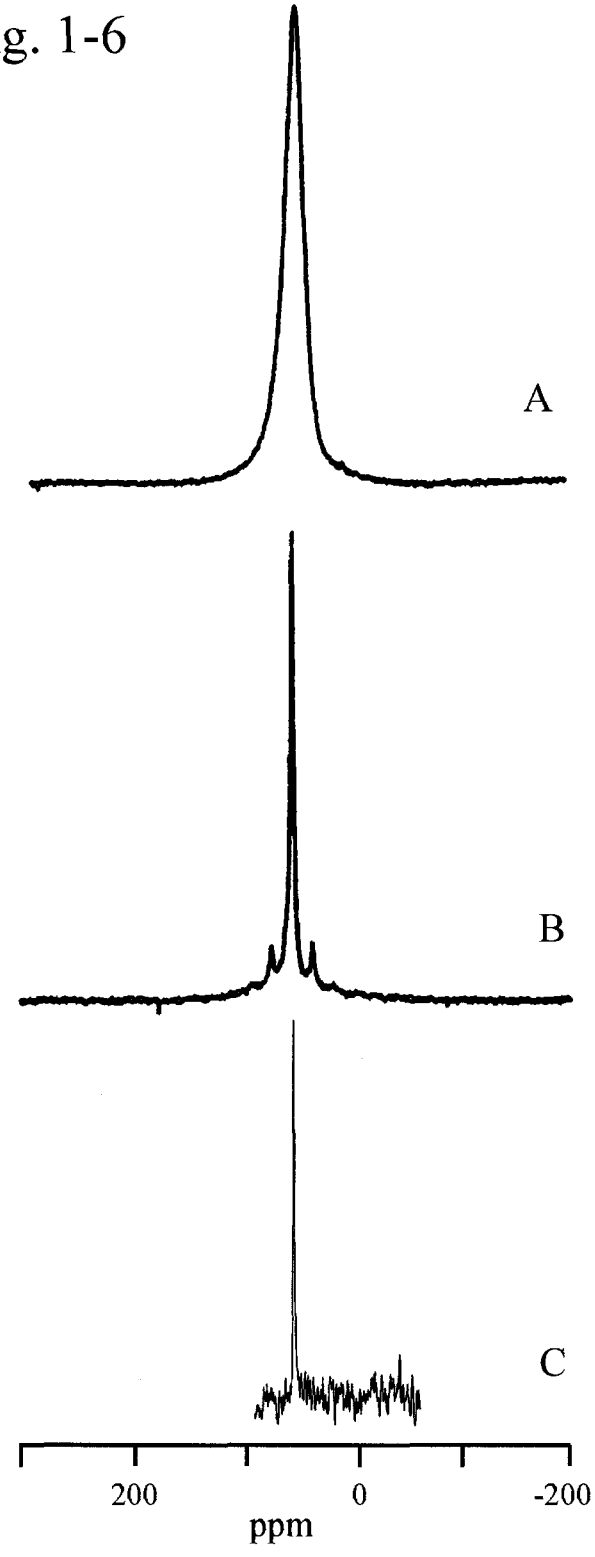

Figure 1-6. 60.7 MHz ^{31}P DP NMR spectra of chlorpyrifos (10 % by wt.) sorbed on Ca-montmorillonite ('as received'): A) Nonspinning DP, with ^{1}H decoupling. B) 1.5 kHz DP-MAS, without ^{1}H decoupling. C) 6.0 kHz DP-MAS, with ^{1}H decoupling.

Fig. 1-7

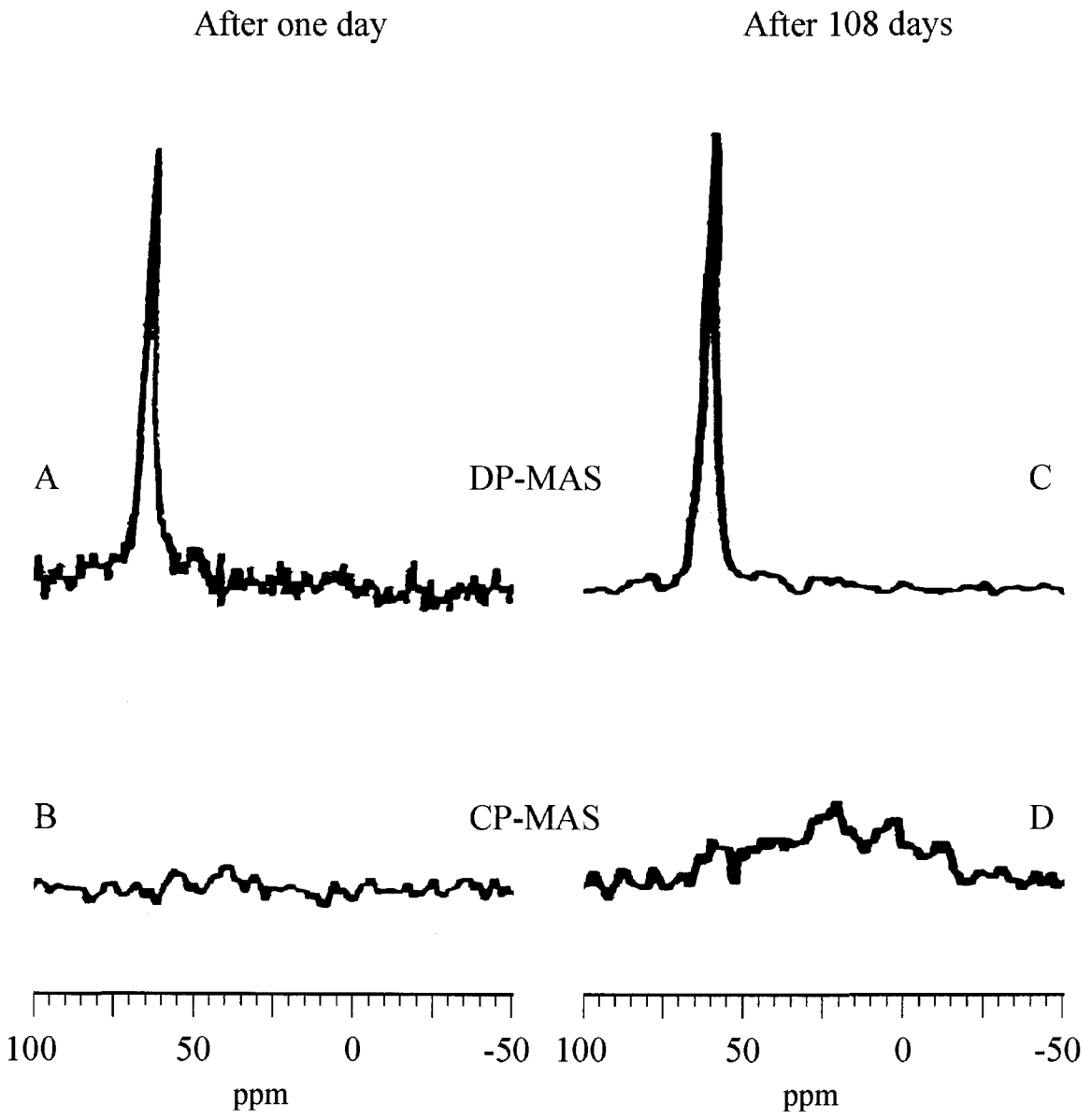

Figure 1-7. 60.7 MHz ^{31}P NMR spectra of chlorpyrifos (1.3 % w/w) adsorbed on partially hydrated kaolinite ('as received', 1.1 % water by wt.), with 1 kHz MAS: A) DP-MAS spectrum after 1 day. B) CP-MAS spectrum after 1 day. C) DP-MAS spectrum after 108 days. D) CP-MAS spectrum after 108 days.

Fig. 1-8

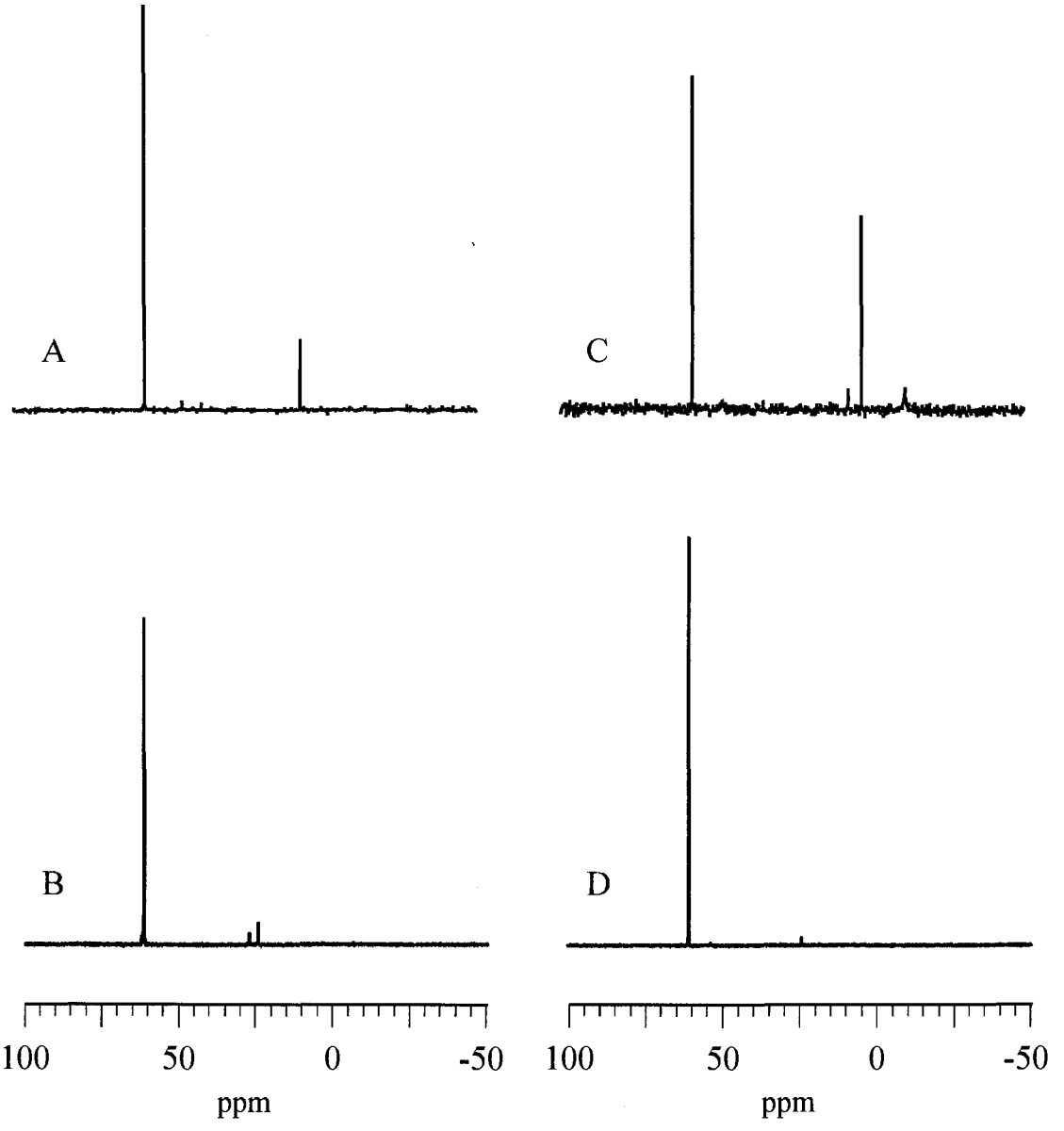

Figure 1-8. 242.9 MHz ^{31}P liquid-sample spectra (obtained with GARP proton decoupling) of extracts of various chlorpyrifos/clay samples. A) DMSO-d_6 extract of 108 day-old sample of chlorpyrifos (1.3 % w/w) adsorbed on partially hydrated kaolinite ('as received', 1.1 % wt. water) shown in Figure 1-7C and 1-7D. B) Acetone-d_6 extract of the 3.7 year-old sample of chlorpyrifos (9.6 % w/w) adsorbed on partially-hydrated Ca-montmorillonite (5.0 % by wt. water), represented in Figure 1-10C and 1-10D. C) DMSO-d_6 extract of the 166 day-old chlorpyrifos-loaded (10 % by wt.) Zn-montmorillonite (5 % water by wt.) sample, represented in Figures 1-21C and 1-21D. D) Chlorpyrifos refluxed in toluene (at 105 ^{o}C) for 4 days (unlocked acquisition).

Fig. 1-9

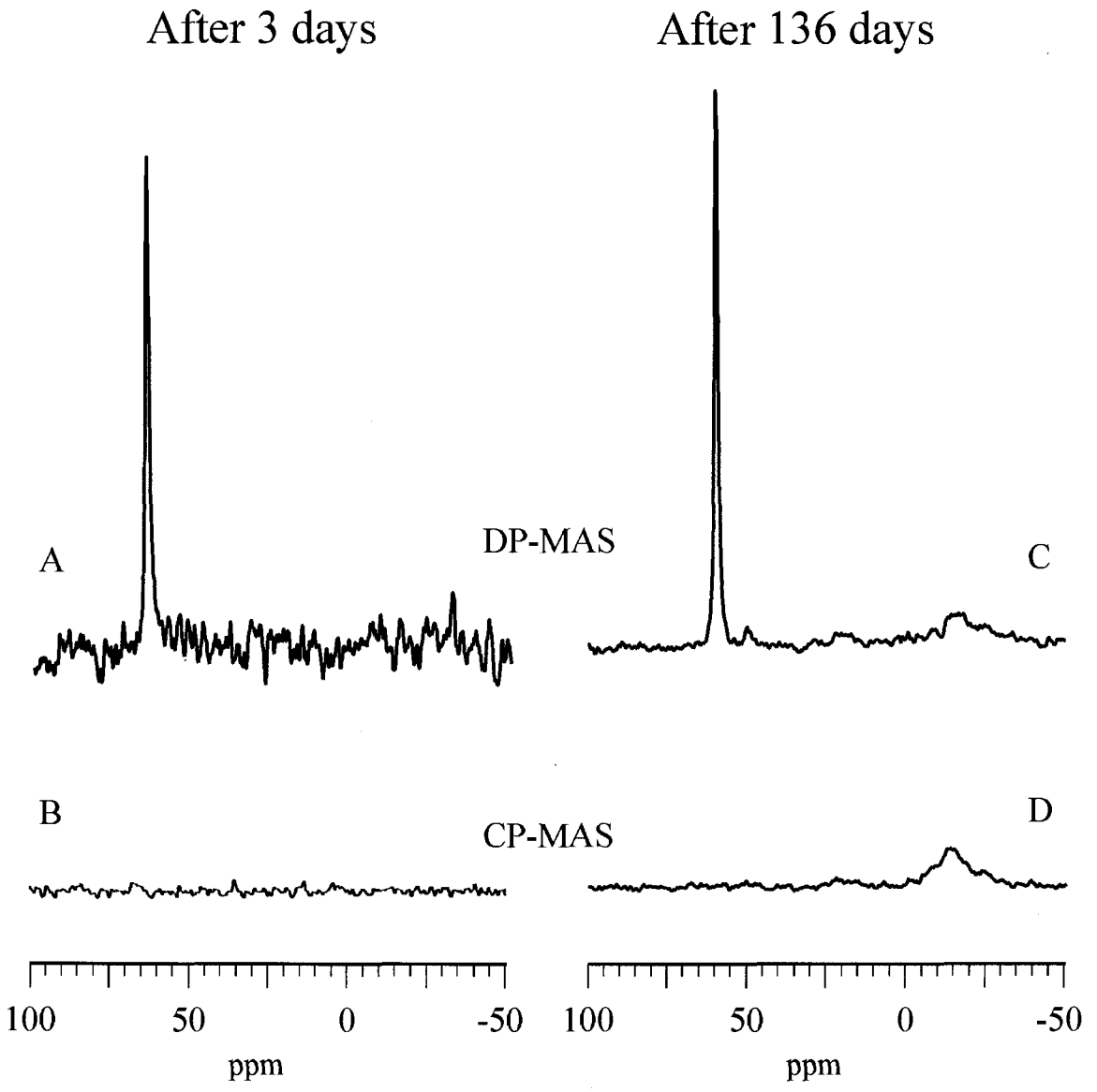

Figure 1-9. 60.7 MHz ^{31}P NMR spectra of chlorpyrifos (1.3 % w/w) adsorbed on partially hydrated kaolinite ('as received', 1.1 % wt. water), with 4.5 kHz MAS: A) DP-MAS spectrum after 3 days. B) CP-MAS spectrum after 3 days. C) DP-MAS spectrum after 136 days. D) CP-MAS spectrum after 136 days.

Fig. 1-10

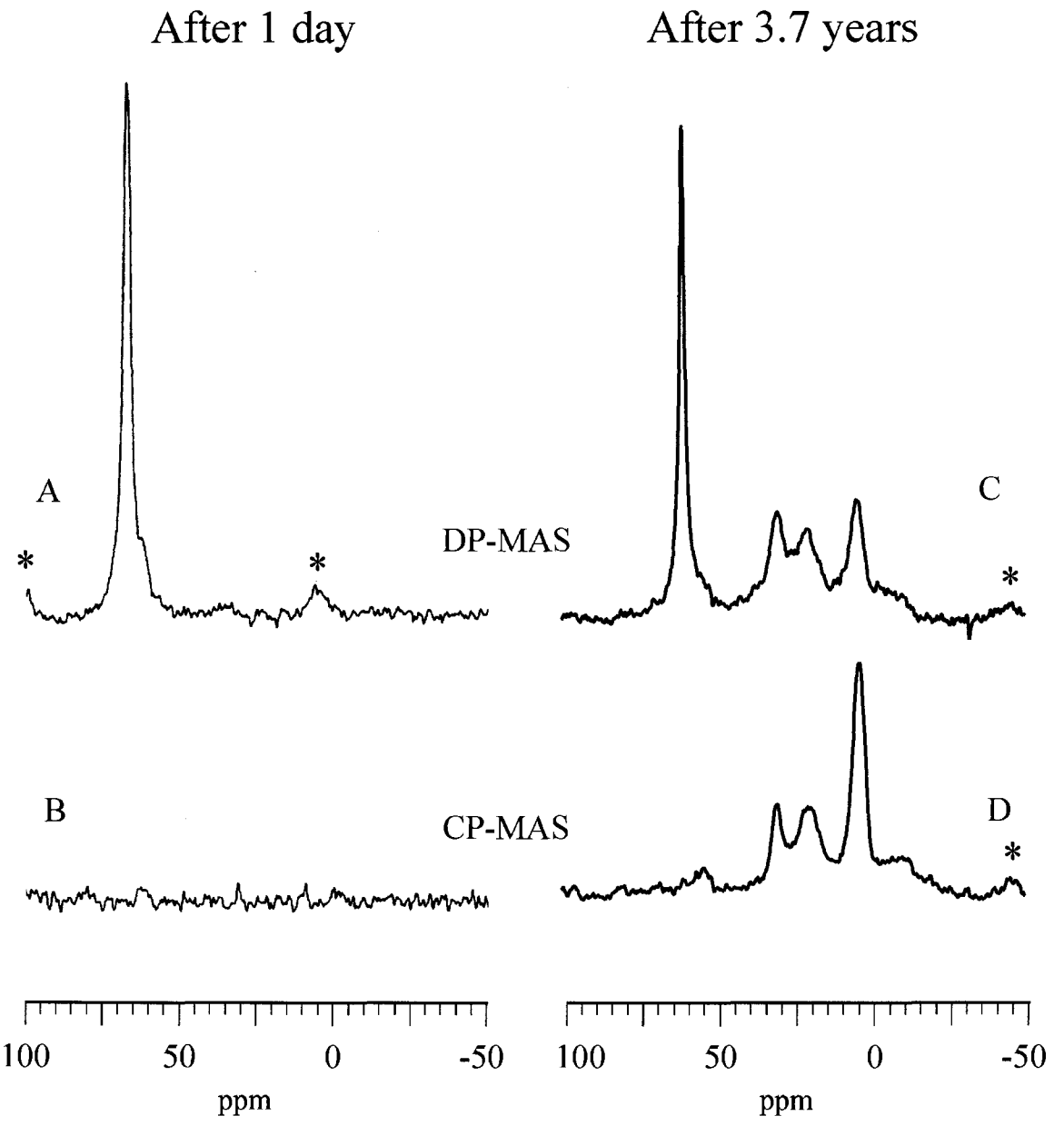

Figure 1-10. 60.7 MHz ^{31}P NMR spectra of chlorpyrifos (9.6 % w/w) adsorbed on partially hydrated Ca-montmorillonite (5.0 % by wt. water), with 4.5 kHz MAS: A) DP-MAS spectrum after 1 day. B) CP-MAS spectrum after 1 day. C) DP-MAS spectrum after 3.7 years. D) CP-MAS spectrum after 3.7 years.

Fig. 1-11

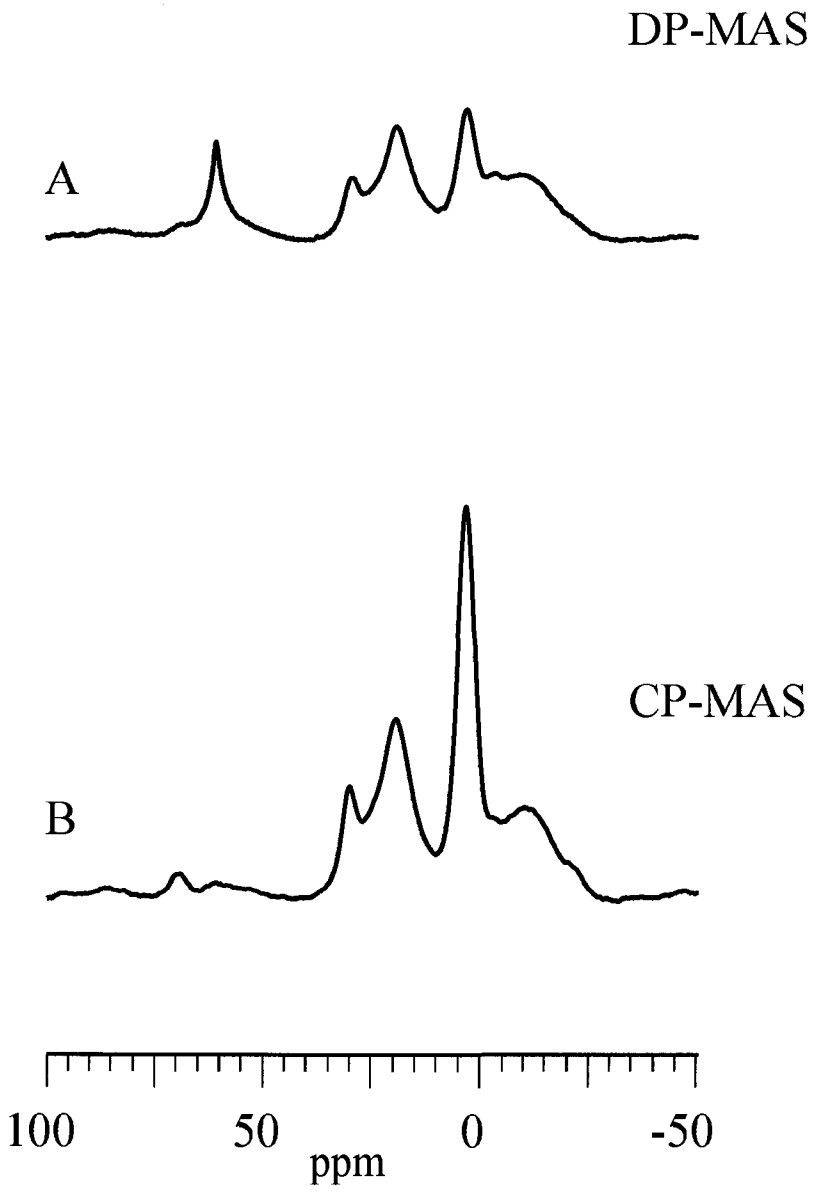

Figure 1-11. 60.7 MHz ^{31}P NMR spectra of the 3.7 year-old sample of chlorpyrifos (9.6 % by wt.) adsorbed on partially-hydrated Ca-montmorillonite (5.0 % water by wt.), represented in Figure 1-10C and 1-10D, after acetone-d_d extraction with 4.5 kHz MAS: A) DP-MAS spectrum. B) CP-MAS spectrum.

Fig. 1-12

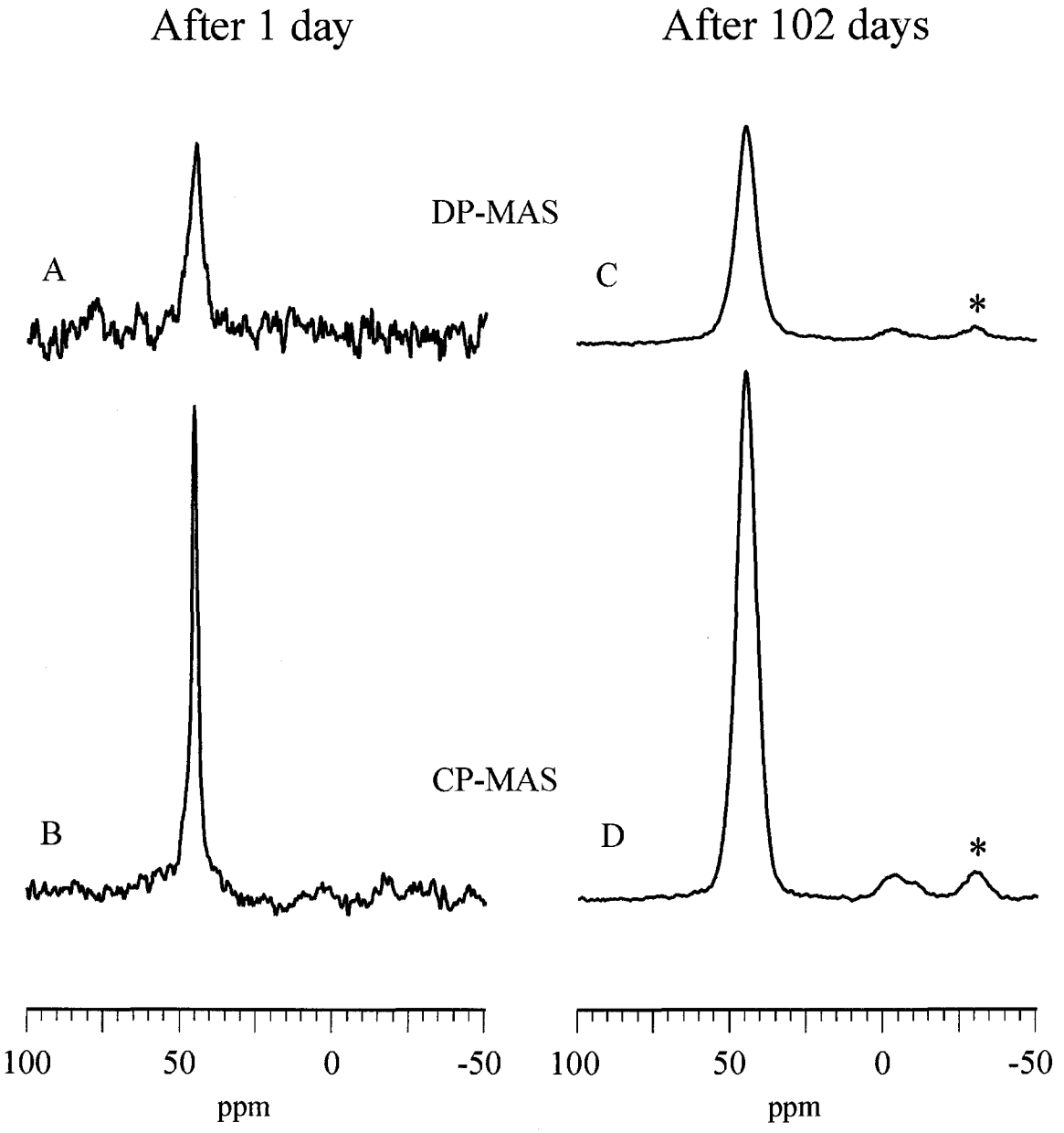

Figure 1-12. 60.7 MHz ^{31}P NMR spectra of compound **II**, the potassium salt of aryl-hydrolyzed chlorpyrifos, sorbed (10 % by wt.) on partially-hydrated (5 % by wt. water) Ca-montmorillonite: A) DP-MAS after 1 day. B) CP-MAS after 1 day. C) DP-MAS after 102 days. D) CP-MAS after 102 days.

Fig. 1-13

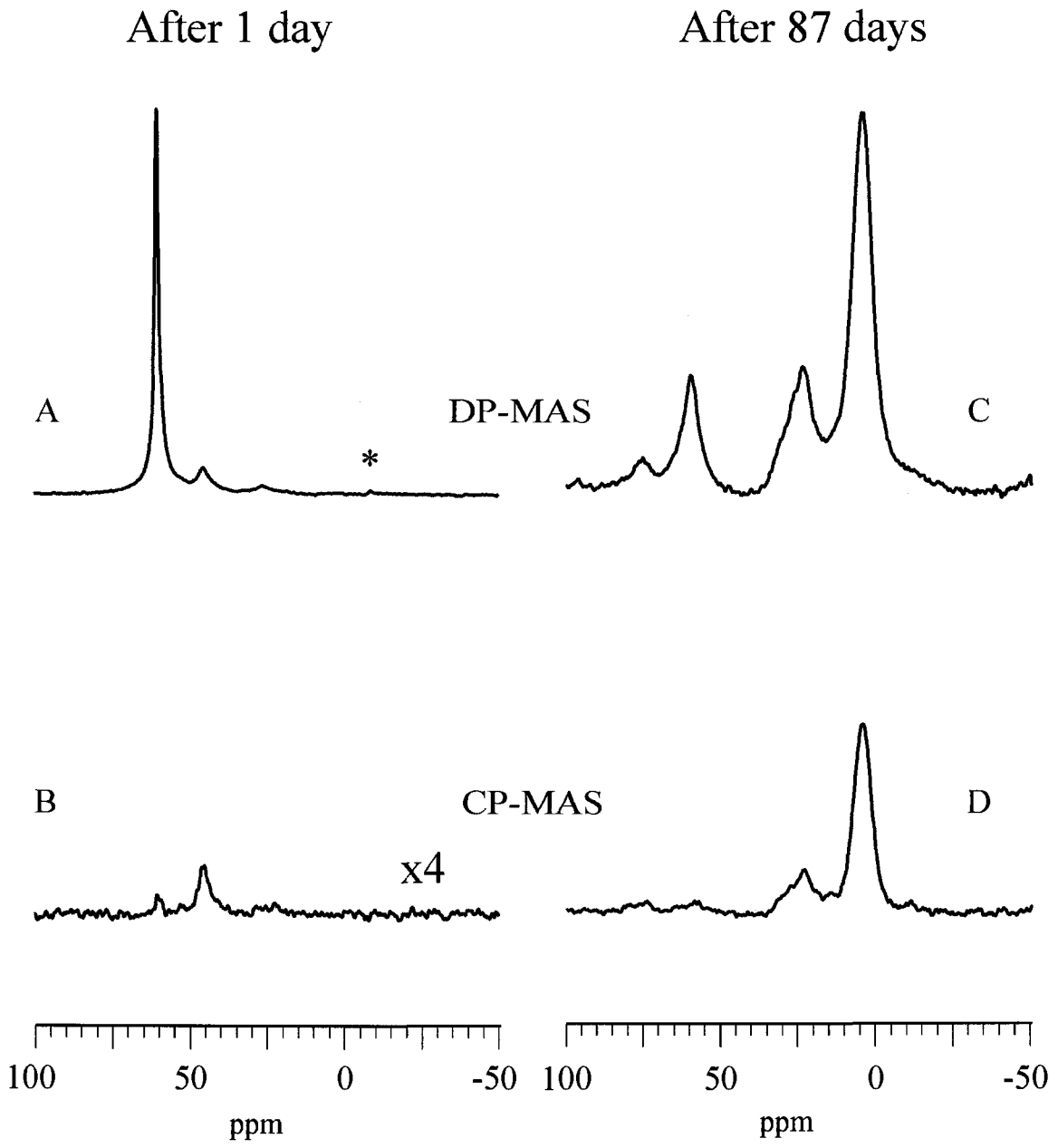

Figure 1-13. 60.7 MHz ^{31}P NMR spectra of chlorpyrifos on partially-hydrated (5 % by wt. water) Zn-montmorillonite: A) DP-MAS after 1 day. B) CP-MAS after 1 day. C) DP-MAS after 166 days. D) CP-MAS after 166 days.

Fig. 1-14

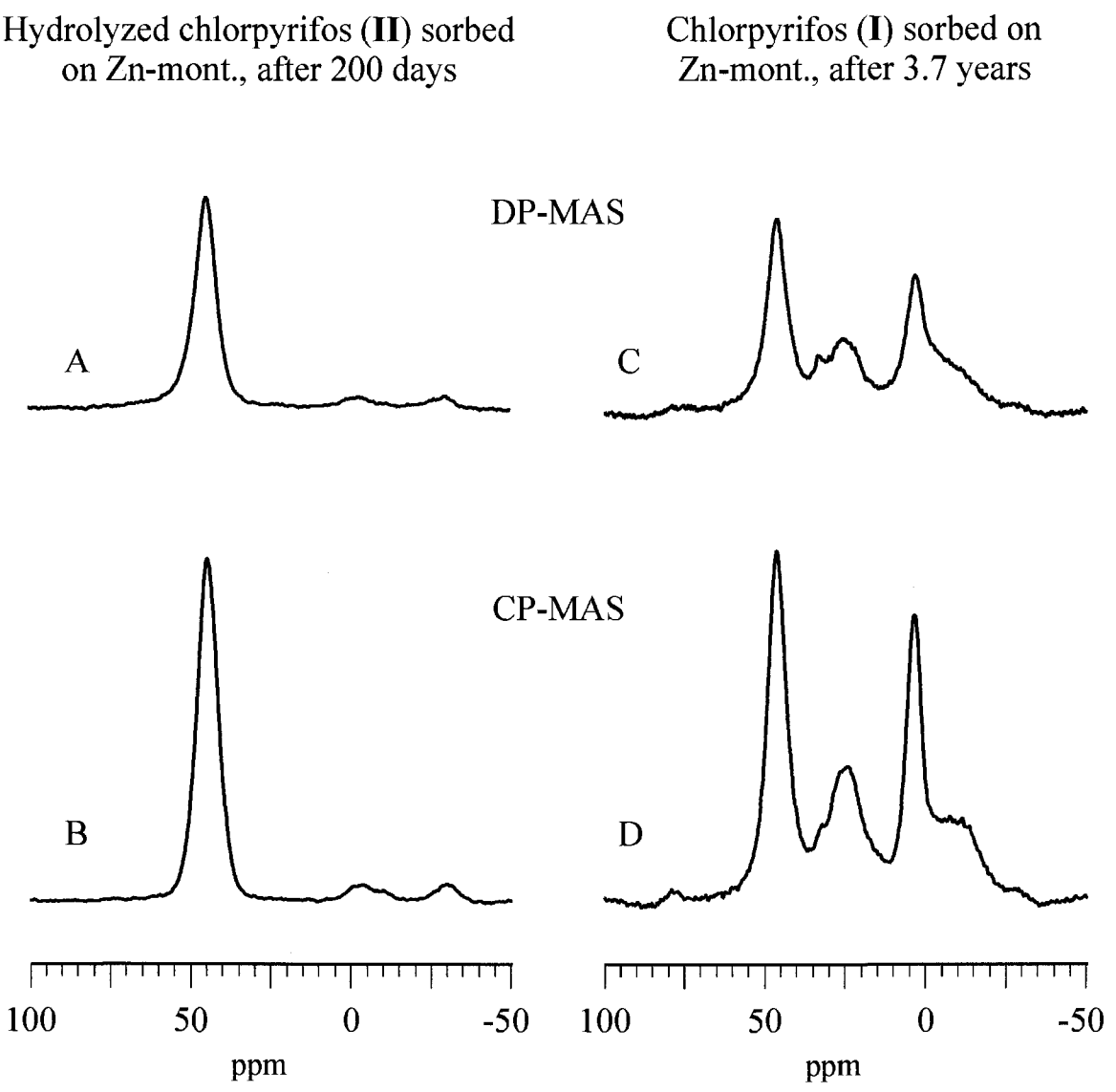

Figure 1-14. 60.7 MHz ^{31}P NMR spectra of aryl-hydrolyzed chlorpyrifos (**II**) adsorbed (10 % by weight) on Zn-montmorillonite (5 % water by wt.), after 200 days: A) DP-MAS spectrum; B) CP-MAS spectrum. 60.7 MHz ^{31}P NMR spectra of chlorpyrifos adsorbed on partially hydrated Zn-montmorillonite (10 % chlorpyrifos and 5 % water by wt.) after 3.7 years: C) DP-MAS spectrum; D) CP-MAS spectrum.

Fig. 1-15

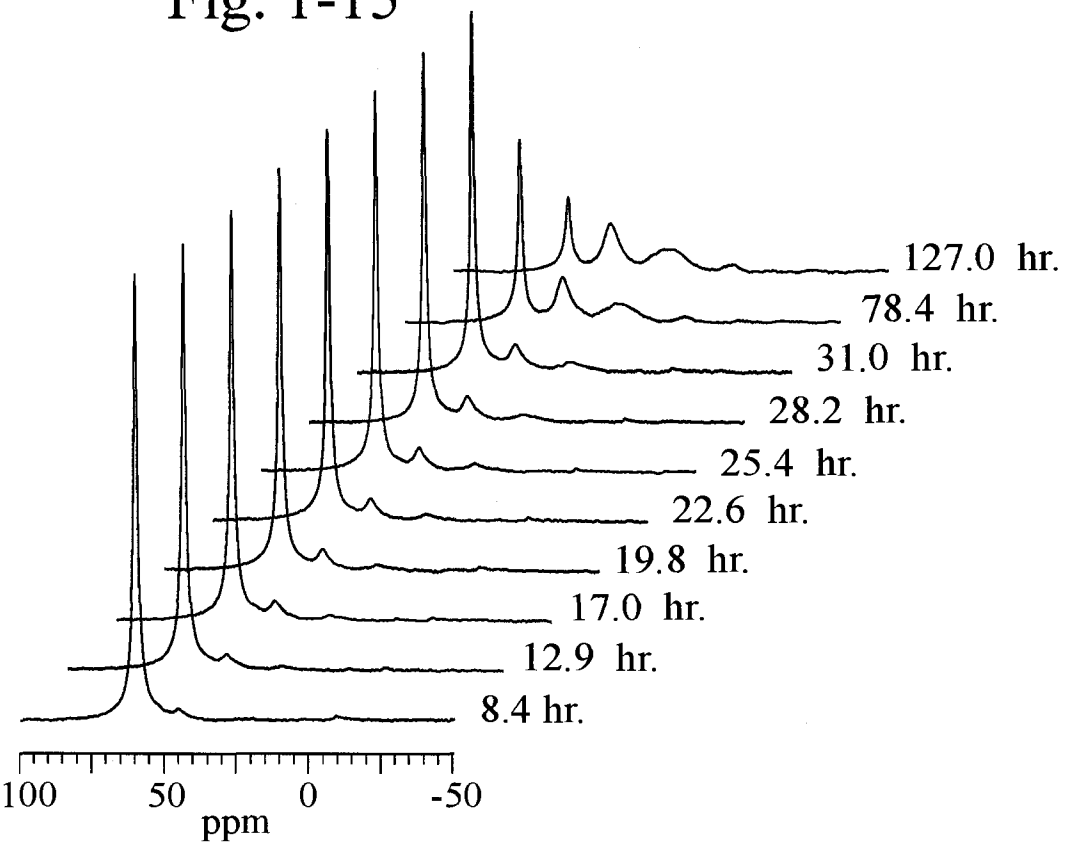

Figure 1-15. Variation in the 60.7 MHz ^{31}P DP-MAS NMR spectrum of chlorpyrifos (10.2 % by wt.) on partially-hydrated Zn-montmorillonite (4.2 % water by wt.) during the first 127 hours of decomposition.

Fig. 1-16

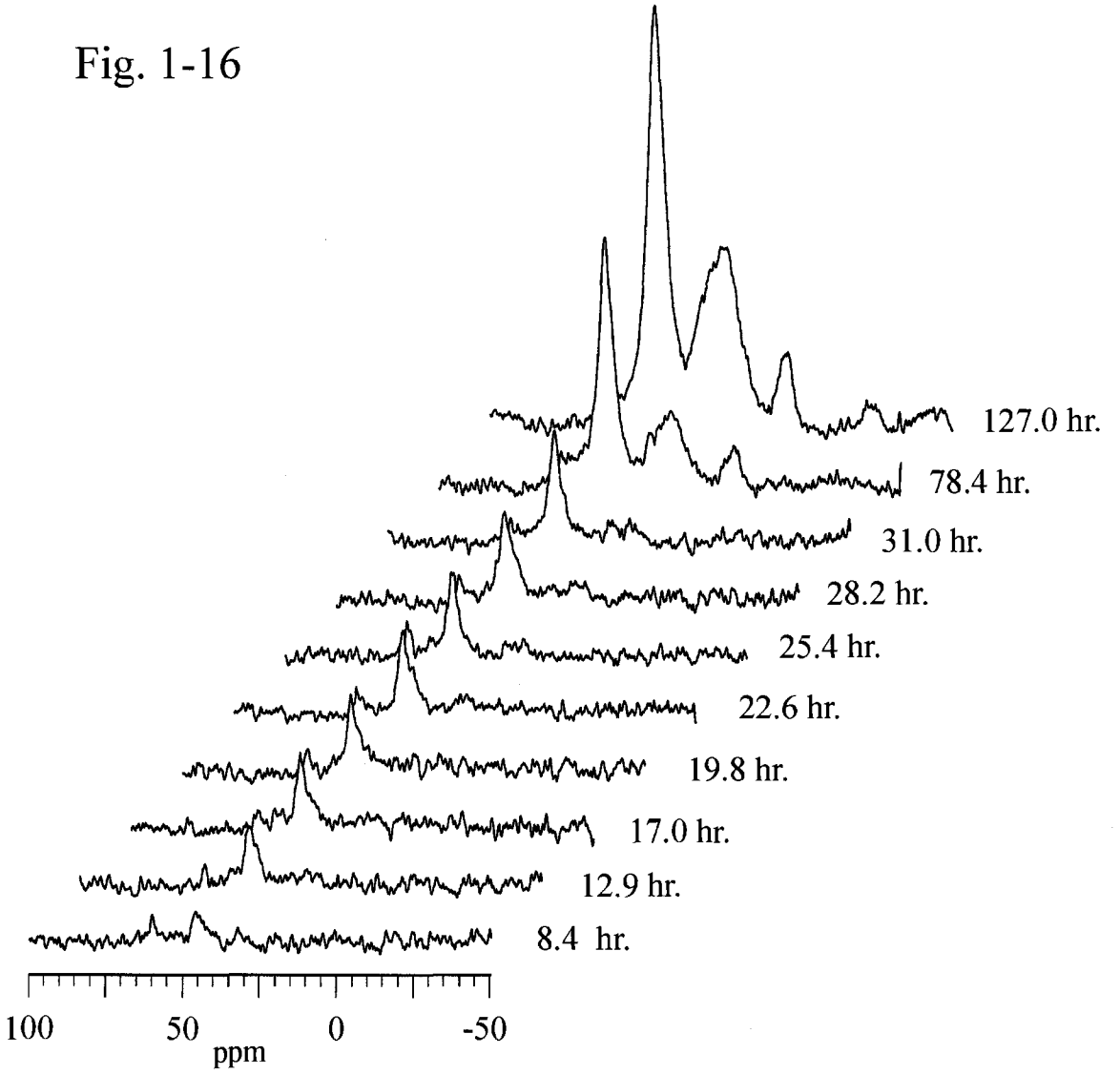

Figure 1-16. Variation in the 60.7 MHz ^{31}P CP-MAS NMR spectrum of chlorpyrifos (10.2 % by wt.) on partially-hydrated Zn-montmorillonite (4.2 % water by wt.) during the first 127 hours of decomposition.

Fig. 1-17

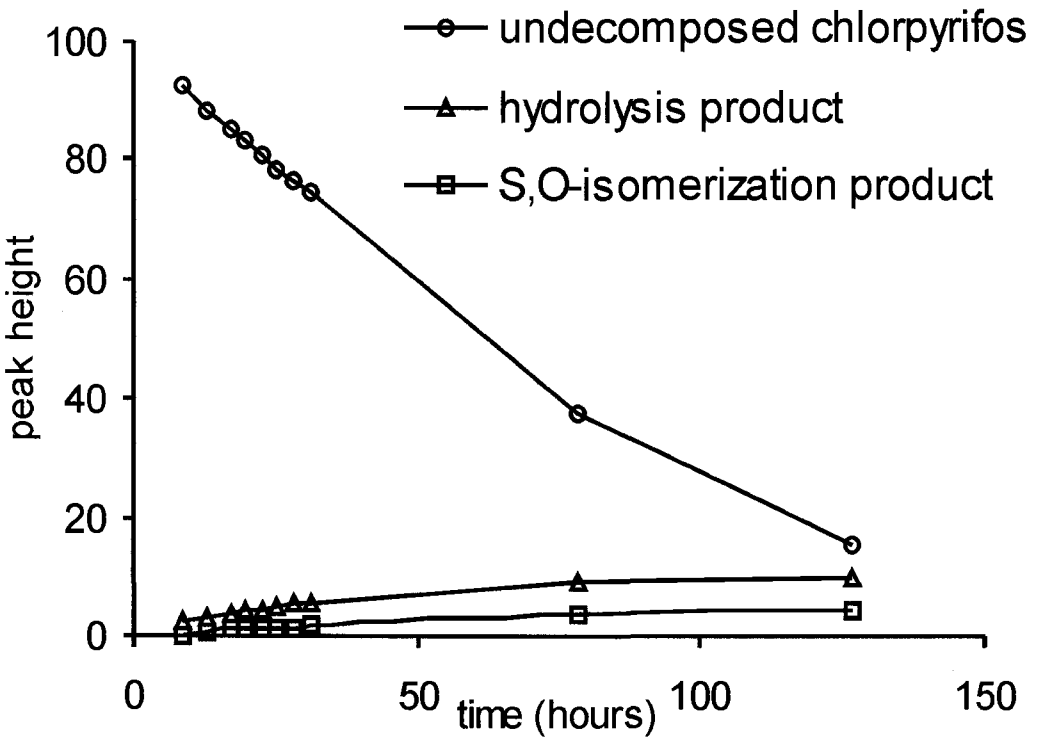

Figure 1-17. Plot of peak height *vs.* time for the three largest peaks observed by 60.7 MHz ^{31}P DP-MAS NMR during the first 127 hours of a sample of chlorpyrifos (10.2 % by wt.) sorbed on partially-hydrated Zn-montmorillonite (4.2 % water by wt.): ○, 61 ppm peak due to physisorbed but undecomposed chlorpyrifos (**I**). Δ, 45 ppm peak due to hydrolyzed chlorpyrifos (**II**). ĩ, 28 ppm peak due to S,O-isomerized chlorpyrifos (**IV** and/or **V**).

Fig. 1-18 through 1-20

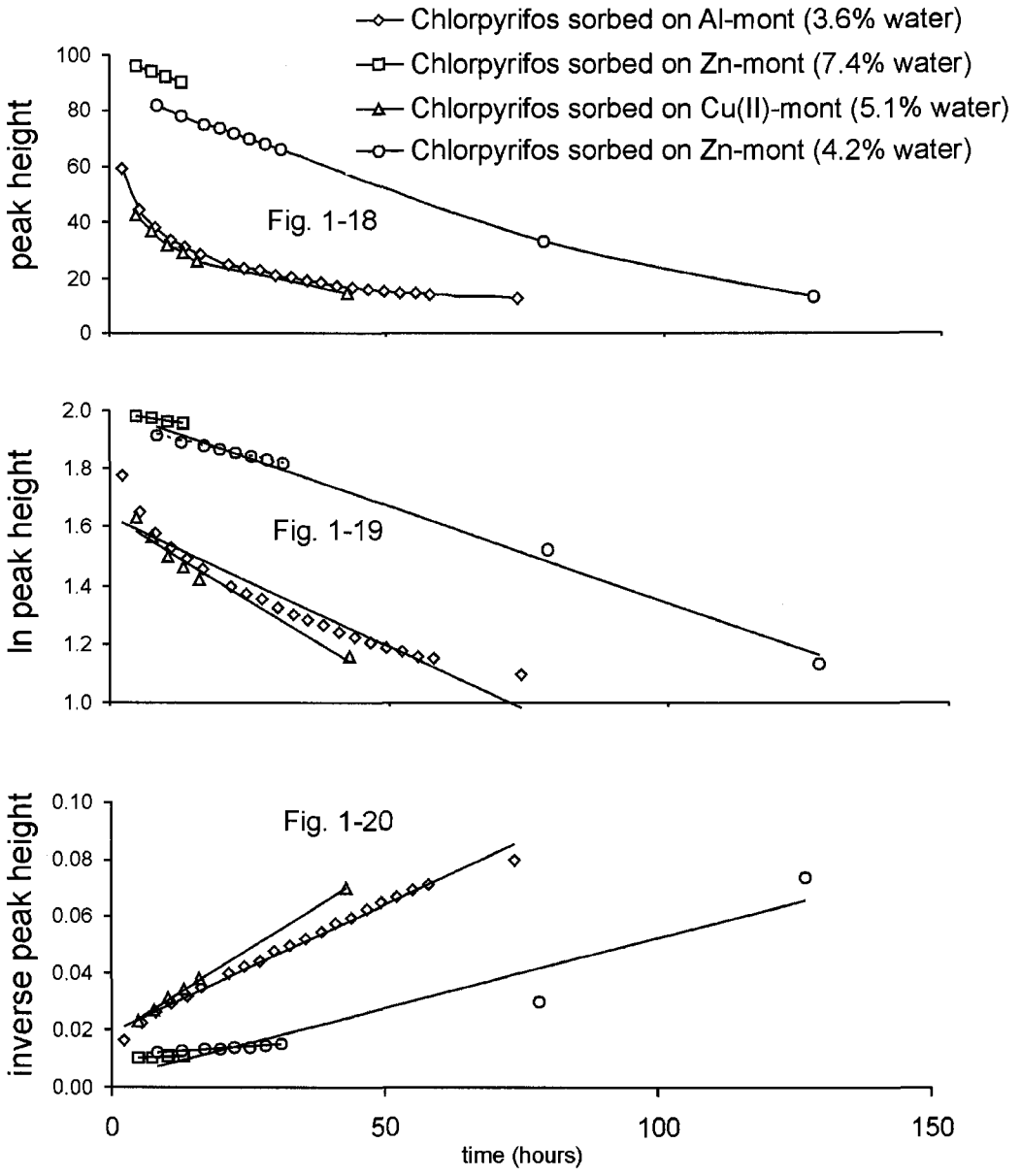

Figure 1-18. ^{31}P DP-MAS NMR peak height of chlorpyrifos *vs.* time when sorbed on various clays.

Figure 1-19. Log of ^{31}P DP-MAS NMR peak height of chlorpyrifos *vs.* time when sorbed on various clays.

Figure 1-20. Inverse of ^{31}P DP-MAS NMR peak height of chlorpyrifos *vs.* time when sorbed on various clays.

Figure 1-21

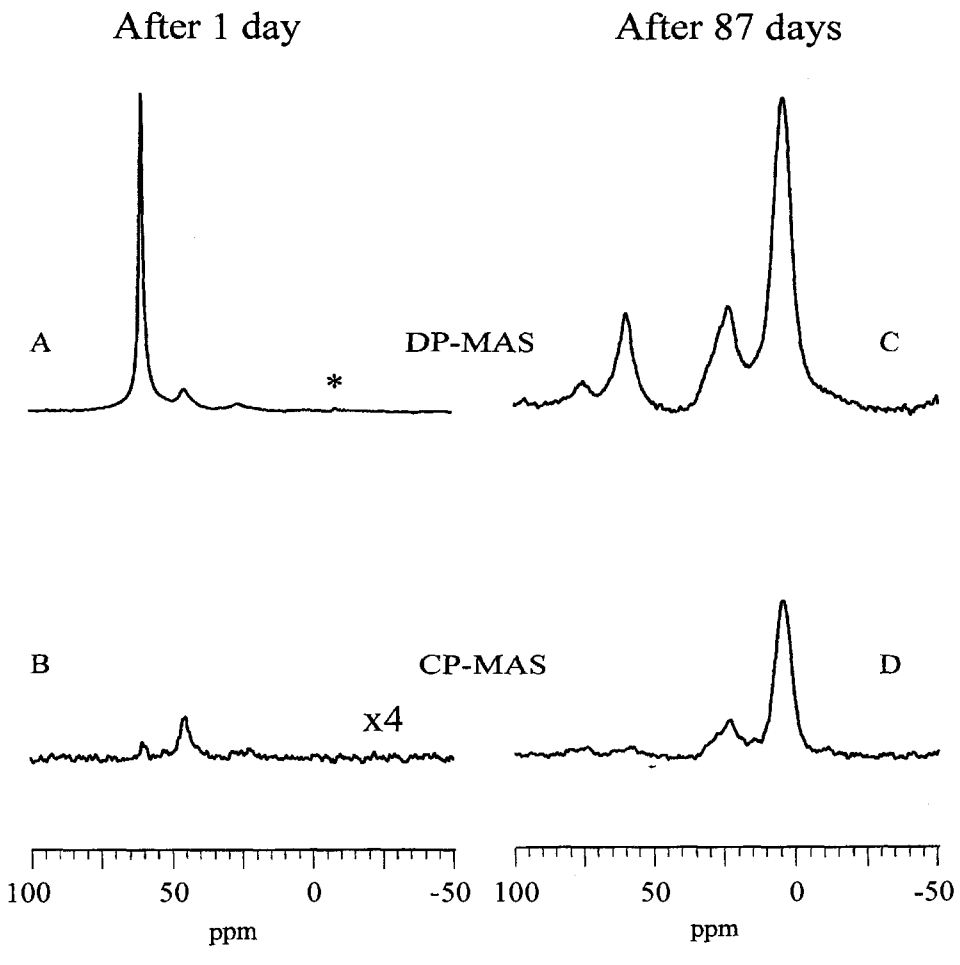

Figure 1-21. 60.7 MHz ^{31}P NMR spectra of chlorpyrifos (9.3 % by wt.) sorbed on partially hydrated (3.6 % by wt. water) Al-montmorillonite: A) DP-MAS after 1 day. B) CP-MAS after 1 day. C) DP-MAS after 87 days. D) CP-MAS after 87 days.

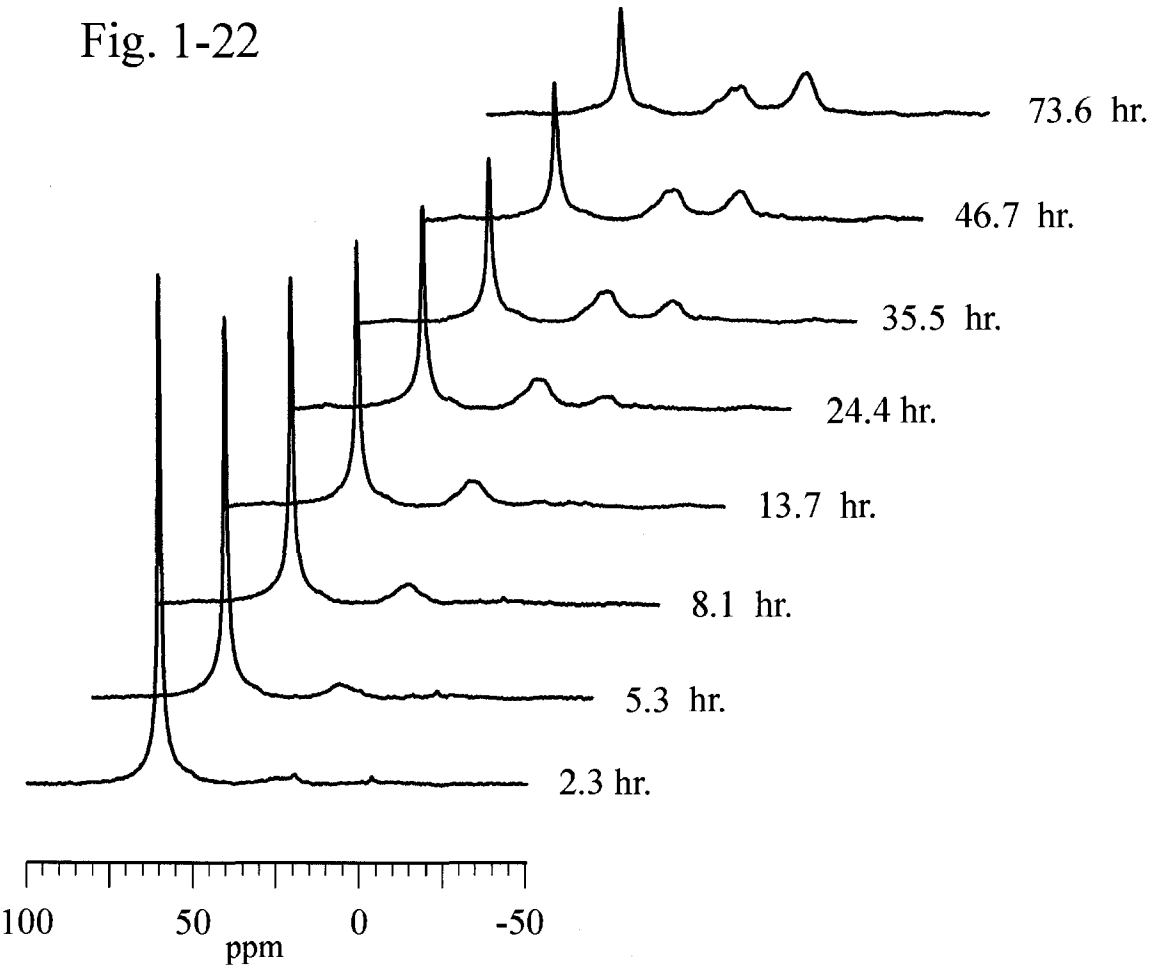

Figure 1-22. 60.7 MHz ^{31}P DP-MAS spectra of chlorpyrifos (10.0 % by wt.) sorbed on partially hydrated (4.3 % by wt. water) Al-montmorillonite during the first 74 hours of decomposition.

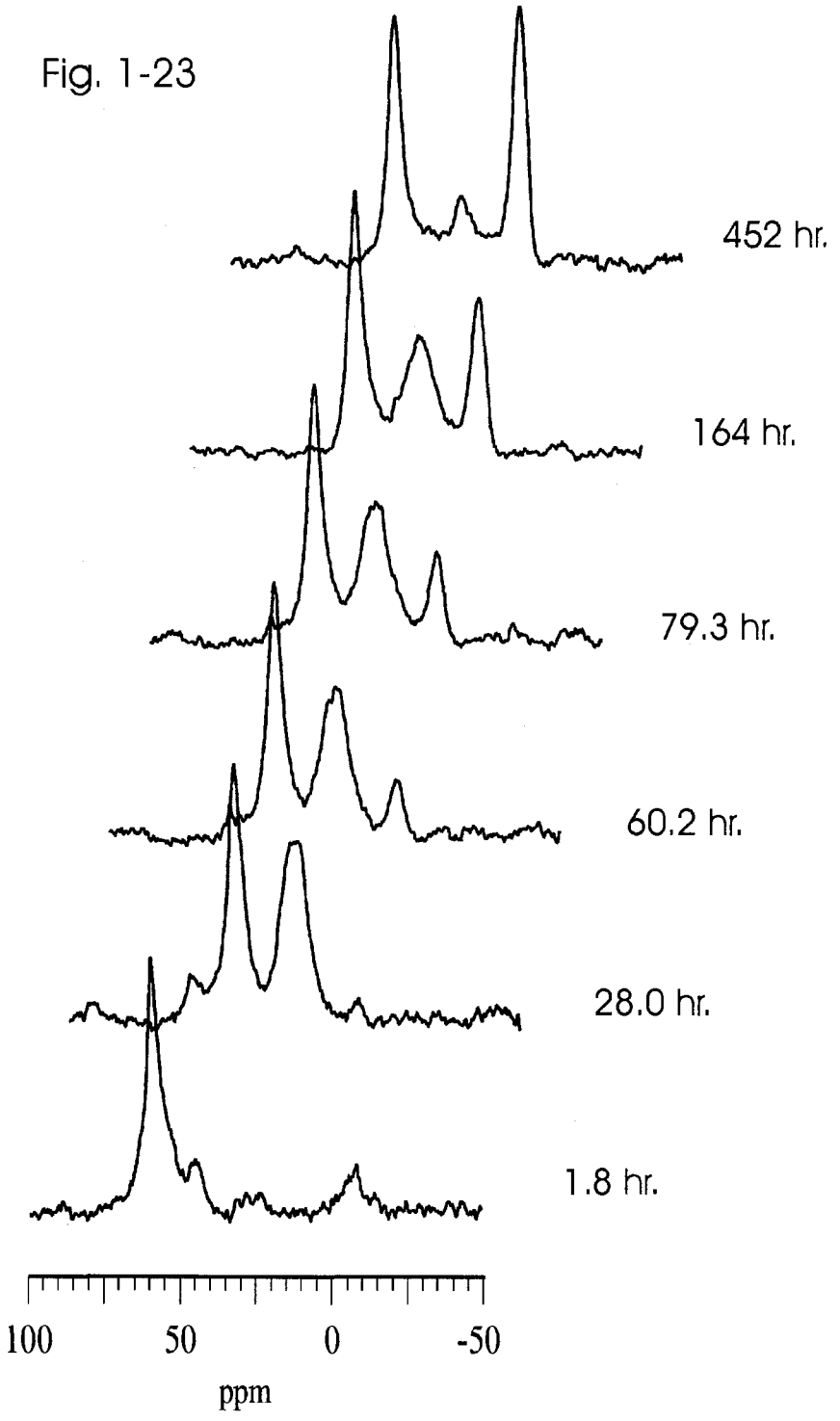

Figure 1-23. 60.7 MHz ^{31}P CP-MAS spectra of chlorpyrifos (10.0 % by wt.) sorbed on partially hydrated (4.3 % by wt. water) Al-montmorillonite during the first 452 hours of decomposition.

Fig. 1-24

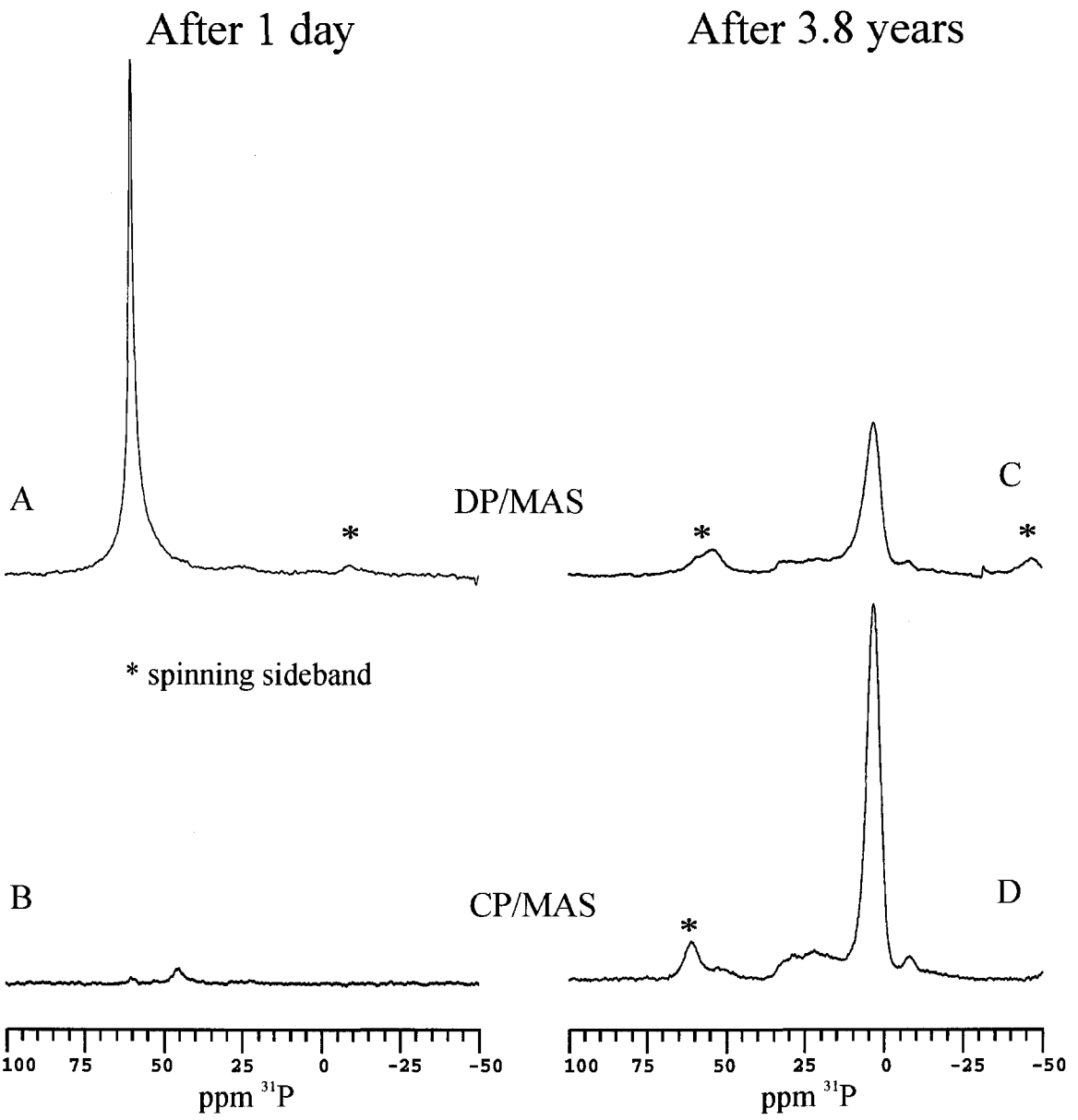

Figure 1-24. 60.7 MHz ^{31}P NMR spectra of chlorpyrifos (8.6 % by wt.) sorbed on partially hydrated (4.6 % water by wt.) Al-montmorillonite: A) DP-MAS after 1 day. B) CP-MAS after 1 day. C) DP-MAS after 3.8 years. D) CP-MAS after 3.8 years.

Fig. 1-25

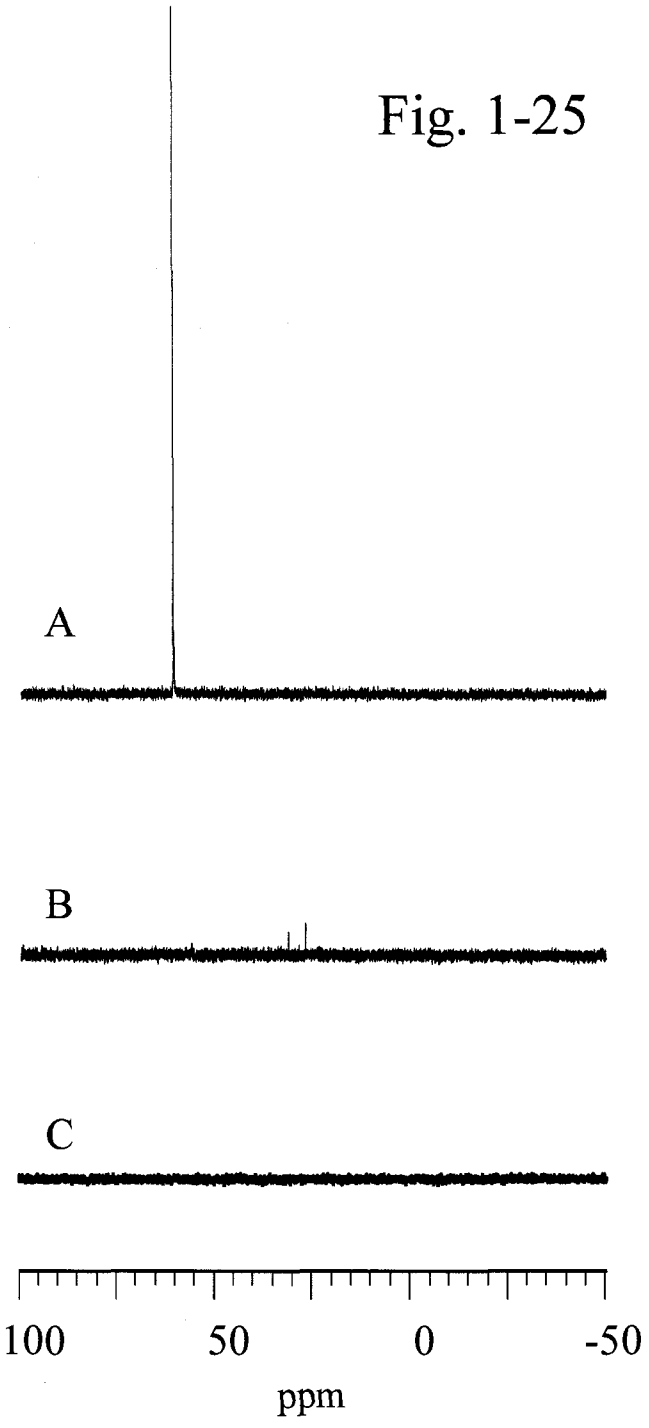

Figure 1-25. 242.9 MHz ^{31}P liquid NMR spectra (with GARP proton decoupling) of DMSO-d_6 extracts: A) Chlorpyrifos/Al-montmorillonite sample after 1 day of decomposition (represented in Figure 1-24A). B) Chlorpyrifos/Al-montmorillonite sample after 3.8 years of decomposition (represented in Figure 1-24B). C) Chlorpyrifos/Cu-montmorillonite sample after 13 hours of decomposition (represented in Figure 1-26).

Fig. 1-26

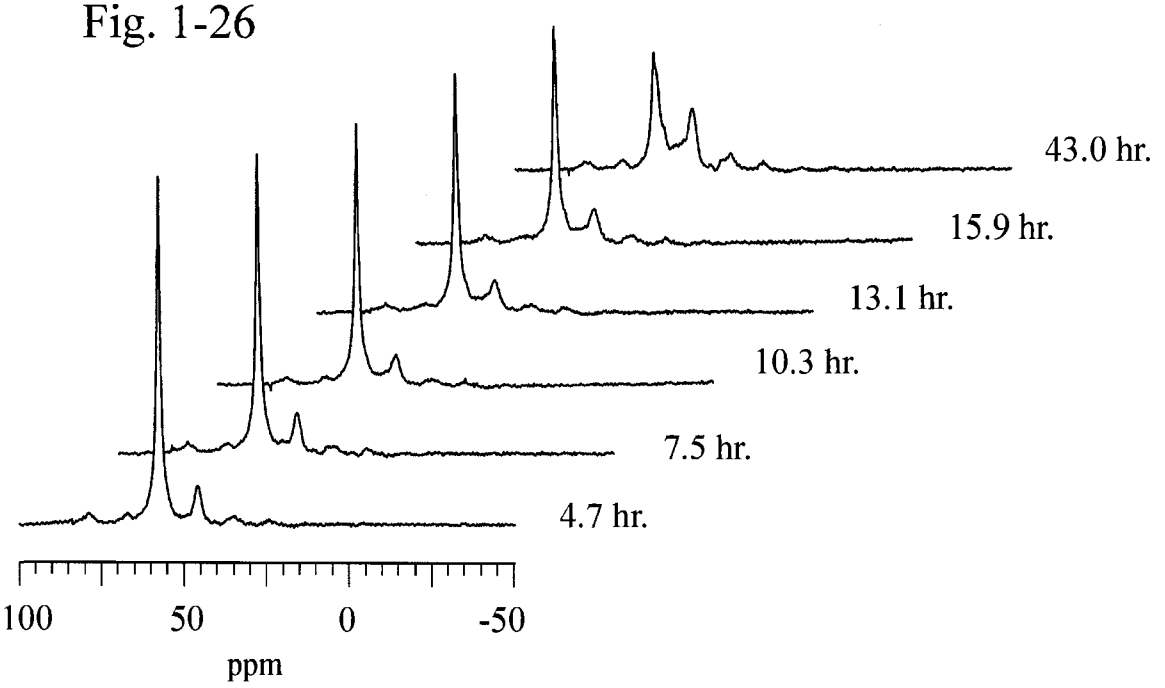

Figure 1-26. 60.7 MHz ^{31}P DP-MAS spectra of chlorpyrifos (9.8 % by wt.) on partially hydrated (5.1 % water by wt.) Cu-montmorillonite during the first 43 hours of decomposition.

Fig. 1-27

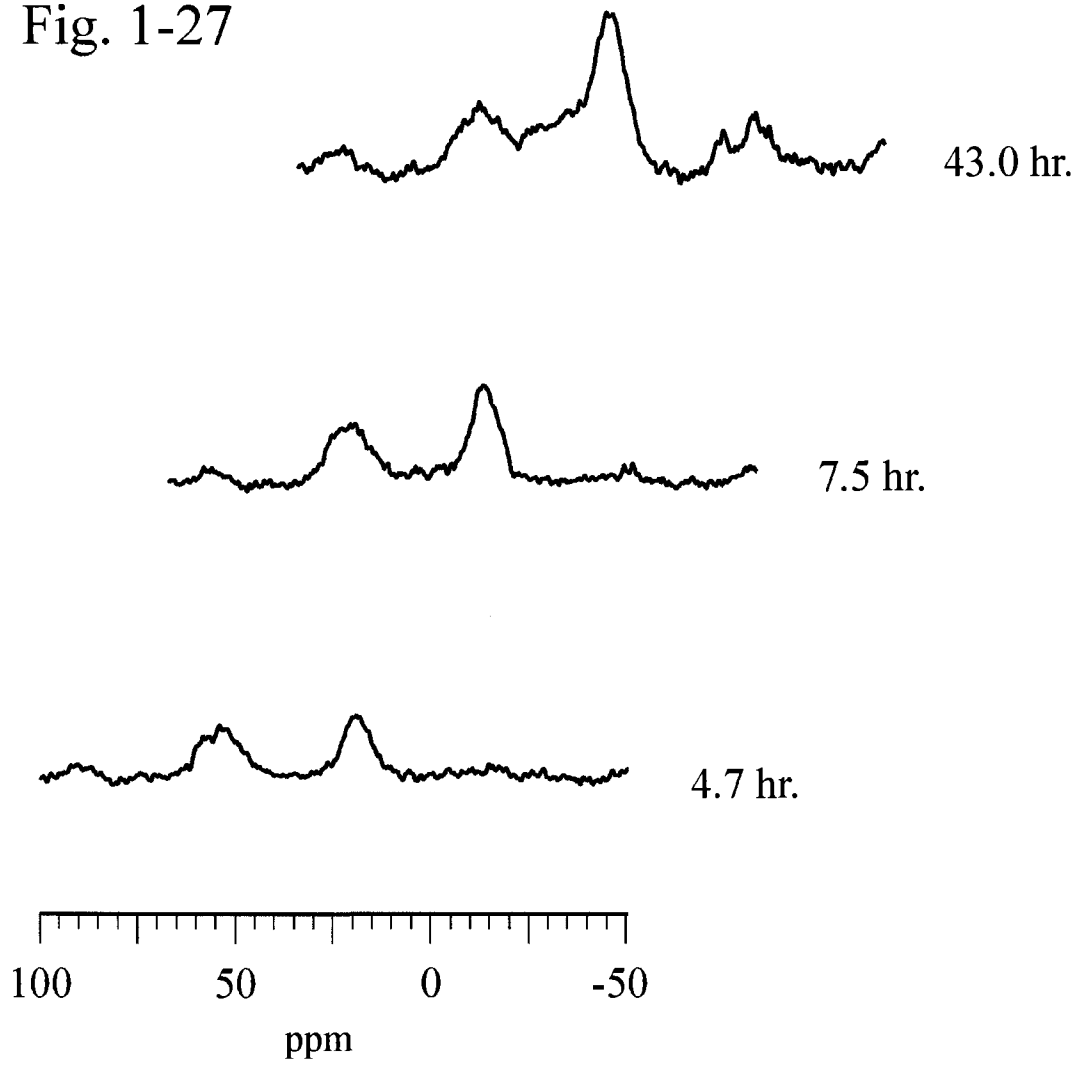

Figure 1-27. 60.7 MHz ^{31}P CP-MAS spectra of chlorpyrifos (9.8 % by wt.) on partially hydrated (5.1 % water by wt.) Cu-montmorillonite during the first 43 hours of decomposition.

Fig. 1-28

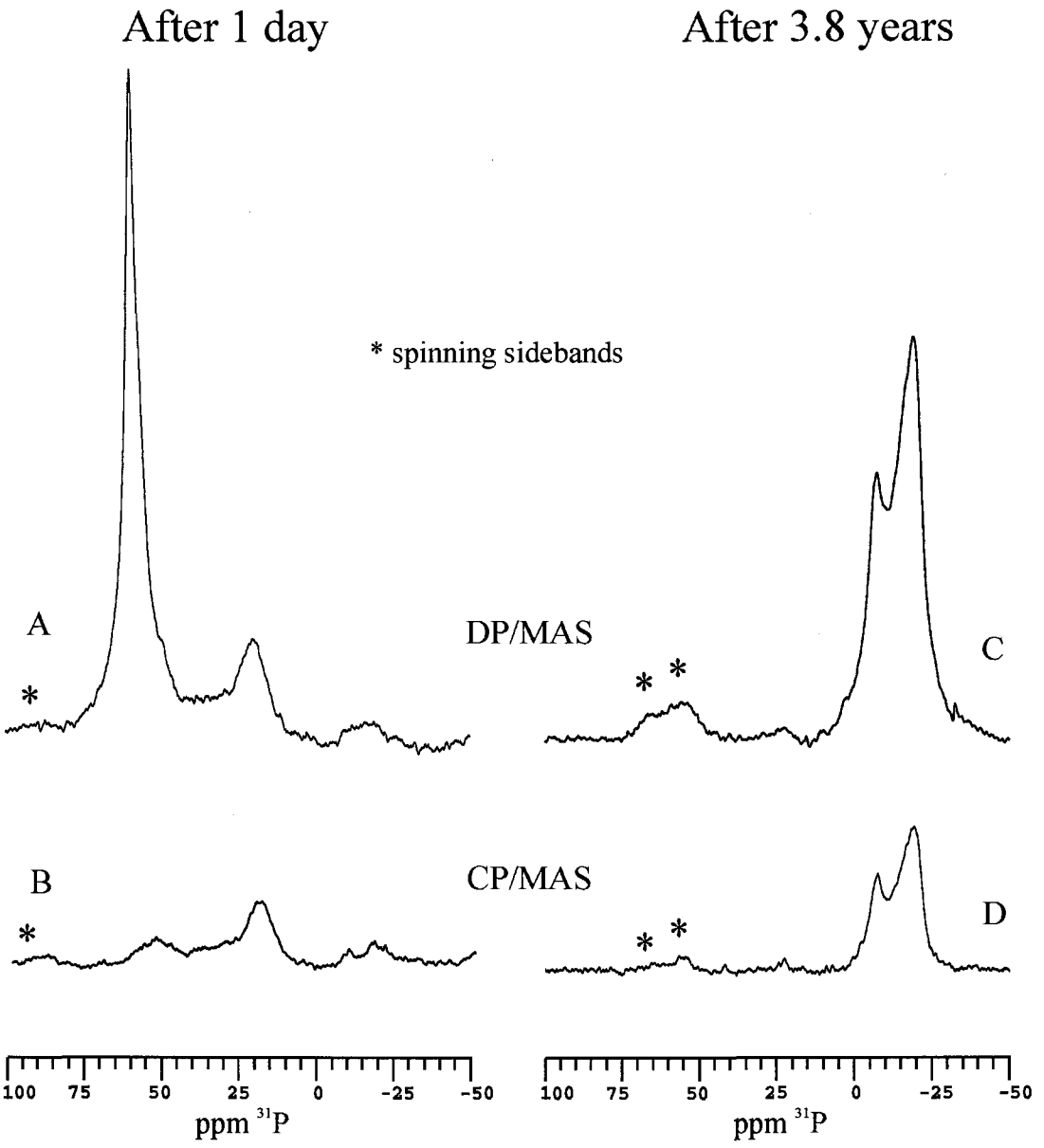

Figure 1-28. 60.7 MHz ^{31}P MAS spectra of chlorpyrifos sorbed on partially hydrated Cu-montmorillonite: A) DP-MAS spectrum of chlorpyrifos (9.8 % by wt.) sorbed on partially hydrated (5.1 % water by wt.) Cu-montmorillonite, after 1 day; B) CP-MAS spectrum, after 1 day. C) DP-MAS spectra of chlorpyrifos (10.5 % by wt.) on partially hydrated (5.3 % water by wt.) Cu-montmorillonite, after 3.8 years; D) CP-MAS spectrum, after 3.8 years.

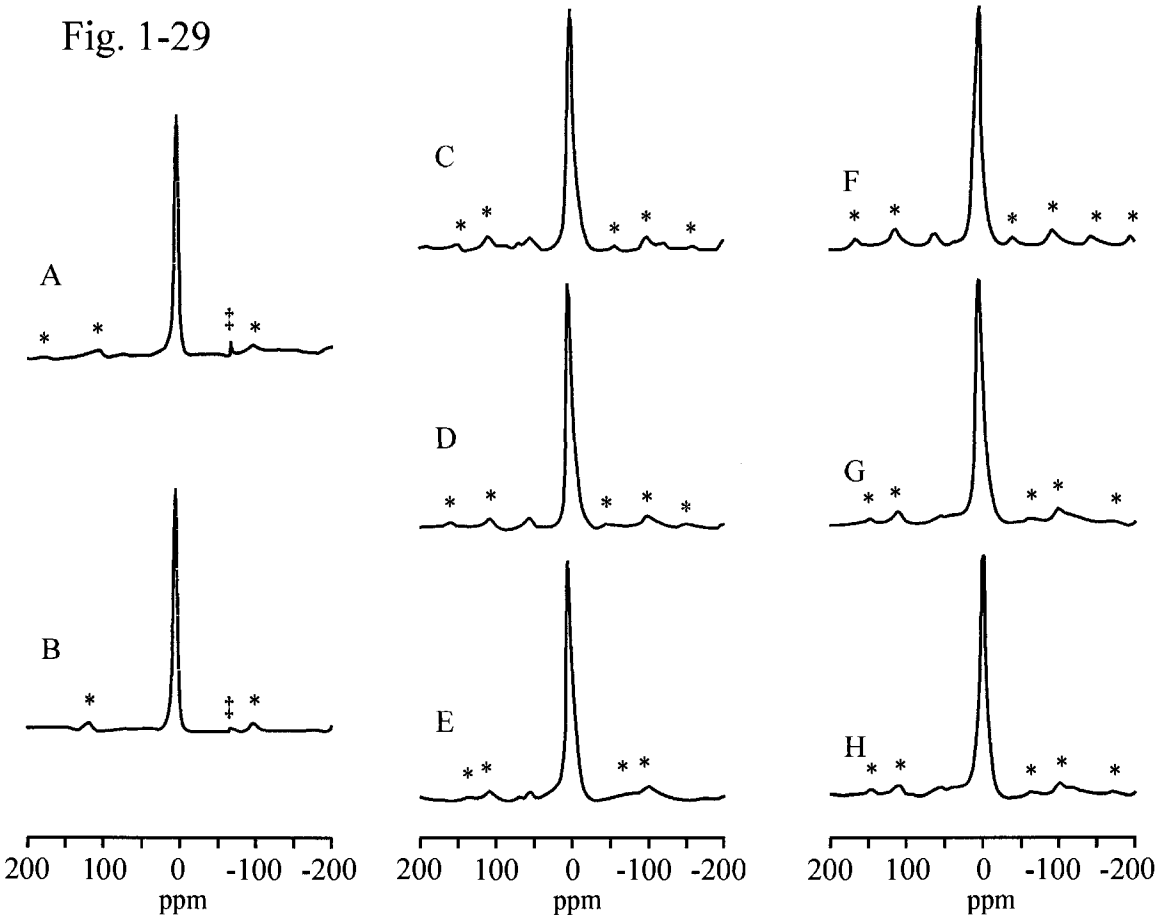

Figure 1-29. 156.3 MHz ^{27}Al DP-MAS spectra of various loaded and unloaded clays: A) 'As received' kaolinite. B) chlorpyrifos loaded (2 % by wt.) on 'as received' kaolinite. C) 'As received' Ca-montmorillonite. D) chlorpyrifos loaded (9.6 % by wt.) on 'as received' Ca-montmorillonite. E) hydrolyzed chlorpyrifos (**II**) loaded (10 % by wt.) on Ca-montmorillonite (5.0 % water by wt.). F) Al-montmorillonite. G) Cu(II)-montmorillonite. H) Zn-montmorillonite. Spinning sidebands are identified by *, instrumental artifacts by #.

Chapter 2: NMR Investigation of the Behavior of Methyl Parathion Sorbed on Clays

INTRODUCTION

The research described in this chapter investigated by ^{31}P NMR the decomposition of methyl parathion sorbed on partially-hydrated kaolinite and various cation-exchanged montmorillonites. The results are compared to those obtained in Chapter 1 for chlorpyrifos.

Methyl parathion (**I**), like chlorpyrifos, is a commonly used agricultural pesticide.

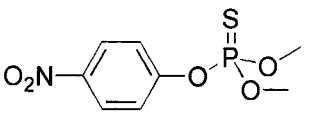

Methyl Parathion **I**

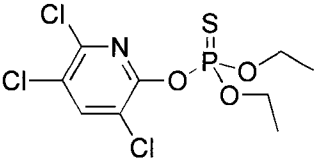

Chlorpyrifos

As with chlorpyrifos, various modes of decomposition are available for methyl parathion in the environment, including biotic and photolytic degradation processes, typically resulting in half-lives for methyl parathion disappearance of hours to days; biotic transformations are thought to be dominant in most ecosystems. (*2-1*) As in Chapter 1, the focus here is the *chemical* decomposition of methyl parathion sorbed on partially-hydrated clays, as represented in Scheme 2-1.

Scheme 2-1

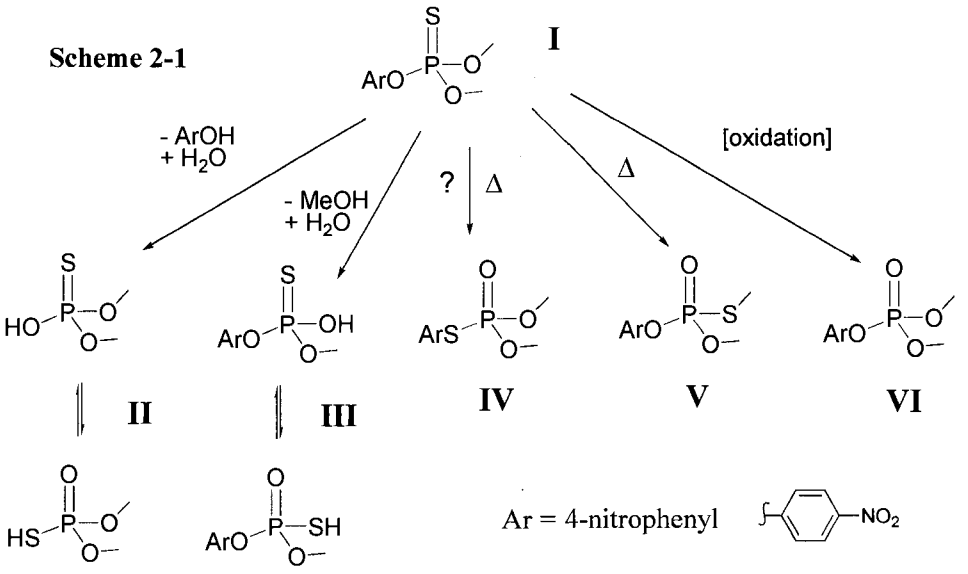

Scheme 2-1 shows possible initial clay-catalyzed decomposition reactions of methyl parathion; these reactions are expected on the basis of the chlorpyrifos results given in Chapter 1. Hydrolysis of methyl parathion, structure **I**, may result in either removal of the *p*-nitrophenoxy group (**II**) or a methoxy group (**III**); the resulting thiophosphoric acids may undergo the indicated tautomerizations (as was seen for chlorpyrifos). Alternatively, methyl parathion may undergo S,O-isomerization to give structures **IV** or **V**, or may be oxidized to the sulfur-free oxon form (**VI**), also known as methyl paraoxon.

The oxon form is much more toxic than is methyl parathion, but the hydrolysis products are less toxic than the starting pesticide, so hydrolysis may be considered a detoxifying process. (*2-1*) (The oxon form is reported to hydrolyze more quickly than methyl parathion). While no toxicity data were found in the literature for the S,O-isomerized forms (structures **IV** or **V**), these forms of similar organothiophosphate pesticides are thought to be similar in toxicity as the starting pesticide.

Although the chlorpyrifos and methyl parathion molecules are somewhat similar, they do exhibit important differences. Scheme 2-2 illustrates the possible bidentate coordination of chlorpyrifos to a metal cation, whereas methyl parathion is thought to exhibit only monodentate coordination through sulfur. Such bidentate coordination was reported to be important in some clay-catalyzed decompositions of another

Scheme 2-2

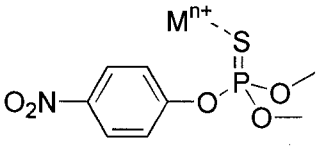

monodentate binding of metal cation to methyl parathion

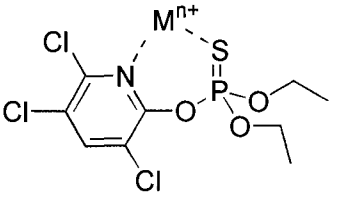

bidentate binding of metal cation to chlorpyrifos

organothiophosphate pesticide, quinalphos. (*2-2*)

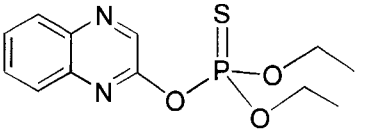

quinalphos

The reported half-life of methyl parathion is longer than that of chlorpyrifos in pure water (175 days and 78 days, respectively), but in most ecosystems methyl parathion appears to disappear more rapidly than does chlorpyrifos. (*2-1*) Methyl parathion has a reported vapor pressure, 1.3 mPa (9.8×10^{-6} Torr) at 20 °C, that is, like that of chlorpyrifos (2.7 mPa at 25 °C), very low (*2-1, 2-3*), so evaporative losses are expected to be quite slow in the environment or in this study.

EXPERIMENTAL

Clay Materials. Calcium montmorillonite, designated STx-1, and kaolinite, designated KGa-1b, were obtained from the Source Clay Mineral Repository (located at

the University of Missouri-Columbia), and are described in the Experimental Section of Chapter 1, as is the cation exchange procedure used to prepare homoionic Zn-, Al- and Cu(II)-montmorillonites.

Methyl Parathion Synthesis. Methyl parathion was synthesized as described in the literature (*2-4*), by the reaction of 310 mmol of sodium 4-nitrophenoxide dihydrate [824-78-2] with 247 mmol dimethyl chlorothiophosphate [2524-03-0] in 75 mL chlorobenzene solvent, using 1 mL triethylamine as catalyst, under reflux (95 °C) for five hours. The supernatant liquid containing the product was decanted from the solid sodium chloride produced by the reaction, and the solvent and catalyst were removed using a rotary evaporator (at 40 °C and 20 Torr). The crude product (an oily yellow liquid) was washed three times each with 80 mL portions of water, 5% aqueous sodium hydroxide, 5% aqueous HCl and finally water again. The resultant oily liquid (52 g; clear and colorless, with a faint mercaptan-like odor) was determined by ^{1}H and ^{31}P NMR to be approximately 75% methyl parathion, corresponding to a yield of about 60%. Attempts to purify a portion of the crude product by vacuum distillation (95 °C at 0.40 Torr) were unsuccessful because the product thermally isomerized (apparently to the O,S-dimethyl analogue) during distillation, a known degradation reaction of methyl parathion. (*2-5*)

The crude methyl parathion product was successfully purified by silica gel column chromatography, using a 50/50 ethyl acetate/hexane mixture and monitored by TLC (silica 60F and visualized by UV). The first major band off the column contained the product, and after rotary evaporation (25 °C at 18 Torr), was determined to be 99.1 % methyl parathion by ^{31}P NMR (in C_6D_6), as shown in Figure 2-1. Based on published spectra (*2-5*) of technical grade ethyl and methyl parathion, Figure 2-1 indicates that the

purified methyl parathion contains traces of the product of methoxy hydrolysis (**III**; peak at 52.6 ppm), a component generating a peak at 57.2 ppm, which may be the result of aryl hydrolysis (**II**) or the bis aryl product (**XIX**), and a component yielding a peak at 91.1 ppm which is tentatively assigned as **XXI**, an aryldimethylphosphorodithioate, $(ArS)(MeO)_2P{=}S$ or (MeS)(MeO)(ArO)P=S (reportedly common impurities in methyl parathion synthesis). (*2-5*) The peak seen in Figure 2-1B at 115.4 ppm is not assigned at this time. Not observed in this 99.1 % methyl parathion sample are S,O isomerization products (which would be expected at about 31 ppm) or methyl paraoxon (-5 ppm), all detectable decomposition products in this study (as will be seen below).

This 99.1 % methyl parathion sample is a slightly cloudy, non-crystalline solid, with an observed melting point range of 31 – 34 °C (literature value (*2-1*), 35 – 36 °C). Attempts were made to further purify this material (for example, by recrystallization or repeated column chromatography), with no success. Hence, the 99.1 % material was used in this study. The trace impurities present were not detectable by solid-state ^{31}P NMR. Although their presence could in principle affect the chemistry observed, that seems unlikely.

An earlier attempt was made to synthesize methyl parathion by the reaction of equimolar amounts of sodium 4-nitrophenoxide dihydrate and dimethyl chlorothiophosphate, using water as the solvent (heated to reflux at 95 °C, without a catalyst), a reaction also described in the literature (*2-6*); this procedure provided a product of much lower purity (54 %, by ^{31}P NMR in $CDCl_3$) with much lower yield (about 28 %). The NMR spectrum indicated most of the dimethyl chlorothiophosphate was hydrolyzed by the water solvent, instead of reacting with the 4-nitrophenoxide. The

dihydrate of the sodium 4-nitrophenoxide was utilized in these syntheses since that commercially-available form had been utilized successfully in previous work, and because the dihydrate was reported to be very difficult to dehydrate. (*2-6*)

Preparation of Pesticide-Loaded Clays. Water was sorbed on the clay materials by placing them in a humidifying chamber (a desiccator in which liquid water at RT is placed in the bottom) for about one hour, following the water adsorption gravimetrically. The humidified clays were then stirred for at least 15 minutes in a sealed round bottom flask. The weighed methyl parathion (99.1 % by ^{31}P NMR) was dissolved in about 30 ml of hexane or pentane, and stirred at RT with the clay for at least one hour. Solvent was removed by evaporation (the clay sample is spread in a thin layer in an open glass dish at room temperature for ten minutes). Typically, the pesticides (or residues) were loaded at a level of about 10 % by weight on the clay; this high loading level was used to facilitate detection of the NMR signals.

NMR Spectroscopy. Liquid-state ^{31}P NMR spectra were collected using a Chemagnetics Infinity-600 NMR spectrometer operating at 242.9 MHz (approximate 90° pulse width = 45 μs; 8.55 s repetition period; GARP proton decoupling (*2-7*) during signal acquisition). Concentrated (85 %) H_3PO_4 served as an external standard, and methyl parathion served as an internal standard in DMSO-d_6 (66.8 ppm) in those samples containing methyl parathion.

Most solid-state ^{31}P NMR spectra were obtained using a Chemagnetics CMX-II-150 NMR spectrometer, operating at 60.7 MHz, using a homebuilt probe with a 9 mm Chemagnetics Pencil-style spinning system, routinely capable of MAS speeds up to about 5 kHz. Some solid-state ^{31}P NMR spectra were obtained using a Chemagnetics CMX-II-

200 NMR spectrometer, operating at 80.9 MHz using a homebuilt probe with a 7 mm Chemagnetics Pencil-style spinning system. Typical sample amounts are 400 - 700 mg for each probe. Further details are provided in the Experimental Section of Chapter 1.

RESULTS

Table 2-1 shows ^{31}P chemical shifts obtained from various literature sources (*2-5, 2-8 through 2-11*) for various expected decomposition products (or synthetic impurities) of methyl parathion, or chemically-related species. These data were used to construct the chemical shift ranges shown in Table 2-2, which was used to assign the ^{31}P NMR signals observed in this study.

Methyl Parathion Sorbed on Kaolinite. Figure 2-2 compares the ^{31}P DP-MAS and CP-MAS spectra obtained for the decomposition of methyl parathion (1.4 % by wt.) on partially-hydrated kaolinite (1.1 % water by wt.), after one day and after 30 days of reaction (in the dark at room temperature). Note that, as was seen for chlorpyrifos, physisorbed but unreacted methyl parathion is easily observed by DP-MAS, but not seen by CP-MAS, after one day of reaction. No apparent decomposition of the adsorbed methyl parathion (67 ppm) has occurred after only one day, but both the DP-MAS and CP-MAS spectra after 30 days provide clear indications of pesticide decomposition. In addition to a peak at 27 ppm in both the DP and CP spectra after 30 days, broad intensity is observed between 35 and 5 ppm, and possibly between –5 and –25 ppm. The peak at 27 ppm is most probably due to the S,O-isomerized structure **V** (the other S,O-isomerized structure, **IV**, is also a possibility), while the oxon (**VI**) would be observed around –5 ppm.

The liquid-state ^{31}P spectrum of the DMSO-d_6 extract of this sample after 11 days reaction is shown in Figure 2-3A. In addition to the unreacted methyl parathion peak (66.8 ppm), decomposition products at 32.5 ppm and 28.2 ppm are assigned as the S,O-isomerized structures (**IV** and **V**). Also seen in Figure 2-3A is a very small, broad peak at 10.6 ppm; the breadth of this peak is similar to that seen in some in DMSO-extract spectra shown in Chapter 1, in which a thiophosphoric acid is undergoing tautomerization (*2-12*):

$$\text{-P(=S)OH} \leftrightarrows \text{-P(=O)SH} \qquad (2\text{-}1)$$

Considering this observation, the 10.6 ppm peak may be due to some type of thiophosphoric acid, possibly as the monomethyl ester, although no supporting evidence for this interpretation could be found in the literature. In fact, the ^{31}P chemical shift of unsubstituted thiophosphoric acid ($S=P(OH)_3 \leftrightarrows O=P(OH)_2(SH)$, structure **VIII**) has been reported several times (*2-10, 2-11*), all within the range 34 to 32 ppm. Another possible explanation for the linewidth of the 10.6 ppm peak in Figure 2-3A could be some other chemical exchange process. In any case, no conclusions can be made at this time regarding the origin of the 10.6 ppm peak; this peak was not observed in the ^{31}P spectra of any other DMSO-d_6 extract. Figure 2-3A also shows a peak at 91.4 ppm, attributed to **XXI**, O,O,S-dimethylarylphosphorodithioate, $(ArS)(MeO)_2P=S$.

An intriguing feature of Figure 2-2D, the ^{31}P CP-MAS spectrum of methyl parathion sorbed on partially-hydrated kaolinite after 30 days, is the peak at 64 ppm. Based on the chemical shift ranges previously established (Table 2-2), this may be some form of unreacted methyl parathion. The observation of ^{31}P CP-MAS intensity with a small higher-shielding shift from the corresponding large DP-MAS peak (Figure 2-2C)

suggests that two forms of unreacted methyl parathion are present after 30 days, one form (dominant in the DP-MAS spectrum) with sufficiently rapid atomic-level motion to interfere with cross polarization of ^{31}P from neighboring protons, and a second form with apparently more restricted motion (more efficient CP). Note in Figure 2-3A that in the DMSO-d_6 extract a very strong methyl parathion peak is seen at 66.8 ppm, but no peak is seen near 64 ppm. The 64 ppm CP-MAS peak in Figure 2-2D is presumably due to a more strongly sorbed form of methyl parathion, with sufficiently slow atomic-level motion that $^{1}H \rightarrow {}^{31}P$ can occur efficiently. The more motionally-restricted form may be strongly coordinated to a metal cation at the kaolinite surface, as shown in Scheme 2-3 as 'chemisorbed' **I**, whereas the 'physisorbed' form (67 ppm) is not observed

Scheme 2-3

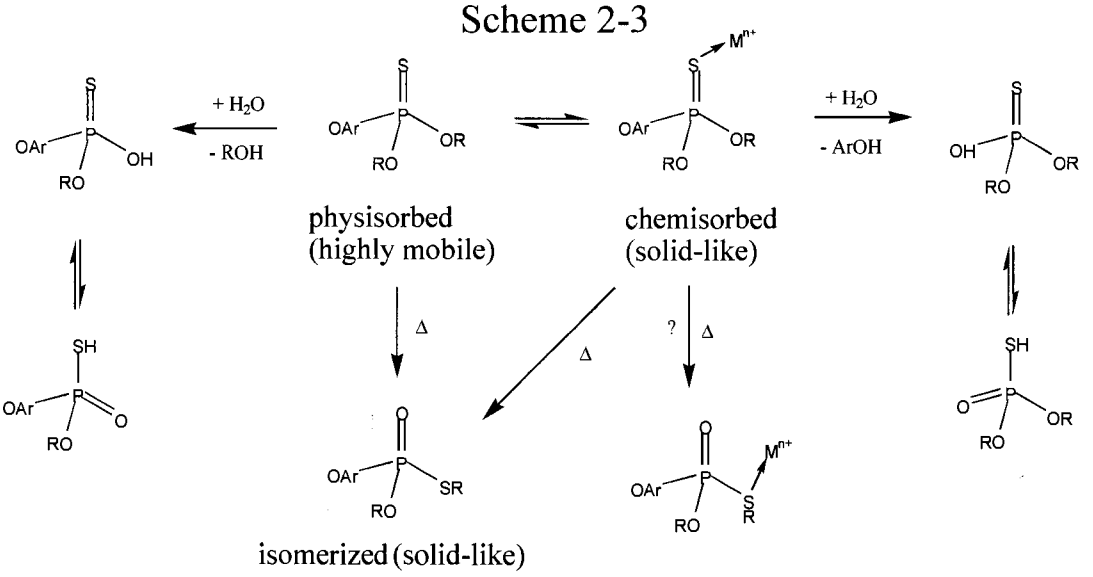

by CP-MAS. In Chapter 1 it was seen that unreacted chlorpyrifos that was physisorbed on kaolinite exhibited no ^{31}P CP-MAS signal, because of rapid atomic-level motion.

A variable-contact time ^{31}P CP-MAS experiment was performed on the 30 day-old sample represented in Figures 2-4C and 2-4D (spectra shown in Appendix 2-A), and the results are presented in Table 2-3 (along with relaxation results from other samples).

The peak at 64 ppm appears to have significantly larger T_{HP} and $T_{1\rho}$ values than do the other peaks, consistent with greater atomic-level motion for this species than for the decomposition products seen at lower chemical shifts. Proton $T_{1\rho}$ values may be increased if the homonuclear dipolar interaction between ^{1}H nuclei is attenuated by atomic-scale motion, as was seen in Chapter 1 for chlorpyrifos physisorbed on kaolinite.

Methyl Parathion Sorbed on Ca-montmorillonite. Figure 2-4 shows the ^{31}P DP-MAS and CP-MAS spectra of methyl parathion (9.2 % by wt.) adsorbed on partially-hydrated calcium montmorillonite (2.1 % water by wt.). After 1 day only a DP-MAS signal is seen (66 ppm) for physisorbed methyl parathion; as with chlorpyrifos, no CP-MAS signal is observed, presumably because of rapid atomic-scale motions. After 3 years, little signal intensity is observed in the DP-MAS spectrum near 66 ppm. Instead, a peak is observed at 33 ppm and a broader resonance is present around zero ppm, with its maximum at about 4 ppm. Quantitative analysis of the DP-MAS signal intensities (after 70,948 scans) indicates that more than 80 % of the total phosphorus signal is missing after 3 years, possibly due, in view of the low vapor pressure reported for methyl parathion (*2-1*), to desorption of one or more methyl parathion decomposition products.

When the 3 year-old sample was extracted into DMSO–d_6 (Figure 2-3B) or acetone–d_6 (not shown), the only liquid-state ^{31}P signal detected after many hours of signal averaging was a small peak at 31.3 ppm. The 32.5 ppm peak in Figure 2-4C is thought to be due to the same extractable species appearing at 31.3 ppm in Figure 2-3B, and is identified as an S,O-isomerized form of methyl parathion (structure **IV**). Since little or no ^{31}P CP-MAS signal is observed near 33 ppm after 3 years (Figure 2-4D), even

after 7 days of signal averaging (323,700 scans), the species involved may have sufficient atomic-level motions to interfere with cross polarization.

The broader resonance in the solid-sample spectra (Figures 2-4C,D) after 3 years (peak maximum at 4 ppm) is thought to be mineralized phosphate, i.e. phosphorus incorporated into the clay framework (*2-13*), and thus unextractable. Whatever the chemical moieties of the phosphorus atoms responsible for the broad peaks are, they are sufficiently immobile and close to proton spins for effective cross polarization, and thus appear in both the ^{31}P DP-MAS and CP-MAS spectra. The oxon form of methyl parathion (structure **VI**) may also be present, as this broad peak also has intensity near –5 ppm; the reported ^{31}P chemical shift of methyl paraoxon is –4.8 ppm. (*2-5*) The CP-MAS lineshape in Figure 2-4D is not well defined. This spectrum is not conclusive, but leaves open the possible presence of both mineralized phosphate and the oxon form. In any case, the species involved appear to be unextractable by DMSO-d_6 under the conditions used (Figure 2-3B).

No attempt was made to measure the kinetics of methyl parathion decomposition on this partially-hydrated Ca-montmorillonite, as a preliminary test indicated the decomposition was very slow over a period of about ten days.

Methyl Parathion Sorbed on Zn-montmorillonite. The decomposition of methyl parathion sorbed on partially-hydrated Zn-montmorillonite was much more rapid than on partially-hydrated kaolinite or Ca-montmorillonite. Figure 2-5 shows results on two samples: the spectra obtained after one day based on a sample of methyl parathion (8.5 % by wt.) sorbed on Zn-montmorillonite containing 4.5 % by wt. water, and the 3 year-old spectra are from a sample of methyl parathion (8.6 % by wt.) sorbed on Zn-

montmorillonite containing 5.3 % by wt. water. After one day, less than 20 % of the ^{31}P DP-MAS intensity is in the 65 ppm peak due to physisorbed methyl parathion; again, this peak is not seen in the corresponding CP-MAS spectrum, suggesting a very mobile state. Also missing from the one-day CP-MAS spectrum is the peak at 27 ppm seen in the corresponding DP-MAS spectrum, which is probably due to one or both of the S,O-isomerized forms of methyl parathion (structures **IV** or **V**, more likely the former). Apparently this (or these) species has (have) sufficient atomic-level motion to interfere with CP.

A broad signal, suggestive of multiple overlapping resonances, is observed in the one-day DP-MAS spectrum in Figure 2-5A, ranging from about 60 to 45 ppm. This chemical shift range is typical of structures **II** and **III**, the two initial hydrolysis products. **II** is the result of aryl hydrolysis, and has a reported ^{31}P chemical shift of 57.7 ppm when dissolved in benzene-d_6. (*2-5*) No literature report was found for the chemical shift of the methyl hydrolysis product, **III**; this chemical shift is estimated to be about 8 ppm less than that for **II**, or about 50 ppm. This estimate is based on the reported chemical shift differences between structures **I** and **XX**, the starting pesticides and their $S{=}P(OR)_3$ counterparts. (*2-5*) If these liquid-sample chemical shift increments are similar in the solid-state ^{31}P spectra of species sorbed on partially-hydrated Zn-montmorillonite, then the DP-MAS results suggest that both hydrolysis products are present. The CP-MAS spectrum obtained after one day (Figure 2-5) shows only a small peak at 50 ppm; thus, it may not be possible to detect **II** by CP-MAS on partially-hydrated Zn-montmorillonite, but a signal due to **III** is observed, though attenuated. No mineralized phosphate or oxon appears to be present after only one day of decomposition.

Figure 2-3C shows the liquid-state ^{31}P spectrum of the DMSO-d_6 extract of the one day old sample seen in Figure 2-5; the results, along with those of other liquid extracts, are summarized in Table 2-3. In addition to the large (off-scale) peak of unreacted methyl parathion at 66.8 ppm in Figure 2-3C, small peaks are seen at 91.5 ppm (previously mentioned synthesis impurity peak, **XXI**), the methyl hydrolysis product (**III**) at 52.3 ppm, and the S,O-isomerized forms at 32.5 and 28.2 ppm (structures **IV** and **V**, respectively). Comparison of the relative intensities of the DMSO-d_6 extract spectrum and the DP-MAS spectrum in Figure 2-5 suggests that physisorbed methyl parathion is more effectively extracted by DMSO than are the decomposition products.

Figure 2-5 also shows the spectra of a similar sample of methyl parathion sorbed on partially-hydrated Zn-montmorillonite, after 3 years of storage in the dark at room temperature. Unlike the results obtained when partially-hydrated Ca-montmorillonite was the adsorbing clay, a large amount of physisorbed methyl parathion (65 ppm) remains after 3 years. Also seen are peaks at 51 ppm, 36 ppm and 3 ppm, with a possible unresolved 'shoulder' at about –5 ppm. The 51 ppm peak is assigned as the methyl hydrolysis product **III**, and the 3 ppm peak is probably mineralized phosphate. The –5 ppm shoulder is assigned as the oxon form (**VI**). More uncertain is the assignment of the 36 ppm peak; it is most likely that this peak represents one the S,O-isomerized structures, probably structure **IV**. The ^{31}P chemical shift is significantly higher than either the 32.6 or 28.2 ppm chemical shifts seen in the DMSO-d_6 extract spectrum of the one day sample (Figure 2-3C). It is possible that coordination to either the Zn^{2+} cation or interaction with the clay framework has shifted the ^{31}P peak to lower shielding than it would experience in a non-interacting state.

Figure 2-3D shows the liquid-state ^{31}P spectrum of the DMSO-d_6 extract of the 3 year old sample. The only extracted species detected (after 2760 scans, almost 7 hours signal averaging) was unreacted methyl parathion at 66.8 ppm.

Figure 2-6 shows the variation in the ^{31}P DP-MAS spectrum over a period from 9.7 to 20.9 hours after sorption of methyl parathion (8.5 % by wt.) on Zn-montmorillonite containing 4.5 % by wt. water. The sorbed methyl parathion signal (65 ppm) is seen to disappear as the 36 ppm peak (due to one the S,O-isomerized structures, probably structure **IV**, as mentioned above) grows. Figure 2-7 shows the variation in the 65 ppm peak intensity over time. Figure 2-8 shows the natural log of the 65 ppm peak height plotted *vs.* decomposition time in hours; a linear least squares fit to this plot gives a pseudo-first order rate constant of $2.50 \pm 0.31 \times 10^{-4}$ min^{-1}, as shown in Table 2-5, although the linearity of the data is not good ($r^2 = 0.9559$). Figure 2-9 shows the inverse peak height of the 65 ppm peak height plotted *vs.* decomposition time in hours; a linear plot is an indication of second-order or pseudo-second order kinetics. The kinetics results of this sample and others will be discussed in more detail below.

Methyl Parathion Sorbed on Al-montmorillonite. Two samples were prepared of methyl parathion sorbed on Al-montmorillonite and monitored by ^{31}P MAS NMR. Figure 2-10 shows the ^{31}P DP-MAS and CP-MAS spectra of a sample containing methyl parathion (9.1 % by wt.) sorbed on a partially-hydrated Al-montmorillonite (4.5 % H_2O by wt.), after 1 day, 7 days and 2.0 years reaction time. As in other spectra, identified spinning sidebands are indicated by asterisks; # indicates an identified instrumental artifact. The largest peak in the DP-MAS spectrum after 1 day is at 67 ppm, and appears to be chemisorbed but unfragmented methyl parathion (as indicated in Scheme 2-3). This

67 ppm peak also appears strongly in the CP-MAS spectrum. Coordination of methyl parathion to Al^{3+} in the interlayer region of the montmorillonite structure may be stronger than coordination to Ca^{2+} or Zn^{2+} cations, because of the greater cation charge; if so, stronger coordination may hinder the atomic-level mobility of the physisorbed methyl parathion more than does coordination to Ca^{2+} or Zn^{2+}, possibly resulting in more efficient cross polarization dynamics and a strong CP signal. Also present in the one-day sample spectra (by both DP-MAS and CP-MAS) is a strong peak at 30 ppm, assigned as an S,O-isomerized product, probably structure **V**, containing a –SMe moiety. No hydrolysis products (such as **III**) are observed near 50 ppm, though some intensity near 60 ppm may be due to the aryl hydrolysis product, **II**. Peaks marked with an asterisk in Figure 2-10 are, as usual, identified as spinning sidebands; because of these peaks, it is not clear in Figure 2-10 whether small centerband peaks are present near 90 ppm and 5 ppm.

Figure 2-10 also shows a peak not previously observed; there appears to be a partially resolved peak at about 73 ppm in the DP-MAS spectra and in the CP-MAS spectrum of the one-day sample. This ^{31}P chemical shift is similar to that of structure **XX**, O,O,O-trimethylphosphorothioate or $S{=}P(OMe)_3$, reported to have a shift of 74 ppm in benzene-d_6 (*2-5*). One possible way to rationalize the presence of **XX** is a transesterification reaction between two methyl parathion molecules:

$$2\ S{=}P(OMe)_2(OAr) \rightarrow S{=}P(OMe)_3 + S{=}P(OMe)(OAr)_2 \qquad (2\text{-}2)$$

(or, 2 **I** → **XX** + **XIX**, using the structure numbers of Table 2-1).

Structure **XIX**, $S{=}P(OMe)(OAr)_2$, known as the bis aryl product, is expected to resonate near 58 ppm, its reported shift in benzene-d_6. (*2-5*) Such a peak may be present in Figure 2-10, but not resolved because of overlap with the large 66 ppm peak.

In Figure 2-10, one sees that, after 7 days of decomposition (in the dark at room temperature), the partial disappearance of physisorbed methyl parathion at 66 ppm, with growth in the 30 ppm peak. The 73 ppm peak is still present (albeit partially resolved) in the DP-MAS spectrum, but does not appear (or is greatly attenuated) in the CP-MAS spectrum, again presumably due to atomic-level motions. Also present after 7 days is some intensity near 57 ppm in both the DP-MAS and CP-MAS spectra. This signal is assigned to the bis aryl derivative of methyl parathion (**XIX**), as discussed in the preceding paragraph. In the spectra obtained after 7 days (Figures 2-10C and D), it is not clear whether any centerbands are located under the spinning sidebands near 90 and 5 ppm; it is not clear whether any mineralized phosphate may be present. The absence of any intensity at –5 ppm suggests that no significant oxon formation has occurred.

Figure 2-11 shows changes in the DP-MAS ^{31}P spectra of the same sample of methyl parathion sorbed on partially-hydrated Al-montmorillonite represented in Figure 2-10, covering the period 2 hours to 3 days after adsorption of starting pesticide. Both the 73 ppm and 66 ppm peaks (assigned to **XX** and **I**, respectively) decrease with time, although in the case of the 73 ppm 'shoulder' the decrease may in fact be the result of the decrease in the intensity of the overlapping 66 ppm peak. The 30 ppm peak, on the other hand, grows rapidly during the first three days of decomposition. The DP-MAS spectra in Figure 2-11 display no significant centerband intensity near 90 ppm or 5 ppm; this may

be seen by comparing the location of the spinning sidebands, since different spinning speeds were used for the 2 day and 3 day spectra.

Figure 2-3E shows the liquid-state ^{31}P spectrum of the DMSO-d_6 extract of the ten day-old material (methyl parathion adsorbed on partially-hydrated Al-montmorillonite). The largest peaks observed are assigned as unreacted methyl parathion (66.8 ppm) and structure **V** (28.4 ppm), the S,O-isomerized pesticide structure with a –SMe moiety. The smaller peak at 32.7 ppm is assigned as structure **IV**, the other S,O-isomerized pesticide structure, this time with a –SAr moiety. The very small peaks at 71 ppm and 12.8 ppm are barely above the noise, but were reproducibly observed when the spectrum was reacquired. The 71 ppm peak may be due to the trimethyl structure (**XX**) seen in the DP-MAS spectrum at 73 ppm. The 12.8 ppm peak has not been assigned; it may represent a sulfur-free, partially-hydrolyzed derivative, such as structure **X** or **XIV**. No hydrolysis products (**II** or **III**, expected near 57 and 53 ppm) were extracted, nor is any oxon intensity seen near –5 ppm. Figure 2-3F shows the liquid-state ^{31}P spectrum of the DMSO-d_6 extract of the two year-old material (methyl parathion adsorbed on partially-hydrated Al-montmorillonite). The spectrum is remarkably similar to that of Figure 2-3E, representing the extract of the ten day-old sample, except for the complete disappearance of the large unfragmented methyl parathion peak.

The ^{13}C CP-MAS spectrum of the sample of methyl parathion on partially-hydrated Al-montmorillonite (9.1 % by wt. methyl parathion, 4.5 % by wt. water), after 4 days decomposition, is shown in Figure 2-12A. The peaks are assigned, from higher to lower chemical shift (left to right) as carbon-4, carbon-1 and overlapping intensity due to carbons-2 and -3 of the aromatic ring; the methoxy carbons appear as a single peak at

about 55 ppm. It is not clear from Figure 2-12 how many carbon-containing species are present in the sample. However, the ^{31}P MAS spectra in Figure 2-10 clearly indicate the presence of multiple phosphorus-containing structures, including both chemisorbed (*i.e.*, strongly-bound but unfragmented methyl parathion) and at least one S,O-isomerized residue. Therefore, as seen in Chapter 1 for chlorpyrifos, ^{13}C CP-MAS NMR appears to be much less useful than ^{31}P MAS NMR to distinguish decomposition products from sorbed methyl parathion.

Figure 2-12B shows the ^{13}C CP-MAS spectrum of crystalline sodium 4-nitrophenoxide dihydrate; note the large changes in the aromatic carbon peak positions compared to the ^{13}C CP-MAS spectrum of the sample of methyl parathion on partially-hydrated Al-montmorillonite (9.1 % by wt. methyl parathion, 4.5 % by wt. water), after 4 days decomposition, shown in Figure 2-12A. This comparison suggest that ^{13}C CP-MAS NMR may have utility to detect the product of aryl hydrolysis of methyl parathion, albeit with much lower sensitivity than by ^{31}P NMR because of the much lower isotopic abundance of carbon-13.

A second sample was prepared of methyl parathion sorbed on Al-montmorillonite, using the anhydrous clay without any added water, although a small amount of water was adsorbed during sample preparation (done in the open lab, not under a controlled, anhydrous atmosphere). The methyl parathion content of this sample is 8.8 % (by wt.), similar to the 9.1 % (by wt.) methyl parathion content when adsorbed onto partially-hydrated Al-montmorillonite. Gravimetric analysis of the adsorption of atmospheric moisture of this anhydrous clay suggests that an estimated 0.2 % of the weight of the clay is due to water adsorbed during handling in air. Thus, this study of methyl parathion

decomposition was carried out when the pesticide was sorbed onto an almost anhydrous Al-montmorillonite. Figure 2-13 shows the ^{31}P DP-MAS spectra of this sample, 8.8 % methyl parathion adsorbed on Al-montmorillonite containing approximately 0.2 % water, after 1 day, 4 days and 19 days reaction. The peak positions observed are the same as when the partially-hydrated Al-montmorillonite was used (Figure 2-10), and the assignments are assumed to be identical to those mentioned above.

Figure 2-14 shows changes in the DP-MAS ^{31}P spectra of the same sample of methyl parathion sorbed on Al-montmorillonite containing < 0.2 % water by wt. (represented in Figure 2-13), covering the first nine hours after adsorption of ,ethyl parathion. Comparison of Figures 2-11 and 2-14 indicate that decomposition of methyl parathion is much faster when sorbed on Al-montmorillonite containing < 0.2 % water (by wt.) than when sorbed on Al-montmorillonite containing 4.5 % water (by wt.). Further analysis of the kinetic results in Figures 2-11 and 2-14 is given below.

Figure 2-15 shows the ^{31}P MAS spectra of the sample seen in Figure 2-10, 8.8 % methyl parathion sorbed on Al-montmorillonite containing < 0.2 % water content, after 1 day and after 2.0 years reaction. As in other spectra, identified spinning sidebands are indicated by asterisks; # indicates an identified instrumental artifact. After two years, the largest peak is still seen at 30 ppm (probably the S,O-isomerized structure **IV**). ^{31}P DP-MAS intensity is also seen in Figure 2-13C from zero ppm to about 20 ppm, where overlap with the 30 ppm peak occurs. The peak maximum in this region occurs about 4 ppm, which may be due to mineralized phosphates. The liquid-state ^{31}P spectrum of the DMSO-d_6 extract of this sample is shown in Figure 2-3G. The only peak observed is that of unfragmented methyl parathion; this spectrum is very different from that of the

DMSO-d_6 extract of 2 year-old methyl parathion sorbed on partially-hydrated Al-montmorillonite (Figure 2-3F). Apparently, the methyl parathion decomposition products formed when sorbed on Al-montmorillonite are much less extractable when the clay is almost anhydrous (< 0.2 % water by wt.), compared to the behavior with partially-hydrated clay (4.5 % water by wt.).

Methyl Parathion Sorbed on Cu-montmorillonite. Figure 2-16 compares the ^{31}P DP-MAS and CP-MAS spectra of methyl parathion (8.5 % by wt.) adsorbed on partially-hydrated Cu(II)-montmorillonite (4.8 % water by wt.), after six hours and after 3 years. After six hours, the largest peak in both the DP-MAS and CP-MAS spectra is at 58 ppm, similar, but not identical, to the chemical shift of methyl parathion (66 ppm). This peak appears to be due to the chemisorbed (but probably unfragmented) pesticide, with sufficiently limited atomic-level motion that cross polarization is possible. However, this CP-MAS peak is less intense than the corresponding peak in the DP-MAS spectrum, suggesting that cross polarization is not highly efficient. Maximum efficiency would entail an enhancement factor equal to the ratio of magnetogyric ratios of ^{31}P and ^{1}H, specifically a value of 2.47. In Figure 2-16B, the observed cross polarization enhancement factor is close to 0.55, equivalent to only about 22 % of the maximum possible signal by CP from protons.

All the CP-MAS ^{31}P peaks in Figure 2-16 are significantly less intense than the corresponding DP-MAS peaks. As mentioned above, for highly efficient cross polarization, the CP-MAS peaks should be roughly 2.5 times as large as those obtained by DP-MAS. The fact that all the ^{31}P CP-MAS are less intense than their DP-MAS counterparts implies that there is a 'sample-wide' explanation, and the responsible effect

is not site-specific or structure-specific. One possible explanation deals with the presence of paramagnetic species in Cu(II)-montmorillonite. Cu(II) complexes are paramagnetic (*2-14, 2-15*), and the presence of the unpaired electronic spins can affect the cross polarization dynamics via strong electron-spin/nuclear-spin dipolar interactions, e.g., by reducing the proton $T_{1\rho}$ values to the degree that magnetization transfer from protons to phosphorus never achieves full ^{31}P magnetization enhancement.

If the 58 ppm peak in Figure 2-16 is indeed due to unfragmented methyl parathion, sorption onto Cu(II)-montmorillonite causes a greater increase in the isotropic ^{31}P shielding (about 9 ppm relative to the pesticide in DMSO solution) than was seen with the other forms of montmorillonite encountered above (0 - 3 ppm increase in shielding upon sorption). It is possible that the manner of methyl parathion adsorption is significantly stronger for partially hydrated Cu(II)-montmorillonite than for the other cation-exchanged forms. For example, perhaps methyl parathion may strongly coordinate to Cu^{2+} *via* the thiophosphate sulfur, slowing atomic-level motion or chemical exchange of the pesticide to other (similar or different) adsorption sites. Another possible assignment for the 58 ppm peak in Figure 2-16 is structure **II**, the aryl hydrolysis product of methyl parathion. The literature value for the ^{31}P chemical shift of **II** is 57.7 ppm (see Table 2-1). If this assignment is correct, then this hydrolysis reaction is much more rapid than in the other samples discussed above, such as chlorpyrifos adsorbed onto a similar partially-hydrated Cu(II)-montmorillonite (Chapter 1).

Also seen in Figure 2-16 (by both DP-MAS and CP-MAS) after one day is a peak at 30 ppm. This peak is assigned as one of the S,O-isomerized forms of methyl parathion

(structures **IV** and **V**). Intensity near 5 ppm is probably due to mineralized phosphate, or one of the sulfur-free, partially-hydrolyzed phosphate esters.

Figure 2-16 also shows the DP-MAS and CP-MAS spectra of the same sample after 3 years of storage in the dark at room temperature. The appearance of the spectra has changed dramatically after three years of pesticide decomposition. What appear to be two overlapping peaks are seen by both DP-MAS and CP-MAS methods. The largest peak has a chemical shift of –11 ppm, and there is a 'shoulder' at about –18 ppm. Assuming this 'shoulder' is due to an almost unresolved peak at about –18 ppm, there appear to be two long-term products of methyl parathion decomposition on partially-hydrated Cu(II)-montmorillonite.

The major product in the decomposition of methyl parathion (8.5 % by wt.) sorbed on Cu-montmorillonite (4.8 % water by wt.) sample appears to be the oxon form of methyl parathion (**VI**), which is reported (Table 2-1) to have a shift of –4.8 ppm in benzene-d_6. Figure 2-3H, the liquid-sample ^{31}P NMR spectrum of the DMSO-d_6 extract of the 3 year old sample shown in Figure 2-16, has only a single peak at –3.6 ppm, assigned as the oxon form. Thus, it is unlikely that after six hours of reaction, all (or almost all) of the starting pesticide was hydrolyzed or S,O-isomerized. It is possible that the –11 ppm major product peak is a partially-hydrolyzed oxon form (such as **IX**, **X** or **XV**), perhaps resulting from oxidation of **II**. The –18 ppm 'shoulder' peak is more difficult to assign, even tentatively; as seen in Table 2-1, none of the listed possible decomposition products for which literature shift values are available has a ^{31}P chemical shift near –18 ppm. Perhaps reaction with (or coordination to) the Cu^{2+} cations may be responsible for this peak.

Figure 2-17 shows changes in the DP-MAS ^{31}P spectrum during the first 267 hours of decomposition of the sample of Figure 2-16 (8.5 % by wt. methyl parathion on Cu(II)-montmorillonite containing 4.8 % water by wt.), with the first data point after 3.8 hours. As the 58 ppm peak did not exhibit an observable decrease in intensity with time, no kinetics analysis was performed on this sample. Apparently the physisorbed methyl parathion is fully converted to the chemisorbed form after only 3.8 hours, and the decomposition of the chemisorbed methyl parathion (58 ppm) is slow within the first 43 hours after sorption.

DISCUSSION

Comparison of Methyl Parathion and Chlorpyrifos – Product Distribution.

In most cases, the predominate mode of decomposition on the various hydrated clays is quite different for methyl parathion and chlorpyrifos, as summarized here:

partially-hydrated clay	**Chlorpyrifos**	**Methyl Parathion**
kaolinite	oxidation	isomerization and mineralization
Ca-montmorillonite	isomerization	isomerization and mineralization
Zn-montmorillonite	hydrolysis	all
Al-montmorillonite	mineralization	isomerization, followed by mineralization
Cu(II)-montmorillonite	oxidation	oxidation

These results show the importance of the exchangeable metal cation in montmorillonite on the pesticide decomposition product distribution. The Al^{3+}-exchanged montmorillonite appears to favor mineralization, i.e., the incorporation of phosphorus into the mineral framework. This may reflect the favorable energetics of P-O-Al bond formation; aluminum phosphate species such as ALPO-5 are well known and very stable

microporous solids. (*2-14*) If P-O-Al linkages are formed in Al-montmorillonite, they may be detectable by $^{31}P/^{27}Al$ cross polarization or double quantum coherence experiments; similar experiments have been applied to the NMR characterization of various aluminophosphates. (*2-19*) Calcium montmorillonite also appears to favor some mineralization, again perhaps reflecting the thermodynamic stability of the resulting mineral phases.

The Cu(II)-montmorillonite, on the other hand, appears to catalyze oxidation of both chlorpyrifos and methyl parathion to their respective oxon forms. Note that among the exchangeable metal cations involved in this study, only copper exhibits more than one stable cation form. Aqueous Cu^{2+} cations are known to be oxidizing agents. (*2-14*)

S,O-isomerization appears to be a more facile mode of decomposition for methyl parathion than for chlorpyrifos, occurring to some degree no matter the clay substrate used. With chlorpyrifos, isomerization is the dominant mode of decomposition only on the partially-hydrated calcium montmorillonite. It is possible that the bidentate coordination possible for chlorpyrifos shown in Scheme 2-2 interferes with the isomerization reactions in some manner that is not applicable to methyl parathion.

A minor difference between the ^{31}P spectra obtained in this study for chlorpyrifos (Chapter 1) and methyl parathion is based on the relative purities of the starting materials, as seen in Figure 2-1. The chlorpyrifos used was a pure crystalline solid with no detectable ^{31}P resonances other than the 61 ppm peak of chlorpyrifos, even after 48 hours of signal averaging; thus the chlorpyrifos used is more than 99.99 % pure. On the other hand, the methyl parathion synthesized in this study had NMR-detectable impurities, even after repeated application of column chromatography. One small but persistent impurity

shows up in the ^{31}P spectra at about 95 ppm in DMSO-d_6, and was tentatively assigned above as an aryldimethylphosphorodithioate, $(ArS)(MeO)_2P{=}S$ or $(MeS)(MeO)(ArO)P{=}S$. (*2-5*) It is hypothesized in this study that the small amounts of synthetic impurities present in the 'purified' methyl parathion sorbed on the clays had no significant impact on the product distributions observed by ^{31}P NMR.

Comparison of Methyl Parathion and Chlorpyrifos – Kinetics of Initial Pesticide Decomposition. Figure 2-7 shows the variation in the intensities of the peaks due to physisorbed (unreacted but sorbed) methyl parathion on pesticide/clay samples; these variations are plotted *vs.* decomposition time in hours, scaled such that the peak height is extrapolated to 100 arbitrary units at time = 0. Figure 2-8 shows plots of the natural log of these peak heights *vs.* time in hours. Figure 2-9 shows the inverse of these peak heights plotted *vs.* time in hours. Similar analyses of the pesticide decomposition on partially-hydrated kaolinite or Ca-montmorillonite were not undertaken because they were judged to be too slow to be followed conveniently by solid state NMR.

Kinetics of the decomposition of methyl parathion sorbed on Cu(II)-montmorillonite was also not amenable to analysis. As Figure 2-17 shows, the disappearance of physisorbed pesticide is virtually complete after only 3.8 hours, and the chemisorbed methyl parathion peak showed no clear decrease in intensity over a period of two days.

The apparent linearity of the log plot representing the disappearance of unreacted methyl parathion in Figure 2-8 is consistent with mechanisms that are first order or pseudo-first order in methyl parathion. Pseudo-first order disappearance of methyl parathion and similar pesticides is commonly observed in many environments. (*2-20*)

Table 2-5 summarizes the pseudo-first order rate constants determined for the disappearance of the physisorbed methyl parathion peak from the ^{31}P DP-MAS spectra when sorbed on the various cation-exchanged clays. Also given in Table 2-5 are the corresponding half-life values, expressed in units of hours. Note that when sorbed on Zn- or Al-montmorillonite, methyl parathion decomposition rates exceed the reported aqueous hydrolysis rate (*2-1*) by 2 or 3 orders of magnitude, presumably reflecting the availability of isomerization and mineralization pathways not available in water, and the effects of heterogeneous catalysis by the clays.

The rate constant for the disappearance of the physisorbed methyl parathion peak (65 ppm) on partially-hydrated Al-montmorillonite appears to be greater for the almost-anhydrous material (Figure 2-8). The partially-hydrated Al-montmorillonite data cover the first 72 hours of decomposition, whereas for the 0.2 % water content clay only the first five data points, covering roughly the first 9 hours, were available because of an instrument malfunction. Methyl parathion sorbed on the almost anhydrous Al-montmorillonite shows quite a bit more deviation from a first-order log plot, with an apparently higher decomposition rate at shorter times. The best linear least-squares fit is shown by a solid line in Figure 2-8. The pseudo-first order rate constant associated with this line is $2.41 \pm 0.72 \times 10^{-3}$ min^{-1}, with a corresponding reaction half-life of only 5 hours. This reaction rate is approximately nine times greater than the rate observed when the pesticide decomposition occurs on the partially-hydrated material. More data points before 6 hours elapsed time would be necessary to confirm the non-linearity at short times. The clay-loading procedures described in the Experimental Section are sufficiently time consuming that (together with spectrometer setup) it is difficult to obtain spectra

before about 4 hours of reaction time. Alternate procedures for sorbing pesticide on clay could possibly expedite the sample preparation and spectrometer setup process.

Chlorpyrifos kinetics results are also included in Table 2-5; plots of physisorbed peak heights *vs.* time are shown in Chapter 1 (along with the corresponding log peak height *vs.* time plot and inverse peak height *vs.* time plot). Note that in Table 2-5 two rate constants (and corresponding half-lives) are reported for some of the chlorpyrifos samples studied. In these cases, a subset of data points representing a shorter period of reaction times was also fit, in an attempt to obtain better values for the initial decomposition rate. Table 2-5 indicates the period of time for which data points were included in the linear-least squares fit.

Several conclusions are immediately obvious from Table 2-5. First, the cation identity strongly affects the initial pesticide decomposition rates. For both chlorpyrifos and methyl parathion, decomposition on partially-hydrated Cu(II)-montmorillonite is significantly faster than with the other cation-exchanged clays. For chlorpyrifos, the slowest decomposition rate measured occurs when the pesticide is loaded on partially-hydrated Al-montmorillonite. For methyl parathion, the initial decomposition rate was approximately equal when loaded on either partially-hydrated Zn- or Al-montmorillonites.

Second, the water content also affects decomposition rates. For both chlorpyrifos on Zn-montmorillonite and methyl parathion on Al-montmorillonite (the two systems studied for which samples were prepared with two different water contents), the disappearance of the physisorbed pesticide was faster at lower water contents. Similar observations have been reported (albeit at much lower loading levels) for the

decomposition of other organothiophosphate pesticides on clays, as determined by extraction followed by GC/MS analysis (*2-17*, *2-18*). One explanation for the slowing of the decomposition with increasing water content involves a scenario based on competition between water and the unreacted pesticide for the adsorption sites that catalyze the pesticide reactions observed.

Third, methyl parathion decomposes more quickly than chlorpyrifos on both Al- and Cu(II)-montmorillonites (with roughly equal water contents). However, when adsorbed on partially-hydrated Zn-montmorillonite, the best pseudo-first order decomposition rate constants of chlorpyrifos and methyl parathion disappearance are approximately equal. The bidentate coordination of chlorpyrifos to Zn^{2+} cations, as shown in Scheme 2, may be responsible for accelerating the chlorpyrifos decomposition to the point were it is roughly equal to that of methyl parathion, which cannot coordinate to the metal cation in a bidentate manner. Aqueous Zn^{2+} and Cu^{2+} cations are known to catalyze hydrolysis of chlorpyrifos and similar organothiophosphate pesticides. (*2-3*)

When similar clay/pesticide/water samples were examined, methyl parathion decomposition was faster than chlorpyrifos decomposition for sorption on Cu(II)- or Al-exchanged montmorillonites. Only with partially-hydrated Zn-montmorillonite were the pseudo-first order pesticide disappearance rate constants similar for these two pesticides. Since chlorpyrifos is thought to form bidentate coordination with metal cations (Scheme 2-2), whereas methyl parathion does not (*2-2*), and since the metal cation is thought to have a direct catalytic role in hydrolysis, differences between these two pesticides may be expected (*2-17*).

In order to test for second-order methyl parathion disappearance behavior, the inverse peak heights corresponding to the data in Figure 2-7 are plotted as a function of time in Figures 2-9. Second-order behavior for methyl parathion disappearance should result in a linear plot. The solid lines represent the best linear least-squares fit to the data points. The second-order plots of Figure 2-9 appear to be no more or less linear than the first-order plots of Figure 2-8. None of the methyl parathion samples was monitored for a sufficiently long period to distinguish between the applicability of either first-order or second-order kinetic models. For chlorpyrifos sorbed on Cu(II)-montmorillonite (5.1 % water) or Al-montmorillonite (3.6 % water), however, there is apparently greater linearity in the second-order kinetics plot than in the first-order plot (see Chapter 1). The possible second-order behavior considered here, if true, raises some intriguing possibilities for bimolecular pesticide decomposition mechanisms. For example, if the first step of a mechanism is a slow (rate-limiting) trans-esterification, followed by rapid isomerization or hydrolysis reactions, second-order kinetics would be expected.

It should be noted that these studies do not attempt (nor warrant) a full kinetics analysis of the decomposition of these pesticides on these clay systems, but instead provide preliminary indications of the overall kinetics behavior and illustrate the applicability of solid state ^{31}P NMR techniques for investigating the decomposition of organothiophosphate pesticides on clays. These preliminary kinetics results were obtained as a byproduct of the qualitative characterization of the chemistry of pesticide decomposition observed, they were not obtained explicitly to elucidate the mechanisms involved.

Summary and Conclusions.

Decomposition of methyl parathion on kaolinite and various cation-exchanged montmorillonites (at room temperature, in the dark) was monitored by ^{31}P NMR. All the expected decomposition products were observable by both DP and CP ^{31}P NMR. Decomposition products included the results of hydrolysis reactions, isomerization reactions and oxidation reactions; mineralization also appears to occur in some cases. Assignments of ^{31}P peaks was based mostly on literature values of chemical shifts of similar structures. Liquid-state ^{31}P NMR experiments on DMSO-d_6 extracts of the pesticide/clay samples aided in the assignment of the solid-state peaks observed.

As with chlorpyrifos, methyl parathion was found to be physisorbed initially on kaolinite and various cation-exchanged montmorillonites (Ca-, Zn-, Cu(II)- and Al-montmorillonites) in a state with rapid liquid-like molecular-level motion, as evidenced by the strong DP ^{31}P NMR signal and lack of ^{31}P CP signal. In some cases, the pesticide appears to be converted to a chemisorbed (but otherwise unfragmented) form that is observable by CP ^{31}P NMR.

On partially hydrated kaolinite and Ca montmorillonite, decomposition of methyl parathion is quite slow, with half-lives for the disappearance of more than one year. On partially-hydrated Zn-, Al- and Cu(II)-montmorillonites, pseudo-first order disappearance of methyl parathion was observed with half-lives ranging from possibly less than one hour to 46 hours. Decomposition is apparently fastest on Cu(II)-montmorillonite, while on Al-montmorillonite and Zn-montmorillonites the methyl parathion half-lives are approximately equal when similar hydration levels were used.

The dominant mode of decomposition of methyl parathion varies with the identity of the partially-hydrated clay and cation form used. On kaolinite, decomposition appears to be mostly isomerization, whereas on Ca-montmorillonite, both hydrolysis and isomerization were observed. On Al-montmorillonite and Cu(II)-montmorillonite, decomposition of methyl parathion is predominately mineralization and oxidation, respectively. On Zn-montmorillonite all modes of decomposition are observed (hydrolysis, isomerization, oxidation and mineralization).

Higher hydration levels of Al-exchanged montmorillonite (4.5% vs. approx. 0.2% water, by weight) were found to reduce the decomposition rate of methyl parathion. This effect is similar to that seen for chlorpyrifos on Zn-montmorillonite, and similar to literature reports for other, similar organothiophosphate pesticides, as studied by non-NMR techniques. (*2-17*) The slower decomposition rates in the presence of added water may reflect a competition between water and the pesticide for active catalytic sites, presumably involving the metal cation.

Chapter 2 Literature Cited

(2-1) "Methyl Parathion - Environmental Health Criteria (Vol. 145)", International Programme on Chemical Safety, World Health Organization, Geneva 1993.

(2-2) Pusino, A.; Gessa, C.; Kozlowski, H. Pestic. Sci. 1988, 24, 1.

(2-3) Racke, K. D. Reviews of Environmental Contamination and Toxicology 1993, 131, 1.

(2-4) Mandelbaum Y. A.; Melnikov N. N.; Bakanova Z. M. Zh. Obshch. Khim., 1958, 29, 1121-1122.

(2-5) Greenhalgh, R.; Blackwell B. A.; Preston C. M.; Murray W. J. J. Agric. Food Chem., 1983, 31, 710-713.

(2-6) Fletcher J. H.; Hamilton J. C.; Hechenbleikner I., Hoegberg E. I.; Sertl B. J.; Cassady J. T. J. Am. Chem. Soc. 1948, 70, 3943-3944.

(2-7) Shaka A. J.; Barker P. B.; Freeman R. J. Magn. Reson. 1985, 64, 547.

(2-8) Gurley T. W.; Ritchey W. M. Anal. Chem. 1976, 48, 1137-1140.
(2-9) Kuivalainen T.; El-Bahraoui J.; Uggla R.; Kostiainen R.; Sundberg M. R. J. Am. Chem. Soc. 2000, 122, 8073-8074.
(2-10) Van Wazer J. R.; Callis C. F.; Shoolery J. N.; Jones R. C. J. Am. Chem. Soc. 1956, 78, 5715-5726.
(2-11) Bielawski, J.; Casida, J. E. J. Agric. Food Chem. 1988, 36, 610.
(2-12) Kabachnik, M. I.; Mastrukova, T. A.; Shipov, A. E.; Melentyeva, T. A. Tetrahedron 1960, 9, 10.
(2-13) Sanchez-Camazano, M.; Sanchez-Martin, M. J. Clay and Clay Miner. 1994, 42, 221.
(2-14) Cotton, F. A.; Wilkinson G. Advanced Inorganic Chemistry, 4th Edition Wiley, New York, 1980, p. 814.
(2-15) Sanchez-Camazano, M.; Sanchez-Martin, M. J. Soil Sci. 1983, 136, 89.
(2-16) Soma, Y.; Soma, M. Environ. Health Perspectives 1989, 83, 205.
(2-17) Yaron, B. Soil Sci. 1978, 125, 210.
(2-18) Saltzman, S.; Mingelgrin, U.; Yaron, B. J. Agric. Food Chem. 1976, 24, 739.
(2-19) Klinowski, J. Encyclopedia of Nuclear Magnetic Resonance Grant, D. M.; Harris, R. K. Eds., Wiley and Sons, Chichester, U. K., 1996, Vol. 5, p. 3098.
(2-20) Steinfeld, J. I.; Francisco, J. S.; Hase, W. L. Chemical Kinetics and Dynamics Prentice-Hall, Engelwood Cliffs, New Jersey, 1989.

Table 2-1. Some possible pesticide decomposition products and relevant ^{13}P chemical shifts from the literature (*2-5, 2-8 through 2-11*).

	structure	**^{13}P chemical shifts (Methyl Parathion: R = Me, Ar = 4-nitrophenyl)**
I methyl parathion	$S=P(OR)_2(OAr)$	66.3 ppm
II	$S=P(OR)_2(OH) \leftrightarrows O=P(OR)_2(SH)$	57.7 ppm
III	$S=P(OR)(OAr)(OH) \leftrightarrows O=P(OR)(OAr)(SH)$	50 ppm ? est.
IV	$O=P(OR)_2(SAr)$	31 ppm (if SC_3H_7 vs. SAr)
V	$O=P(OR)(SR)(OAr)$	27.5 ppm 25.2 ppm
VI oxon	$O=P(OR)_2(OAr)$	- 4.8 ppm
VII	$S=P(OR)(OH)_2 \leftrightarrows O=P(OR)(OH)(SH)$	
VIII	$S=P(OH)_3 \leftrightarrows O=P(OH)_2(SH)$	32 to 34 ppm
IX	$O=P(OR)_2(OH)$	-1.3 ppm (+3.8 ppm as Na^+ salt)
X	$O=P(OR)(OH)_2$	
XI	$O=P(OH)_3$	0 ppm
XII	$O=P(OR)(SAr)(OH)$	
XIII	$O=P(SAr)(OH)_2$	
XIV	$O=P(OR)(OAr)(OH)$	
XV	$O=P(OAr)(OH)_2$	-5 ppm (if Ar = phenyl, R = Et) 0 ppm (if Na^+ salt and Ar = phenyl, R = Et)
XVI	$O=P(SR)(OAr)(OH)$	
XVII	$O=P(SR)(OH)_2$	
XVIII	$S=P(OAr)(OH)_2 \leftrightarrows O=P(OAr)(OH)(SH)$	
XIX bis	$S=P(OR)(OAr)_2$	58.3 ppm
XX	$S=P(OR)_3$	74.0 ppm
XXI	$(ArS)(MeO)_2P=S$	91 ppm (this study)

Table 2-2. ^{31}P chemical shift ranges in organothiophosphate pesticide residues and contaminants. [a]

67 – 60 ppm	unreacted pesticides
58 – 48 ppm	initial hydrolysis products containing P=S
31 – 23 ppm	S,O-isomerized residues
3 – -5 ppm	phosphate and alkyl phosphates
-4 – -10 ppm	oxidized pesticides (oxon)
56 – 59 ppm	bis aryl alkyl thiophosphates (common pesticide synthesis contaminant)
68 – 74 ppm	trialkyl thiophosphates (common pesticide synthesis contaminant)

[a] ^{31}P peaks are assigned based on literature-derived chemical shift ranges. (*2-5, 2-8 through 2-11)*

Table 2-3 . ^{31}P chemical shifts [a] of DMSO-d_6 extracts of methyl parathion (MeP) and its decomposition products sorbed on partially-hydrated clays.

				peaks observed (ppm) with qualitative peak intensities and tentative assignments [b]											
sample	**age**	**MeP content**	**H_2O content % by wt.**	**?**	**XXI**	**XX**	**I**	**II or XIX**	**III**	**IV or VIII**	**V or XVI**	**?**	**?**	**various phosphates ?**	**VI or XV**
impure MeP	NA	*ca.* 75 mol% P	0	115.7 s	91.4 vs	74.0 vs	66.8 vl		53.5 s		27.5 m	12.2 vs		2.4 vs 1.4 vs	-4.4 m -5.3 s
purified MeP	NA	99 mol% P	0	115.4 vs	91.1 vs		66.8 vl	57.2 vs	52.6 vs						
MeP aged in DMSO	6 mos.	initially 99 mol% P	0				66.8 s				28.3 vs				-4.5 m -5.3 m
MeP on kaolin	11 days	1.4 wt%	1.1 %		91.4 s		66.8 l			32.5 s	28.2 l		10.6 vs		
MeP on Ca-mont.	> 3 yr.	9.2 wt%	1.9 %							31.3 s					
MeP on Zn-mont.	1 day	8.5 wt%	4.5 %		91.5 s		66.8 l		52.3 s	32.6 s	28.3 m				
MeP on Zn-mont	> 3 yr.	8.5 wt%	4.5 %				66.8 s								
MeP on Al-mont.	10 days	9.1 wt%	4.5 %			71 vs	66.8 m			32.7 s	28.4 l	12.8 vs			
MeP on Cu-mont.	> 3 yr	8.5 wt%	4.8 %												-3.6 s

[a] relative to 85 % H_3PO_4

[b] Qualitative peak intensities: vl = very large, l = large, m = medium, s = small, vs = very small.

Table 2-4 . ^{31}P NMR relaxation times of methyl parathion and its decomposition products adsorbed on partially-hydrated clays.

clay	methyl parathion content % by wt.	H_2O content % by wt.	peak (ppm)[a]	^{31}P T_1 (s)	^{1}H T_1 (s)	T_{HP} (ms) [b]	^{1}H $T_{1\rho}$ (ms) [b]
kaolin	1.4 %	1.1 %	64	< 2	< 1	0.75	10.5
			27			0.39	7.7
			17			0.32	5.0
			-11			0.25	5.5
Ca-mont.				< 2	< 1		
Zn-mont.	8.5 %	4.5 %		< 2	< 1		
Al-mont.	8.8 %	0.2 % (est.)		< 2	< 1		
			29			0.37 (+.08/-.07)	5.6 (+.7/-.5)
Al-mont.	9.1 %	4.5 %	65	< 2	< 1	0.52	6.3
			30			0.71	6.8
Cu-mont.	8.5 %	4.8 %	61	< 2	< 1	0.34	1.8
			30			0.42	1.8
			-13			0.23	3.6

[a] ^{31}P chemical shift relative to 85 % H_3PO_4.

[b] 95 % confidence limits are shown in parentheses.

Table 2-5. Pseudo-first order rate constants observed for the disappearance of chlorpyrifos and methyl parathion when loaded on various homoionic montmorillonites.

pesticide (% by wt.)	**clay**	**H_2O content (% by wt.)**	**initial k_1 ($min.^{-1}$) r^2**	**half-life (hrs.)**	**period fit (hrs.)**
aqueous chlorpyrifos	*none*	*acidic aqueous solution*	*$6.2 \pm 0.9 \times 10^{-6}$*	*1860 (78 days)*	
chlorpyrifos (10.8 %)	Zn-mont.	7.4 %	$1.32 \pm 0.05 \times 10^{-4}$ ($r^2 = 0.9975$)	87	13
chlorpyrifos (10.2 %)	Zn-mont.	4.2 %	$2.52 \pm 0.09 \times 10^{-4}$ ($r^2 = 0.9908$)	46	127
			$1.57 \pm 0.02 \times 10^{-4}$ ($r^2 = 0.9994$)	74	31
chlorpyrifos (9.3 %)	Al-mont.	3.6 %	$9.16 \pm 5.06 \times 10^{-5}$	126	296
chlorpyrifos (9.8 %)	Cu-mont.	5.1 %	$4.47 \pm 0.42 \times 10^{-4}$ ($r^2 = 0.9652$)	26	43
			$7.21 \pm 0.49 \times 10^{-4}$ ($r^2 = 0.9862$)	16	16
aqueous methyl parathion [a]	*none*	*acidic aqueous solution*	*2.8×10^{-6}*	*4200 (175 days)*	
methyl parathion (8.5 %)	Zn-mont.	4.5 %	$2.50 \pm 0.31 \times 10^{-4}$ ($r^2 = 0.9559$)	46	23
methyl parathion (8.8 %)	Al-mont.	0.2 % (estimated)	$2.41 \pm 0.72 \times 10^{-3}$	5	9
methyl parathion (9.1 %)	Al-mont.	4.5 %	$2.76 \pm 0.19 \times 10^{-4}$	42	72
methyl parathion (8.5 %)	Cu-mont.	4.8%	? (fast?)	< 1	NA

[a] Taken from reference *2-1*.

Figure 2-1

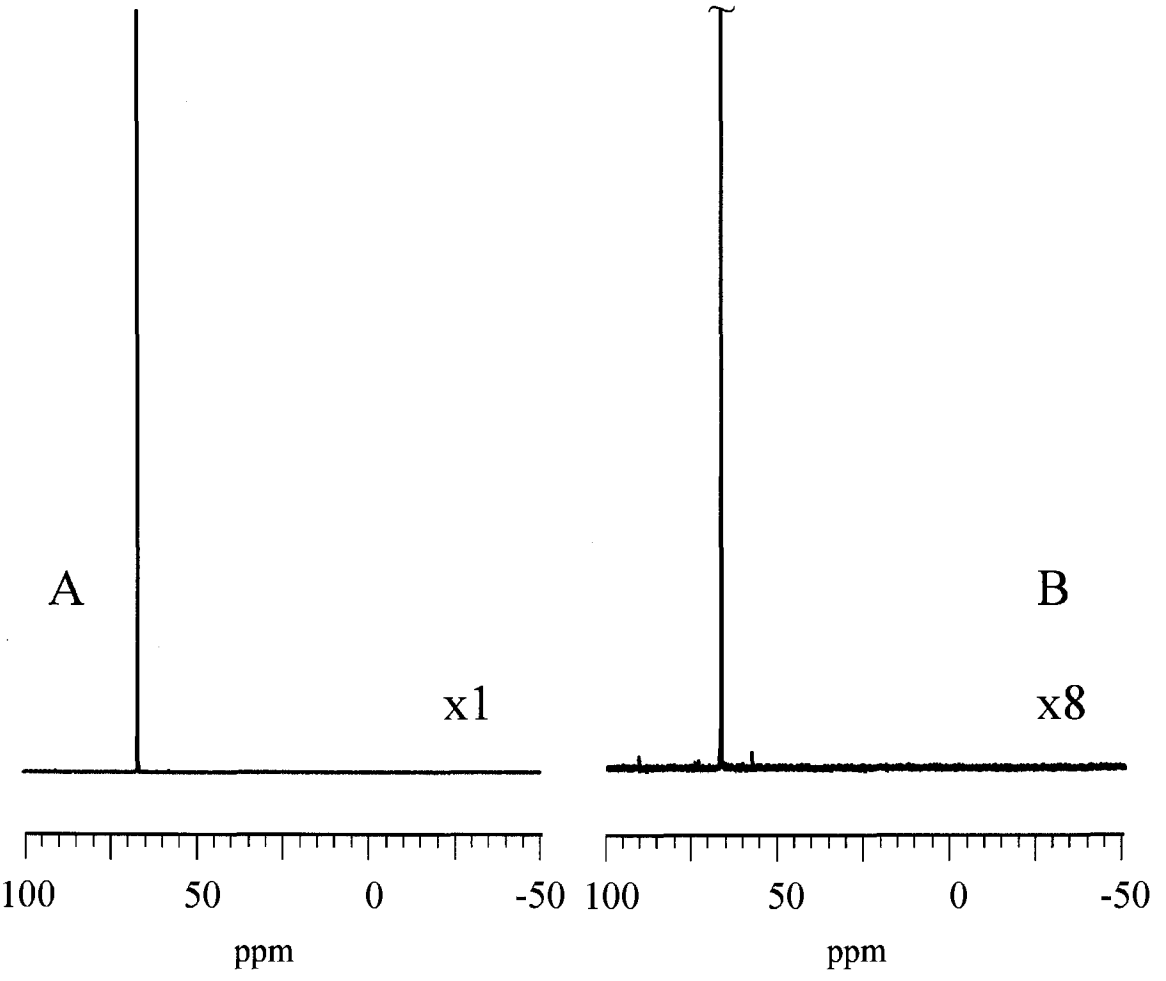

Figure 2-1 A) 242.9 MHz liquid-sample ^{31}P NMR spectrum of 99.1 % methyl parathion in C_6D_6. B) Same as Figure 2-1A, except the spectrum is vertically expanded by a factor of 8.

Figure 2-2

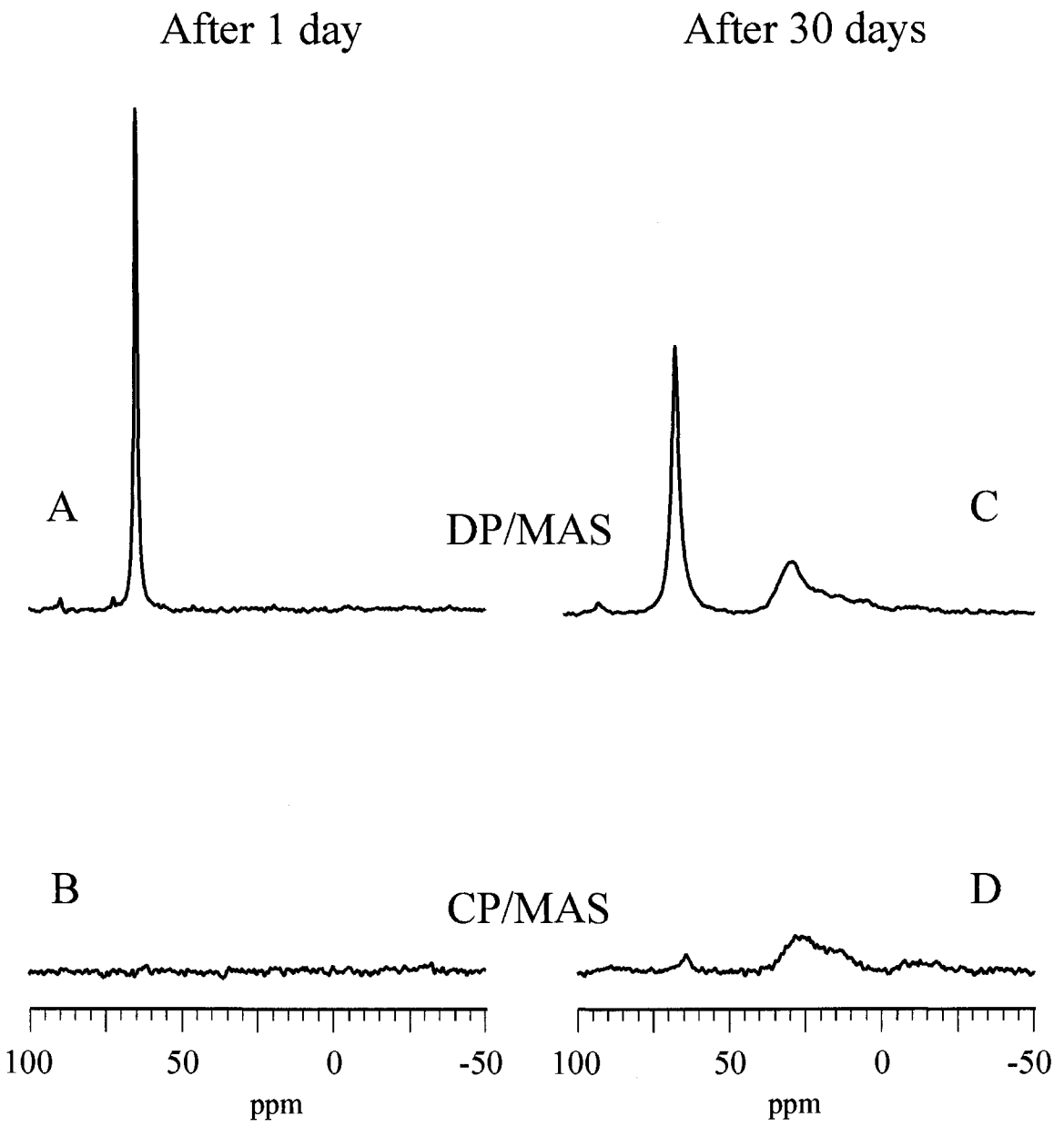

Figure 2-2 60.7 MHz solid-state ^{31}P spectra (each 1000 scans) of methyl parathion (1.4 % by wt.) sorbed on partially-hydrated kaolinite (1.1 % water by wt.): A) DP-MAS after one day. B) CP-MAS after one day. C) DP-MAS after 30 days. D) CP-MAS after 30 days.

Figure 2-3

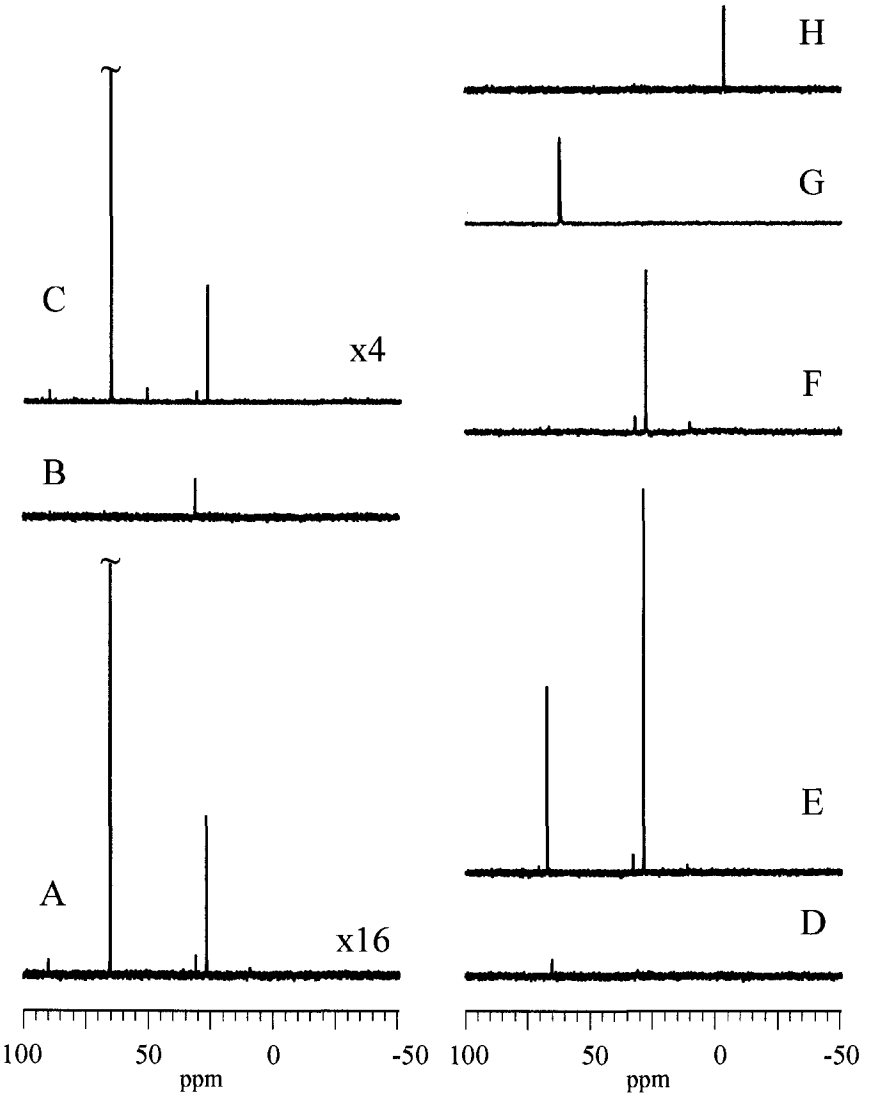

Figure 2-3 242.9 MHz liquid-sample ^{31}P spectra of the DMSO-d_6 extracts of methyl parathion sorbed on various clays: A) methyl parathion (1.4 % by wt.) sorbed on kaolinite (1.1 % water by wt.) after 11 days, 8864 scans; spectrum is vertically expanded such that largest peak is 16 times larger than shown. B) methyl parathion (9.2 % by wt.) sorbed on Ca-montmorillonite (1.9 % water by wt.) after >3 years, 2080 scans. C) methyl parathion (8.5 % by wt.) sorbed on Zn-montmorillonite (4.5 % water by wt.) after 1 day, 7232 scans; spectrum is vertically expanded such that largest peak is 4 times larger than shown. D) methyl parathion (8.6 % by wt.) sorbed on Zn-montmorillonite (5.3 % water by wt.) after >3 years, 2760 scans. E) methyl parathion (9.1% by wt.) sorbed on Al-montmorillonite (4.5 % water by wt.) after 10 days, 6632 scans. F) methyl parathion (9.1% by wt.) sorbed on Al-montmorillonite (4.5 % water by wt.) after 2.0 years, 5930 scans. G) methyl parathion (8.8 % by wt.) sorbed on Al-montmorillonite (<0.2 % water by wt.) after 2.0 years, 19220 scans. H) methyl parathion (8.5 % by wt.) sorbed on Cu-montmorillonite (4.8 % water by wt.) after >3 years, 17988 scans.

Figure 2-4

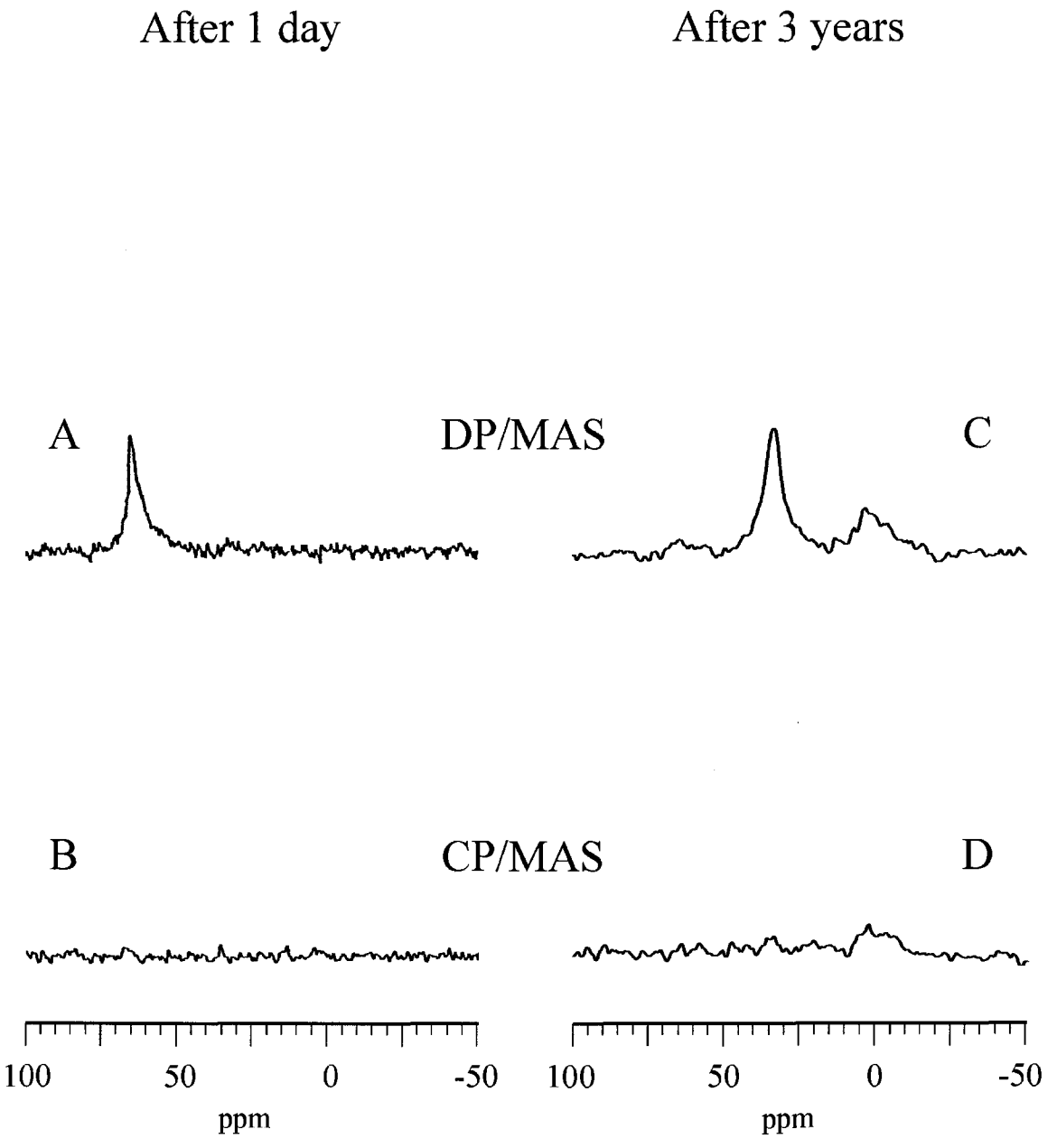

Figure 2-4 60.7 MHz ^{31}P DP-MAS and CP-MAS spectra of methyl parathion (9.2 % by wt.) adsorbed on partially-hydrated calcium montmorillonite (1.9 % water by wt.):. A) DP-MAS after 1 day, 1000 scans. B) CP-MAS after 1 day, 1000 scans. C) DP-MAS after 3 years, 70948 scans. D) CP-MAS after 3 years, 323700 scans.

Figure 2-5

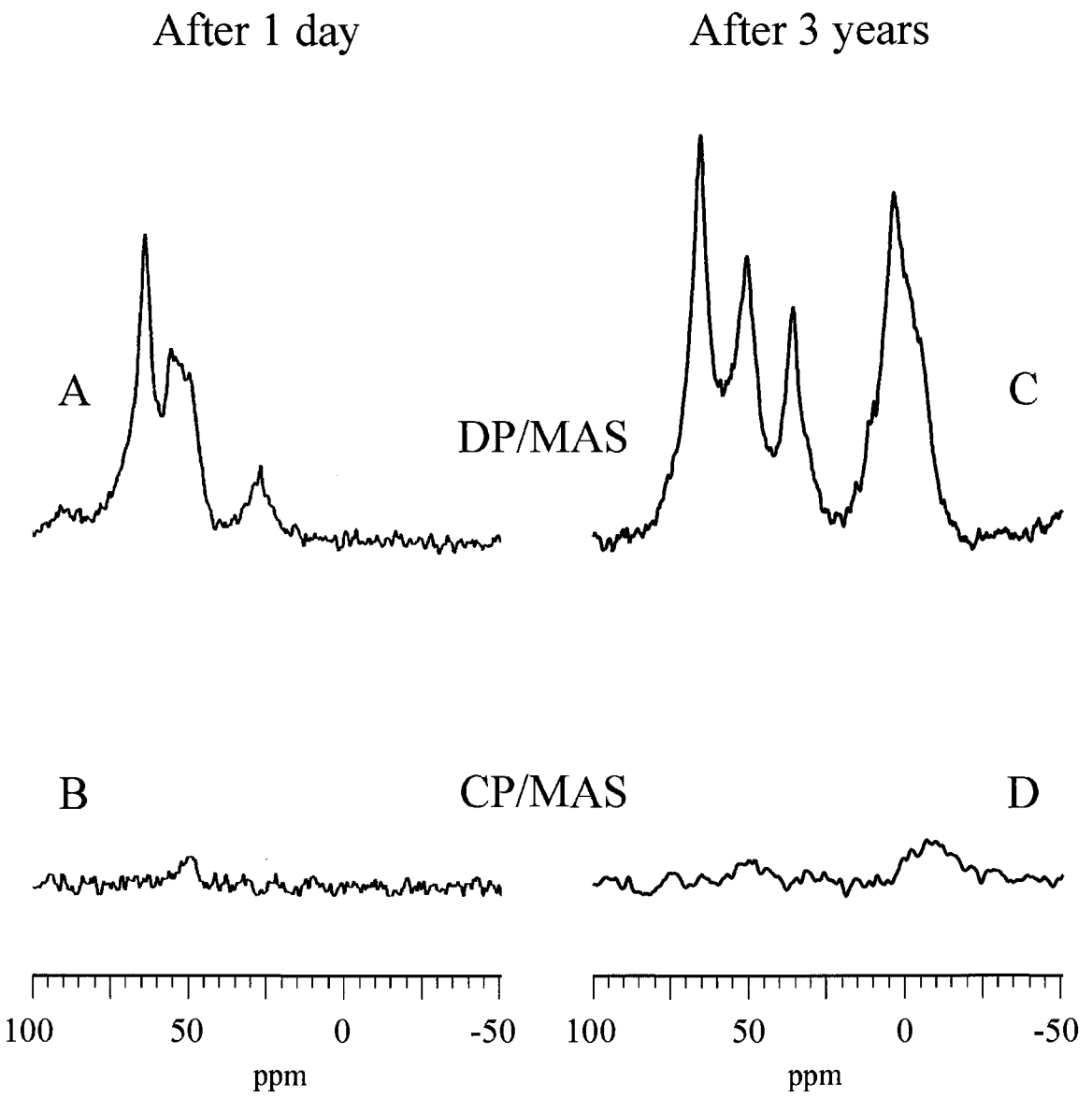

Figure 2-5 60.7 MHz ^{31}P DP-MAS and CP-MAS spectra of methyl parathion sorbed on partially-hydrated Zn-montmorillonite: A) DP-MAS of 8.5 % by wt. methyl parathion sorbed on Zn-montmorillonite containing 4.5 % by wt. water, after 1 day, 1000 scans. B) CP-MAS of sample in Figure 2-5A, after 1 day, 1000 scans. C) DP-MAS of 8.6 % by wt. methyl parathion adsorbed on Zn-montmorillonite containing 5.3 % by wt. water, after 3 years, 70948 scans. D) CP-MAS of sample in Figure 2-5C, after 3 years, 323700 scans.

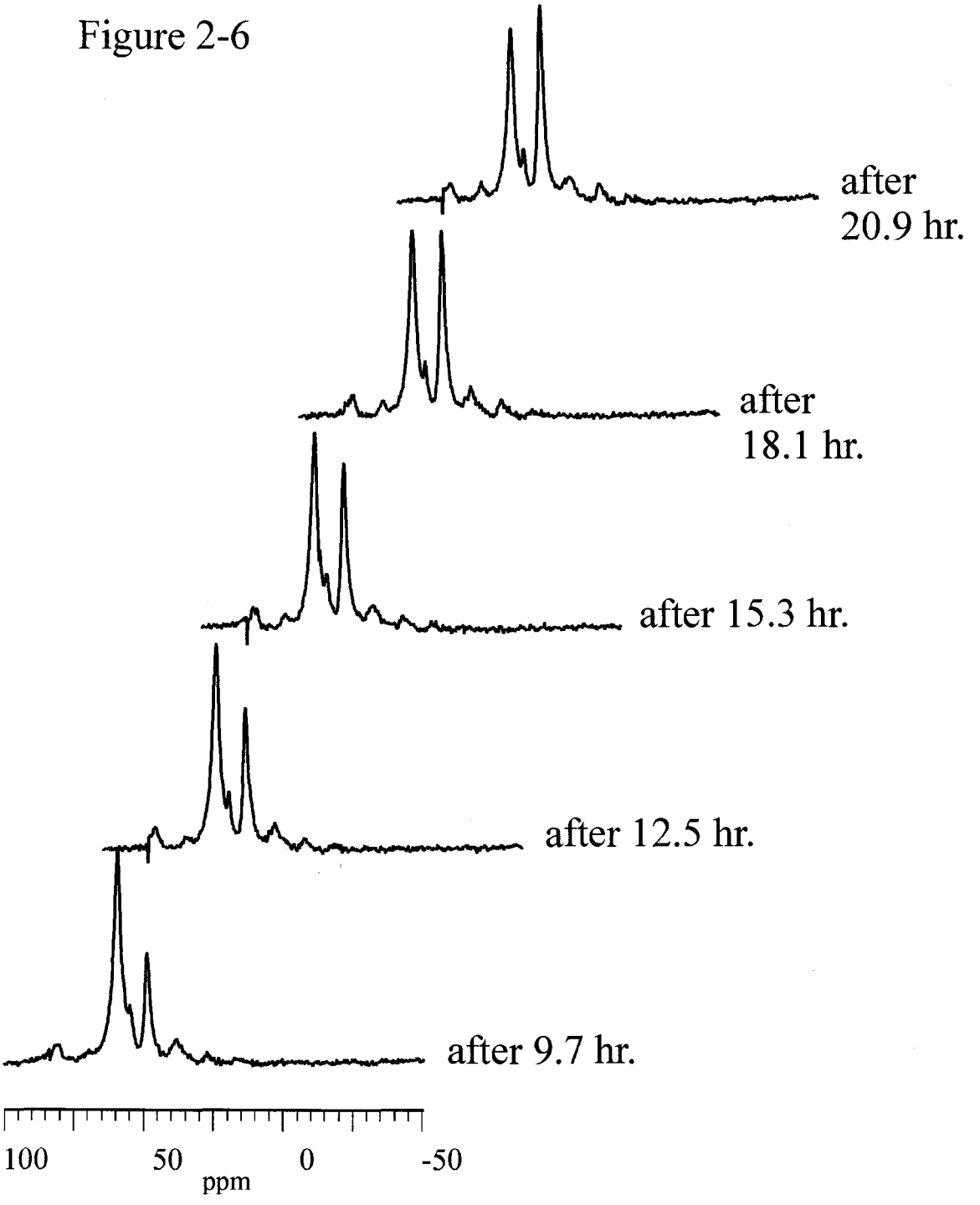

Figure 2-6 60.7 MHz ^{31}P DP-MAS spectra (each 1000 scans) from 9.7 to 20.9 hours after adsorption of methyl parathion (8.5 % by wt.) sorbed on Zn-montmorillonite containing 4.5 % by wt. water.

Figs. 2-7 through 2-9

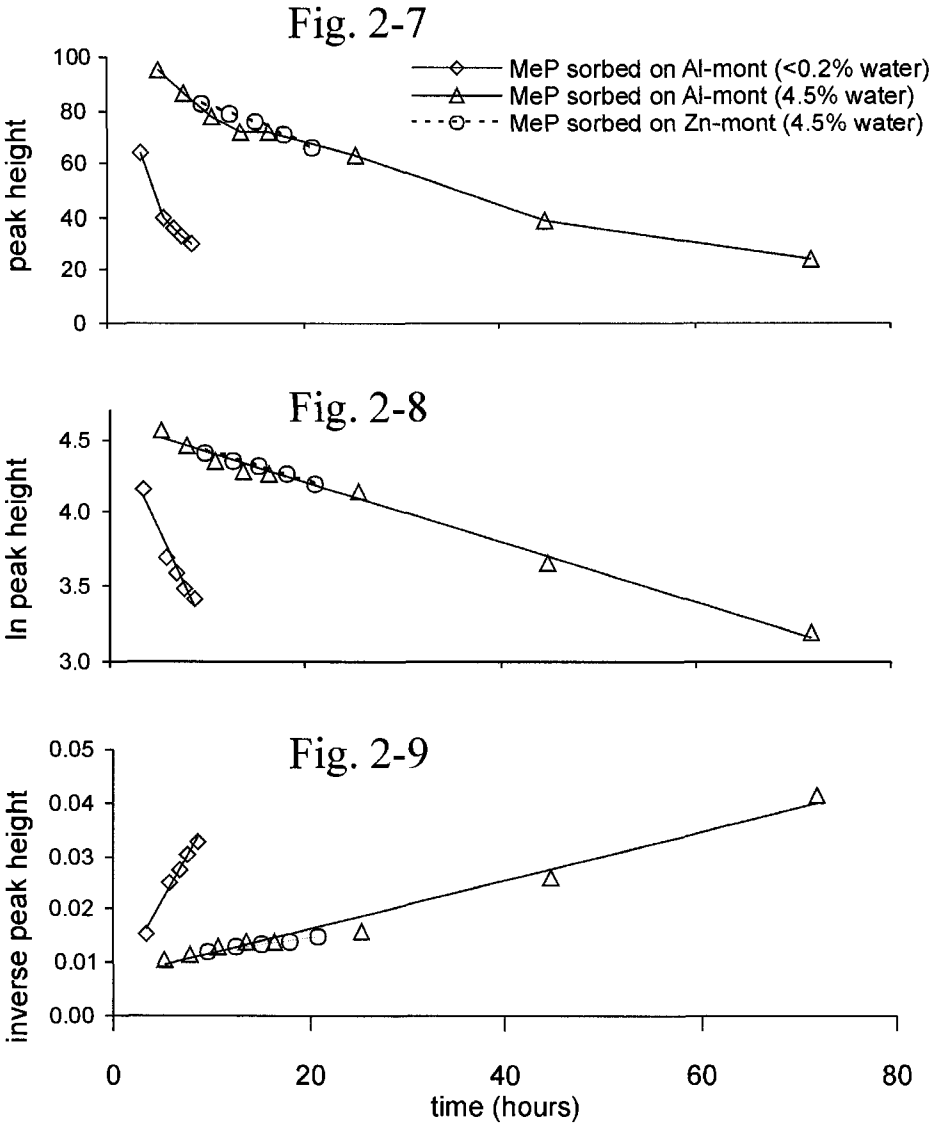

Figure 2-7 Plot of 60.7 MHz ^{31}P DP-MAS peak heights (scaled such that peak height = 100 arbitrary units at time = 0) *vs.* reaction time in hours for the sorbed (but unreacted) methyl parathion peak on three partially-hydrated clays: ◆, methyl parathion (8.5 % by wt.) sorbed on 'almost'-dry Al-montmorillonite (<0.2 % by wt. water); ▲, methyl parathion (9.1 % by wt.) sorbed on partially-hydrated Al-montmorillonite (4.5 % by wt. water); ●, methyl parathion (8.5 % by wt.) sorbed on Zn-montmorillonite (4.5 % by wt. water). Solid lines represent the least-squares fit of the data to a pseudo-first order model for the disappearance of methyl parathion.

Figure 2-8 Same as Figure 2-7, except the natural logarithms of the methyl parathion peak heights (scaled such that peak height = 100 arbitrary units at time = 0) are plotted *vs.*

reaction time in hours, as a test of pseudo-first order kinetics. Solid lines represent the least-squares fit of the data to a pseudo-first order model for the disappearance of methyl parathion.

Figure 2-9 Same as Figure 2-7, except the inverse of the methyl parathion peak heights (scaled such that peak height = 100 arbitrary units at time = 0) are plotted *vs.* reaction time in hours, as a test of pseudo-second order kinetics. Solid lines represent the least-squares fit of the data to a pseudo-second order model for the disappearance of methyl parathion.

Figure 2-10

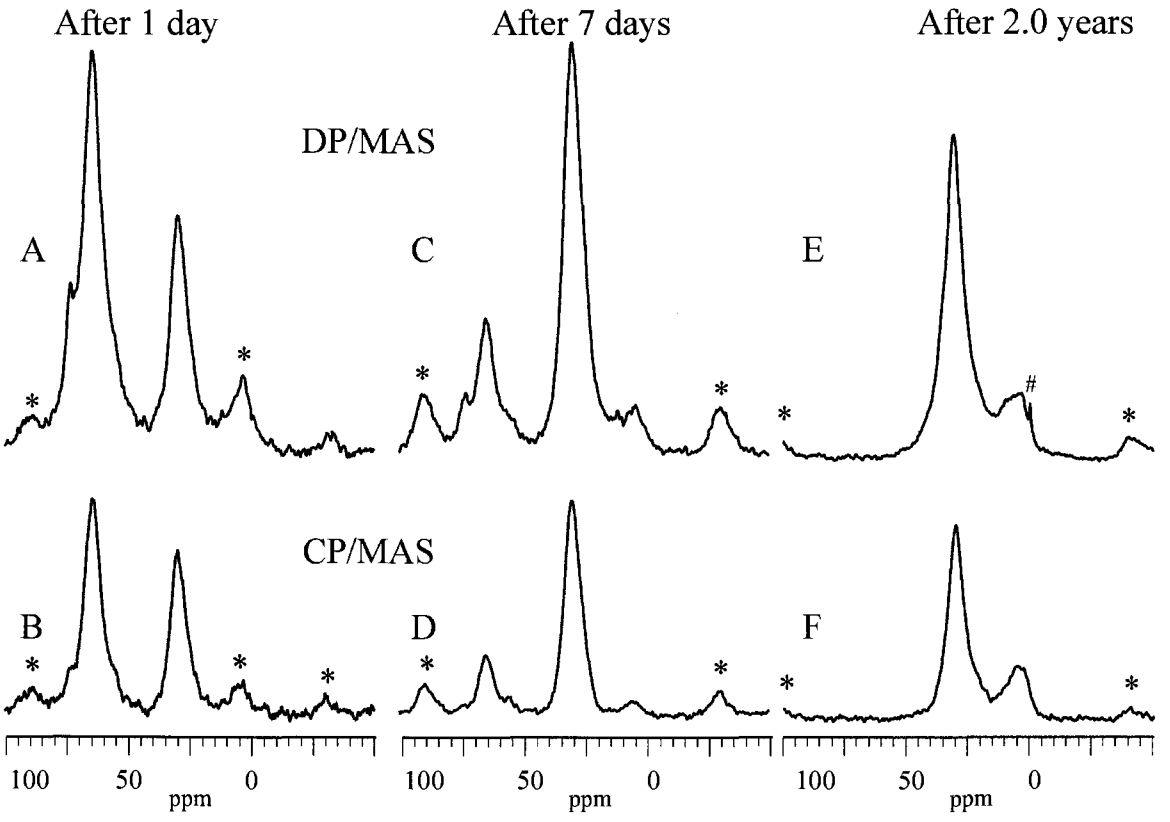

Figure 2-10 60.7 MHz ^{31}P DP-MAS and CP-MAS spectra (each 1000 scans) of a sample containing 9.1 % by wt. methyl parathion sorbed on a partially-hydrated Al-montmorillonite with 4.5 % by wt. water content: A) DP-MAS after 1 day. B) CP-MAS after 1 day. C) DP-MAS after 7 days. D) CP-MAS after 7 days. E) DP-MAS after 2.0 years. F) CP-MAS after 2.0 years. Asterisks indicate spinning sidebands, and # indicates an identified instrumental artifact.

Figure 2-11

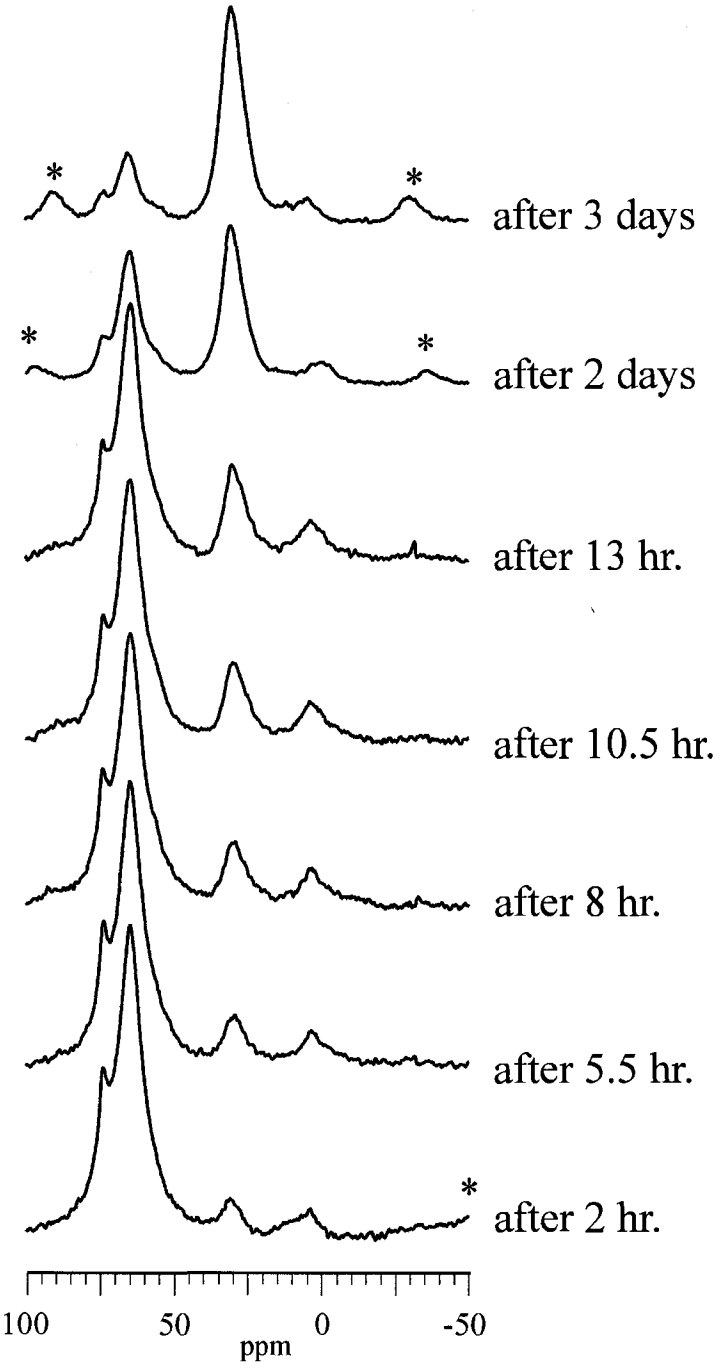

Figure 2-11 60.7 MHz ^{31}P DP-MAS spectra (each 1000 scans) of the same sample of methyl parathion shown in Figure 2-10, sorbed on partially-hydrated Al-montmorillonite, covering the period 2 hours to 3 days after sorption. Asterisks indicate spinning sidebands.

Figure 2-12

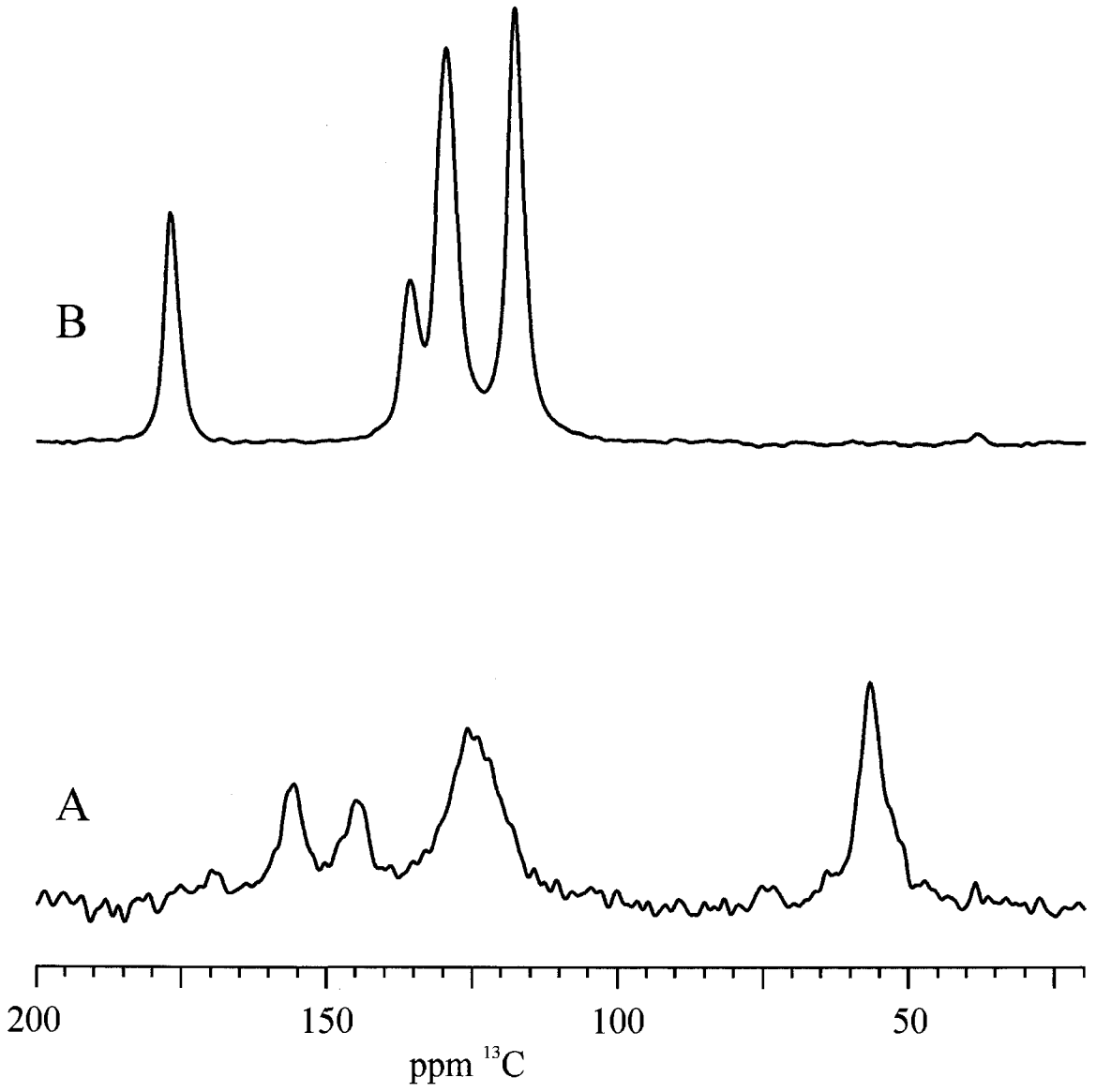

Figure 2-12 50 MHz ^{13}C CP-MAS spectrum of the sample shown in Figure 2-10, containing 9.1 % by wt. methyl parathion sorbed on a partially-hydrated Al-montmorillonite with 4.5 % by wt. water content, after 4 days, 31333 scans.

Figure 2-13

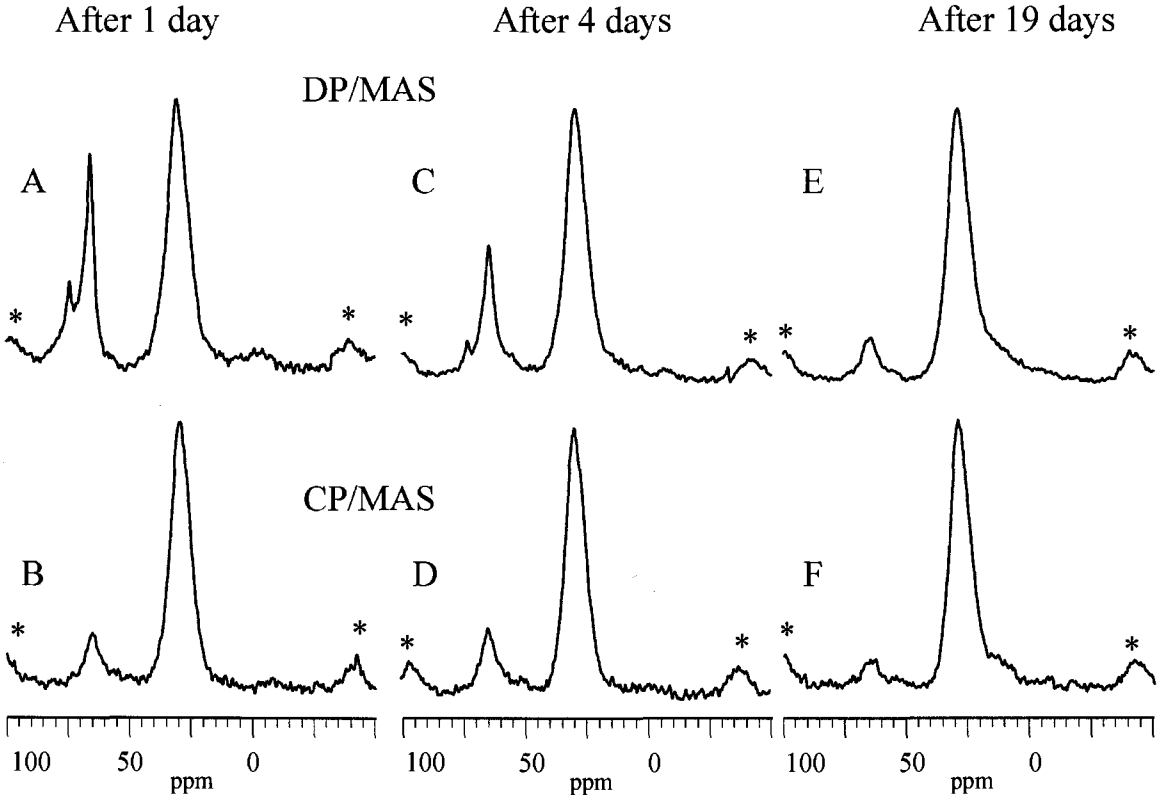

Figure 2-13 60.7 MHz ^{31}P DP-MAS and CP-MAS spectra of a sample containing 8.8 % by wt. methyl parathion sorbed on a Al-montmorillonite with less than 0.2 % by wt. water content: A) DP-MAS after 1 day, 400 scans. B) DP-MAS after 4 days, 1000 scans. C). DP-MAS after 19 days, 1000 scans. D) CP-MAS after 4 days, 1000 scans. E) CP-MAS after 1 day, 1000 scans. F) CP-MAS after 19 days, 1000 scans. Asterisks indicate spinning sidebands.

Figure 2-14

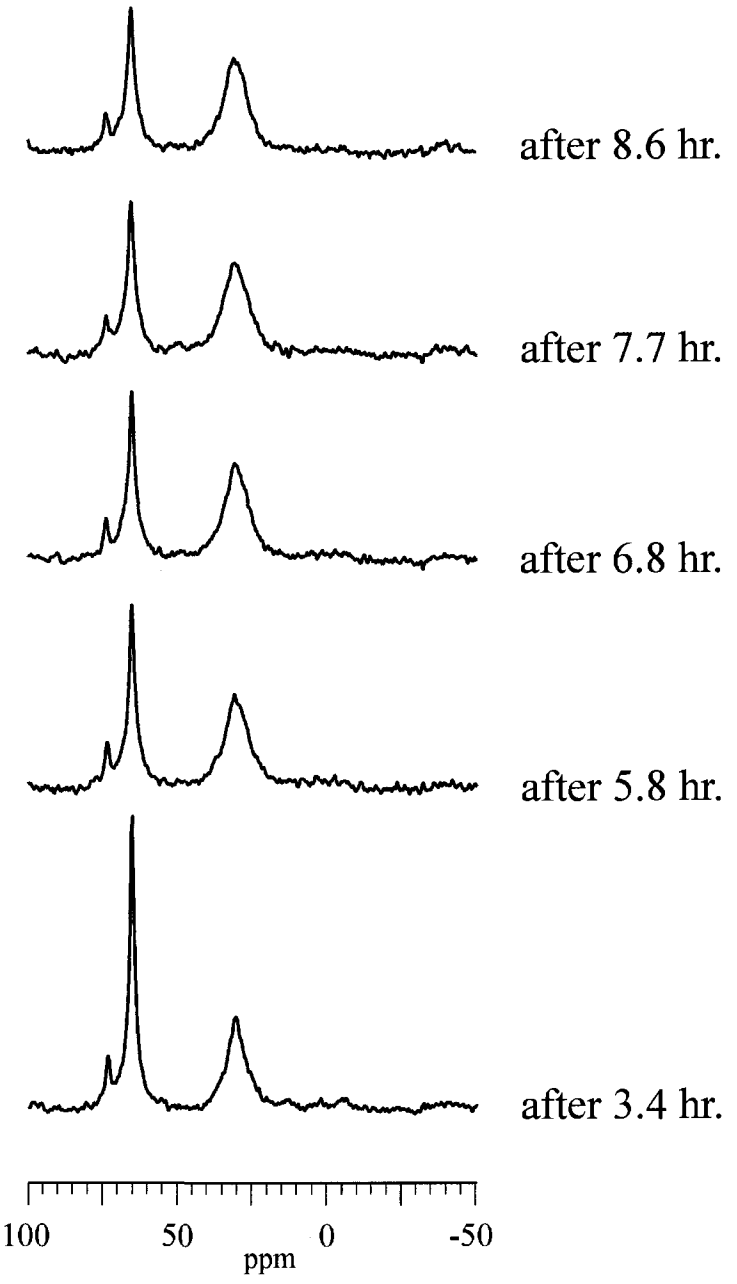

Figure 2-14 60.7 MHz ^{31}P DP-MAS spectra (each 80 scans) during the first 9 hours of decomposition of methyl parathion (8.8 % by wt.) sorbed on a Al-montmorillonite with less than 0.2 % by wt. water content.

Figure 2-15

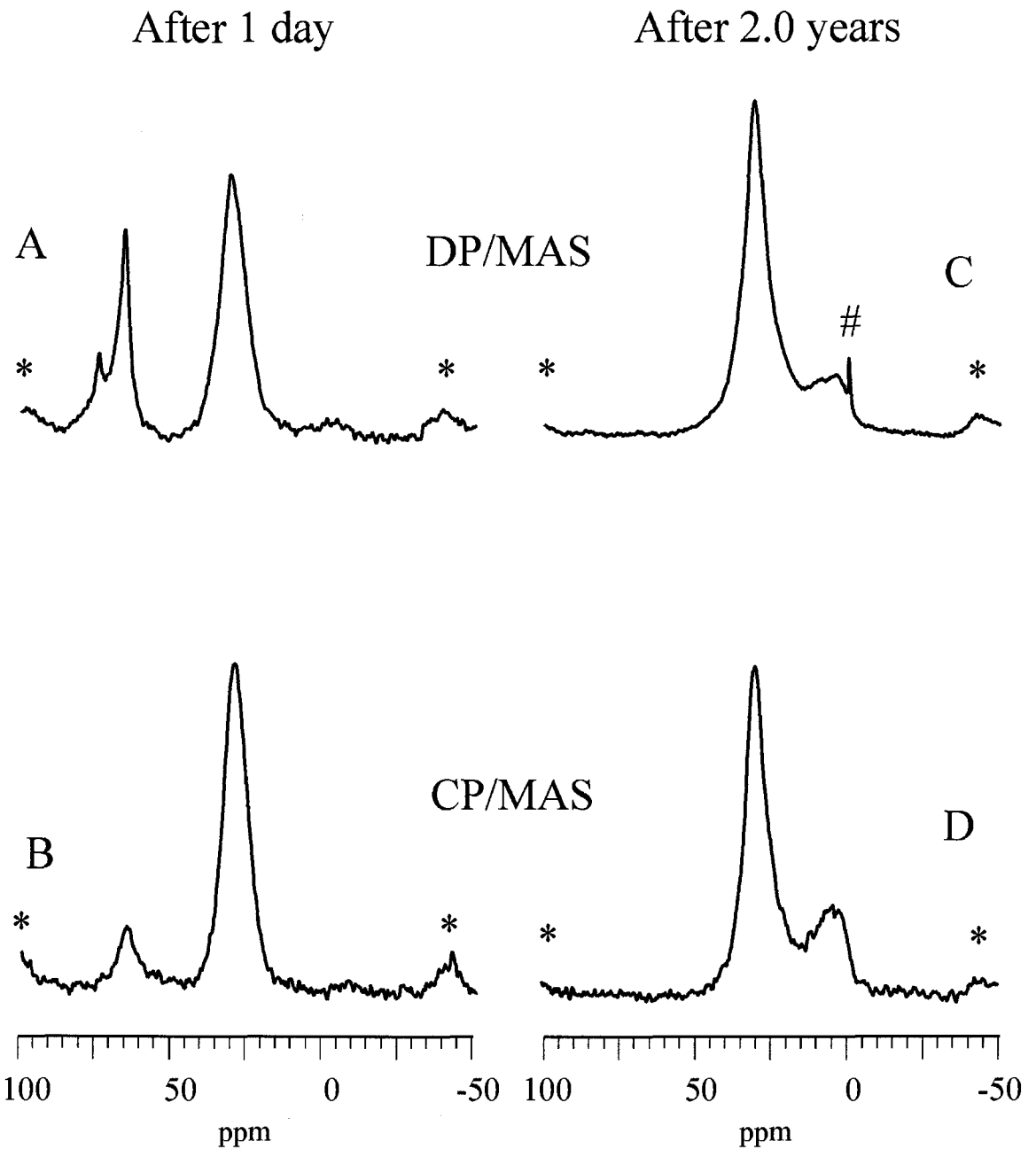

Figure 2-15 60.7 MHz ^{31}P DP-MAS and CP-MAS spectra of a sample containing 8.8 % by wt. methyl parathion sorbed on a Al-montmorillonite with less than 0.2 % by wt. water content: A) DP-MAS after 1 day, 400 scans. B) CP-MAS after 1 day, 1000 scans. C). DP-MAS after 2.0 years, 1000 scans. D) CP-MAS after 2.0 years, 1000 scans.

Figure 2-16

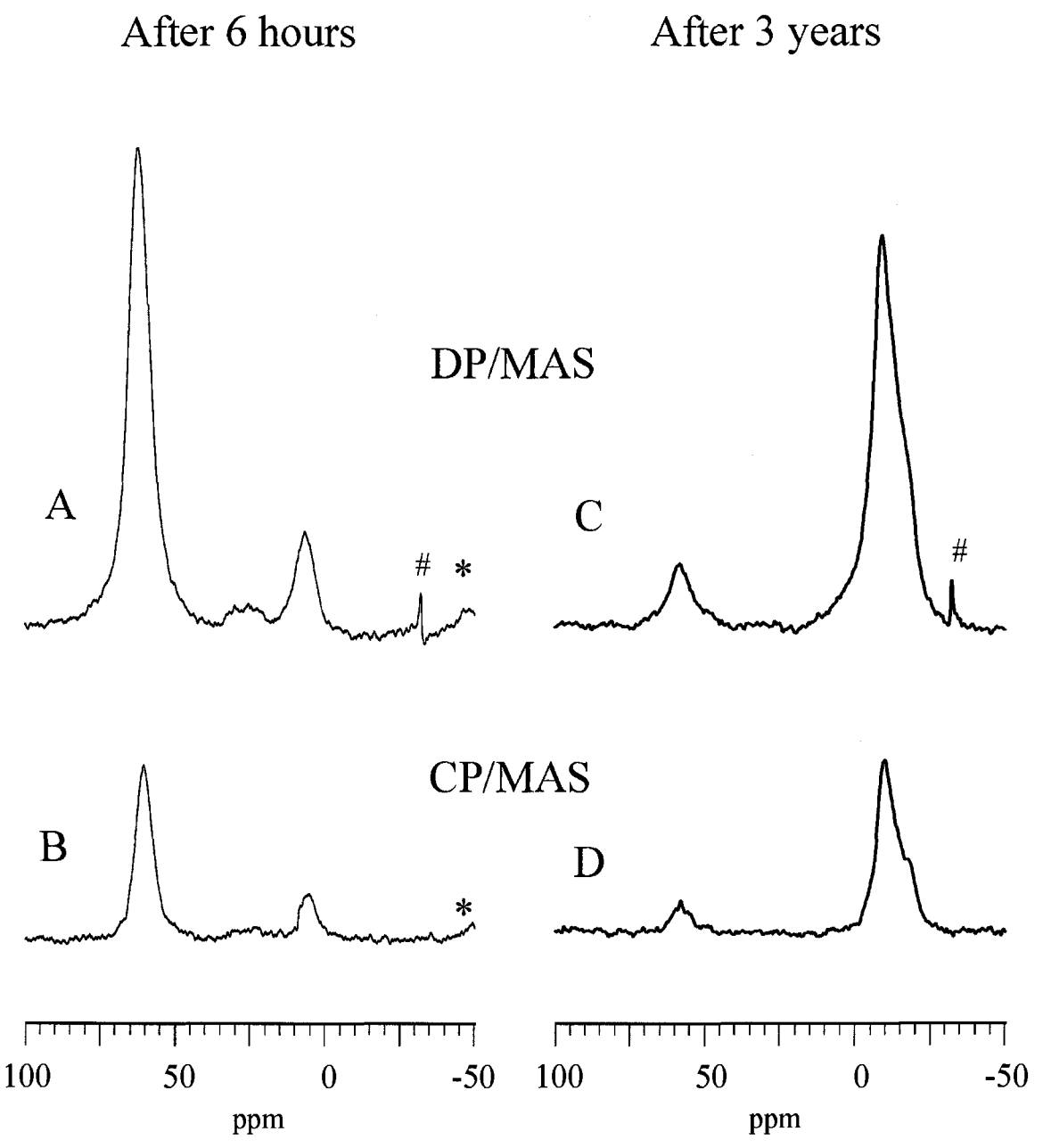

Figure 2-16 60.7 MHz ^{31}P DP-MAS and CP-MAS spectra of methyl parathion (8.5 % by wt.) adsorbed on partially-hydrated Cu(II)-montmorillonite (4.8 % water by wt.): A) DP-MAS after 1 day, 1000 scans. B) CP-MAS after 1 day, 1000 scans. C) DP-MAS after 3 years, 70948 scans. D) CP-MAS after 3 years, 323700 scans.

Figure 2-17

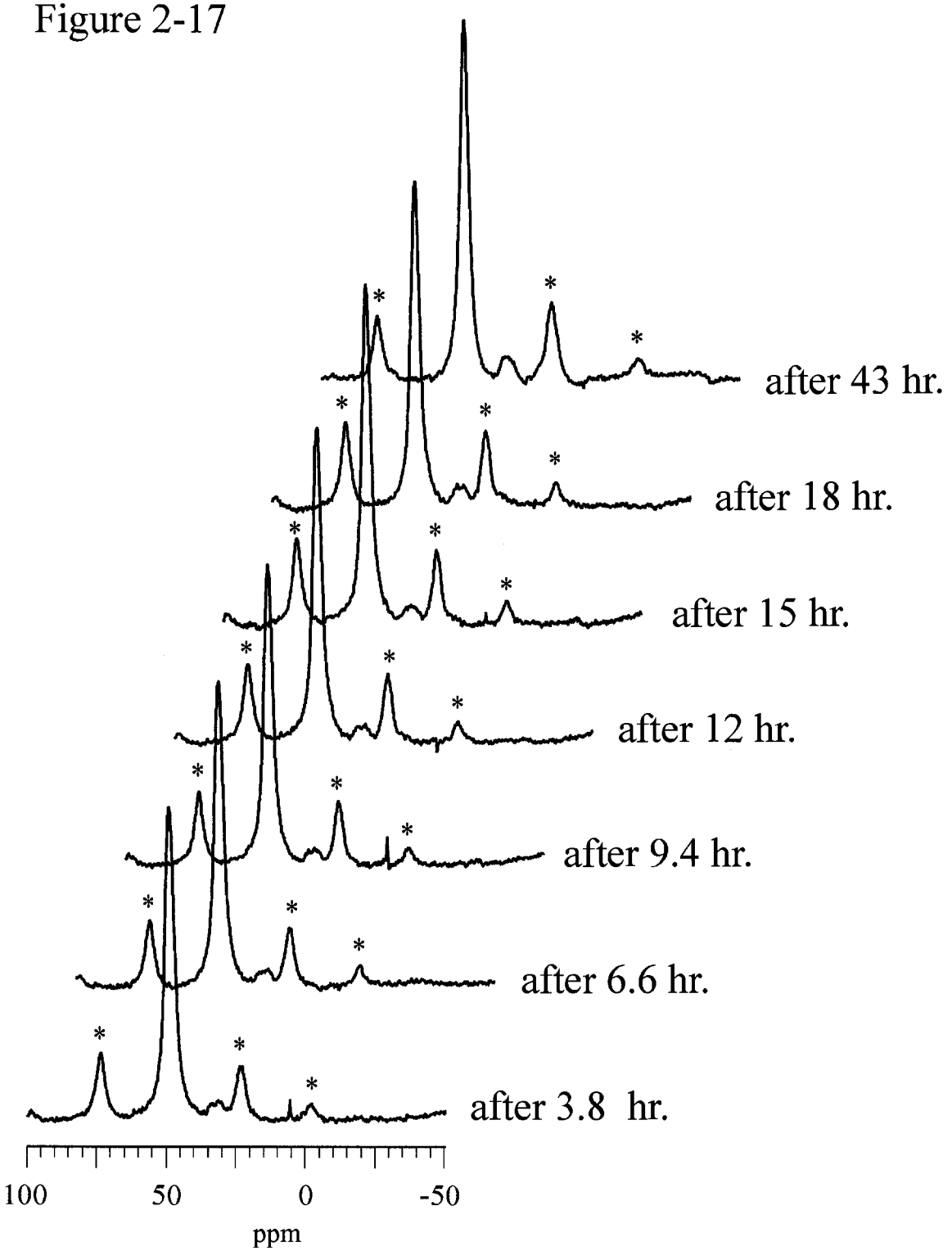

Figure 2-17 60.7 MHz ^{31}P DP-MAS spectra (each 1000 scans) during the first 43 hours of decomposition of the sample shown in Figure 2-16 (8.5 % by wt. methyl parathion sorbed on Cu(II)-montmorillonite containing 4.8 % water by wt.).

Chapter 3: Quantitative ^{13}C NMR Analysis of Sequence Distributions in Poly(ethylene-co-1-hexene).

INTRODUCTION

Recent advances in low-pressure transition-metal catalysis of ethylene polymerization can provide a high degree of control of branching and narrow molecular weight ranges. (*3-1*) Polyethylene polymers with controlled branching can be prepared by 1) ethylene homopolymerization using group-10 diazadiene complexes as catalysts, or 2) copolymerization of ethylene and a 1-alkene using group-4 metallocenes. These catalyst systems are examples of single-site catalysts (*i.e.*, only one type of catalytic site), and produce very uniform polymers with narrow molar mass distributions ($M_w / M_n \approx 2$). Conventional multisite catalysts give complex mixtures of branched polyethylenes with varying amounts of branching, related to the molar mass of the polymer.

The ethylene-only homopolymerization mechanism (the first mechanism mentioned in the preceding paragraph) can produce alkyl side chains via what is alternatively known as "2,ω-polymerization" (*3-2*) or "chain-walking". (*3-3*) Group-10 metal alkyls can migrate along a growing polyethylene polymer chain by repeated β-eliminations followed by reinsertions. When chain growth occurs exclusively at the chain end, this mechanism produces methyl branched polyethylene polymers.

Group-4 metallocene catalysts produce branched polyethylenes by copolymerizing ethylene with 1-alkenes; 1-butene produces ethyl side chains, 1-hexene produces n-butyl side chains, etc. Examples of 1-olefins used to produce controlled branching in polyethylene include propylene, 1-butene, 1-hexene, 1-octene, and 1-decene. Control of branching is provided by properly choosing the molecular architecture of the metallocene catalysts. A variety of important commercial products are made by this means, including linear low density polyethylene (LLDPE), very low density polyethylene (VLDPE), and very flexible thermoplastic elastomers (known as plastomers and rubbers). The LLDPE family of polyethylene products alone is a multibillion dollar per year worldwide market. Of particular importance is the improved processing characteristics of LLDPE, as compared to high density polyethylenes (HDPE, mostly unbranched) and low density polyethylene (LDPE, a high degree of uncontrolled branching, including long branches). The physical characteristics of LLDPE, such as melting temperature and crystallization behavior, can be easily "fine-tuned" by changing the 1-olefin monomer identity or concentration, or by altering the metallocene catalyst.

In this study the branching of poly(ethylene-co-1-hexene) copolymers containing 2 - 6 mol % 1-hexene was investigated by liquid-state ^{13}C Nuclear Magnetic Resonance (NMR). These copolymers are commercially important LLDPE products with a wide range of applications from plastic grocery bags to agricultural weed control.

Isomers of poly(ethylene-co-1-hexene). Several types of poly(ethylene-co-1-hexene) isomers are possible, but not all are distinguishable by liquid-state NMR. For a given incorporation level of 1-hexene, possible types of isomer variations include 1) conformational, 2) configurational and 3) substitutional. (*3-4*)

Conformational isomers result from bond rotations along the polymer backbone, *e.g.*, trans versus gauche chain configurations. As interconversion between conformational isomers is usually rapid on the NMR timescale, when these polymers are dissolved at 125 °C, conformational effects are averaged.

Configurational isomers arise because of the potentially asymmetric branch (methine) carbon formed when 1-hexene is incorporated into the polymer backbone. A single n-butyl branch on a polyethylene backbone, far removed from any other potentially asymmetric branch, may be referred to as 'pseudoasymmetric', as two of the methine carbon's substituents are essentially identical, the polymer backbone stretching away in two directions. Likewise, in a sufficiently long polymer chain, chain-end effects can be neglected when considering configurational isomers. It is only when two branch points are 'close' together that the relative configurations of these potentially asymmetric centers matter. In a poly(ethylene-co-1-hexene) copolymer, this will occur only when two 1-hexene monomers are incorporated 'close' together, such as two consecutive 1-hexene monomer units, or two 1-hexene units separated by an ethylene monomer. How 'close' together must the 1-hexenes be? As a rule of thumb, an alkane carbon atom's chemical shift is usually undetectably insensitive to structural differences more than about four bonds away. (*3-5*) This limits the detection of relative configuration to 1-hexenes separated by no more than a single ethylene monomer unit.

If two 'close' branching methines have opposite absolute configurations, the resulting relative stereochemical relationship is termed *meso*. Two 'close' asymmetric centers with the same absolute configurations is referred to as a *racemic* relationship.

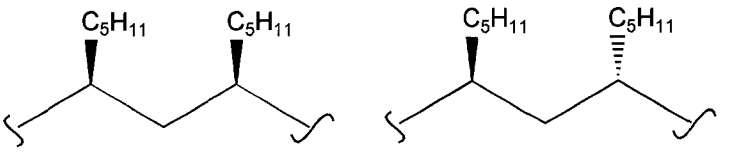

meso racemic

Note that either two or three monomer units (two of which must be branched) are required for each meso or racemic relationship. With liquid-sample ^{13}C NMR, configurational isomers in poly(ethylene-co-1-hexene) copolymer are usually not resolvable, though some exceptions will be described below.

Substitutional isomers may be of two varieties. *Sequence* isomers result from the particular order in which ethylene or 1-hexene monomer units are added to a growing polymer chain. *Addition direction* isomers can result when 1-hexene units are added to the growing chain in either a head-to-head, a tail-to-tail or a head-to-tail manner, as shown in Figure 3-1. As an ethylene monomer unit has no 'head' nor 'tail', head-to-tail, etc. additions must refer to 1-hexene additions only. Furthermore, variations in head-to-head, tail-to-tail or head-to-tail additions will not be detectable unless two 1-hexene monomer units are 'close' together, *i.e.*, with no more than a single intervening ethylene monomer unit. Previous NMR analyses of poly(ethylene-co-1-hexene) and similar copolymers summarized in the literature (*3-6*) reported no sign of tail-to-tail additions of 1-alkene. These possible addition variations will be re-examined in the Results section.

The main types of structural isomers detectable by liquid-sample ^{13}C NMR are *sequence* isomers. These are the result of adding either an ethylene or 1-hexene monomer unit to the end of a growing polymer chain, whereas the previous monomer unit added may also be either ethylene or 1-hexene. The best way to describe these sequences is by means of *n*-ads, namely monads, diads, triads, tetrads, etc. There are two possible

monads in the poly(ethylene-co-1-hexene) copolymer system: E and H. Monad concentrations are normalized so that [E] + [H] = 1, where [E] and [H] are the mole fractions of ethylene and 1-hexene monomers incorporated into the polymer.

There are three possible diads possible in poly(ethylene-co-1-hexene) copolymers: EE, EH and HH, such that [EE] + [EH] + [HH] = 1. Note that EH (which represents an ethylene-based monomer unit adjacent to a 1-hexene unit) is equivalent to HE, since one direction on a 'long' poly(ethylene-co-1-hexene) polymer backbone is essentially equivalent to the other direction. Similarly, six triads are possible: EEE, EEH, HEH, EHE, EHH and HHH, such that the sum of their mole fractions is unity. Note again that EEH and HEE are equivalent, as are EHH and HHE. The first three triads listed above, EEE, EEH and HEH, are all E-centered triads; EHE, EHH and HHH are H-centered triads. It is not difficult to demonstrate that

$$[EEE] + [EEH] + [HEH] = [E] \text{ and} \tag{1}$$

$$[EHE] + [EHH] + [HHH] = [H]. \tag{2}$$

The two monads, three diads, six triads, ten tetrads and twenty pentads of the EH copolymer system are listed in Table 3-1. The number of each *n*-ad possible, N(*n*), in a two-monomer copolymer (determined in this study) is given by the expression

$$N(n) = 2^{n-1} + 2^{m-1}, \tag{3}$$

where $m = n/2$ if n is even and $m = (n+1)/2$ if n is odd.

Table 3-2 list a set of equations known as the *necessary relationships* (*3-4*) for the EH copolymer system. Necessary relationships are expressions that algebraically relate various *n*-ad mole fractions (*e.g.*, relate diad to triads), independent of polymerization mechanism or statistics. In addition to stating the normalization condition for each *n*-ad

set (monads, diads, triads, etc. may be referred to generically as *n*-ads, where an *n* of 3 would specify triads), these equations show relationships between *n*-ads of different orders *n*. These necessary relationships fall into three categories: 1) *normalization* (e.g., triad-triad relationships), 2) *centering* (e.g., monad-triad relationships) and 3) *cleaving* (e.g., diad-triad relationships).

Equations (1) and (2) above are *centering* necessary relationships, which relate monad mole fractions to triad mole fractions. These equations exemplify the fact that any *n*-ad mole fraction is the sum of the (*n*+2)-ad mole fractions with that particular *n*-ad at their center. For another example, we can state that the mole fractions of all the tetrads containing EH at their center must sum to the mole fraction EH:

$$[EH] = [E\underline{EH}E] + [E\underline{EH}H] + [H\underline{EH}E] + [H\underline{EH}H]. \quad (4)$$

The center EH diad in each EH-centered tetrad is underlined for clarity in equation (4).

The necessary relationships in Table 3-2 show that monads, triads, pentads, etc. form a set related by centering a lower order ad within all possible higher order ads. Likewise, diads, tetrads, hexads, etc. also form a set related by centering.

Cleaving necessary relationships relate (*n*+1)-ad mole fractions to *n*-ad mole fractions. These may be written by inspection upon the realization that each (*n*+1)-ad contains two *n*-ads. For example, the EHH triad contains one EH diad and one HH diad, the EHE triad contains two EH diads, the HEH triad contains two EH diads and the EEH triad contains one EH and one EE. Since these are the four triads containing EH, it follows that

$$2[EH] = 2[EHE] + [EHH] + 2[HEH] + [EEH], \text{ or} \quad (5)$$

$$[EH] = [EHE] + \tfrac{1}{2}[EHH] + [HEH] + \tfrac{1}{2}[EEH]. \quad (6)$$

One way to express equation (5) in words is that there are two E-to-H progressions (often referred to as "transitions" in the literature) each in EHE and HEH, whereas EHH and EEH each contain a single E-to-H progression. The coefficient 2 preceding [EH] in equation (5) reflects the fact that we have in essence counted each E-to-H progression twice. (*3-4*) This will be confirmed below when considering the normalization requirements.

Note that an E-to-H progression is equivalent to an H-to-E progression, since there is no 'correct' direction on the polymer backbone. Thus [HE] ≡ [EH], and we obtain a triad-triad necessary relationship (*3-4*):

$$2[EHE] + [EHH] = 2[HEH] + [EEH]. \quad (7)$$

Substituting equation (7) into equation (5) gives one of the diad-triad necessary relationships (*3-4*):

$$[EH] = 2[EHE] + [EHH] = 2[HEH] + [EEH]. \quad (8)$$

Similarly, EE is found within only the EEE triad (twice) and the EEH triad (once), so

$$2[EE] = 2[EEE] + [EEH], \text{ or} \quad (9)$$

$$[EE] = [EEE] + \tfrac{1}{2}[EEH]. \quad (10)$$

Likewise, $$[HH] = [HHH] + \tfrac{1}{2}[EHH]. \quad (11)$$

As a check, we can sum equations (6), (10) and (11) and utilize the normalization of diads and triads (i.e., all diad mole fractions must sum to unity, as do all triad mole fractions, etc.):

$$[EH] + [EE] + [HH] = [EHE] + [EHH] + [HEH] + [EEH] + [EEE] + [HHH] = 1. \quad (12)$$

If the values of all six triad mole fractions were known, the necessary relationships could be used to determine the diad and triad mole fractions. In general, if a complete *n*-ad set

of mole fractions is known, all (n-1)-ad mole fractions can be determined. (*3-4*) Knowing a complete n-ad set of mole fractions is not sufficient, however, to determine the (n+1)-ad (or higher) mole fraction values by use of the necessary relationships alone. For example, using the necessary relationships and knowing the mole fractions of all ten possible tetrads allows one to determine the mole fractions of all six triads, three diads and two monads. Determination of pentad and higher mole fractions is not possible in this case.

Nomenclature. The poly(ethylene-co-1-hexene) copolymers examined in this study are members of the class of polymers known as chain-growth polymers, in which individual monomer units are no longer identifiable after polymerization. In other words, the polymer backbone carbons are not necessarily associated with a particular monomer unit, as there are usually two ways that a particular backbone and side chain sequence may have arisen. For example, Figure 3-2 shows two views of a portion of the same poly(ethylene-co-1-hexene) polymer chain, showing how this structure may have arisen in two ways by the co-polymerization of ethylene and 1-hexene. (By contrast, a step-growth polymer, such as a protein, retains identifiable monomer units after polymerization, and a particular protein sequence can arise from only one combination of monomer units.)

Since poly(ethylene-co-1-hexene) is a chain-growth polymer, the backbone carbons must be designated by the resultant polymer structure, not in terms of the contributing monomer unit. In this study, the carbon nomenclature first developed by Randall (*3-7*) and Carmen (*3-8*) (and later extended by others) will be used.

Backbone methylene carbons are identified by a pair of Greek letters indicating the distance to the nearest branch along both directions of the backbone. For example, an $\alpha\gamma$ carbon is a backbone carbon next to a branching methine (in one direction), but the

third carbon away from the nearest branch in the other direction. Figure 3-3 shows various poly(ethylene-co-1-hexene) substructures with the appropriate labels. If the nearest branch point is four or more carbons away, the label δ+ is used, as ^{13}C chemical shifts in alkanes are seldom affected by carbon atoms more than four atoms away. Hence, by this nomenclature system, a completely unbranched polyethylene chain would consist of only δ+δ+ methylenes; for this reason the usually very large δ+δ+ methylene peak in the ^{13}C NMR spectrum is sometimes also referred to as the "PE" peak.

This nomenclature system does not always distinguish between two methylenes with potentially different chemical shifts. As seen in Figure 3-3, the two nearest branch points for an αα methylene are only one carbon away in both directions along the polymer backbone. This nomenclature system neglects to specify whether there are any other branch points within four carbons along the chain, which may be expected to affect the αα methylene ^{13}C chemical shift. As such, the notations in Figure 3-3 follow the usage of Hsieh and Randall (*3-9*), in which the *n*-ad type is parenthetically appended to the Greek letters: αα(EHHE) or αα(EHHH) or αα(HHHH) distinguishes three different αα methylenes with potentially different carbon chemical shifts.

Methine carbons represent the branch points of the polymer, the site of attachment of the n-butyl side chains arising from 1-hexene incorporation. They are labeled CH(EHE), CH(EHH) or CH(HHH), depending on which particular H-centered triad for which they are the center carbon. For example, CH(EHH) represents the branch methine (indicated by the CH) of a 1-hexene monomer unit (the center H in the parenthesis), with an ethylene monomer unit (E) on one side and another 1-hexene unit (H) on the other side. Alternatively, they might be labeled as the center carbon of an H-centered pentad,

CH(EEHEE), CH(EEHEH), CH(EEHHE), CH(EEHHH), CH(EHHHE), CH(EHHEH), CH(HEHEH), CH(EHHHH) or CH(HHHHH), but the lack of sensitivity of the methine carbon chemical shift to structural differences more than four carbons away means that not all of these H-centered pentads may be distinguishable in the ^{13}C spectrum.

Side chain carbons are labeled using the format nB_m, where n and m are integers (B refers to "branch", identifying the carbon as belonging to a side chain). (*3-4*) The value m represents the length of the side chain, while n refers to the position of the carbon in question, as counted from the *end* of the chain. Thus $1B_4$ is the methyl carbon of an n-butyl side chain, the methylene adjacent to it would be labeled $2B_4$, etc.

Chemical Shift Assignments. The chemical shift assignments of the ^{13}C spectrum of poly(ethylene-co-1-hexene) dissolved in dichloro- or trichlorobenzenes are well reported in the literature (*3-9*), with essentially full agreement between independent reports, except for very small differences in reported chemical shifts (for example, the very large δ+δ+ methylene peak is reported to occur at either 29.98 ppm or 30.00 ppm). One set of chemical shifts and their assignment is shown in Table 3-3. These assignments were made by a variety of techniques, especially the use of both low and high molecular weight model compounds. NMR methods utilized included off-resonance decoupling, spectral editing techniques such as DEPT (*3-3*) and APT (*3-10*), and two-dimensional methods, such as J-resolved spectroscopy (*11*) and heteronuclear shift correlation spectroscopy (HETCOR) in conjunction with proton COSY results. (*3-11*) It should be noted that the necessary relationships mentioned above have also been used as an assignment aid, assuming quantitative results are obtained, as the necessary relationships must always be true for sufficiently long polymer chains, no matter the

sequence distribution of monomer incorporation in the polymer chain. The necessary relationships can be often be used to select between alternative assignments, or confirm tentative assignments.

Empirical chemical shift predictions were also used in the initial assignment of the ^{13}C spectrum of poly(ethylene-co-1-hexene). The predictions were not quantum mechanical in nature; rather, empirical calculations using structural parameters were utilized. One of the most widely used (and earliest) empirical ^{13}C chemical shift prediction methods uses the alkane parameters of Grant and Paul. (*3-12*)

In the Grant and Paul method, ^{13}C chemical shifts are calculated on the basis of the number and bonding connectivity of nearby carbon atoms. Starting with the chemical shift of methane (-2.97 ppm vs. TMS), add 9.09 ppm for each α carbon (carbon atoms directly attached to the carbon in question), add 9.40 ppm for each next-nearest carbon (β carbons), subtract 2.49 ppm for each γ carbon, add 0.31 ppm for each δ carbon, and add 0.11 ppm for each ε carbon. Steric corrections are then frequently necessary, especially at or near tertiary carbons: for example, if a tertiary carbon's chemical shift is being calculated, subtract 3.65 ppm for every directly bonded secondary carbon. When calculating the chemical shift of primary or secondary carbons, subtract 2.50 ppm or 1.12 ppm (respectively) for every directly bonded tertiary carbon. The parameters given here are sufficient to predict the ^{13}C chemical shifts of all the sequence structures expected for poly(ethylene-co-1-hexene). These predictions are compared in Table 3-3 to the experimentally observed values reported by Randall. (*3-9*)

Clearly, the simple ^{13}C chemical shift predictions based on the method of Paul and Grant are as much as 3 ppm away from the experimental values, especially when

calculating methine chemical shifts (the predicted methylene chemical shifts are mostly within one ppm of the experimental values). Other, usually more complex empirical shift calculation techniques have been described in the literature (*3-13*), with some improvement in the accuracy of the predictions, although no empirical technique has yet appeared that can predict the carbon chemical shifts in polyethylene/1-alkene copolymers to within a few tenths of a ppm. One problem is the applicability of chemical shift parameters derived from small alkane model compounds; while electronically they may be similar, steric effects and rotamer populations can be expected to be different for small molecules and large polymer chains.

In spite of the quantitative shortcomings of empirical chemical shift calculations, even simple methods such as that of Grant and Paul were useful in the assignment of the ^{13}C chemical shifts of poly(ethylene-co-1-hexene). For example, Table 3-3 shows that the Grant and Paul method correctly predicts the relative order of methylene carbon chemical shifts (from high frequency to low): $\alpha\alpha > \alpha\gamma \approx \alpha\delta+ > \gamma\gamma > \gamma\delta+ > \delta+\delta+ > \beta\delta+ > \beta\beta$. Careful comparison of the ^{13}C chemical shifts of poly(ethylene-co-1-hexene) with those for poly(ethylene-co-1-butene) strongly suggests that the Grant and Paul parameter ε is essentially zero for these polymers, justifying the assumption that we need consider only the presence or absence of carbons four or fewer bonds away from any given carbon.

Another issue must be considered when assigning the ^{13}C spectrum of poly(ethylene-co-1-hexene). Clearly, while the polymer chains are quite long, they are not infinite. What are the structure and ^{13}C chemical shifts of the chain ends? Randall and Hsieh (*3-14*) report the detection of two types of polymer chain ends: an n-alkyl-like chain end ($-CH_2-CH_2-CH_2-CH_3$; labeled as s for saturated) and a terminal olefin ($-CH_2-$

$CH=CH_2$). Table 3-4 shows the chemical shifts they report for these chain ends, where 1s, 2s and 3s are the carbons counting from the end of the saturated chain end, 1v and 2v are the olefinic carbons, again counting from the chain end ("v" for vinylic), and "a" refers to the allylic carbon. As most commercial poly(ethylene-co-1-hexene) materials are of high molecular weight, these chain ends contribute only very small ^{13}C NMR peaks, if detectable. The ^{13}C chemical shifts for the saturated chain end (1s, 2s and 3s) are quite similar to the chemical shifts for a butyl branch, differing only at the fourth carbon (methylene as compared to methine). Thus, while 1s is very similar to $1B_4$, 3s is not as similar to $3B_4$.

Collective Assignments. In practice, separate resonances are not observed for all the ^{13}C chemical shifts listed in Table 3-3. Many of the carbon resonances are partially or completely overlapped; this is not surprising considering the similarity of some of the chemical shifts and the linewidths achievable for these viscous polymer solutions. The issue of peak resolvability will be discussed in more detail in the Results and Discussion section, but clearly, peak overlap can complicate a quantitative analysis of the carbon spectrum.

Hsieh and Randall dealt with resonance overlap by means of the concept of *collective assignments*. (*3-9*) Instead of trying to *separately* integrate overlapping peaks, the spectrum is divided into baseline-resolved regions and integrated region by region. The total integral of each region is then compared algebraically to the *n*-ads with ^{13}C chemical shifts contributing to that region. This procedure not only simplifies quantitative analysis of a spectrum, but also simplifies the shift assignments, since configurational splittings or long-range sequence effects (which often give rise to line

broadening or poorly resolved peak splittings) can be neglected. In this way, the spectrum need only be assigned in terms of triad and tetrad contributions, and stereochemical effects (such as meso vs. racemic relative configurations) can be ignored.

For the sake of brevity, an in-depth analysis of the tetrads and triads contributing to each spectral region will be omitted; instead, a summary is presented in Table 3-5. Suffice it to state that these collective assignments have been confirmed by this author and other researchers. (*3-15*) Nevertheless, a few comments about specific regions are warranted.

Region A is the highest-frequency (lowest shielding) region (above 40 ppm) in the ^{13}C NMR spectra. Contributing to this region are the $\alpha\alpha$ carbons, the methylenes located between two branch points, resulting from the consecutive addition of (at least) two 1-hexene monomers to a growing polymer chain. Thus, this region directly indicates the amount of 1-hexene clustering in the co-polymer. Contributing tetrads are HHHH, EHHH and EHHE; if appropriate experimental conditions are used, each of these three tetrads contributes equal signal intensity to region A. We can use the necessary relationships to relate *A*, the integrated intensity of region A, to either diad, triad or tetrad mole fractions:

$$A = k \{ [HHHH] + [EHHH] + [EHHE] \}, \text{ or} \quad (13)$$

$$A = k [HH] , \text{ or} \quad (14)$$

$$A = k \{ [HHH] + \tfrac{1}{2} [EHH] \}. \quad (15)$$

These expressions relate the absolute integrated intensities to *n*-ad mole fractions, where k is the so-called "NMR constant" (a parameter that empirically accounts for known and unknown factors associated with characteristics of the instrumentation and techniques

employed). (*3-4*) If the spectrum is collected using truly quantitative experimental conditions, there is only a single value of k for a given spectrum. Normalization of triad concentrations (or any complete set of *n*-ads) will serve to determine k and thus remove it from experimentally derived mole fractions.

Clearly region A will be important in the analysis of the sequence distribution of poly(ethylene-co-1-hexene), as it directly indicates 1-hexene clustering. As we shall see later, a portion of region C can provide some of the same information, although perhaps not as simply.

Regions B, E and F are rather simple, as each has contributions from a single triad. Region B is due to the methine carbons of the EHE triad, and thus its intensity (*B*) is easily expressed as

$$B = k\,[EHE]\,. \tag{16}$$

Likewise, region E is due to the βδ+ methylene of the EEH triad and region F is due to the ββ methylene of the HEH triad, giving the expressions

$$E = k\,[EEH] \text{ and} \tag{17}$$

$$F = k\,[HEH]\,. \tag{18}$$

Regions G and H each arise from the H monad. They represent the ^{13}C chemical shifts of the last two carbons of the butyl branch arising from the incorporation of 1-hexene monomer into the polymer chain. Hence,

$$G = k\,[H] = k\,\{\,[EHE] + [EHH] + [HHH]\,\} \text{ and} \tag{19}$$

$$H = k\,[H] = k\,\{\,[EHE] + [EHH] + [HHH]\,\}\,. \tag{20}$$

Region H is due to the methyl group terminating the butyl branch; as these methyl carbons typically have the longest T_1 value (by far) of the polymer carbons, they may be the most difficult to integrate accurately; this topic will be explored in more detail below.

Regions C and D are much more complex. They each arise from several contributing carbon sites and several specific *n*-ads. Using the *n*-ads assignments in Table 3-5 and the necessary relationships between *n*-ads (Table 3-2), the integrals of these two regions can be solved algebraically in terms of triad contributions as follows:

$$C = k \{ 2 [HHH] + 3 [EHH] + 3 [EHE] \} , \text{ and} \quad (21)$$

$$D = k \{ 2 [EEE] + \tfrac{1}{2} [EEH] + [EHE] + [EHH] + [HHH] \} . \quad (22)$$

Equation (22) is the only "region expression" (equations 15 - 22) that contains [EEE]. In other words, region D is the only region that contains contributions from polymer sequences with three or more consecutive ethylene monomer units. Thus, this region is necessarily involved in any complete quantitative analysis of a poly(ethylene-co-1-hexene) carbon spectrum, even to the monad level. Region D *must* be involved, even if we wish only to determine the amount of 1-hexene incorporation in poly(ethylene-*co*-1-hexene). Therefore, the integral of region D is necessary for determining the NMR constant, k, in a quantitative ^{13}C chemical spectrum. Ignoring region D can give at best only relative, but not absolute, triad concentrations (H containing triads only).

Triad Expressions. The region expressions given in equations (15) - (22) can be combined and solved in terms of the six triad mole fractions in many different ways, representing an overdetermined algebraic system. We have seven unknowns: [EEE], [EEH], [EHE], [EHH], [HEH], [HHH], and k; we also have ten equations: equations (15) - (22), plus the normalization condition for triads, and plus the triad-triad necessary

condition, 2[EHE] + [EHH] = 2[HEH] + [EEH]. The region integrals *A* through *H* are measured values with experimental uncertainty.

Hsieh and Randall (*3-9*) recommended one set of triad expressions in 1982, shown in equations (23) - (28):

$$k\,[EHE] = B \tag{23}$$

$$k\,[EHH] = 2\,(G - B - A) \tag{24}$$

$$k\,[HHH] = 2A + B - G \tag{25}$$

$$k\,[HEH] = E \tag{26}$$

$$k\,[EEH] = 2\,(G - A - F) \tag{27}$$

$$k\,[EEE] = \tfrac{1}{2}\,(A + D + F - 2G) \tag{28}$$

They chose this particular set of triad expressions for several reasons. They chose to eliminate expressions involving regions E and H, the former because of the potential for a slight overlap of spectral intensity between regions D and E, and the latter because the long T_1 value of the H methyl carbons requires long relaxation delays. Sufficiently long relaxation delay for quantitative integration of the methyl region H would adversely affect overall spectral sensitivity, an important issue, since many of the important regions (such as A and F) have very small but important signals. Region C was also eliminated from the expressions because of the potential presence of allylic carbons from terminal olefin polymer chain ends. Also, they selected these triad expressions (equations 23 - 38) for their apparent simplicity.

Many other possible triad expressions are possible, especially if some of Hsieh and Randall's choices for region elimination are altered. Further possibilities involve the creation of spectral subregions; Randall has pointed out this possibility, especially with

region C. (*3-14*) Hsieh and Randall chose to ignore the potential presence of saturated polymer chain end signals, which can affect the values of the integrals *D*, *G* and *H*. These issues are examined later in this chapter.

Sequence Distribution Models. Accurate triad mole fractions provide information about the sequence distribution of monomers within the copolymer, which in turn is related to the physical properties of the polymer and the mechanism of polymerization. As ethylene and 1-hexene are polymerized, a variety of monomer sequences may be created, including ethylene-only portions of the polymer chain, 1-hexene-only sequences, and sequences with both ethylene and 1-hexene units included. Monad mole fractions provide only the content of each comonomer within the copolymer, but diads and higher order *n*-ads provide information about the number and types of sequences present. For example, a blocky copolymer of ethylene and 1-hexene would consist of long stretches of only ethylene monomer units and long stretches of only 1-hexene monomers. In this case, the only EH sequences observed would be where an ethylene-only block is joined to a 1-hexene-only block, and thus the value of [EH] would be very small compared to either [EE] or [HH]. Considering triad mole fractions for this same blocky copolymer example, one would expect relatively large values for [EEE] and [HHH], very small values for [EEH] and [EHH], and zero for [EHE] and [HEH]. As another example, consider a perfectly alternating copolymer of equal numbers of ethylene and 1-hexene monomers. In this case, [EH] =1 and [EE] = [HH] = 0, while for triads [EHE] = [HEH] = 0.5 and [EEE] = [HHH] = [EHH] = [EEH] = 0.

In the two examples given so far, there is no apparent additional information gained by knowing the triad mole fractions as compared to the diad mole fractions.

Consider, however, a copolymer of the type ...EEHHEEHHEEHHEEHHEEHH...vs. a copolymer such as ...EEEHHHEEEHHHEEEHHH... In both cases, the diad mole fractions are equal (i.e., [EE] = [EH] = [HH] = 1/3), but the triad mole fractions would distinguish the two cases. In the first case, [EEH] = [EHH] = 1/2 are the only non-zero triad mole fractions, while for the second case, [EEE] = [HHH] = 1/6 and [EEH] = [EHH] = 1/3 are the only non-zero triad mole fractions. Thus, we see that higher order *n*-ads can distinguish between sequences with longer continuous 'blocks' (runs) of a given monomer. In practice, the resolution achievable in the ^{13}C NMR spectrum of poly(ethylene-co-1-hexene) makes triad analysis practical; although tetrad-level descriptions may be possible, pentad and higher *n*-ad analyses do not appear to be possible with present-day ^{13}C NMR capabilities.

Unlike the examples given above, commercial poly(ethylene-co-1-hexene) materials usually contain less than 6 mol % 1-hexene. The 1-hexene copolymer is added during ethylene polymerization to lower polymer density and melting point, and improve processability. The presence of butyl branches disrupts the crystal packing of polyethylene chains. (*3-16*) It is thought that widely dispersed butyl branches are more effective in this regard than would be an equal number of butyl branches in close mutual proximity. Considering that 1-hexene is a much more expensive raw material than is ethylene, poly(ethylene-co-1-hexene) manufacturers are interested in the sequence distribution of the monomers in order to maximize branching effects, while using minimal amounts of 1-hexene copolymer.

Sequence distribution information can provide insight regarding the mechanism of polymer catalysis. If the addition of either ethylene or 1-hexene to the growing polymer

chain occurs after the rate-determining step of the catalytic cycle, the probability of adding 1-hexene vs. ethylene (P_H) may not depend on the identity of the previous monomer added; 1-hexene would be equally likely to be added to a growing polymer chain ending in 1-hexene as adding to a chain ending in ethylene. Such a polymer is known as a Bernoullian copolymer (*3-17*), and is characterized by a single probability for adding a 1-hexene monomer, independent of the identity of the last monomer unit added. For Bernoullian copolymers, a specific random distribution of 1-hexene is obtained, with a predictable set of diad and triad mole fractions, as shown in Table 3-6. (*3-17*)

Clearly, block copolymers or alternating copolymers do not correspond to a Bernoullian triad distribution. It should be noted, however, that not all random copolymers give the same triad distributions. Consider a situation in which 1-hexene is twice as likely to add to a growing polymer chain to which another 1-hexene was the last monomer unit added, relative to its adding to a chain with an ethylene added last . The triad distribution expected would be quite different from a Bernoullian polymer, with larger values for [EHH] and [HHH].

The example in the preceding paragraph illustrates the case of a random distribution that is based on two independent probability parameters; such a case is known as a first-order Markov sequence. (*3-17*) In a first-order Markov model, there are four probabilities that characterize the addition process: $P_{E/E}$, $P_{E/H}$, $P_{H/E}$ and $P_{H/H}$, such that, for example, $P_{E/H}$ represents the probability of adding a 1-hexene monomer to a growing chain in which ethylene was the last monomer unit added. However, only two of these probabilities are independent, since $P_{E/E} + P_{E/H} = 1$ and $P_{H/E} + P_{H/H} = 1$, and since every monomer addition must add either an ethylene or a 1-hexene unit. Following

literature precedent (*3-17*), we choose to utilize $P_{E/H}$ and $P_{H/E}$ as the independent probabilities. The diad and triad mole fractions expected for a first-order Markov copolymer are given in Table 3-7, and can be different from those expected for a Bernoullian copolymer. (*3-17*) If $P_{E/H} = P_{H/E}$ the first-order Markov model becomes the Bernoullian model. (*3-17*)

It is certainly possible to envision higher-order Markov models. (*3-17*) For example, a second-order Markov model would have four independent probabilities, depending on the last two monomer units previously added to the polymer chain. (By extension, then, we can consider a Bernoullian model as being the zero-order Markov case, as only a single independent probability is utilized, P_H). As Bovey and others (*3-4,5*) have shown, the utility of higher-order models is limited by the amount of sequence information available. For example, a set of diad mole fractions is sufficient to test whether a given polymer is consistent with a Bernoullian distribution, whereas a set of triad mole fractions is required to test whether a given polymer is consistent with a first-order Markov model. Likewise, tetrad mole fractions are necessary to test for consistency with a second-order Markov model. (*3-17*)

Other models have been developed for monomer addition to growing polymer chains, including the Coleman-Fox Two-State Model (*3-18*), giving *n*-ad mole fractions that are potentially different than for higher order Markov models. The Coleman-Fox model appears to have six independent parameters (expressed as rate constants, not probabilities) and would require pentad-level (or greater) sequence distribution information for testing. As will be shown later in this chapter, pentad resolution exceeds the capabilities currently achievable for the poly(ethylene-co-1-hexene) system. Thus,

within the scope of this research we are limited to testing with respect to Bernoullian and first-order Markov models.

Sequence Distribution Parameters. A number of parameters have been developed to characterize the sequence distribution in copolymers, based on diad and triad mole fraction values. Harwood (*3-19*) developed the *run number* (sometimes also know as the *sequence number*), the average number of times the monomer switches from E to H (or H to E, but not both, according to the updated definition given by Randall (*3-5*)) per 100 monomer units. In terms of diads or triads,

$$\text{run number} = 50\ [EH], \tag{29}$$

$$\text{run number} = 100\ \{\ [EHE] + \tfrac{1}{2}\ [EHH]\ \} = 100\ \{\ [HEH] + \tfrac{1}{2}\ [EEH]\ \} \tag{30}$$

The *average sequence length* is the average number of monomers in an E-only or H-only monomer sequence (or "run"), and is given in terms of triads (*3-19*) as:

$$n_E = \{\ [EEE] + [EEH] + [HEH]\ \} / \{\ [HEH] + \tfrac{1}{2}\ [EEH]\ \} \tag{31}$$

$$n_H = \{\ [EHE] + [EHH] + [HHH]\ \} / \{\ [EHE] + \tfrac{1}{2}\ [EHH]\ \} \tag{32}$$

For example, a value of $n_E = 5$ would mean that, on average, ethylene monomer units occur as five consecutive ethylene units. The average sequence lengths can also be expressed in terms of diads:

$$n_E = 1 + 2\ [EE] / [EH] \tag{33}$$

$$n_H = 1 + 2\ [HH] / [EH]\ . \tag{34}$$

The *persistence ratio*, ρ, was defined by Coleman and Fox (*3-20*) in 1963 as

$$\rho = 2\ [E]\ [H] / [EH]\ . \tag{35}$$

Using the necessary relationships in Table 3-2, this can be re-expressed as

$$\rho = 2\ \{\ [EE] + \tfrac{1}{2}\ [EH]\ \}\ \{\ [HH] + \tfrac{1}{2}\ [EH]\ \} / [EH] \quad \text{or} \tag{36}$$

$$\rho = 2\{[EEE] + [EEH] + [HEH]\}\{[EHE] + [EHH] + [HHH]\}/\{[EEH] + 2\,[HEH]\} \quad (37)$$

The persistence ratio provides a simple test for Bernoullian character, as $\rho = 1$ for the Bernoullian case. A polymer exhibiting a persistence ratio greater than unity would have monomer clustering greater than expected by Bernoullian statistics. For first-order Markov statistics, $\rho = (P_{E/H} + P_{H/E})^{-1}$, since

$$P_{E/H} = [EH] / 2\,[E] \quad \text{and} \quad (38)$$

$$P_{H/E} = [EH] / 2\,[H]\,. \quad (39)$$

Another parameter (apparently unnamed) defined by Coleman and Fox (*3-18*) is omega, Ω :

$$\Omega_E = [E]\,[EE] / [EEE] \quad (40)$$

$$\Omega_H = [H]\,[HH] / [HHH] \quad (41)$$

In these two equations Ω is defined two different ways, in terms of each monomer, E or H. Ideally, the two definitions are equivalent (i.e., $\Omega_E \equiv \Omega_H$), but when using experimentally determined *n*-ad mole fractions, which contain experimental error, one could obtain different values for Ω_E and Ω_H. By either definition, a value of unity is expected for both Bernoullian and first-order Markov statistics (to within experimental error), and thus this may serve as a test for consistency to the latter model.

The *cluster index* was defined by Randall (*3-7*) as follows:

$$\text{cluster index} = 10\,\{\,[H] - [EHE]\,\} / \{2\,[H]^2 - [H]^3\,\} \quad (42)$$

A cluster index of zero would indicate that all H monomer units are separated by at least one E unit (i.e., no clustering of H), while a cluster index of ten is consistent with Bernoullian statistics. A value greater than ten would thus indicate more clustering than expected by the Bernoullian model.

The *average reactivity ratio product*, $\langle r_1 r_2 \rangle$, is also a useful measure (*3-21*) of sequence distribution. The parameters, r_1 and r_2, represent the reactivity of monomers 1 and 2 in a copolymerization reaction. Randall (*3-22*) and Cozewith (*3-23*) have shown that, for a copolymer made by a single site catalyst at constant co-monomer concentrations, and ignoring diffusion or mixing effects, reactivity ratios can be used to relate the relative molar monomer concentration in the feedstock, $M = M_1/M_2$, to the relative molar monomer concentration incorporated into the copolymer, $m = m_1/m_2 = [E]/[H]$:

$$m = M(r_1 M + 1)/(r_2 + M) \tag{43}$$

If the copolymer follows first-order Markov statistics, then

$$r_1 M = (1 - P_{12})/ P_{12} \equiv (1 - P_{E/H})/ P_{E/H} \tag{44}$$

$$r_2/M = (1 - P_{21})/ P_{21} \equiv (1 - P_{H/E})/ P_{H/E} \tag{45}$$

As the copolymer samples examined in this study were obtained (from commercial and third-party sources) without data regarding the relative molar monomer concentration in the feedstock, M, r_1 and r_2 cannot be individually determined. However, the reactivity ratio product, $r_1 r_2$, does not depend on M, as can be seen by multiplying equations (44) and (45).

$$r_1 r_2 = (1 - P_{E/H})(1 - P_{H/E}) / P_{E/H} P_{H/E} \tag{46}$$

The average reactivity ratio product, $\langle r_1 r_2 \rangle$, is defined (*3-21*) on the basis of experimental diad mole fractions, as follows:

$$\langle r_1 r_2 \rangle = 4\,[EE]\,[HH] / [EH]^2 \ , \tag{47}$$

and is thus not model-specific. Instead, $\langle r_1 r_2 \rangle$ can serve as a sequence distribution parameter, since $\langle r_1 r_2 \rangle = 1$ if either Bernoullian or first-order Markov statistics are

followed during copolymerization, and single-site catalysis is involved. Significant deviations of $\langle r_1 r_2 \rangle$ from unity may indicate that either multiple catalytic sites (with different reactivities) are involved, or non-Markovian (or second-order or higher-order Markovian) distributions are involved. (*3-23*)

In the work described in this chapter, several of these sequence distribution parameters have been determined from experimental ^{13}C NMR results, in order to evaluate the utility of these proposed parameters in describing hexane clustering in poly(ethylene-co-1-hexene) copolymers.

Experimental.

Sample Description. Poly(ethylene-co-1-hexene) samples were obtained from Exxon-Mobil Corporation (sample H) and Eastman Chemicals (sample L). Copolymer samples were designated H and L for "higher" and "lower" 1-hexene content. The 1-hexene incorporation levels were determined to be 5.3 mol % and 3.5 mol %, respectively.

Sample Preparation. For each polymer material, NMR samples were prepared for both 5mm and 10 mm tubes as follows: weighed amounts of polymer and solvent, 1,2,4-trichlorobenzene-d_3 (TCB-d_3) or 1,4-dichlorobenzene-d_4 (DCB-d_4), and hexamethyldisiloxane (HMDS) reference were placed in the NMR tube at room temperature; approximate weight percentages are 15 %, 83 % and 2 %, respectively. HMDS was included in most samples to provide a narrow resonance to assess magnetic field homogeneity. Typically, the total solution weight was 1.1 g for 5 mm NMR tubes,

while typically 5.5 g of the polymer/TCB-d_3/HMDS solution was used for 10 mm NMR tubes, resulting in sample heights of 50 mm and 70 mm, respectively.

The mixtures in the NMR tubes were heated to 155 °C in a stirred silicone oil bath for at least 8 hours (but not more than 12 hours). The polymer/TCB-d_3/HMDS mixtures were stirred three times with a thin quartz rod during the first four hours of dissolution. The solutions became quickly transparent at 155 °C, but required at least four hours of heating to appear visibly uniform with respect to refractive index, and homogeneous with respect to viscosity when probed by the quartz rod. When removed from the silicone oil bath and cooled to room temperature, the outside of the NMR tubes were wiped with trichloroethylene to remove any traces of silicone oil (no evidence of residual silicone oil was detected in either ^1H or ^{13}C NMR spectra of similar samples lacking HMDS). At room temperature the polymer solutions solidified to a translucent white soft gel. No attempt was made to de-gas any of the polymer samples. Dissolved O_2 in the samples, if significantly present at these elevated temperatures, would serve as a relaxation agent due to the paramagnetism of O_2, reducing carbon T_1 values and potentially permitting more rapid data acquisition.

NMR Spectroscopy. Liquid-state ^1H and ^{13}C NMR experiments of the above-described copolymer solutions were performed using Varian Inova-400 and Varian Inova-500 NMR spectrometers, with static magnetic field strengths of 9.4 T and 11.7 T, respectively. The former was equipped with a Varian 5 mm triple-resonance indirect detection probe, while two Varian probes were utilized on the Varian Inova-500 NMR spectrometer, a 5 mm triple resonance probe and a 10 mm double resonance probe.

The NMR tubes were heated to 125 °C in the NMR probes, using the built-in Varian temperature controllers. Dry nitrogen gas (obtained from liquid nitrogen boil off) was used for the variable-temperature (VT) gas and to flush the probes. Temperature calibration was done by replacing the NMR sample tubes with a tube containing neat ethylene glycol of the same sample height as the polymer solutions. (*3-4*) Actual temperatures within the neat ethylene glycol were determined using the Varian *tempcal* routine, inputting the observed ^{1}H chemical shifts of the methylene and hydroxyl protons. Typically, the 5 mm NMR tubes required a VT controller setting of 128 °C to obtain an actual sample temperature of 125 (+/-1) °C, while the 10 mm sample tubes required a VT controller setting of 131 °C. Temperatures were stable to within 0.1 °C over the course of the NMR observations, according to the built-in thermocouple sensor positioned in the probe about 5 mm below the sample tube. At least one hour of thermal equilibration delay was required with the 5 mm probes, whereas the 10 mm probe required at least three hours to thermally equilibrate, as judged but constancy in probe shimming and probe tuning.

In all the NMR experiments of this study, the deuterium NMR signals of either the TCB-d_3 or DCB-d_4 solvent provided a signal for field-frequency lock. Magnetic field shimming was based on the deuterium lock signal intensity; shimming on the time domain signal (FID shimming, based on the signal ringdown characteristics) did not provide better ^{13}C NMR lineshapes. Shimming of the copolymer samples was somewhat insensitive, presumably due to viscosity broadening of the deuterium signals. Typical HMDS linewidths (at half-height) were 0.5 Hz for 5 mm copolymer solution samples and

1.0 Hz for 10 mm samples. When the system was properly shimmed, sample spinning did not affect the observed ^{13}C NMR lineshapes.

^{1}H and ^{13}C NMR chemical shifts were referenced using the methyl proton signal of HMDS (determined in this study to be at 0.02 ppm) and the largest ^{13}C copolymer peak (the polyethylene-like polymer backbone with a reported chemical shift of 29.98 ppm. (*3-9*)), respectively. Unless stated otherwise, all ^{13}C NMR spectra were obtained with a spectral width covering (at least) the chemical shift range from 50 ppm to –10 ppm, taking care that any aliased aromatic carbon signals from the solvent do not overlap with the copolymer peaks. ^{13}C pulse angles of 90° (typically about 14 μs, corresponding to a 17.6 kHz ^{13}C radio-frequency field, B_1) were used with WALTZ-16 proton decoupling (*3-24*) at a ^{1}H power level of about 2 watts, corresponding to a 2.3 kHz ^{1}H B_1 field). At least 32,000 data points were acquired for each free induction decay (FID); spectral processing included zero-filling the time-domain signal to 256k points and 2 Hz exponential apodization prior to Fourier transformation. Signal-to-noise ratios were determined using the Varian *dsnmax* algorithm, utilizing the most intense ^{13}C peak (29.98 ppm) and finding the lowest root-mean-squared noise region (2 ppm wide) in the spectral region between 45 ppm and 10 ppm.

For the purpose of determining triad mole fractions, quantitative ^{13}C NMR spectra were obtained using either 25 or 30 s relaxation delays; the latter value is more than 5 T_1's for all copolymer carbons in both samples, except methyl carbons. (*3-14*) Proton decoupling typically involved the composite WALTZ-16 pulse sequence (*3-24*), centered on the most intense proton resonance at 1.25 ppm (due to the polyethylene-like polymer backbone methylenes more than 4 bonds away from a polymer side chain). Some

quantitative ^{13}C NMR spectra were obtained using CW proton decoupling (again, centered on the most intense proton resonance) to eliminate the small decoupler sidebands observed with WALTZ-16 decoupling; the appearance of decoupler sidebands will be discussed later in this chapter.

^{13}C T_1 values were determined by the inversion recovery method, using relaxation delays of 50 s, on the un-degassed polymer solutions at 125 °C. ^{13}C nuclear Overhauser enhancement (nOe) factors were determined from comparison of signal intensities or integrals in the presence or absence of proton decoupling during the relaxation delay (both 25 and 50 second relaxation delays were used). (*3-25*) For most nOe experiments, WALTZ-16 proton decoupling was utilized during the data acquisition period (whether or not decoupling is applied during the relaxation delays). Some nOe experiments used other proton decoupling techniques, including continuous wave (CW) proton decoupling or even no proton decoupling (resulting in proton-coupled ^{13}C NMR spectra).

All ^{13}C NMR spectra were obtained in the double precision digitization mode, without additional digital signal processing.

It was decided to select manually the start and end points for integration, since decoupler sidebands can be observed at various chemical shift values, depending on the WALTZ-16 cycle frequency. For subregions lacking complete baseline separation, start and end points for integration were visually placed at the minimum intensity 'valley' between overlapping peaks. Once integral regions were selected, baseline correction was performed using the *bc* command of the Varian software. This baseline correction involves a polynomial fit using anchor points selected by the operator, which are set as points of zero intensity.

The absolute intensity of each integral region was determined, in some instances, using a single set of baseline correction parameters for the entire aliphatic region (45 to 10 ppm). No zero-order and first-order integral corrections were used in these cases. The resultant integral values are termed *machine* integrals here, as they do not depend on human decisions or evaluation.

For comparison, baseline correction of each integral region separately by the operator provides what we refer to as *manual* integral values. Manual adjustment of the zero and first order integral correction parameters were made visually to flatten the integration plot over noise regions without peaks or decoupler sidebands. Regions 3s, D and E are baseline-corrected together because of apparent peak overlap on the broad wings of the very intense D region. Likewise, the integral of each C subregion is not baseline-corrected individually but as a group, and regions F, G and 2s are baseline-corrected together.

The accuracy and precision of machine *vs.* manual integration techniques are evaluated below in the Results and Discussion section.

RESULTS AND DISCUSSION.

Spectral regions. ^{13}C NMR spectral regions used for integration purposes are listed in Table 3-5, along with the corresponding structural assignments. In addition to previously defined integral regions based on collective assignments (*3-9*), some new subregions are proposed in this work. Hsieh and Randall previously suggested (*3-14*) the C1 and C2 subregions such that C = C1 + C2. In the work reported here, the C region was separated into four subregions for integration: C = C1 + C2a + C2b + C2c. The C2

integral value then equals C2a + C2b + C2c. The D region was likewise divided in this study into 3 subregions such that D = D1 + D2 + D3. The proposed new subregions appear to lack complete baseline separation from neighboring peaks, although better resolution can now be achieved than was possible in the work of Hsieh and Randall about 20 years ago. These more detailed spectral regions were included in the current work in order to examine possible alternate triad distribution and sequence parameter algorithms.

Comparison of available NMR techniques. The determination of the triad mole fractions in a poly(ethylene-co-1-hexene) copolymer sample may in principle be achieved by quantitative NMR analysis using either ^{1}H or ^{13}C spectra. Furthermore, the copolymer sample can be analyzed in one of three physical states: 1) a solid at room temperature, 2) a neat but viscous melt above about 150 ^{o}C (melting point decreases with increasing branching), or 3) as a solution (typically 10 to 20 wt. %) in hot (125 ^{o}C) chlorinated aromatic solvents. In any case, the degree to which a copolymer's NMR spectrum can be analyzed quantitatively depends on both spectral resolution and sensitivity. Peak resolution is required to distinguish signals arising from different triad environments, while good sensitivity is necessary to adequately detect signals arising from carbons located in low probability structural environments, such as the HHH triads for the poly(ethylene-co-1-hexene) samples of interest here.

Prior to the 1980's most triad analysis of copolymer systems utilized liquid-state proton NMR analysis of hot copolymer solutions. (*3-4*) These efforts were necessarily limited to those copolymer systems for which some degree of peak resolution was achieved. Liquid-state ^{13}C NMR capabilities were shown in the 1980's to provide much better peak resolution for many copolymer systems (*3-7*), including ethylene/α-olefin

copolymers (*3-9*) . Liquid-state ^{13}C NMR spectroscopy has the advantage of a much larger chemical shift range than observed by ^{1}H NMR, resulting in a greater spectral dispersion as a function of differences in the copolymer's structural variations. The greater the spectral resolution of peaks due to various branching structures, the better the opportunities for *n*-ad analysis.

Carbon-13 NMR has the major disadvantage of much lower sensitivity compared to proton NMR. The largest factor involved is the 1.1% natural abundance of the ^{13}C isotope as compared to the almost 100% natural abundance of the ^{1}H isotope. The lower magnetogyric ratio of ^{13}C *vs.* ^{1}H (about 4 times smaller) also contributes a factor of about 64 (ratio of the magnetogyric ratios to the third power) to the lower sensitivity of carbon-13 (*3-26,27*) . Another sensitivity disadvantage is the fact that T_1 values are typically longer for ^{13}C than for ^{1}H. (*3-4*) Since quantitative analysis usually requires a delay of at least five T_1's for complete relaxation back to equilibrium between scans, typically many fewer scans per hour can be achieved for ^{13}C than for ^{1}H. (*3-26*)

When contrasting the requirements of sufficient resolution vs. sufficient sensitivity, the resolution requirements can be more difficult to address. The physical state of the copolymer sample (whether solid, liquid melt or liquid solution) determines the molecular motions in the sample, and thus determines the maximum resolution achievable at a given sample temperature and magnetic field strength. Assuming the spectrometer and probe are properly optimized (e.g., shimming, decoupling, etc.), there is little one can do to improve further the spectral resolution achievable. Sensitivity, on the other hand, is (in principle) not limited to a maximum achievable value, but can always be improved by further signal averaging. Furthermore, NMR instrumentation

improvements such as the availability of higher field magnets and modern probe design results in significantly more sensitivity per scan than was achievable even ten years ago.

Figures 3-4 and 3-5 compare the solid-state room temperature ^{13}C CP-MAS spectrum of sample H with the liquid-state ^{13}C NMR spectrum of sample H dissolved in 1,2,4-trichlorobenzene-d_3 at 125 °C (with WALTZ-16 proton decoupling). The former spectrum was obtained at a carbon resonant frequency of 37.7 MHz (equivalent to a proton frequency of 150 MHz) using the $^{1}H \rightarrow ^{13}C$ cross polarization method (*3-28*), while the latter was obtained at 125.8 MHz (500 MHz proton frequency). Note the much poorer resolution obtained for the solid sample at room temperature; none of the peaks observed are baseline resolved from the others. In the solid-state room temperature spectrum (Figure 3-4) the linewidths at half height range from 20 to 150 Hz, whereas in the liquid-solution spectrum (Figure 3-5) the linewidths exhibit a range from 4 to 15 Hz; both spectra include 2 Hz added exponential broadening.

One contribution to the larger ^{13}C linewidths observed with the solid copolymer sample, compared to the linewidths observed with liquid solutions, is due to isotropic chemical shift dispersion, resulting from "frozen-in" variations in the microstructural environment for a given carbon site within the solid copolymer structure, variations that would be averaged by the motion present in a liquid sample. For example, in the absence of atomic-level motion, conformational isomerization can give rise to a distribution of isotropic ^{13}C chemical shifts for a given carbon site. Sufficiently rapid molecular motion on the NMR time scale (*i.e.*, correlation times shorter than the inverse frequency dispersion due to structural variations) of the copolymer dissolved in a hot liquid solvent

serves to average out many microstructural variations in the solid, resulting in sharper resonances when dissolved. (*3-4*)

Morphological effects can also contribute to the observed ^{13}C NMR linewidths in the solid state, since ethylene/α-olefin copolymers are reported to form both amorphous and crystalline phases (*3-16*), which may be expected to exhibit slightly different isotropic ^{13}C chemical shifts for a given type of carbon. Earl and VanderHart (*3-29*) have previously shown that the isotropic carbon chemical shift of polyethylene in the crystalline phase is about 2 ppm greater than for the amorphous phase. Similar morphological effects might be present in the copolymers study herein, exhibiting possibly different ^{13}C chemical shifts for amorphous and crystalline copolymer phases.

The solid-state room temperature ^{13}C CP-MAS spectrum shown in Figure 3-4 exhibits such poor resolution that only monad level analysis appears to be possible, albeit using spectral deconvolution (i.e., lineshape fitting) to quantify the contribution of each peak. Thus, the spectrum of the solid sample at room temperature might be utilized to estimate the 1-hexene content of the copolymer, but appears to be useless for either diad or triad analysis (as required to determine clustering of 1-hexene units in the copolymer). Table 3-8 shows the quantitative deconvolution results of the room temperature ^{13}C CP-MAS spectrum of copolymer sample H, seen in Figure 3-4 (deconvolution results are graphically shown in Figure 3-6). Comparing the methyl integral obtained by deconvolution to the total spectral integral gives a value of 2.0 mol % 1-hexene content; this analysis assumes that the signal response is identical for each carbon-13 nucleus in the sample. The 2.0 mol % estimated 1-hexene content is significantly lower than the 5.2

mol % 1-hexene content determined later in this study using the 125 °C liquid-solution ^{13}C spectrum of the same copolymer.

The erroneously low estimate of the 1-hexene content reflects the fact that ^{13}C CP-MAS spectra are usually not quantitative as obtained, unless CP dynamics have been properly characterized. (*3-30*) Certainly, careful analysis of the variable contact time (VCT) results can provide intensity correction factors for each peak integral, and thus provide a more accurate estimate of the 1-hexene content in copolymer sample H. Indeed, as expected, a variable contact time experiment (Figure 3-7) indicates that the methyl carbon signal has a longer T_{HC} value (slower buildup of carbon magnetization via cross polarization) than do the other carbon signals, presumably because of fast rotation of methyl groups, which partially averages the dipolar interaction between the methyl carbon and the surrounding proton spin bath.

Alternatively, cross polarization enhancements can be avoided entirely by utilizing a direct polarization (DP) detection of the carbon spectrum, but at the cost of less sensitivity per scan and longer equilibration delays between scans. In any case, the solid-state room temperature ^{13}C CP-MAS method was deemed to be inappropriate for triad level analysis of poly(ethylene-co-1-hexene), because of the poor spectral resolution obtained.

Another experimental option mentioned above is to convert the solid copolymer sample to the melt, to speed up molecular motion and average out isotropic chemical shift heterogeneity effects. Hatfield *et al.* (*3-31*) used direct polarization ^{13}C together with MAS and high power proton decoupling to examine the effect of temperature on the ^{13}C spectrum of poly(ethylene-co-α-olefin)s in the solid and liquid (molten) states. The

copolymers included a poly(ethylene-co-1-hexene) containing 3.9 mol % 1-hexene monomer (as determined by the Proposed ASTM Method X70-8605-2 liquid-solution ^{13}C analysis). They compared the 50.3 MHz ^{13}C DPMAS spectra of the copolymers at 30 °C (solid phase) and at 200 °C (liquid melt phase), with the 100.6 MHz ^{13}C liquid solution spectrum of the copolymers dissolved at 15 wt % concentration in an unspecified solvent at 125 °C. They showed that the spectrum of the 200 °C liquid melt provides much narrower carbon peaks than does the 30 °C solid-sample ^{13}C DPMAS spectrum (the latter is similar in appearance to Figure 3-4), but less resolution than observed in the 125 °C solution spectrum. No linewidth values were reported.

The results of Hatfield *et al.* (*3-31*) strongly indicate that the liquid solution spectrum at 125 °C is most suitable for triad analysis. The smallest peaks (such as in region A or F) are not clearly observed in their published 200 °C melt spectrum of poly(ethylene-co-1-hexene). They also obtained lower α-olefin contents from analysis of the 200 °C melt spectra than the values obtained from the corresponding 125 °C liquid solution spectra. In the case of the poly(ethylene-co-1-hexene) sample, the melt spectrum indicated a 1-hexene content of 3.4 mol %, compared to a value of 3.9 mol % by analysis of the solution spectrum.

Figure 3-8 shows the 500 MHz ^{1}H NMR spectrum of sample H dissolved (15 wt %) in 1,2,4-trichlorobenzene-d_3 acquired at 125 °C. Also present in the sample is hexamethyldisiloxane, used as a shift reference and to monitor sample shimming; it provides the relatively sharp singlet at 0.04 ppm (relative to TMS). Although a deuterated solvent was used, the isotopic enrichment is 99 %; the remaining 1 % of hydrogens that are ^{1}H give rise to the aromatic proton peaks at 7.2, 7.1 and 6.9 ppm. The

largest peak in the proton spectrum, an asymmetric peak at 1.25 ppm that is about 16 Hz wide at half-height, is due to the polyethylene-like methylene protons that dominate the copolymer hydrogen content. The side chain methyl protons, observed as an 18 Hz wide singlet at a chemical shift of 0.86 ppm, are not resolved from the other copolymer resonances. The other proton resonances of the butyl side chains arising from 1-hexene incorporation are not visible under the base of the largest peak. Similarly, the methine and methylene protons located on the copolymer chain at or near the branch points are also hidden by the largest peak. Liquid-sample ^{1}H 500 MHz NMR relaxation times determined for sample H at 125 °C are shown in Table 3-9.

The proton spectrum of poly(ethylene-co-1-hexene) sample H in Figure 3-8 is clearly not amenable to any level of *n*-ad analysis beyond monad (*i.e.*, the 1-hexene content). Even for monad analysis, the proton spectrum provides more challenges for quantitative analysis than present in the ^{13}C spectrum. The 1-hexene content can be estimated by comparing the methyl integral to the total copolymer proton integral, assuming that an accurate determination of the unresolved methyl integral can be obtained. The degree of peak overlap with the methyl resonance necessitates the use of deconvolution analysis (*i.e.*, lineshape analysis), as direct integration can be expected to be quite inaccurate in this case.

Deconvolution of the proton spectrum in Figure 3-8 gives the following integrals (arbitrary units): 2404.044 for the methyl peak compared to 31135.563 for the total aliphatic proton region (minus the hexamethyldisiloxane resonance). The equation, $I_{Me} = k_H\, 3\, [H]$, states the relationship between the methyl proton integral and the 1-hexene mol fraction (where k_H is the spectral response factor), while the equation, $I_{total} = k_H \{ 4\, [E] +$

12 [H] } = k_H { 4 + 8 [H] }, gives the total copolymer integral as a function of [H], since [E] = 1 – [H]. Solving both equations for k_H provides the following expression: [H] = 4 I_{Me} / (3 I_{total} – 8 I_{Me}). In this case, the deconvolution integrals provide an estimate of 13.0 mol % for the 1-hexene content, more than twice as large as the value obtained below using ^{13}C spectral analysis of the same sample (sample H). It is not clear why the deconvolution-derived value is so erroneously large.

When direct integration (*i.e.*, "manual" integration of peaks, using operator-optimized integral break points and baseline correction; no peak deconvolution involved) of the proton spectrum in Figure 3-8 was attempted, [H] was estimated to be 7.4 mol % (I_{total} = 100.00 and I_{Me} = 4.84 in different arbitrary integral units than for the deconvolution results). Again, this value is significantly greater than the ^{13}C-determined value discussed below. Here, the inaccuracies of integrating badly overlapped peaks would be expected to give an inaccurate 1-hexene content. It is not clear why the deconvolution value appears to be more inaccurate than the direct integration result, as deconvolution would be expected to handle the peak overlap better.

Solid-state proton NMR techniques were not attempted for this study. While, in principle, techniques such CRAMPS (Combined Rotation and Multiple Pulse Sequence) (*3-32*) can give fairly high resolution proton spectra of solids, the more successful CRAMPS methods such as BR-24 (*3-33*) typically give proton peaks with linewidths of about 0.5-1.0 ppm, and then only for solids with high crystallinity. As seen in Figure 3-8, the copolymer proton resonances all occur within a range of about one ppm, so solid-state proton NMR would not be expected to give any better resolution than observed in

the 125 °C liquid-solution ^{1}H spectrum. Furthermore, methods such as CRAMPS are not easily made quantitative.

Other NMR techniques can also be considered and rejected. For example, many modern NMR spectrometers can perform indirectly-detected ^{13}C NMR using 2D pulse sequences; in this approach the ^{13}C chemical shifts are encoded as a modulation of the 2D proton signal. (*3-34*) While accurate ^{13}C chemical shifts can be obtained with greater sensitivity than by direct detection (since proton, not ^{13}C magnetization is actually measured), the technique is again inherently non-quantitative.

The analysis in the preceding paragraphs demonstrates that ^{13}C NMR analysis of poly(ethylene-co-1-hexene) dissolved in solution at 125 °C is indeed the most suitable approach for the quantitative determination of accurate triad distributions. This conclusion was reached by researchers in the 1980's and is still true today, in spite of many advances in NMR technology, such as ^{1}H CRAMPS and indirectly-detected ^{13}C spectroscopy. The capabilities of modern-day NMR spectrometers do, however, provide higher quality spectra than available twenty years ago, in regard to the sensitivity and resolution obtainable using high-field spectrometers and modern probe electronics.

Influence of Static Magnetic Field Strength. The 126 MHz ^{13}C NMR spectrum of sample H dissolved in 1,2,4-trichlorobenzene-d_3 at 125 °C shown in Figure 3-5 was closely inspected to compare the observed carbon peaks to the published spectra of similar poly(ethylene-co-1-hexene) copolymers. Those previous results were obtained at lower magnetic fields and with lower signal-to-noise characteristics than shown in Figure 3-5. When comparing the present results with the published spectra (*3-14,15*), the qualitative agreement is seen to be quite good. The general appearance of the spectrum in

Figure 3-5 is very similar to the published results, albeit with improved sensitivity (signal-*vs*.-noise). The resolution obtained in the study reported here is similar to or just slightly better than that of the published poly(ethylene-co-1-hexene) spectra, although the magnetic field strength is higher in the present study; previous results were mostly obtained using 200 or 300 MHz (^{1}H frequency) spectrometers, whereas the results reported herein were obtained on a 500 MHz (for ^{1}H) spectrometer. This comparison suggests that the ^{13}C linewidths in Hz increases with increasing external magnetic field strength. The observed linewidth of each ^{13}C peak can be divided into two portions: 1) the "natural" linewidth of a single, un-overlapped peak is related to T_2^*; specifically, FWHH = $(\pi T_2^*)^{-1}$ where FWHH is the full-width at half-height and T_2^* is the spin-spin relaxation time (the signal dephasing time constant) in the presence of a homogeneous external magnetic field, and 2) inhomogeneous contributions, including the effects of an inhomogeneous static magnetic field and chemical shift dispersion (the presence of similar-type carbons in slightly different chemical environments). An example of chemical shift dispersion is the observation that all the methyl carbons arise from butyl branches on the polymer, and they all appear at about 14 ppm in the ^{13}C spectrum. The slight differences in possible methyl environments, such as methyl groups in an EHE triad vs. an EHH triad, give slightly different methyl carbon chemical shifts, contributing to the observed linewidth; the structural differences between these two methyl cases are sufficiently long-range that the observed chemical shifts differ by less than 0.1 ppm, which is insufficient to resolve into separate peaks. Instead, these very small but non-zero shift differences give rise to a methyl resonance broader than would be expected if only one type of structural environment existed for all methyl carbons.

If chemical shift dispersion effects dominate an observed linewidth, as one increases the applied magnetic field strength one would expect the linewidth to increase in units of Hz, but remain constant in units of ppm. Since the amount of peak overlap does not appear to change significantly upon increasing magnetic field strength (when comparing Figure 3-5 to published lower-field poly(ethylene-co-1-hexene) ^{13}C spectra), we can conclude that chemical shift dispersion effects dominate the observed linewidths.

Decoupler Sidebands. During the process of determining and confirming the chemical shift assignments for the ^{13}C spectrum of poly(ethylene-co-1-hexene), small peaks were observed that were never previously reported for similar samples. For example, a small peak was reproducibly observed at about 26 ppm, a region that was previously reported to be lacking any significant resonances arising from the polymer; similarly, a small peak at about 37 ppm is seen in this study, but not previously reported. At first, the presence of impurities was thought to be responsible for these previously unreported peaks, although the peaks involved were difficult to assign as arising from a particular carbon atom in a particular impurity. Upon consulting with other NMR spectroscopists (at Exxon) familiar with this type of copolymer NMR analysis, the suggestion was made that these apparent impurity peaks were actually "decoupler sidebands" (*3-33,34*) of the very large δ+δ+ peak at 29.98 ppm, due to polyethylene-like carbons. This isolated methylene peak is the only peak intense enough that its much smaller decoupler sidebands are observable at the signal-to-noise ratios attained in this study. Decoupler sidebands result from periodic modulations of the ^{13}C magnetization due to the cyclic nature of most proton decoupling methods based on pulse sequences. (*3-35*)

Indeed, a comparison of the ^{13}C spectra of the same poly(ethylene-co-1-hexene) (sample H), acquired with two different decoupler modes, is shown in Figure 3-9. The top spectrum was acquired using standard WALTZ-16 decoupling (2.5 kHz decoupler field strength) while the bottom spectrum was obtained using continuous wave (CW) decoupling, using the same decoupler field strength. The peaks at about 26 ppm and about 37 ppm are not generated with CW decoupling, indicating that these are probably decoupler sidebands occurring during the WALTZ sequence. The concern then became whether there are other decoupler sidebands in the WALTZ-decoupled spectrum that may overlap with peaks whose integrals are used in the quantitative triad analyses. If so, these decoupler sidebands may present a source of systematic error in the analysis, by slightly distorting the true intensities of the various peaks and regions. For example, the integral of the δ+δ+ peak (region D) would be reduced by a very small fraction, while integral regions C and G may significantly increase, due to overlap with a δ+δ+ decoupler sideband.

In order to determine the location and intensity of these decoupler sidebands, a spectrum containing only the δ+δ+ peak would be ideal for analysis. For this purpose, three polyethylene samples were prepared, but upon ^{13}C NMR analysis all showed additional ^{13}C peaks due to branching, which complicates detection of the decoupler sidebands. Instead, a model compound (dimethyl sulfoxide, DMSO) was analyzed at the same temperature and instrumental conditions as used for Sample H.

Figure 3-10 shows the 126 MHz ^{13}C liquids NMR spectrum of neat DMSO at 125 ^{o}C, obtained with either WALTZ-16 decoupling (spectrum A) or with CW decoupling (spectrum B). The ^{13}C peak of DMSO was arbitrarily set to a chemical shift of 29.98 ppm

(instead of the correct chemical shift of 39.5 ppm relative to TMS) to facilitate comparison to the copolymer spectrum; thus, Figure 3-10 should show where the decoupler sidebands are expected that arise from the large δ+δ+ peak at 29.98 ppm in the copolymer spectrum. Figure 3-10A (with WALTZ-16 decoupling) shows the presence of six larger decoupler sidebands, symmetrically disposed about the central peak, and possibly eight smaller decoupler sidebands. Peaks arising from impurities in the DMSO are labeled in Figure 3-10 with a lower-case letter i; these two known impurity peaks are observed in both spectra, whereas the decoupler sidebands are seen in the WALTZ-16 spectrum, but are absent during CW decoupling.

Analysis of the positions of the observed decoupler sidebands in Figure 3-10 shows that they are all located with frequency offsets (from the large centerband peak) that are the inverse of various integer multiples of the decoupler cycle period. For example, the decoupler sidebands located at 30.5 and 29.5 ppm occur at frequency offsets of 270 Hz from the centerband, which arises from two subcycles of the WALTZ-16 supercycle (*3-35*) :

WALTZ-16 : $\underline{3}4\underline{2}3\underline{1}2\underline{4}2\underline{3}$ $\underline{3}4\underline{2}3\underline{1}2\underline{4}2\underline{3}$ $\underline{3}4\underline{2}3\underline{1}2\underline{4}2\underline{3}$ $\underline{3}4\underline{2}3\underline{1}2\underline{4}2\underline{3}$

where 1 represents a 90°(+x) pulse, $\underline{2}$ represents a 180°(-x) pulse, $\underline{4}$ represents a 360°(-x) pulse, etc. Offsetting the decoupler frequency from the peak maximum did not alter the position of the observed decoupler sidebands, but merely altered the sideband intensities in an irregular manner. Other multipulse decoupling schemes tested included GARP, MLEV, FM-FM, XY32 and square-wave decoupling (*3-35*), but they all gave rise to similar or larger decoupler sidebands and were not used to acquire copolymer ^{13}C NMR spectra in the study reported here.

Early attempts to describe broadband decoupling theoretically by Average Hamiltonian Theory were not very successful, but in 1982 Waugh (*3-36*) developed an exact theory of decoupling in liquids that accurately analyzed composite pulse decoupling sequences such as WALTZ-16, and described the origins of decoupler sidebands. Briefly, the key points related to decoupler sidebands will be mentioned now.

Decoupling of ^{1}H from ^{13}C in liquids requires that the proton spin vectors should be repeatedly inverted at a rate faster than J_{CH} (typically about 125 Hz for alkanes). This may be achieved by continuous wave (CW) irradiation at a single frequency, if sufficient decoupler power is available, and the probe hardware can tolerate such a high power level (with a 100 % duty cycle if nOe enhanced spectra are acquired). Sample heating during CW decoupling may also be problematic for certain samples, especially ionic ones. In the current study, the samples were not very "lossy" electrically, and sample heating effects were not an issue during variable temperature operation at 125 °C.

In this study, during CW decoupling the on-resonance protons were inverted at a rate of 1.25 kHz, about ten times the value of J_{CH}. The effective decoupling field experienced by protons offset in frequency from the decoupler irradiation frequency is reduced, resulting in a slower proton spin flip rate. At high magnetic fields the proton resonance frequencies in a sample are further spread apart (in frequency units, not ppm), resulting in less efficient decoupling of protons offset from the decoupler frequency. Fortunately, the proton spectrum of poly(ethylene-co-1-hexene) exhibits only a small range of proton chemical shifts (see Figure 3-8), about 2.0 ppm (1 kHz at 500 MHz). In all the ^{13}C spectra obtained in this study (using any decoupling method), the ^{1}H irradiation frequency was set to the maximum of the largest proton peak, at 1.25 ppm, so

all the copolymer proton resonances are within about 500 Hz of the decoupler frequency. Even so, Figure 3-8 shows that the observed proton linewidths are larger with CW decoupling than using WALTZ-16, especially for methine and methyl carbons, whose proton chemical shifts are furthest offset from the decoupler frequency. In fact, the methyl carbon resonance appears as a partially resolved quartet, indicating only partial decoupling of methyl protons.

Alternatives to CW decoupling have been in existence for many years; the goal of these methods is to achieve broadband decoupling that utilizes less radio frequency (rf) power than does CW decoupling, and covers a larger range of proton frequencies. Among the simplest and oldest alternatives to CW decoupling are 1) a repetitive train of 180° proton pulses, and 2) pseudo-random noise decoupling. During the 1980's composite pulse decoupling schemes (such as WALTZ-16) were developed which are based on a repetitive train of composite 180° proton pulses. (*3-35*) For example, a 90°(+x) 180°(-x) 270°(+x) sequence (or 1$\underline{2}$3 in the notation given above) has the same overall effect as a single 180°(+x) inversion pulse, but with better compensation of frequency offset effects. Further compensation can be achieved by combining basic 1$\underline{2}$3 composite pulses with their phase-inverted versions to create the WALTZ-4 cycle (*3-35*):

WALTZ-4 : 1$\underline{2}$3 1$\underline{2}$3 $\underline{1}$2$\underline{3}$ $\underline{1}$2$\underline{3}$ which is equivalent to 1$\underline{2}$4$\underline{2}$3$\underline{1}$2$\underline{4}$2$\underline{3}$.

Further phase inversions and combinations lead to WALTZ-8 and finally WALTZ-16:

WALTZ-16 : $\underline{3}$4$\underline{2}$3$\underline{1}$2$\underline{4}$2$\underline{3}$ 3$\underline{4}$2$\underline{3}$1$\underline{2}$4$\underline{2}$3 3$\underline{4}$2$\underline{3}$1$\underline{2}$4$\underline{2}$3 $\underline{3}$4$\underline{2}$3$\underline{1}$2$\underline{4}$2$\underline{3}$

WALTZ-16 is currently the most used broadband proton decoupling method in liquid-sample ^{13}C NMR. Its effective decoupling bandwidth is about twice the proton decoupling field strength expressed in units of Hz; thus, for this study, we may expect an

effective decoupling bandwidth of about 5 kHz during WALTZ-16, which is equivalent to ten ppm at 500 MHz.

Although the WALTZ-16 method produces efficient broadband decoupling, it is not perfect; decoupler sidebands result from imperfections such as rf field inhomogeneity and frequency offset effects. Each $^{13}C^{1}H_2$ methylene present gives rise to a pair of ^{13}C satellites in the ^{1}H spectrum about 63 Hz from the $\delta+\delta+$ proton peak (at 1.25 ppm), corresponding to the two possible ^{13}C spin states. During a composite pulse decoupling sequence these two satellites experience slightly different spin trajectories. The net result of the train of decoupler pulses can be described as a single rotation for each proton spin; different protons may experience different angles and axes of rotation. Because of rf field inhomogeneity and frequency offset effects, the overall rotation of the satellite proton spin coupled to a (+) ^{13}C spin state will be slightly different from the overall rotation of the satellite proton spin coupled to the (-) ^{13}C spin state. If we define **n(+)** and **n(-)** as the unit axes around which the overall rotation of each satellite transition occurs, and $\beta(+)$ and $\beta(-)$ are the overall rotation angles achieved about those axes, carbon decoupler sidebands occur in pairs with frequency offsets (in Hz) equal to $\pm [\beta(+) + \beta(-)] / 2\pi t$, where t can be a multiple of the composite pulse subcycle or cycle time. The intensity of the resulting decoupler sidebands is given as

$$I_{sideband} = [1 - \mathbf{n(+)} \bullet \mathbf{n(-)}] / 2, \qquad (48)$$

where $\mathbf{n(+)} \bullet \mathbf{n(-)}$ is the dot product of these unit vectors. In comparison, the centerband during composite pulse decoupling will have an intensity

$$I_{centerband} = [1 + \mathbf{n(+)} \bullet \mathbf{n(-)}] / 2. \qquad (49)$$

An efficient composite phase decoupling scheme will have **n(+)** and **n(-)** unit vectors that are almost co-linear, and the dot-product will have a value very close to 1.0. Thus, during WALTZ-16, a relatively efficient decoupling scheme, $I_{sideband}$ is non-zero, but much smaller than $I_{centerband}$. The centerband/decoupler sideband integral ratios are expected to be different for each copolymer proton resonance, but apparently this ratio is sufficiently small for all proton peaks that only the most intense carbon peak (δ+δ+ at 29.98 ppm) gives rise to detectable decoupler sidebands at the sensitivity levels achieved in this study.

^{13}C relaxation times. Table 3-10 shows the 126 MHz ^{13}C T_1 and T_2 values measured for samples H and L at 125 °C; the uncertainties shown equal ± 2 standard deviations, equivalent to 90 % confidence limits. These values were obtained using the Varian *T1* and *T2* routines, which analyzes peak heights from inversion recovery (*3-26*) and Carr-Purcell-Meiboom-Gill (*3-35*) experimental data sets, respectively. This involves a non-linear least squares fit of peak heights to the following equations:

$$I_z = I_0 [\, 1 - 2 \exp(-\tau / T_1) \,] \text{ , and} \qquad (50)$$

$$I_z = I_0 \exp(-\tau / T_2) \text{ .} \qquad (51)$$

The best-fit T_1 and T_2 values were determined, along with standard error estimates.

The T_1 values were needed in order to obtain quantitatively significant ^{13}C integrals, since for full 90° ^{13}C excitation pulses, one needs to wait at least five T_1's between ^{13}C pulses. (*3-26*) Table 3-10 shows that the ^{13}C T_1 values measured are as small as 0.75 s for regions C2a and F. The C2a region contains αγ methylenes from HEHH and EHEH, αδ+ methylenes from EEHH and $4B_4$ methylenes from EHH, while the F region is a ββ methylene carbon in the HEH triad. In general, the smallest T_1

values are for methylene carbons that are α or β to a branch point (a methine carbon). Presumably, methylenes close to branch points may have more restricted motions than isolated methylenes (such as δ+δ+), which can undergo a "crankshaft"-type motion. (*3-17*)

The largest T_1 values belong to the n-butyl side chains resulting from the incorporation of 1-hexene into the copolymer. Except for the methylene groups closest to the branch point ($4B_4$), the T_1 values of the branch carbons are greater than 2 seconds. The largest T_1 is for the methyl carbon ($1B_4$; region H); these largest ^{13}C T_1 values may reflect more rapid (and more isotropic) motion for branch carbons than for backbone carbons.

Table 3-10 also shows the corresponding ^{13}C T_1 values for sample L. In all cases for which there is a significant difference between the samples, the T_1 values for sample L are larger than the values for the corresponding sites in sample H, although the two samples were prepared and analyzed as similarly as possible. (We note that the differences in the T_1 values for the two samples are not significant for some of the weakest carbon peaks, such as regions A, C1 and F.) Assuming that the greater the correlation time for the molecular motion, the larger the T_1 values (*i.e.*, correlation times are larger than ω_O^{-1}), then copolymer L appears to have slower molecular motion, although (or perhaps, since) it contains less 1-hexene and fewer butyl side chains.

Additionally, Table 3-10 indicates that the ^{13}C T_1 (also know as T_1^C) values are, except for cases of large experimental uncertainties, slightly smaller at 126 MHz than at 101 MHz (corresponding to 500 and 400 MHz ^1H frequencies, respectively). These differences are close to being within the observed confidence limits of the T_1^C

measurements. In terms of well known relationships (*3-27*) between relevant spectral densities and molecular reorientation correlation time (τ_C), as represented in Figure 3-11A, these small (or zero) T_1^C differences imply, at least qualitatively, that the relevant correlation time is much smaller than the inverse of the Larmor frequency, ω_o^{-1}, i.e., τ_C is smaller than $(101\ MHz)^{-1}$ and $(126\ MHz)^{-1}$. This situation is commonly known as the "extreme narrowing" condition (*3-4*). However, comparison of ^{13}C T_1 and T_2 values in Table 3-10 shows that $T_2^C << T_1^C$, a situation that is commonly understood as manifesting the condition $\tau_C >> \omega_o^{-1}$, as represented in Figure 3-11B.

^{13}C T_2 values for sample H are also shown in Table 3-10. These were determined in order to compare the "natural" ^{13}C linewidths to those observed in the spectrum. The former are the inherent linewidths of a single carbon signal (as determined by T_2^C), while the observed linewidths may be the result of chemical shift dispersion (the extreme overlap of individual ^{13}C signals due to slightly different structural environments) and static magnetic field inhomogeneities. Table 3-10 compares the observed full-width at half-height (FWHH) values obtained from the spectrum of sample H to the natural linewidths calculated from the measured T_2^C values. For most peak regions listed in Table 3-10, the predicted linewidths are significantly smaller than the experimentally observed linewidths, indicating that the largest linewidth contributions arise from isotropic chemical shift dispersion.

The T_1^C and T_2^C behavior mentioned above can be reconciled, as has been done previously for various organic polymers (*3-25,30*) by recognizing the dependence of T_1 and T_2 on various spectral density terms, $J(\omega)$, that describe the relevant molecular dynamics (*3-30*). In large polymer molecules, T_2^C is dominated by a zero-frequency term,

J(0), for the dipole-dipole interaction between ^{13}C and directly attached (or nearby) protons. This J(0) term is large because it depends on the *overall* reorientation of the main polymer chain, which is very slow. Since there is no contribution of a J(0) term to $(T_1^C)^{-1}$, spin-lattice relaxation is much slower (than spin-spin relaxation) and is dominated by much faster motions that do not involve the reorientation of the entire polymer molecule, and which have much smaller correlation times, i.e., $\tau_C < \omega_o^{-1}$. Of course, this simple, qualitative interpretation should be qualified by realization that a) the motions involved may not be isotropic, b) there is likely to be a distribution of correlation times, and c) relaxation other than that due to the dipolar mechanism may contribute, especially to T_1^C. (*3-30*)

nOe Enhancements. The nuclear Overhauser enhancement (nOe) effect (*3-35*) is a key concern whenever liquid-state ^{13}C NMR is performed in a mode aimed at quantitation. Proton decoupling can cause saturation of the proton spins coupled to ^{13}C, resulting in enhanced carbon signals. Saturation of proton resonances is the equalization of proton spin-up and spin-down populations. The resulting ^{13}C resonances may be as much as 2.99 times larger than the intensities obtained without nOe (*i.e.*, without saturation of the proton resonances). If the nOe ratio is identical for all carbon-13 nuclei in the sample, the peak integrals obtained are all scaled by the same factor, and no corrections need to be applied in order to do a quantitative triad analysis. If the nOe ratios are different for different carbons, they must be determined so that the appropriate factors can be applied.

The experimental conditions chosen can affect whether, or the extent to which, nOe enhancement of ^{13}C signals occurs. If the decoupling is continuously applied

(whether CW or a composite sequence such as WALTZ-16), saturation of the proton spins can occur very quickly, and ^{13}C signals may be enhanced thereafter. If one wishes to detect carbon resonances without nOe enhancement, a technique known as gated decoupling may be used. (*3-26*) In this case, the decoupler is turned off except during data acquisition. On the time scale involved here, ^{13}C / ^{1}H decoupling occurs almost immediately when the decoupler is turned on, whereas saturation of the proton spins is not instantaneous. In general, for ^{13}C / ^{1}H spin pairs in compounds such as the copolymers examined here, it may take several seconds for the nOe to build to its steady-state value, because of the $^{13}C/^{1}H$ relaxation mechanisms involved. By turning the decoupler on only during data acquisition (off during the long relaxation delay time after data acquisition), ^{13}C signals are acquired without nOe enhancement. By comparing the signal intensities with and without gated decoupling, nOe factors can be measured.

Not all systems give the full nOe enhancement possible. The nOe effect operates *via* ^{1}H-^{13}C (usually dipolar) coupling; maximum ^{13}C nOe values are obtained when the heteronuclear dipolar interaction with protons is the dominant relaxation mechanism of the observed carbons. Alternate ^{13}C relaxation mechanisms, such as chemical shift anisotropy, ^{1}H-^{13}C scalar coupling, or dipolar interactions with the unpaired electrons of a paramagnetic impurity, can compete with proton-mediated dipolar ^{13}C relaxation, and lead to less than full nOe enhancement. The amount of enhancement achieved also depends on the details of molecular motion, and on the degree of proton saturation.

The nOe ratio, f, as used here is defined as the ratio of ^{13}C signal integrals with (I_z) and without (I_0) nuclear Overhauser enhancement:

$$f = I_z / I_0 = \eta + 1 \quad , \text{or} \tag{52}$$

$$\eta = (I_z - I_0) / I_0 . \qquad (53)$$

The symbol η is called the nuclear Overhauser enhancement factor.

This enhancement arises because of the redistribution of ^{13}C spin populations during continuous saturation of the proton spins. (*3-35*) For simplicity, let us consider a spin system consisting of a single ^{13}C and ^{1}H, as shown in Figure 3-11. W_0, W_{1H}, W_{1C}, and W_2 are the relaxation transition probabilities for the labeled transitions. W_{1H} refers to single quantum transition (due to a ^{13}C - ^{1}H interaction) and involves the flip of a proton spin while the ^{13}C spin state remains unchanged. The double quantum transition labeled by W_2 corresponds to the simultaneous flip of the proton and carbon spins, where both flip in the same sense (both to spin-up or both to spin-down). W_0 also involves simultaneous flips of both spins, but in an opposite sense; this is the zero-quantum transition. Finally, W_{1C} is a single-quantum transition in which only the ^{13}C spin state changes.

Figure 3-11 also shows the excess populations (from a Boltzmann distribution) of the ^{13}C / ^{1}H spin system (which may include the condition of proton irradiation), in terms of the quantities a and b, where

$$2\,a = P_z^C - P_0^C \qquad \text{and} \qquad 2\,b = P_z^H - P_0^H . \qquad (54)$$

P_z^C is the ^{13}C spin population excess during proton irradiation, P_0^C is the equilibrium (*i.e.*, Boltzmann) ^{13}C spin population excess, etc. When the proton spins are saturated, the spin-state populations connected by the W_{1H} transitions have equal populations. Spin lattice relaxation causes a flux of spins in a direction that will attempt to return the spin system back to the Boltzmann population distribution. After a few seconds of continuous

proton saturation, a steady-state condition is reached. The rate equations for the change in the ^{13}C spin populations may be solved for such a steady-state proton saturation, giving

$$- a / b = (W_2 - W_0) / (2W_{1C} + W_2 + W_0) \quad \text{and} \tag{55}$$

$$\eta = (P_z^C - P_0^C) / P_0^C = (\gamma_H / \gamma_C) (W_2 - W_0) / (2W_{1C} + W_2 + W_0) . \tag{56}$$

Note that W_{1H} does not appear explicitly in equations (55) and (56), as single-quantum proton transitions do not affect the ^{13}C spin population differences.

The details of the molecular motions (including spectral densities at the sum and difference of the proton and ^{13}C resonance frequencies) determine the relative values of W_{1C}, W_2 and W_0, and thus determine the amount of nOe experienced by a ^{13}C nucleus during proton saturation. (*3-35*) If double quantum transitions occur more frequently than the zero-quantum transitions, *i.e.*, $W_2 > W_0$ (as is the case for the modulation of the ^1H - ^{13}C dipolar interaction by rapid isotropic motion), then the nuclear Overhauser effect leads to positive ^{13}C signal enhancements. If $W_2 < W_0$ (common for many macromolecules with very slow atomic-level motions), then the ^{13}C spin population difference is reduced as compared to the case of no proton saturation, and ^{13}C signal intensities are reduced by the nuclear Overhauser effect. (*3-35*) As the ^{13}C NMR signals observed for the copolymers in the study reported here exhibit positive nOe values (see, for example, Table 3-11), we conclude that atomic-level motion in the copolymer samples is sufficiently rapid (and isotropic) that positive nOe enhancements are generated.

If the single quantum ^{13}C relaxation mechanism is entirely due to ^1H - ^{13}C dipolar interactions in the condition of fast isotropic motion, then relative values of W_2, W_{1C} and W_0 are 12 to 3 to 2. The expression for the nuclear Overhauser ratio then becomes

$$f = 1 + \eta = 1 + \tfrac{1}{2}(\gamma_H / \gamma_C) = 2.99\,, \qquad (57)$$

where γ_H and γ_C are the magnetogyric ratios for ^{13}C and ^{1}H. This nOe value of 2.99 has been shown (*3-27*) to be the maximum possible enhancement for ^{13}C during proton saturation, even if several protons are coupled (*via* the dipolar interaction) to the observed carbon.

Schaefer and Natusch (*3-25*) developed an expression for η, the nOe enhancement factor, for the case of incomplete saturation of the proton spins, and the presence of ^{13}C relaxation mechanisms other than via the dipolar interaction with protons:

$$\eta = \rho_{CH}\, S_H\, (\gamma_H / \gamma_C)\, (T_{1,C}^{tot} / T_{1,C}^{CH}) \qquad (58)$$

where ρ_{CH} is a factor dependent on molecular motion, S_H is the degree of proton saturation ($S_H = 1$ corresponds to full saturation), $T_{1,C}^{tot}$ is the overall ^{13}C spin-lattice relaxation time constant, and $T_{1,C}^{CH}$ is the ^{13}C T_1 value for relaxation due to dipolar coupling of carbon to protons. $T_{1,C}^{tot}$ can be expressed in terms of contributions from $T_{1,C}^{CH}$ and $T_{1,C}^{other}$, the time constant for other ^{13}C spin-lattice relaxation mechanisms:

$$(T_{1,C}^{tot})^{-1} = (T_{1,C}^{CH})^{-1} + (T_{1,C}^{other})^{-1}\,. \qquad (59)$$

Schaefer and Natusch also provide an expression for S_H, the degree of proton saturation,

$$S_H = 1 - [\,1 + (\gamma_H B_2)^2\, T_1^H\, T_2^H\,]^{-1}\,, \qquad (60)$$

where B_2 is the field strength of the decoupler irradiation, while T_1^H and T_2^H are the proton spin-lattice and spin-spin relaxation time constants.

If $(\gamma_H B_2)^2$ is large compared to the inverse of $T_1^H\, T_2^H$, the value of S_H will be very close to 1, corresponding to full proton saturation. This is indeed the situation in the study reported here, since $\gamma_H H_2 = 2500$ Hz, leading to values of S_H of greater than 0.99997 (Table 3-9 lists the measured T_1^H and T_2^H values obtained for sample H). Note

that the effective decoupler field strength is somewhat reduced for methyl and methine protons, since their ^1H resonances are slightly offset (less than 1 ppm) from the decoupler frequency, which was set at the methylene peak maximum (1.25 ppm). These frequency offsets are sufficiently small compared to $\gamma_H H_2$ that $H_2^{eff} \cong H_2$, and we conclude that saturation is complete ($S_H \cong 1$) for all the copolymer protons. This conclusion is also valid when composite pulse decoupling sequences such as WALTZ-16 are used, as they exhibit a smaller frequency-offset dependence of the decoupler field strength (H_2^{eff}) than does CW decoupling.

Complete proton saturation does not necessarily imply that the proton spins are completely decoupled from carbon. As noted above, the term saturation is defined as equal populations of spin-up and spin-down protons. Complete decoupling occurs when the ^{13}C magnetization evolves during the data acquisition period in a manner independent of the spin state of any protons, *i.e.*, no splitting or broadening of the carbon signals due to protons. In this study, incomplete decoupling of methyl (and some methylene) carbons is observed, though complete saturation is achieved, as discussed above.

As stated above, ρ_{CH} is the factor that depends on the details of molecular motion:

$$\rho_{CH} = [-f(\omega_H - \omega_C) + 6\, f(\omega_H + \omega_C)] / [-f(\omega_H - \omega_C) + 3\, f(\omega_C) + 6\, f(\omega_H + \omega_C)] \quad (61)$$

where $f(\omega) = \tau_{CH} (1 + \omega^2 \tau_{CH}^2)^{-1}$, τ_{CH} is the single rotational correlation time for the ^1H - ^{13}C coupling, and ω_H and ω_C are the resonance frequencies for protons and ^{13}C. In the limit of rapid isotropic molecular tumbling, known as the extreme narrowing condition, $\omega_C \tau_{CH} << 1$ and ρ_{CH} equals ½. This is the situation usually encountered in liquid-state NMR of small molecules. (*3-25*) In the case of large polymer molecules, however, details of the molecular motions (including spectral densities) must be known to calculate

a value for ρ_{CH}. Restricted motions can reduce this factor to values less than 0.5, leading to nOe ratios below the maximum value of 2.99. No attempt was made in this study to investigate the details of molecular motion, and thus quantitatively *predict* ρ_{CH}.

The presence of paramagnetic impurities can provide a very efficient alternate relaxation mechanism, and then $T_{1,C}^{tot} / T_{1,C}^{CH}$ would be much less than unity, leading to reduced nOe factors. Furthermore, paramagnetic impurities can interfere with proton saturation by reducing T_1^H and T_2^H. No attempt was made to measure the paramagnetic content of the copolymer samples in this study, nor remove paramagnetic oxygen gas dissolved in the sample (not thought to be significant at 125 °C). Since the ^{13}C and proton T_1 values measured are fairly long, ranging from about 0.5 to 8 s, paramagnetic impurities are not thought to play a major role in determining the nOe factor.

When nOe factors were measured, the data were acquired in blocks of roughly one or two hours apiece, interleaving continuous decoupling with gated decoupling (i.e., with and without nOe), although nOe values obtained without interleaving did not differ significantly from those obtained with interleaving.

The nOe values obtained from high signal-to-noise 126 MHz ^{13}C spectra of sample L are shown in Table 3-11. The nOe measurements were made over several months using the same spectrometer and probe, and with, as much as possible, identical experimental conditions. Each experiment was typically run for a 24 to 48 hour period, every few weeks. In the interim, the spectrometer configuration was changed as needed by other users. Efforts were made to reproduce, as exactly as possible, the spectrometer setup each time. The power levels and probe tuning (and thus the 90^o ^{13}C and decoupler pulse lengths) were consistent the entire time, and the variable temperature operating

conditions were reproduced as much as possible (e.g., VT air and probe body flow rates). Care was taken that the decoupler frequency was set for the very large δ+δ+ methylene proton peak (1.25 ppm) to be exactly on resonance for the majority of protons in the copolymer sample.

In Table 3-12 we can see that the measured nOe ratios for sample L varied over time, measured over a period spanning about two and a half months. For all but the smallest peaks (e.g., regions A and F), the week-to-week variation of the values is greater than expected by random error, as indicated by the confidence limits shown. During continuous operation of the spectrometer over as much as a five day period, variations in the nOe ratios were minimal (insignificantly small compared to the estimated confidence limits). The significantly larger variations shown in Table 3-12 occurred over a larger timescale, and involved reconfiguration of the spectrometer.

Several months into this project, the Varian 10 mm probe used in this study started to show symptoms of 'crosstalk'. Specifically, the decoupler signal started producing a very noticeable interference in the lock and observe channels. When the decoupler was on, the ^{13}C signal intensity was significantly attenuated and the lock signal intensity also diminished. Within hours, the interference was so great that the spectrometer was unable to lock on the deuterium signal of the solvent, and the ^{13}C signal became unobservable amid 'crosstalk' noise from the decoupler! Repairs and modifications then made to the probe by Varian eliminated any signs of decoupler 'crosstalk'.

It was theorized that perhaps this 'crosstalk' occurred to a lesser degree during the early nOe measurements, which could affect the values obtained in Table 3-12. A small

amount of interference from the decoupler could result in somewhat diminished ^{13}C intensities, especially during the 'with-nOe' data blocks. The decoupler is active during the acquisition time in both the 'with-nOe' and 'without-nOe' (i.e., gated decoupling) portions of an nOe experiment, but off during the relaxation delay in the 'without-nOe' blocks. The 'crosstalk' interference observed was qualitatively different whether the decoupler was on continuously or not.

After the probe was repaired, the significant variations in the observed nOe ratios continued from week-to-week, but again not during continuous operation over several days. Hence, it appears that the 'crosstalk' interference affected only some of the data collected, especially during the period in which the problem was obviously present. The nOe experiments done well before the advent of the 'crosstalk' problem, and certainly those obtained after the repair, appear to be reliable.

The significant variations in nOe ratios observed in Table 3-12 are not due to unintentional variations in the choice and adjustment of integrals. In addition to nOe ratios obtained using 'manual' integrals, nOe ratios were also determined using peak heights and 'machine' integrals. For each peak, the values obtained by the three methods were very similar, with variations much less than the uncertainties in the values. In Table 3-11, only 'manual' integral nOe values are shown, as these values have smaller standard deviations during repeated nOe experiments than do intensities from peak heights or 'machine' integrals.

The variations observed in the nOe values in Table 3-12 are more likely due to unintentional variations in the VT (variable temperature) performance. Although attempts were made to reproduce the same VT setup as much as possible, it is possible

that the temperature variations across the sample may have been significantly different week-to-week. Since ρ_{CH} in Equation (58) above depends on the details of molecular motion, differences in the temperature profile across the sample can affect the overall value of ρ_{CH} throughout the sample, and thus may lead to variations in the observed nOe ratios.

Researchers in other laboratories have apparently observed slow changes in poly(ethylene-co-1-hexene) samples when dissolved in chlorinated aromatic solvents at the elevated temperatures such as used in this study; significant decreases in viscosity have been reported, suggesting the scission of long polymer chains at these temperatures. (*3-38*) If polymer chains are indeed breaking at 125 °C in the samples analyzed in this study, one might expect significant changes in the atomic-level motions experienced by the spins, and thus potentially significant changes in the observed nuclear Overhauser enhancements. There are no clear trends in the observed nOe values, however, that would indicate that polymer chain-breaking is the dominant cause for the nOe variations. Long spectrometer runs (as long as five days) showed little variation in the nOe values, whereas time-separated shorter runs (involving instrument reconfiguration prior to data acquisition) tended to have larger nOe value variations. This suggests that experimental variations were responsible for the largest part of the observed nOe variations (in spite of attempts to maintain experimental consistency), though thermally-induced sample changes cannot be eliminated as a contributing factor.

The importance of using accurate and precise nOe values should not be minimized. If one chooses to take advantage of the much greater sensitivity during nOe enhancement, quantitative analysis requires that nOe ratios be well known. In fact, as we

shall see later, the uncertainty in nOe ratio values is the largest source of random error in the subsequent triad mole fraction determinations.

What then are the 'correct' nOe ratio values for samples H and L? Clearly, for the spectrometer and probe used in this study, the best approach involves measuring nOe ratios just prior to (or immediately after) acquisition of the high-sensitivity spectrum being quantitatively analyzed. Under the experimental conditions used in this research, the nOe values should be considered experimental parameters, not NMR constants.

By interleaving data acquisition with and without nOe enhancement, the applicable nOe factors can be obtained during the acquisition of the high-sensitivity nOe-enhanced spectra. Note, however, that if we determine nOe factors from the ratio of the enhanced and un-enhanced integrals, and then use these factors to divide the enhanced integrals in order to correct for variable enhancement effects, the results are merely the un-enhanced integral values! The advantage of higher signal-to-noise in the nOe-enhanced spectra is lost; in fact, we would be essentially ignoring all the enhanced data completely and thus all the time spent signal averaging during nOe enhancement would be wasted (aside from having determined nOe factors, which might otherwise be useful in their own right).

Using nOe factors determined during only a single run of interleaved experiments (with and without nOe enhancement) can provide accurate nOe factors for that particular sample and experimental setup, but is clearly inefficient if all we seek are quantitatively accurate integrals. If we are not interested in measuring the observed nOe factors, it would be more efficient to use the available spectrometer time only to signal average in the absence of nOe enhancement. If however, reproducible nOe factors are obtained for a

sample after several interleaved experimental runs, use of the mean nOe factor as the 'correct' value when determining accurate integrals may be appropriate in subsequent analyses. The uncertainty in the integral values will then be determined by the uncertainty in the mean nOe values, which are obtained from several different (but experimentally-similar) runs. This approach is equivalent to obtaining the nOe factors that would result when summing all the blocks of data obtained without enhancement in all the experimental runs, and likewise summing all the with-enhancement blocks, and calculating the resulting ratio for every spectral region. Averaging the nOe factors obtained from different (but consistent) experimental runs is a simpler procedure than summing spectra obtained on different days for different runs.

Keeping the above considerations in mind, Table 3-11 lists typical nOe values determined in this study for samples H and L, where 'typical' refers to representative values routinely obtained for each ^{13}C spectral region when all appropriate measures are taken to maximize reproducibility, as discussed above. These typical nOe factors were reproducible only to within about $\pm$ 0.2 ($\pm$ 0.1 for the most intense peaks, and $> \pm$ 0.2 for the smallest peaks), and appear to be often significantly smaller than nOe factors reported in the literature for similar polymer structures (*3-37*). For example, Hansen *et al.* (*3-37*) reported an observed nOe factor of 2.67 for the large δ+δ+ peak (region D2, 29.98 ppm) in a low-density polyethylene sample containing butyl side chains (in addition to ethyl and hexyl branches), as compared to the nOe factors of 2.43 and 2.59 determined here for samples H and L, respectively. Dissolved oxygen may be responsible in part for the differences, as samples H and L were not intentionally degassed, whereas Hansen *et al.* purged their sample with nitrogen gas before analysis. It should be noted, however, that

Hansen *et al.* do report most nOe factors determined are significantly below the theoretical maximum of 2.99, as is also seen in the study reported here (Table 3-11). Randall (*3-38*) reports that, in his experience, poly(ethylene-*co*-1-hexene) polymers with less than 5 mol % 1-hexene incorporation can be analyzed quantitatively assuming the nOe factors are all equal (and can thus be neglected). The sample L results in Table 3-11 would seem to contradict this conclusion, at least for the samples and experimental setup used in this study.

Chain Ends and Head-to-Head, Head-to-Tail, and Tail-to-Tail Linkages. Figure 3-12 shows the 126 MHz ^{13}C NMR spectrum obtained for sample L (with CW decoupling and nOe enhancement), which can be compared to the corresponding spectrum for sample H shown in Figure 3-5. Considering the chain-end group assignments made by Hsieh and Randall (*3-9*) shown in Table 3-4, both samples H and L contain easily-detected saturated end-groups, as indicated by the 3s and 2s peaks at 32.2 and 22.9 ppm, respectively (the 1s peak overlaps with the $1B_4$ peak, the methyl at the end of each butyl branch). No peaks were observed for the 2v and 1v carbons (139.5 and 114.3 ppm, respectively) of an unsaturated (vinylic) chain end; the corresponding allylic carbon peak (labeled "a" in Table 3-4) at 33.9 ppm, if present, would be obscured by the $4B_4$ peak at 34.1 ppm. Assuming the chain-end groups are all saturated, the number-average molecular weight is determined (by ^{13}C NMR) to be 5.1×10^4 g/mol for sample H, and 3.0×10^4 g/mol for sample L. On average, the polymer chains in sample H contain 1565 ethylene monomer units and 88 1-hexene monomer units, while polymer chains in sample L (on average) contain 964 ethylene monomer units and 36 1-hexene monomer units, as determined by ^{13}C NMR results in the study reported here.

One issue raised earlier is the possibility of head-to-head or tail-to-tail polymerization of 1-hexene monomers, as shown in Figure 3-1. Randall and other authors (*3-9*) report no signs of such linkages between consecutive 1-hexene monomers. Use of the Lindemann and Adams method (*3-13*) predicts ^{13}C chemical shifts of 37.05 ppm and 39.52 ppm for the methine carbons of the head-to-head and tail-to-tail cases, respectively. Examination of Figures 3-5 and 3-12 indicates that very small amounts of these linkages *might* be present in both samples L and H, as there appear to be very small peaks at 37.5 ppm and 39.6 ppm that are barely discernable above the noise in these high sensitivity spectra. The $4B_4$ carbon in the tail-to-tail linkage may also be resolvable, with a chemical shift of 31.78 ppm, as predicted by the Lindemann and Adams method; there is a very small peak at 31.5 ppm in both Figures 3-5 and 3-12 which *may* be due to this carbon site. In any case, if head-to-head or tail-to-tail linkages exist in these samples, they represent less than 1 % of HH diads. A more precise value cannot be determined, as these very small peaks are very difficult to integrate meaningfully.

Comparison of integration methods and triad expressions. Table 3-13 shows two published methods for determining triad mole fractions from experimental collective assignment region integrals, along with two other approaches developed as part of this study: Seger (2000) and Solver (2000). These methods are applied to integral data in Tables 3-14 and 3-15, which show the resultant triad mole fractions determined for sample H using three different methods of integration ("machine", "manual" and "deconvolution" integrals, as discussed above). The Hsieh and Randall (1982) triad method (*3-9*) is shown in Equations (23) through (28), the Randall (1989) method is given in reference *3-5*, and the Seger (2000) method is the same as the Randall (1989)

method, except that [HHH] was determined using the expression k[HHH] = A1 + ½ A2. Also included in Tables 3-14 and 3-15 are 90 % confidence limits determined from multiple repetitive analyses. Analysis of these uncertainties indicates that the reproducibility is significantly better using deconvolution-derived integrals than those obtained by either the "machine" or "manual" integration methods. Similarly, the Seger (2000) triad method has better reproducibility than either the Hsieh and Randall (1982) or Randall (1989) triad methods.

In Table 3-15, a fourth triad method was utilized, the Solver (2000) method. This method uses the *Solver* subroutine of Microsoft Excel to determine the best least-squares fit of the "deconvolution" integral data to the region assignment relationships (as shown in Equations (13) through (22), requiring that the (model-independent) necessary relationship, [EEH] + 2 [HEH] = [EHH] + 2 [EHE], be maintained. The Solver (2000) linear regression method appears to be superior, as far as reproducibility, to the other triad methods shown which all involve analytical formulae to determine triad mole fractions. The Solver (2000) method may be expected to be less affected by systematic errors than the other methods, as *all* the spectral integral information is used simultaneously. A similar conclusion was reached by Chen (*3-39*) who used a simplex routine to determine the best triad mole fraction values in ethylene/propylene copolymers.

One conspicuous problem with the results from the Hsieh and Randall (1982) method shown in Table 3-15 is the negative value determined for [HHH], a clearly unrealistic result. It is not clear why this method gives an [HHH] value significantly below zero, but negative [HHH] values were obtained in almost every instance in which

the Hsieh and Randall (1982) method was utilized in this study. Systematic errors appear to be involved, but have not been identified.

Table 3-16 explores some of the possible methods for determining [HHH] from integral data. The algebraically over-determined system involved here (as discussed in the Introduction) allows for many possible expressions for [HHH]; Table 3-16 includes only *most* of the simpler possible [HHH] expressions, as the cumulative uncertainty increases as more terms are included in the expression for [HHH]. Note that [HHH] is more susceptible to random error than the other triad mole fractions, owing to the low level of 1-hexene incorporation in samples H and L, which results in very small [HHH] values. Table 3-16 shows that several of the expressions for [HHH] lead to negative values, though these are sometimes not significantly non-zero. Careful evaluation of uncertainties (as discussed above) reveals that the Solver method provides the most reproducible [HHH] values. However, in Table 3-16 the value determined for [HHH] is smaller for sample H than for sample L, although sample H has greater 1-hexene incorporation. When taking the estimated ± 0.02 mol % uncertainty into account, both [HHH] values are not significantly non-zero. We know from Figures 3-5 and 3-12 that the αα(EHHH) carbon peak is clearly present at 40.9 ppm in the ^{13}C NMR spectra of both samples, so polymers H and L must contain some HHH triads, in spite of the fact that we cannot quantify the HHH mole fraction meaningfully even in the highest sensitivity spectra obtained.

Mole fractions and 1-hexene incorporation in samples H and L. Table 3-17 shows triad mole fractions obtained for samples H and L, from ^{13}C spectra acquired with gated CW decoupling (*i.e.*, without nOe enhancement), integrated by the "deconvolution"

method, and analyzed using the published Hsieh and Randall (1982), Randall (1989) and Solver (2000) triad methods. Note that Table 3-17 is based on spectra obtained *without* Overhauser enhancement (nOe), whereas Tables 3-14 through 3-16 utilize earlier spectra obtained with nOe; due to the variations in nOe encountered in this study (as seen in Table 3-12), it was decided to obtain high signal-to-noise spectra absent Overhauser enhancement. Based on the reproducibility considerations mentioned above, the Solver (2000) values are thought to be most reliable. Summing the Solver (2000) values for [EHE], [EHH] and [HHH] gives a value of 5.32 mol % for [H]; in other words, 1-hexene is incorporated into the copolymer at a level of 5.32 mol %. The corresponding value for sample L is 3.62 mol %. Use of the Hsieh and Randall (1982) triad method indicates [H] = 5.35 mol % for sample H and 3.84 mol % for sample L; similarly, the Randall (1982) triad method gives values of 5.17 mol % and 3.56 mol % for samples H and L, respectively. Thus, the choice of triad method can affect the [H] value obtained experimentally for a copolymer, especially when the 1-hexene incorporation level is low.

Comparison of Sequence Distribution Parameters for Samples H and L.

Table 3-18 shows the values determined for various sequence distribution parameters for samples H and L, based on the Solver (2000) triad mole fractions given in Table 3-17, and the parameter definitions given in the Introduction. Also included in Table 3-18 are the values of the sequence distribution parameters expected on the basis of either Bernoullian or first-order kinetic Markov models. Note that, by all parameters except the H-based omega value, sample H appears to follow Bernoullian statistics very closely. The deviation of the H-based omega value from unity is not significant, since this parameter is extremely sensitive to random errors in the integral values, as discussed in the

Introduction. Sample L, on the other hand, shows greater deviations from the parameter values that are expected on the basis of Bernoullian or first-order Markov statistics.

The large deviation from unity in the average reactivity ratio ($<r_1r_2>$) for sample L in Table 3-18 suggests that polymer L *may* be the result of multiple-site catalysis, in contrast to polymer H which appears to result from single-site Bernoullian catalysis. (*3-40,41*) It should be noted that, while other mechanistic models may be capable of rationalizing the deviation from unity in the average reactivity ratio for sample L, it is still worthwhile to examine whether a simple two-site Bernoullian model fits well to the experimental triad mole fractions.

Tables 3-19 and 3-20 compare the best fits (using *Solver*) of one-site and two-site Bernoullian models to the experimental triad values for samples H and L. For sample L, there is a fairly good fit of a two-site Bernoullian model to the experimentally-determined triad mole fractions. This two-site Bernoullian model catalyst system would produce a mixture of polymer chains: site A produces a Bernoullian ethylene/1-hexene copolymer with 6.4 mol % 1-hexene content and contributes 57 % of sample L (i.e., 57 % of the monomer units in sample L), while site B appears to polymerize only ethylene and contributes 43 % of sample L. The two-site Bernoullian model reproduces the experimentally-determined triads for sample L with a residual-sum-of-squares that is three times smaller than that of the one-site Bernoullian model, a statistically meaningful improvement, even in view of the additional statistical degrees of freedom in the two-site model. (*3-4*) Examination of the residuals shown in Table 3-20 indicates, however, that the quality of fit to the E-centered triad mole fractions is substantially poorer than the quality of fit to the H-centered triad mole fractions. This suggests that more complex

mechanistic models (such as a two-site first-order Markovian model, or a three-site Bernoullian model) may provide a significantly better fit, and thus a more realistic model of polymerization kinetics.

A similar comparison for sample H shows no statistically significant improvement in the quality of fit (only 24% reduction in the triad residual-sum-of-squares) when a two-site Bernoullian model is used instead of the one-site model; the latter provides an excellent fit to the experimental data. Thus we may conclude that sample H is well modeled as resulting from a simple, single-site Bernoullian catalyst system. Several other poly(ethylene-*co*-1-alkene) copolymers have been shown (*3-40,41*) to result from single-site or multisite catalysis models, depending on the catalyst system used to prepare the copolymer.

If the catalyst system used to polymerize samples H and L were identified, more appropriate catalytic models could be fit to the experimental triad distribution, especially if the mechanism and kinetics of polymerization have been previously investigated and reported in the literature. In the absence of knowledge about the catalyst, it is difficult to determine whether a given kinetic-model prediction of the sequence distribution is chemically reasonable, even if it provides a good fit to the experimental triad distribution.

Possible Future Work.

Further possibilities exist, beyond what is reported in this study, for the quantitative description of sequence distributions in poly(ethylene-*co*-1-hexene) copolymers, especially in the area of modeling the comparison of single-site and multi-site catalyst systems, as is also being explored by Randall and others (*3-40,41*). The development of additional sequence distribution parameters, especially any that may help

distinguish multi-site Markovian catalysis from non-Markovian single-site catalyst systems, might be of value in the NMR analysis of poly(ethylene-*co*-1-hexene) copolymers.

Opportunities also exist for the extension of the study reported here to terpolymer systems, such as poly(ethylene-*co*-1-butene-*co*-1-hexene), another commercially available form of LLDPE (linear low-density polyethylene). Table 3-21 lists the necessary relationships (to the triad-triad level) of the ABC terpolymer system, as determined in this study by comparison to (and extension of) the necessary relationships that were published for AB copolymers (*3-4*), and shown in Table 3-2.

Recently, a new approach to the elimination of decoupler sidebands has been described in the literature. (*3-42*) Named DESIRE (for DEcoupler SIdeband REsolved spectroscopy), this approach is based on a two-dimensional experiment in which the ^{13}C magnetization that leads to decoupler sidebands (during proton decoupling) is frequency encoded during a pre-acquisition evolution period. When Fourier transformed, the decoupler sidebands are dispersed along the indirectly-detected frequency axis, F_1, whereas the centerbands (which are not frequency-modulated during the variable evolution period) appear at $F_1 = 0$. DESIRE has been shown to be very effective for the reduction of decoupling sidebands in ^{13}C-decoupled ^{1}H NMR spectroscopy of liquid samples. A one-dimensional version of DESIRE (*3-42*) appears to be well suited for the reduction of decoupler sidebands in ^{1}H-decoupled ^{13}C NMR spectroscopy of dissolved copolymer samples, potentially providing some narrower ^{13}C lines than did the CW decoupling used in the study reported here.

CONCLUSIONS

Two samples of poly(ethylene-*co*-1-hexene), designated samples H and L, were found to contain 5.3 mol % and 3.6 mol % 1-hexene incorporation, respectively. Integrals obtained by spectral deconvolution were found to provide more reproducible results than by either "machine" or "manual" integration methods. The accurate determination of nOe factors can be problematic, but sufficient sensitivity can be obtained with such copolymer samples that un-enhanced (non-nOe) integrals can be used. Triad mole fractions were determined most reproducibly (and presumably most accurately) using a least-squares Microsoft Excel *Solver* linear regression. Polymer H is well described as a simple Bernoullian triad distribution, and thus Polymer H appears to result from a single-site Bernoullian catalyst system.

On the basis of a value of the average reactivity ratio of 1.87, polymer L does not appear to follow very closely either Bernoullian or first-order Markov statistics for a single-site catalyst; hence polymer L may have been produced by a multiple-site catalyst system. The experimentally-determined triad mole fractions and $\langle r_1 r_2 \rangle$ value determined for sample L fit fairly well to a two-site Bernoullian catalyst model, producing a mixture of polymer chains: site A produces a Bernoullian ethylene/1-hexene copolymer with 6.4 mol % 1-hexene content, and contributes 57 % of polymer L, while site B appears to polymerize only ethylene and contributes 43 % of polymer L. Significant residuals in the E-centered triad mole fractions for the best fit of a two-site Bernoullian catalyst model for sample L suggest that more complex mechanistic models may be more appropriate.

Chapter 3 Literature References:

(3-1) Maeder, D.; Heinemann, J.; Walter P.; Muelhaupt, R. *Macromolecules*, **2000**, *33*, 1254-1261.

(3-2) Moerhring, V.; Fink, G. *Angew. Chem.*, **1985**, *97*, 982.

(3-3) Jurkiewicz, A.; Eilerts, N. W.; Hsieh, E. T. *Macromolecules*, **1999**, *32*, 5471; Johnson, L.K.; Killian, C.M.; Brookhart, M. *J. Am. Chem. Soc.*, 1995, **117**, 6414.

(3-4) Bovey, F. A. "High Resolution NMR of Macromolecules", Academic Press, New York, 1972.

(3-5) Randall, J. C. *Rev. Macromol. Chem. Phys.*, **1989**, *C29*, 201.

(3-6) Axelson, D. E.; Levy, G. C.; Mandelkern, L. *Macromolecules*, **1979**, *12*, 41.

(3-7) Randall, J. C. *J. Polym. Sci., Polym. Phys. Ed.*, **1973**, *11*, 275.

(3-8) Carmen, C. J.; Wilkes, C. E. *Rubber Chem. Technol.*, **1971**, *44*, 781.

(3-9) Hsieh, E. T.; Randall, J. C. *Macromolecules*, **1982**, *15*, 1402.

(3-10) Galland, G. B.; deSouza, R. F.; Mauler, R. S.; Nunes, F. F. *Macromolecules*, **1999**, *32*, 1620.

(3-11) Bruch, D.; Payne, W. G. *Macromolecules*, **1986**, *19*, 2712.

(3-12) Grant, D. M.; Paul, E. G. *J. Am. Chem. Soc.*, **1964**, *86*, 2984.

(3-13) Tonelli, A. E.; Schilling, F. C. *Macromolecules*, **1980**, *13*, 270; Lindemann, L. P.; Adams, J. Q. *Anal. Chem.*, **1971**, *43*, 1245.

(3-14) Randall, J. C.; Hsieh, E. T. *J. Am. Chem. Soc.*, **1984**, *131*, .

(3-15) DePooter, M.; Smith, P. B.; Dohrer, K. K.; Bennett, K. F.; Meadows, M. D.; Smith, C. G.; Schouwenaars, H. P.; Geerards, R. A. *J. Appl. Polym. Sci.*, **1991**, *42*, 399-408.

(3-16) Wignall, G. D.; Alamo, R. G.; Laondono, J. D.; Mandelkern, L.; Kim, M. H.; Lin, J. S.; Brown, G. M. *Macromolecules*, **2000**, ***33***, 551-561.

(3-17) Bovey, F. A. "Polymer Conformation and Configuration", Academic Press, New York, 1969.

(3-18) Coleman, B. D.; Fox, T. G. *J. Am. Chem. Soc.*, **1963**, *85*, 1241.

(3-19) Harwood, H. J.; Ritchey, W. M. *J. Polym. Sci., Part B*, **1964**, *2*, 601.

(3-20) Coleman, B. D.; Fox, T. G. *J. Chem. Phys.*, **1963**, ***38***, 1065.

(3-21) Kakugo, M.; Naito, Y.; Mizunuma, K.; Miyatake, T. *Macromolecules*, **1982**, *15*, 1150-1152.

(3-22) Randall, J. C. "Polymer Sequence Determination", Academic Press, New York, 1977.

(3-23) Cozewith, C. *Macromolecules*, **1987**, *20*, 1237-1244.

(3-24) Kupce, E.; Freeman, R. *J. Magn. Reson.*, **2001**, *151*, 142.

(3-25) Schaefer, J.; Natusch, D. F. S. *Macromolecules*, **1972**, *5*, 416.

(3-26) Farrar, T. C.; Becker, E. D. "Pulse and Fourier Transform NMR", Academic Press, New York, 1969.

(3-27) Slichter, C. P. "Principles of Magnetic Resonance", 2nd Ed., Springer-Verlag, Berlin, 1978.

(3-28) Schaefer, J.; Stejskal, E. O. *J. Am. Chem. Soc.*, **1976**, *98*, 1031-1032.

(3-29) Earl, W. L.; VanderHart, D. L. *Macromolecules*, **1979**, *12*, 762-767.

(3-30) Mehring, M. "High Resolution NMR in Solids", 2nd Ed., Springer-Verlag, Berlin, 1983.
(3-31) Hatfield, G. R.; Killinger, W. E.; Zeigler, R. C. *Anal. Chem.*, **1995**, *67*, 3082-3085.
(3-32) Maciel, G. E.; Bronnimann, C. E.; Hawkins, B. L. *Adv. Magn. Reson.* **1990**, *14*, 125.
(3-33) Burum, D. P.; Linder, M.; Ersnt, R. R. *J. Magn. Reson.*, **1981**, *44*, 173.
(3-34) Ernst, R. R.; Bodenhausen, G.; Wokaun, A. "Principles of Nuclear Magnetic Resonance in One and Two Dimensions", Clarendon Press, Oxford, 1986.
(3-35) Freeman, R. "Double Resonance", "Encyclopedia of NMR", 1740-1749 (1999).
(3-36) Waugh, J. S. *J. Magn. Reson.*, **1982**, *50*, 30.
(3-37) Hansen, E. W.; R. Blom,; Bade, O. M. *Polymer, 1997, 38*, 4295.
(3-38) Randall, J. C. private communication.
(3-39) Chen, H. N. *Anal. Chem.*, 1982, **54**, 1828 ().
(3-40) Randall, J. C. *J. Polymer Sci., A: Polymer Chem.*, **1998**, *36*, 1527.
(3-41) Alamo, R. G.; Blanco, J. A.; Agarwal, P. K.; Randall, J. C. *Macromolecules*, **2003**, *36*, 1559.
(3-42) Kupce, E.; Freeman, R. *J. Magn. Reson.*, **2001**, *151*, 142.

Table 3-1. *n*-Ads for the poly(ethylene-co-1-hexene) system. (*3-4*)

n	**Name**	**N(*n*)**	***n*-ads**
1	monads	2	**E, H**
2	diads	3	EE, EH, HH
3	triads	6	EEE, EEH, HEH, EHE, EHH, HHH
4	tetrads	10	EEEE, EEEH, HEEH, EEHE, EEHH, HEHH, EHEH, EHHE, EHHH, HHHH
5	pentads	20	EEEEE, EEEEH, HEEEH, EEEHE, EEEHH, HEEHH, EHEEH, EHEHE, EHEHH, HHEHH, EEHEE, EEHEH, HEHEH, EEHHE, EEHHH, EHHEH, HEHHH, EHHHE, EHHHH, HHHHH

Table 3-2. Necessary relationships for the poly(ethylene-co-1-hexene) system. (*3-5*)

Type	Necessary relationship
monad - monad	[E] + [H] = 1
diad -diad	[EE] + [EH] + [HH] = 1
monad -diad	[E] = [EE] + ½ [EH] [H] = [HH] + ½ [EH]
triad - triad	[EEE] + [EEH] + [HEH] + [EHE] + [EHH] + [HHH] = 1 [EEH] + 2 [HEH] = [EHH] + 2 [EHE]
monad - triad	[E] = [EEE] + [EEH] + [HEH] [H] = [EHE] + [EHH] + [HHH]
diad -triad	[EE] = [EEE] + ½ [EEH] [EH] = [EEH] + 2 [HEH] = [EHH] + 2 [EHE] [HH] = [HHH] + ½ [EHH]
tetrad - tetrad	[EEEE] + [EEEH] + [HEEH] + [EEHE] + [EEHH] + [HEHH] + + [EHEH] + [EHHE] + [EHHH] + [HHHH] = 1 2 [HEEH] + [EEEH] = [EEHE] + [EEHH] 2 [EHHE] + [EHHH] = [HEHH] + [EEHH]
diad - tetrad	[EE] = [EEEE] + [EEEH] + [HEEH] [EH] = [EEHE] + [EEHH] + [HEHH] + [EHEH] [HH] = [EHHE] + [EHHH] + [HHHH]
triad - tetrad	[EEE] = [EEEE] + ½ [EEEH] [EEH] = 2 [HEEH] + [EEEH] = [EEHE] + [EEHH] [HEH] = ½ [EHEH] + ½ [HEHH] [EHE] = ½ [EHEH] + ½ [EEHE] [EHH] = 2 [EHHE] + [EHHH] = [HEHH] + [EEHH] [HHH] = [HHHH] + ½ [EHHH]

Table 3-3. ^{13}C chemical shift assignments for the poly(ethylene-*co*-1-hexene) system, as determined by Hsieh and Randall (*3-9*).

Carbon type	**Sequence**	**Observed ^{13}C chemical shift (ppm)**	**Predicted ^{13}C chemical shift (ppm) by the Grant and Paul method (*12*)**
αα	HHHH	41.40	40.37
αα	EHHH	40.86	39.95
αα	EHHE	40.18	39.53
CH(EHE)	EHE	38.13	35.23
CH(EHH)	EHH	35.85	33.16
$4B_4$	HHH	35.37	35.12
αγ	HEHH	35.00 – 34.90	35.54
αγ	EHEH	35.00 – 34.90	35.12
αδ+	EEHH	35.00 – 34.90	35.12
$4B_4$	EHH	35.00 – 34.90	34.70
αδ+	EEHE	34.54	34.70
$4B_4$	EHE	34.13	34.28
CH(HHH)	HHH	33.47	31.09
γγ	HEEH	30.94	30.71
γδ+	EEEH	30.47	30.29
δ+δ+	$(EEE)_n$	29.98	29.87
$3B_4$	EHE	29.51	29.87
$3B_4$	EHH	29.34	29.98
$3B_4$	HHH	29.18	30.09
βδ+	EEHE	27.28	27.80
βδ+	EEHH	27.09	27.91
ββ	EHEHE	24.53	25.71
ββ	EHEHH	24.39	25.82
ββ	HHEHH	24.25	25.93
$2B_4$	EHE+EHH+ HHH	23.37	22.65
$1B_4$	EHE+EHH+ HHH	14.12	13.56

Table 3-4. ^{13}C chemical shift assignments for chain-end groups, as assigned by Hsieh and Randall. (*3-9*)

Carbon type	**^{13}C chemical shift (ppm vs. TMS)**
2v	139.46
1v	114.34
a	33.91
3s	32.18
2s	22.86
1s	14.15

Table 3-5. Collective assignment regions for poly(ethylene-co-1-hexene). (*3-9*)

Region	**^{13}C chemical shift range (ppm)**	**Carbon type(s)**	**Contributing *n*-ads**
A	42 – 39.5	αα	HHHH+EHHH+EHHE
B	38.1	CH(EHE)	EHE
C	36.0 – 33.0	CH(EHH) CH(HHH) $4B_4$ αγ αδ+	EHH HHH EHE+EHH+HHH EHEH+HEHH EEHE+EEHH
D	31.0 – 28.5	γγ γδ+ δ+δ+ $3B_4$	HEEH EEEH $(EEE)_n$ EHE+EHH+HHH
E	27.5 – 26.5	βδ+	EEHE+EEHH
F	25.0 – 24.0	ββ	EHEHE+EHEHH+HEHEH
G	23.4	$2B_4$	EHE+EHH+HHH
H	14.1	$1B_4$	EHE+EHH+HHH

Table 3-6. Bernoullian *n*-ad probabilities, for the poly(ethylene-co-1-hexene) system, in terms of P_H, the probability of adding H to a polymer chain. (*3-17*)

***n*-ad type**	**Designation**	**Bernoullian probability**
monad	[E]	$1 - P_H$
	[H]	P_H
diad	[EE]	$(1 - P_H)^2$
	[EH]	$2 P_H (1 - P_H)$
	[HH]	P_H^2
triad	[EEE]	$(1 - P_H)^3$
	[EEH]	$2 P_H (1 - P_H)^2$
	[HEH]	$P_H^2 (1 - P_H)$
	[EHE]	$P_H (1 - P_H)^2$
	[EHH]	$2 P_H^2 (1 - P_H)$
	[HHH]	P_H^3
tetrad	[EEEE]	$(1 - P_H)^4$
	[EEEH]	$2 P_H (1 - P_H)^3$
	[HEEH]	$P_H^2 (1 - P_H)^2$
	[EEHE]	$2 P_H (1 - P_H)^3$
	[EEHH]	$2 P_H^2 (1 - P_H)^2$
	[HEHH]	$2 P_H^3 (1 - P_H)$
	[EHEH]	$2 P_H^2 (1 - P_H)^2$
	[EHHE]	$P_H^2 (1 - P_H)^2$
	[EHHH]	$2 P_H^3 (1 - P_H)$
	[HHHH]	P_H^4

Table 3-7. First-order Markov *n*-ad probabilities for the poly(ethylene-co-1-hexene) system in terms of $P_{E/H}$, the probability of adding H to E, and $P_{H/E}$, the probability of adding E to H. (*3-17*)

***n*-ad type**	**Designation**	**First-order Markovian probability**
diad	[EE]	$P_{H/E}\,(1 - P_{E/H}) / (P_{E/H} + P_{H/E})$
	[EH]	$2\,P_{E/H}\,P_{H/E} / (P_{E/H} + P_{H/E})$
	[HH]	$P_{E/H}\,(1 - P_{H/E}) / (P_{E/H} + P_{H/E})$
triad	[EEE]	$P_{H/E}\,(1 - P_{E/H})^2 / (P_{E/H} + P_{H/E})$
	[EEH]	$2\,P_{E/H}\,P_{H/E}\,(1 - P_{E/H}) / (P_{E/H} + P_{H/E})$
	[HEH]	$2\,P_{E/H}^2\,P_{H/E} / (P_{E/H} + P_{H/E})$
	[EHE]	$2\,P_{E/H}\,P_{H/E}^2 / (P_{E/H} + P_{H/E})$
	[EHH]	$2\,P_{E/H}\,P_{H/E}\,(1 - P_{H/E}) / (P_{E/H} + P_{H/E})$
	[HHH]	$P_{E/H}\,(1 - P_{H/E})^2 / (P_{E/H} + P_{H/E})$

Table 3-8. Deconvolution results for the ^{13}C CP-MAS NMR spectrum of sample H. [a]

Peak chemical shift (ppm)	**Peak Intensity (arbitrary units)**	**Peak Full Width at Half-Height (Hz)**	**Peak Integral (% of total)**
37.4	169872	70.8	2.4
32.2	1895132	144.5	52.3
30.0	2757440	62.7	34.6
27.9	303592	143.6	8.4
22.9	247872	26.7	1.3
13.9	236072	20.0	1.0

[a] The spectrum is represented in Figure 3-4; the deconvolution is represented graphically in Figure 3-6.

Table 3-9. Liquid-solution ^{1}H NMR parameter values[a] for sample H at 125 °C.

Assignment	^{1}H peak chemical shift (ppm)	T_1 (s)	T_2 (ms)	Predicted linewidth, FWHH (Hz)	Observed linewidth, FWHH (Hz)
methine	1.96	0.73 ± 0.46	9 ± 3	35	> 200 ?
methylene	1.25	1.80 ± 0.01	80 ± 22	4.0	15.8
methyl	0.86	2.83 ± 0.15	37 ± 13	8.6	16.7

[a] The uncertainties indicated equal two standard deviations.

Table 3-10. ^{13}C liquid-sample NMR relaxation parameters for sample H at 125 °C. [a,b,c]

Region	Peak chemical shift (ppm)	T_1 (s) at 101 MHz	T_1 (s) at 126 MHz	T_2 (ms) at 126 MHz	Predicted "natural linewidth" [d] at 126 MHz (FWHH in Hz)	Linewidth observed at 126 MHz (FWHH in Hz)
A	40.2	1.2 ± 0.6	1.2 ± 0.4	165 ± 79	1.9 ± 0.9	9.19
B	38.1	1.71 ± 0.06	1.62 ± 0.01	200 ± 78	1.6 ± 0.6	3.89
C1	35.8	0.83 ± 0.28	0.94 ± 0.12	438 ± 60	0.7 ± 0.1	3.53
C2a	35.0	0.79 ± 0.20	0.75 ± 0.06	292 ± 113	1.1 ± 0.4	5.74
C2b	34.5	1.13 ± 0.02	1.09 ± 0.01	191 ± 57	1.7 ± 0.5	5.08
C2c	34.1	1.36 ± 0.06	1.30 ± 0.02	162 ± 59	2.0 ± 0.7	4.86
D1	30.4	1.64 ± 0.02	1.62 ± 0.01	290 ± 33	1.1 ± 0.1	5.06
D2	29.98	2.11 ± 0.01	2.12 ± 0.01	81 ± 21	3.9 ± 1.0	4.64
D3	29.5	2.40 ± 0.03	2.27 ± 0.02	172 ± 81	1.9 ± 0.9	3.65
E	27.2	1.44 ± 0.02	1.38 ± 0.01	251 ± 67	1.3 ± 0.3	4.12
F	24.5	0.64 ± 0.26	0.75 ± 0.18	52 ± 24	6 ± 3	4.02
G	23.3	4.57 ± 0.04	4.48 ± 0.02	761 ± 330	0.4 ± 0.2	3.40
H	14.1	8.3 ± 0.2	8.2 ± 0.1	200 ± 127	1.6 ± 1.0	~ 5

[a] Data obtained with CW decoupling.
[b] Intensities obtained as peak heights.
[c] Indicated uncertainties correspond to two standard deviations.
[d] Predicted "natural linewidth" = $(\pi T_2)^{-1}$

Table 3-11. ^{13}C T_1 and typical nOe values measured for samples H and L at 126 MHz and 125 °C. [a,b,c]

Region	Peak chemical shift (ppm)	Sample H T_1 (s) [c]	Sample H nOe factor [d]	Sample L T_1 (s) [c]	Sample L nOe factor [d]
A	40.2	1.2 ± 0.4	2.8 ± 2.0	?	2.8 ± 3.0
B	38.1	1.62 ± 0.01	2.71 ± 0.10	2.01 ± 0.04	2.70 ± 0.25
C1	35.8	0.94 ± 0.12	2.54 ± 0.52	1.09 ± 0.22	2.71 ± 0.76
C2a	35.0	0.75 ± 0.06	2.66 ± 0.10	0.92 ± 0.10	2.61 ± 0.35
C2b	34.5	1.09 ± 0.01	2.64 ± 0.09	1.34 ± 0.01	2.77 ± 0.11
C2c	34.1	1.30 ± 0.02	2.60 ± 0.11	1.55 ± 0.03	2.77 ± 0.24
D1	30.4	1.62 ± 0.01	2.26 ± 0.11	1.94 ± 0.02	2.52 ± 0.27
D2	29.98	2.12 ± 0.01	2.43 ± 0.16	2.59 ± 0.005	2.59 ± 0.06
D3	29.5	2.27 ± 0.02	2.81 ± 0.16	2.75 ± 0.04	2.69 ± 0.34
E	27.2	1.38 ± 0.01	2.57 ± 0.10	1.67 ± 0.01	2.73 ± 0.15
F	24.5	0.75 ± 0.18	2.41 ± 0.71	1.01 ± 0.23	2.42 ± 1.05
G	23.3	4.48 ± 0.02	2.65 ± 0.28	5.28 ± 0.07	2.61 ± 0.09
H	14.1	8.23 ± 0.10	2.40 ± 0.11 [e]	9.58 ± 0.27	2.29 ± 0.09 [e]

[a] Indicated uncertainties correspond to two standard deviations.
[b] Data obtained with CW decoupling.
[c] Intensities taken as peak heights.
[d] Integrals obtained by deconvolution (sample H) or manual integration (sample L).
[e] Accuracy of nOe values for sample H is affected by insufficient relaxation between scans.

Table 3-12. ^{13}C nOe values [a] measured over time for sample L. [a,b,c]

Region	Peak chemical shift (ppm)	Run #1 CW nOe factor	Run #2 CW nOe factor	Run #3a CW nOe factor	Run #3b WALTZ-16 nOe factor
A	40.2	2.83 ± 0.72	2.04 ± 0.49	2.99 ± 0.77	2.57 ± 0.77
B	38.1	2.70 ± 0.12	2.60 ± 0.08	3.01 ± 0.12	2.81 ± 0.12
C1	35.8	2.71 ± 0.35	2.96 ± 0.24	2.79 ± 0.38	2.32 ± 0.38
C2a	35.0	2.61 ± 0.16	2.78 ± 0.11	2.96 ± 0.17	2.74 ± 0.17
C2b	34.5	2.77 ± 0.05	2.64 ± 0.03	2.87 ± 0.05	2.76 ± 0.05
C2c	34.1	2.77 ± 0.11	2.73 ± 0.07	2.96 ± 0.12	2.77 ± 0.12
D1	30.4	2.52 ± 0.12	2.50 ± 0.08	2.77 ± 0.13	2.66 ± 0.13
D2	29.98	2.59 ± 0.03	2.43 ± 0.02	2.66 ± 0.03	2.56 ± 0.03
D3	29.5	2.69 ± 0.16	2.50 ± 0.11	2.82 ± 0.17	2.78 ± 0.17
E	27.2	2.73 ± 0.07	2.58 ± 0.05	2.84 ± 0.08	2.70 ± 0.08
F	24.5	2.42 ± 0.48	3.08 ± 0.33	2.71 ± 0.52	3.01 ± 0.52
G	23.3	2.61 ± 0.04	2.53 ± 0.03	2.89 ± 0.04	2.83 ± 0.04
H	14.1	2.29 ± 0.08	1.92 ± 0.05	2.57 ± 0.08	2.56 ± 0.08

[a] Measured over a period spanning two and a half months.
[b] Indicated uncertainties correspond to two standard deviations.
[c] Data obtained at 126 MHz and at 125 °C, with CW decoupling. Integrals obtained by manual integration.

Table 3-13. Some alternate methods for determining triad mole fractions from collective assignment region integrals, including methods developed as part of this study.

Method	**Triads**
Hsieh and Randall (1982):	k [EHE] = B k [EHH] = 2 $(G - B - A)$ k [HHH] = 2 $A + B - G$ k [HEH] = F k [EEH] = 2 $(G - A - F)$ k [EEE] = ½ $(A + D + F - 2\ G)$
Randall (1989):	k [EHE] = B k [EHH] = $C1$ k [HHH] = $A - ½\ G$ k [HEH] = F k [EEH] = E k [EEE] = ½ D – ½ G – ¼ E
Seger (2000): (as proposed in this study)	k [EHE] = B k [EHH] = $C1$ k [HHH] = $A1 - ½\ A2$ (where $A1 + A2 = A$) k [HEH] = F k [EEH] = E k [EEE] = ½ D – ½ G – ¼ E
Solver (2000): (as proposed in this study)	Linear least-squares analysis with the constraint [EEH] +2 [HEH] = [EHH] +2 [EHE].

Table 3-14. Triad mole fractions determined for sample H by various methods, using "machine" and "manual" integrals of spectra obtained with nOe. Descriptions of the methods are found in Table 3-13.

Peak area method	**Triad method**	**Sample H results (mol%)** [a]
"machine" integral	Hsieh and Randall (1982):	[EHE] = 4.76 ± 0.11 [EHH] = 0.89 ± 0.41 [HHH] = - 0.25 ± 0.29 [HEH] = 0.37 ± 0.36 [EEH] = 9.67 ± 0.29 [EEE] = 84.55 ± 0.31
	Randall (1989):	[EHE] = 4.78 ± 0.11 [EHH] = 0.44 ± 0.06 [HHH] = - 0.02 ± 0.10 [HEH] = 0.37 ± 0.07 [EEH] = 9.47 ± 0.19 [EEE] = 84.95 ± 0.27
	Seger (2000):	[EHE] = 4.78 ± 0.11 [EHH] = 0.44 ± 0.06 [HHH] = 0.11 ± 0.09 [HEH] = 0.37 ± 0.07 [EEH] = 9.47 ± 0.19 [EEE] = 84.95 ± 0.27
"manual" integral	Hsieh and Randall (1982):	[EHE] = 4.74 ± 0.16 [EHH] = 0.84 ± 0.35 [HHH] = - 0.20 ± 0.24 [HEH] = 0.34 ± 0.04 [EEH] = 9.64 ± 0.16 [EEE] = 84.63 ± 0.15
	Randall (1989):	[EHE] = 4.76 ± 0.16 [EHH] = 0.42 ± 0.09 [HHH] = 0.01 ± 0.09 [HEH] = 0.35 ± 0.04 [EEH] = 9.42 ± 0.15 [EEE] = 85.03 ± 0.25
	Seger (2000):	[EHE] = 4.76 ± 0.16 [EHH] = 0.42 ± 0.09 [HHH] = 0.13 ± 0.05 [HEH] = 0.35 ± 0.04 [EEH] = 9.41 ± 0.15 [EEE] = 84.93 ± 0.26

[a] Indicated uncertainties equal two standard deviations.

Table 3-15. Triad mole fractions determined for poly(ethylene-*co*-1-hexene) sample H by various triad methods, using "deconvolution" integrals of spectra obtained with nOe. Descriptions of the methods are found in Table 3-13.

Peak area method	**Triad method**	**Sample H results (mol%)** [a]
"deconvolution" integral	Hsieh and Randall (1982):	[EHE] = 4.76 ± 0.02 [EHH] = 0.96 ± 0.09 [HHH] = - 0.19 ± 0.09 [HEH] = 0.35 ± 0.03 [EEH] = 9.78 ± 0.13 [EEE] = 84.34 ± 0.14
	Randall (1989):	[EHE] = 4.79 ± 0.02 [EHH] = 0.43 ± 0.04 [HHH] = 0.07 ± 0.07 [HEH] = 0.35 ± 0.03 [EEH] = 9.47 ± 0.05 [EEE] = 84.89 ± 0.09
	Seger (2000):	[EHE] = 4.79 ± 0.02 [EHH] = 0.43 ± 0.04 [HHH] = 0.18 ± 0.05 [HEH] = 0.35 ± 0.03 [EEH] = 9.47 ± 0.05 [EEE] = 84.89 ± 0.09
	Solver (2000):	[EHE] = 4.80 ± 0.03 [EHH] = 0.47 ± 0.03 [HHH] = 0.10 ± 0.04 [HEH] = 0.32 ± 0.03 [EEH] = 9.44 ± 0.05 [EEE] = 84.87 ± 0.06

[a] Indicated uncertainties equal two standard deviations.

Table 3-16. Some alternate expressions for determining [HHH], using "deconvolution" integrals of spectra obtained with nOe. (*3-9,14,15*)

Expression	**[HHH] mol% for Sample H**	**[HHH] mol% for Sample L**
k[HHH] = 2A + B – G Hsieh and Randall (1982) method (*3-9*)	-0.21	- 0.31
k[HHH] = A – ½C1 Randall (1989) method *(3-15)*	- 0.02	- 0.02
k[HHH] = 3G – C	0.14	0.87
k[HHH] = C2c – B	0.25	-0.06
k[HHH] = A1 + ½A2 Seger (2000) method (as proposed in this study)	0.02	0.02
k[HHH] = ½(4A + E + 2F – C1 – 2G)	- 0.08	- 0.31
k[HHH] = G – B – C1	0.17	0.28
k[HHH] = 2G – C2A – C2B	0.22	0.53
k[HHH] = ½(2G – E – 2F – C1)	0.04	0.27
k[HHH] = 2A – C + G + 2F + E Randall (1989) (*3-15*)	0.03	0.28
k[HHH] = ½(2C2c – E – 2F + C1)	0.12	-0.07
mean of above values	**0.06**	**0.13**
standard deviation of above values	**0.14**	**0.36**
Solver (2000) linear regression method	0.01	0.02

Table 3-17. Triad mole fractions determined for poly(ethylene-*co*-1-hexene) samples H and L by various methods (*3-9,14,15*), using spectra obtained without nOe.

Method	**Triads**	**Sample H results (mol%)**	**Sample L results (mol%)**
Hsieh and Randall (1982):	k [EHE] = B k [EHH] = 2 $(G - B - A)$ k [HHH] = 2 $A + B - G$ k [HEH] = F k [EEH] = 2 $(G - A - F)$ k [EEE] = ½ $(A + D + F - 2\,G)$	[EHE] = 4.67 [EHH] = 0.89 [HHH] = - 0.21 [HEH] = 0.34 [EEH] = 9.55 [EEE] = 84.76	[EHE] = 3.18 [EHH] = 0.97 [HHH] = - 0.31 [HEH] = 0.49 [EEH] = 6.34 [EEE] = 89.33
Randall (1989):	k [EHE] = B k [EHH] = $C1$ k [HHH] = $A - ½\,G$ k [HEH] = F k [EEH] = E k [EEE] = ½ D – ½ G – ¼ E	[EHE] = 4.68 [EHH] = 0.51 [HHH] = - 0.02 [HEH] = 0.34 [EEH] = 9.46 [EEE] = 85.03	[EHE] = 3.20 [EHH] = 0.38 [HHH] = - 0.02 [HEH] = 0.50 [EEH] = 5.80 [EEE] = 90.13
Solver (2000):	Linear least-squares analysis with the constraint [EEH]+2[HEH] = [EHH]+2 [EHE].	[EHE] = 4.76 [EHH] = 0.55 [HHH] = 0.01 [HEH] = 0.31 [EEH] = 9.44 [EEE] = 84.93	[EHE] = 3.18 [EHH] = 0.42 [HHH] = 0.02 [HEH] = 0.49 [EEH] = 5.79 [EEE] = 90.10

Table 3-18. Comparison of sequence distribution parameter values obtained for poly(ethylene-*co*-1-hexene) samples H and L, using the Solver (2000) results from Table 3-17.

Parameter name	**Bernoullian value**	**1st-order Markovian value**	**Sample H value**	**Sample L value**
persistence ratio	1.0000	any	1.001	1.031
cluster index	10.00		10.16	17.10
omega (E-based)	1.0000	1.0000	0.999	0.995
omega (H-based)	1.0000	1.0000	1.516	0.416
reactivity ratio product r_1r_2	1.0000	1.0000	1.028	1.907
average reactivity ratio product $\langle r_1r_2 \rangle$	1.0000	1.0000	1.010	1.867

Table 3-19. Best fit (using *Solver*) of one-site and two-site Bernoullian models to experimentally-determined triad mole fractions from the Solver (2000) results of Table 3-17.

	Triad	Sample H triad mol fractions	Sample L triad mol fractions
experimental	EHE	0.0476	0.0318
	EHH	0.0055	0.0042
	HHH	0.0001	0.0002
	HEH	0.0031	0.0049
	EEH	0.0944	0.0579
	EEE	0.8493	0.9010
	sum	1.0000	1.0000
1-site model best fit	EHE	0.0477	0.0336
	EHH	0.0054	0.0025
	HHH	0.0002	0.0000
	HEH	0.0027	0.0013
	EEH	0.0954	0.0673
	EEE	0.8487	0.8953
	sum	1.0000	1.0000
residual sum of squares		1.48×10^{-6}	1.40×10^{-4}
2-site model best fit	EHE	0.0451	0.0559
site A:	EHH	0.0048	0.0076
71% of sample H	HHH	0.0001	0.0003
([H] = 5.0 %)	HEH	0.0024	0.0038
57% of sample L	EEH	0.0903	0.1117
([H] = 6.4 %)	EEE	0.8573	0.8208
	sum	1.0000	1.0000
site B:	EHE	0.0539	0.0000
29% of sample H	EHH	0.0070	0.0000
([H] = 6.1 %)	HHH	0.0002	0.0000
43% of sample L	HEH	0.0035	0.0000
([H] = 0.0 %)	EEH	0.1078	0.0000
	EEE	0.8275	1.0000
	sum	1.0000	1.0000
residual sum of squares		1.20×10^{-6}	4.65×10^{-5}
Ratio of residual sum of squares (1-site model vs. 2-site model)		1.24	3.00

Table 3-20. Population-weighted results and residuals from the best fit (using *Solver*) of one-site and two-site Bernoullian models to experimentally-determined triad mole fractions using the Solver (2000) results from Table 3-17.

Model results	**Experimental triad mole fractions**		**1-site model triad mole fractions**		**2-site model triad mole fractions**	
	sample H	sample L	sample H	sample L	sample H	sample L
EHE	0.0476	0.0318	0.0477	0.0336	0.0477	0.0318
EHH	0.0055	0.0042	0.0054	0.0025	0.0054	0.0043
HHH	0.0001	0.0002	0.0002	0.0000	0.0002	0.0001
HEH	0.0031	0.0049	0.0027	0.0013	0.0027	0.0022
EEH	0.0944	0.0579	0.0954	0.0673	0.0953	0.0637
EEE	0.8493	0.9010	0.8487	0.8953	0.8487	0.8978
sum	1.0000	1.0000	1.0000	1.0000	1.0000	1.0000

Model residuals		**1-site model triad mole fraction residuals**		**2-site model triad mole fraction residuals**	
		sample H	sample L	sample H	sample L
EHE		-0.0001	-0.0018	0.0000	0.0001
EHH		0.0001	0.0017	0.0001	-0.0001
HHH		-0.0001	0.0002	-0.0001	0.0001
HEH		0.0004	0.0036	0.0004	0.0027
EEH		-0.0010	-0.0094	-0.0009	-0.0056
EEE		0.0006	0.0057	0.0005	0.0028
residual sum of squares		1.48 x 10^{-6}	1.40 x 10^{-4}	1.20 x 10^{-6}	4.65 x 10^{-5}

Table 3-21. Necessary relationships for the ABC terpolymer system. (3 monads, 6 diads, 18 triads, 45 tetrads).

Type	**Necessary relationship**
monad - monad	[A] + [B] + [C] = 1
diad -diad	[AA] + [AB] + [AC] + [BB] + [BC] + [CC] = 1
monad -diad	[A] = [AA] + ½ [AB] + ½ [AC] [B] = [BB] + ½ [AB] + ½ [BC] [C] = [CC] + ½ [AC] + ½ [BC]
diad - triad and triad - triad	[AA] = [AAA] + ½ [AAB] + ½ [AAC] [BB] = [BBB] + ½ [ABB] + ½ [BBC] [CC] = [CCC] + ½ [ACC] + ½ [BCC] [AB] = [AAB] + 2 [BAB] + [BAC] = [ABB] + 2 [ABA] + [ABC] [AC] = [AAC] + 2 [CAC] + [BAC] = [ACB] + 2 [ACA] + [ACC] [BC] = [ABC] + 2 [CBC] + [BBC] = [ACB] + 2 [BCB] + [BCC] [AAA] + [AAB] + [AAC] + [ABA] + [ABB] + [ABC] + [ACA] + [ACB] + [ACC] + [BAB] + [BAC] + [BBB] + [BBC] + [BCB] + [BCC] + [CAC] + [CBC] + [CCC] = 1

Figure 3-1.

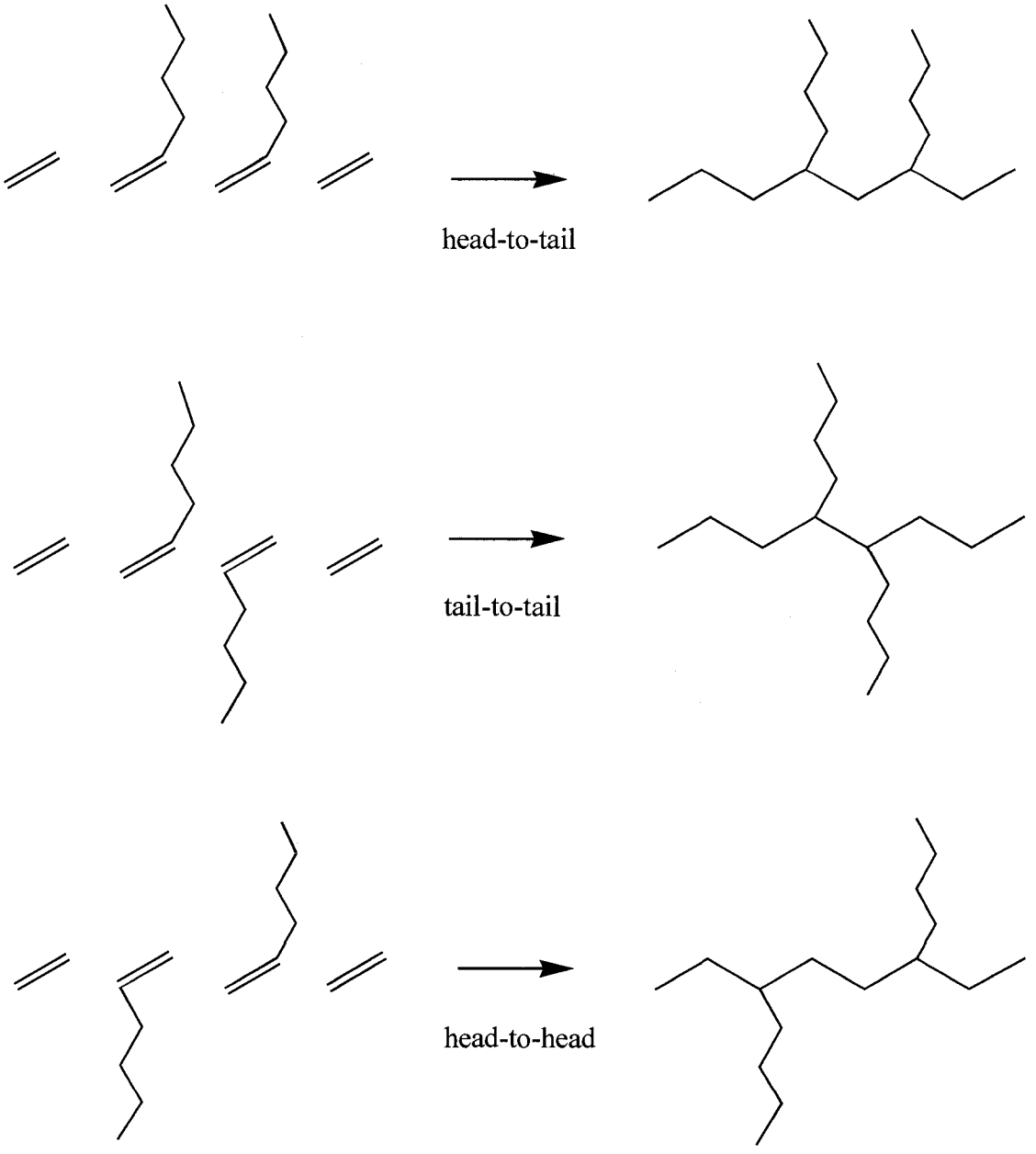

Figure 3-1 Head-to-tail,. tail-to-tail and head-to-head polymerization of 1-hexene in poly(ethylene-*co*-1-hexene).

Figure 3-2.

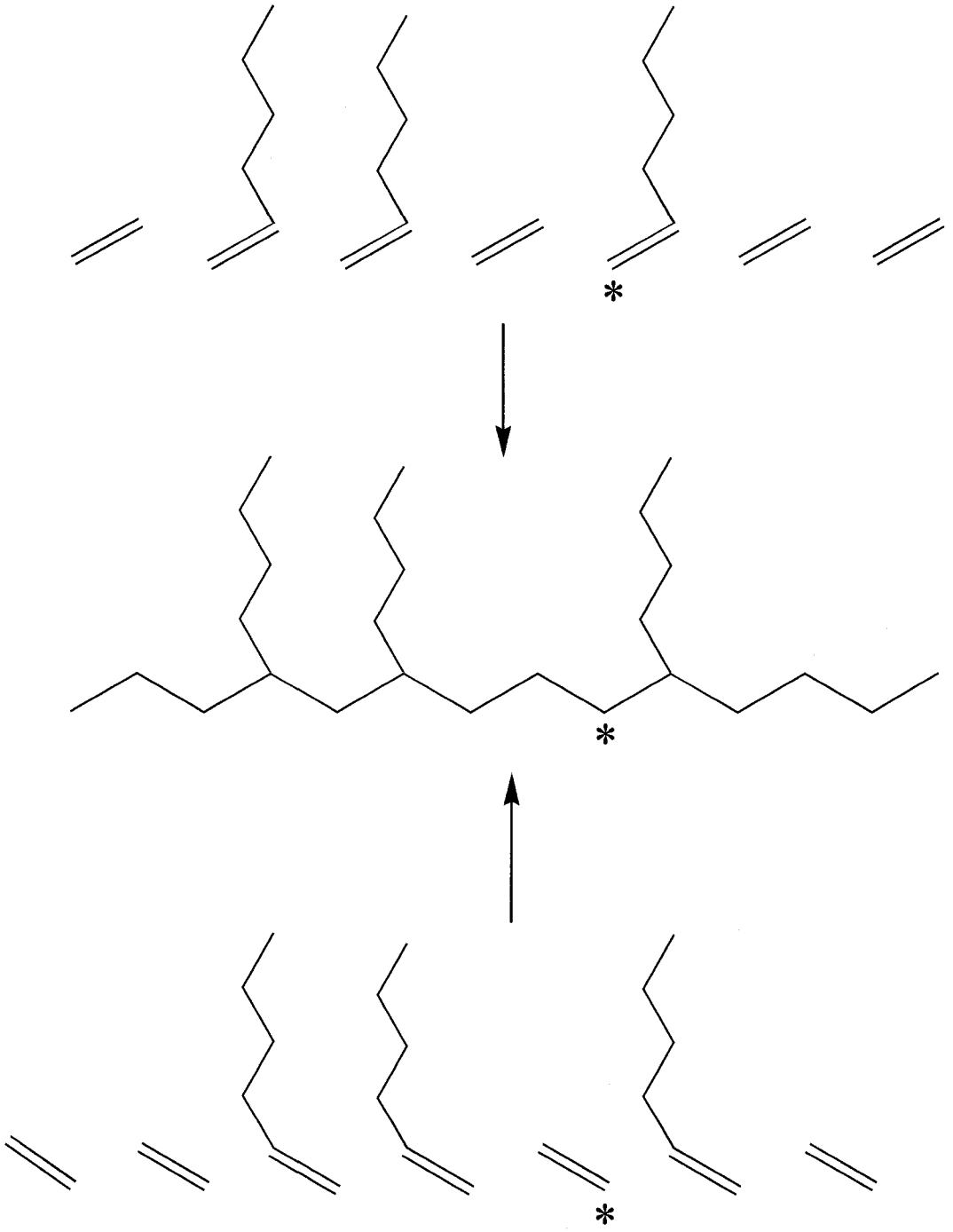

Figure 3-2 Two ways to create a given poly(ethylene-*co*-1-hexene) structure.

Figure 3-3.

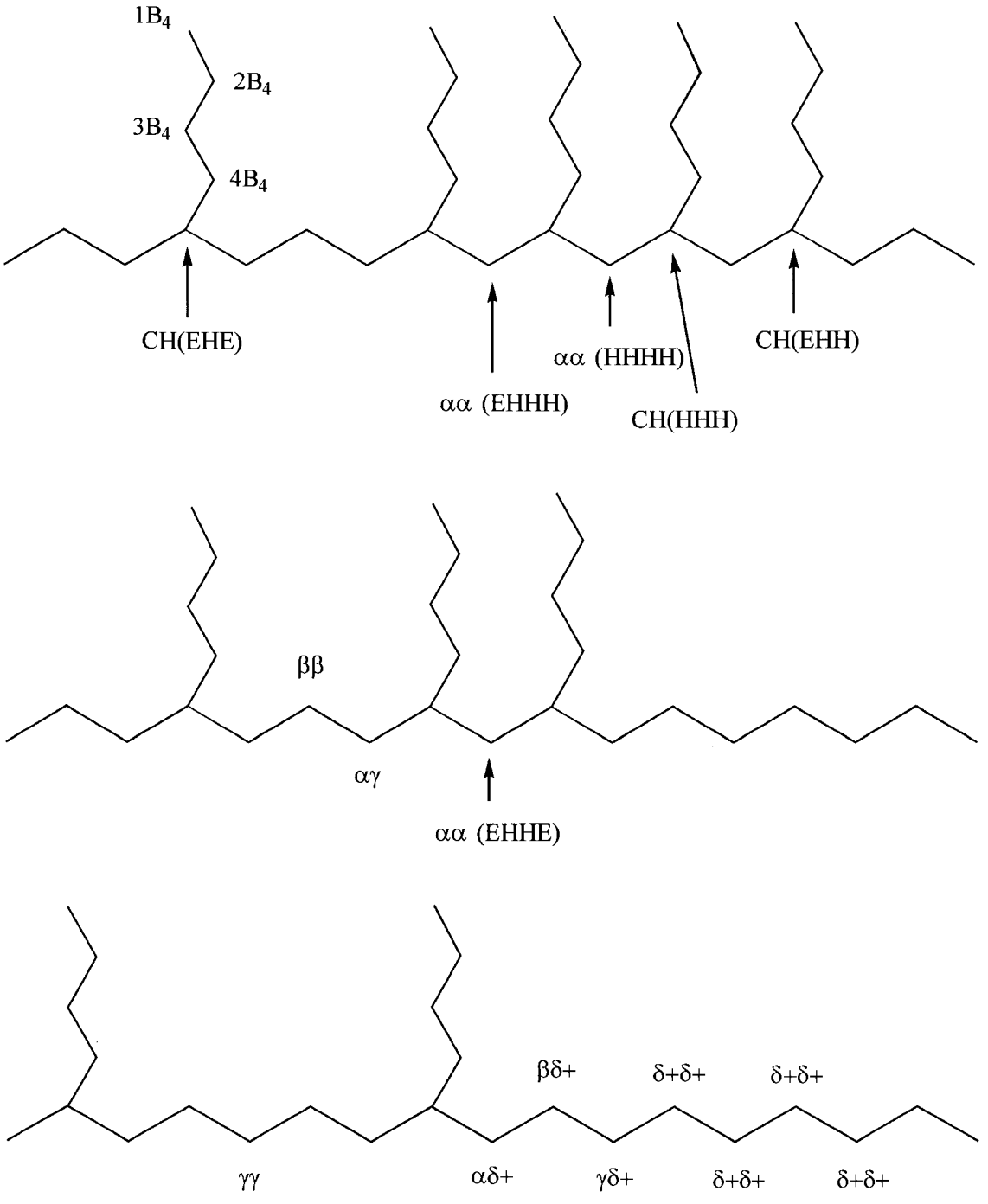

Figure 3-3. Nomenclature examples for poly(ethylene-co-1-hexene) substructures.

Figure 3-4

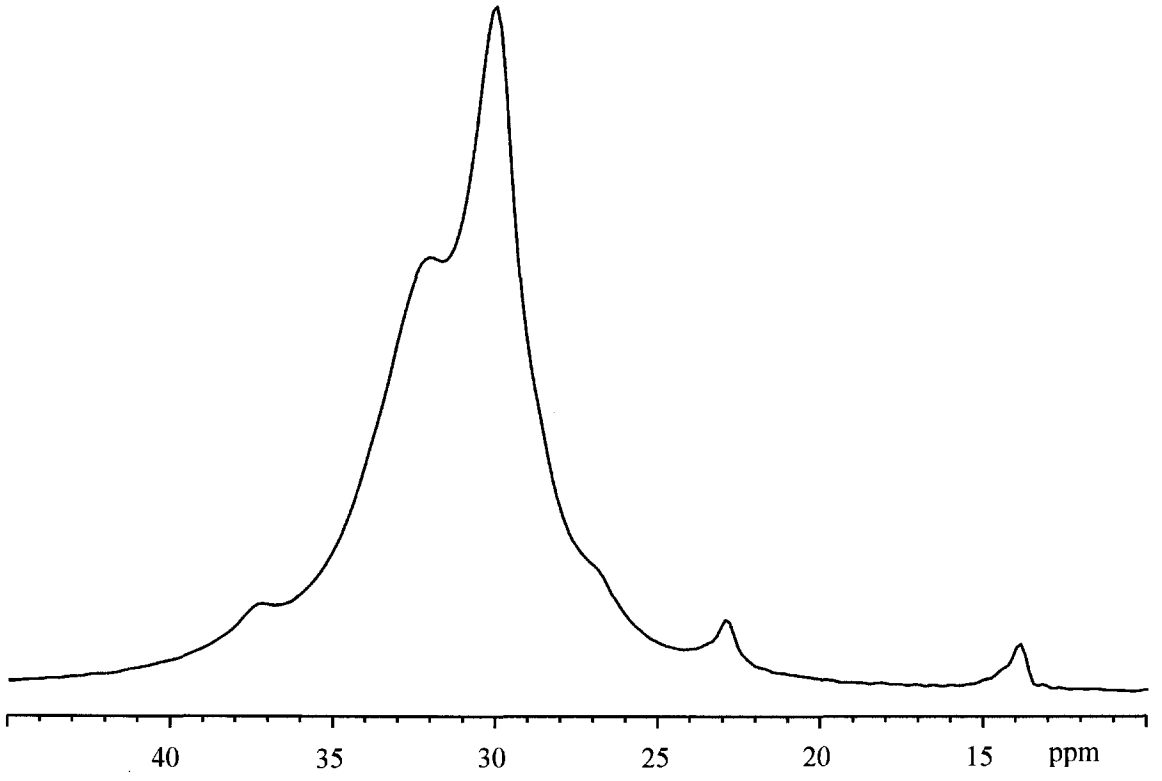

Figure 3-4. Solid-state room temperature ^{13}C CP-MAS spectrum of poly(ethylene-*co*-1-hexene) sample H.

Figure 3-5

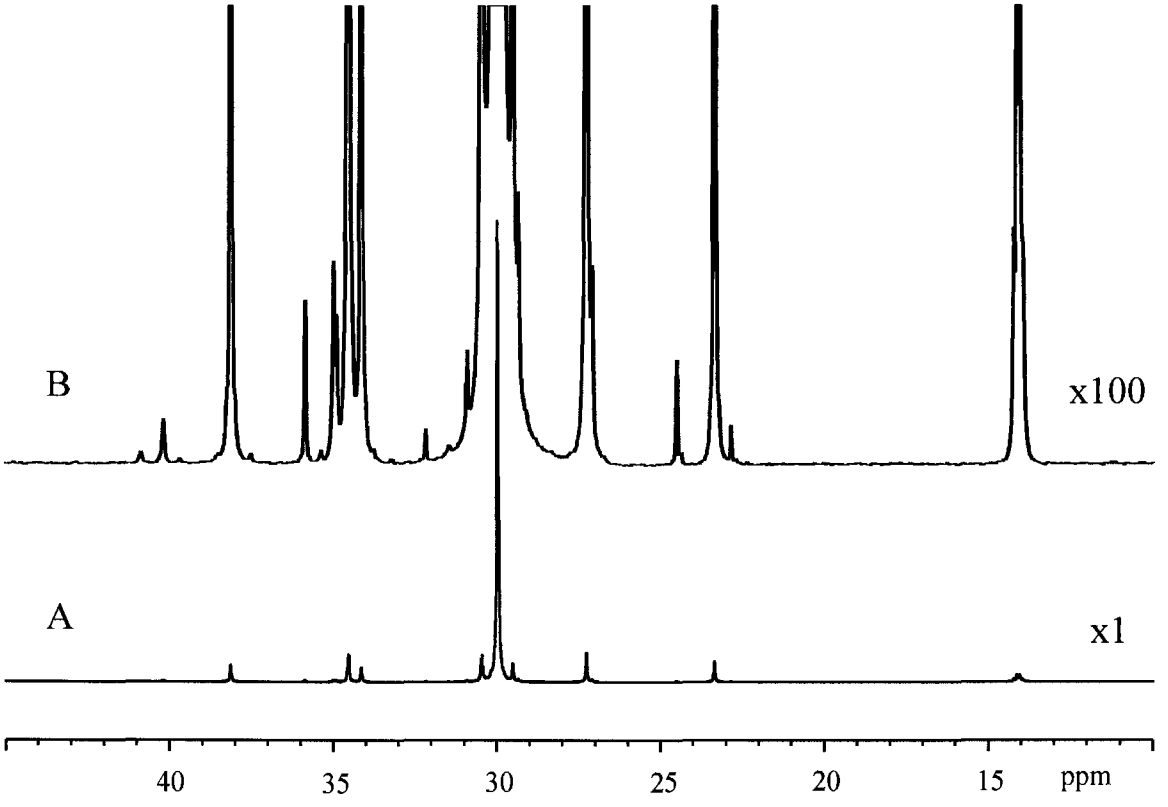

Figure 3-5. Liquid-state ^{13}C NMR spectrum of sample H dissolved in 1,2,4-trichlorobenzene-d_3 at 125 °C (with WALTZ-16 decoupling). A) x1; all peaks on scale. B) x100; most intense peaks are off scale.

Figure 3-6

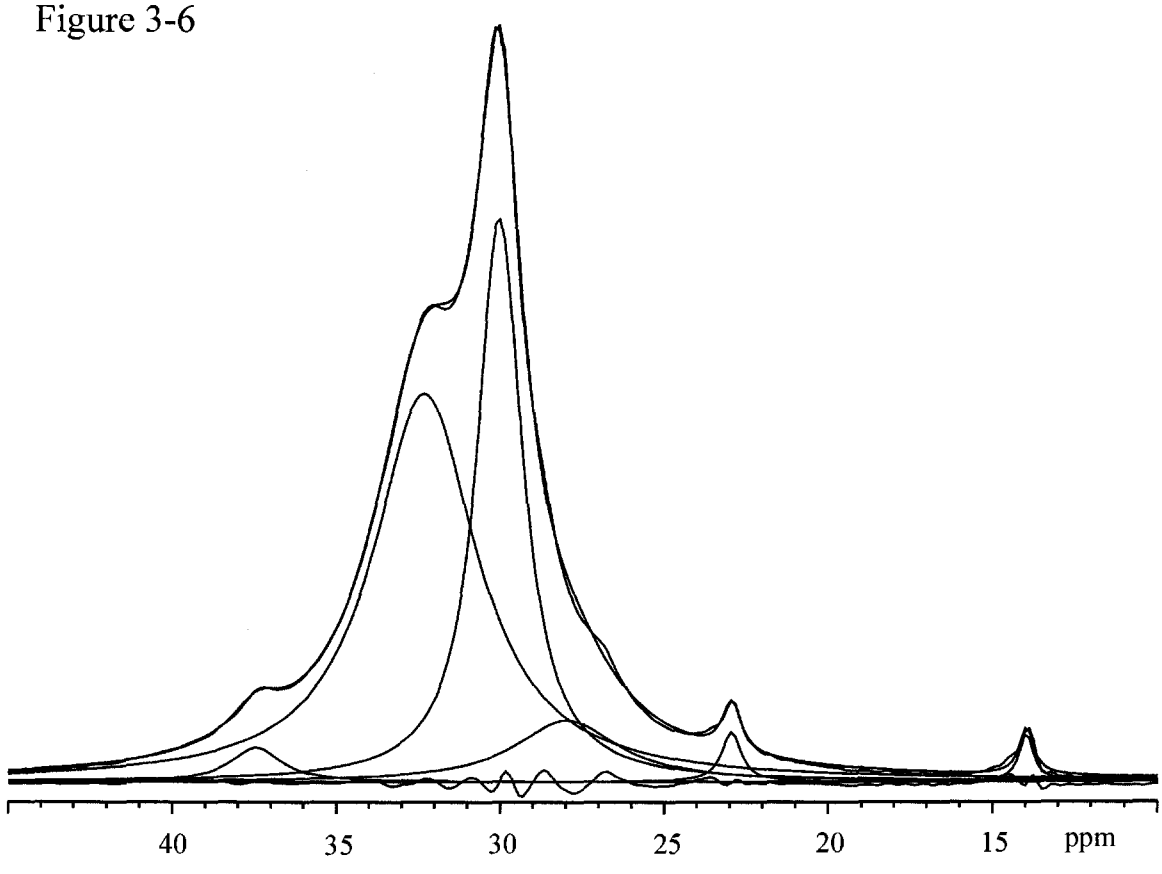

Figure 3-6. Deconvolution of the solid-state room temperature ^{13}C CP-MAS NMR spectrum of poly(ethylene-*co*-1-hexene) sample H.

Figure 3-7

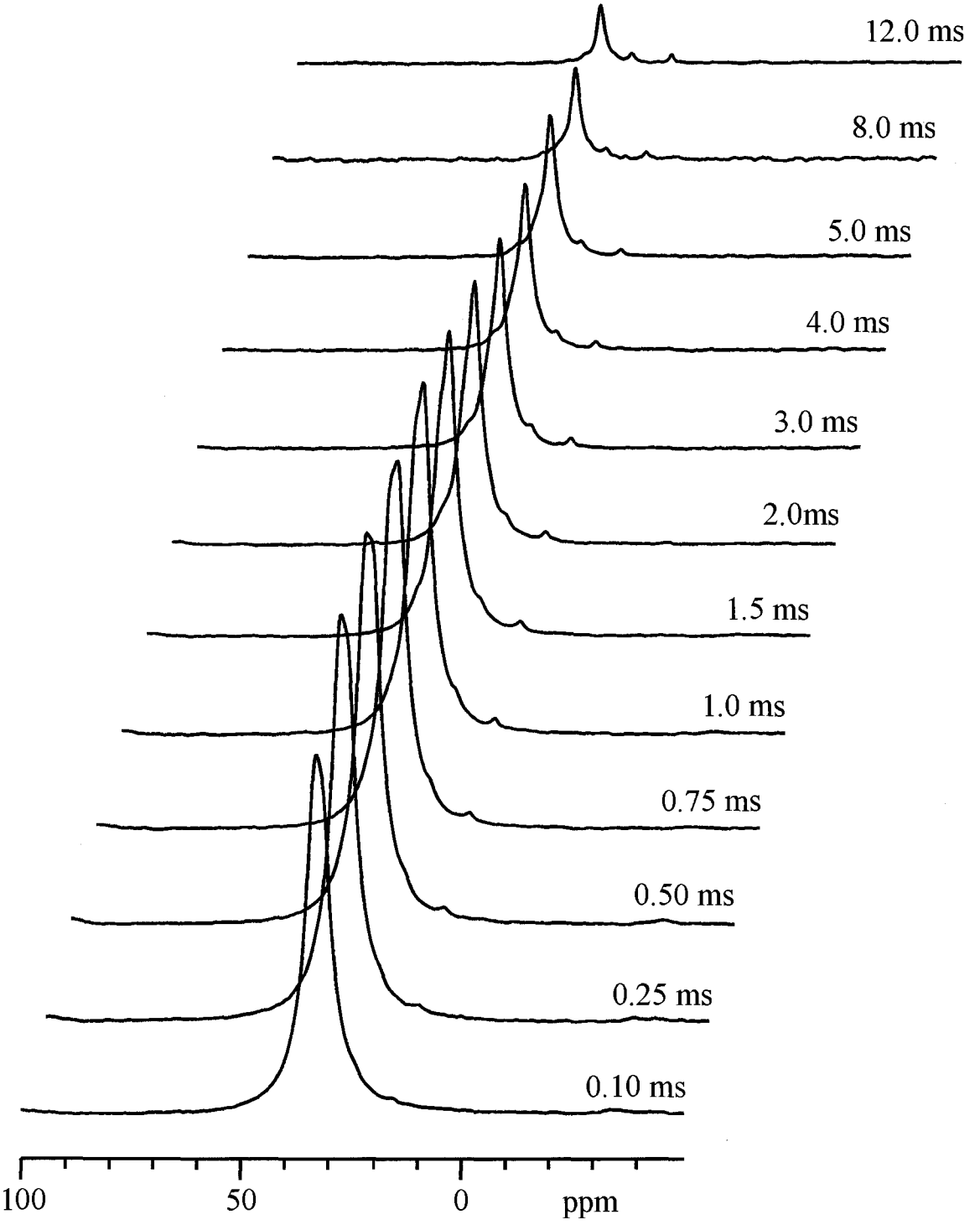

Figure 3-7 Variable Contact Time (VCT) ^{13}C CP-MAS NMR of solid sample H.

Figure 3-8

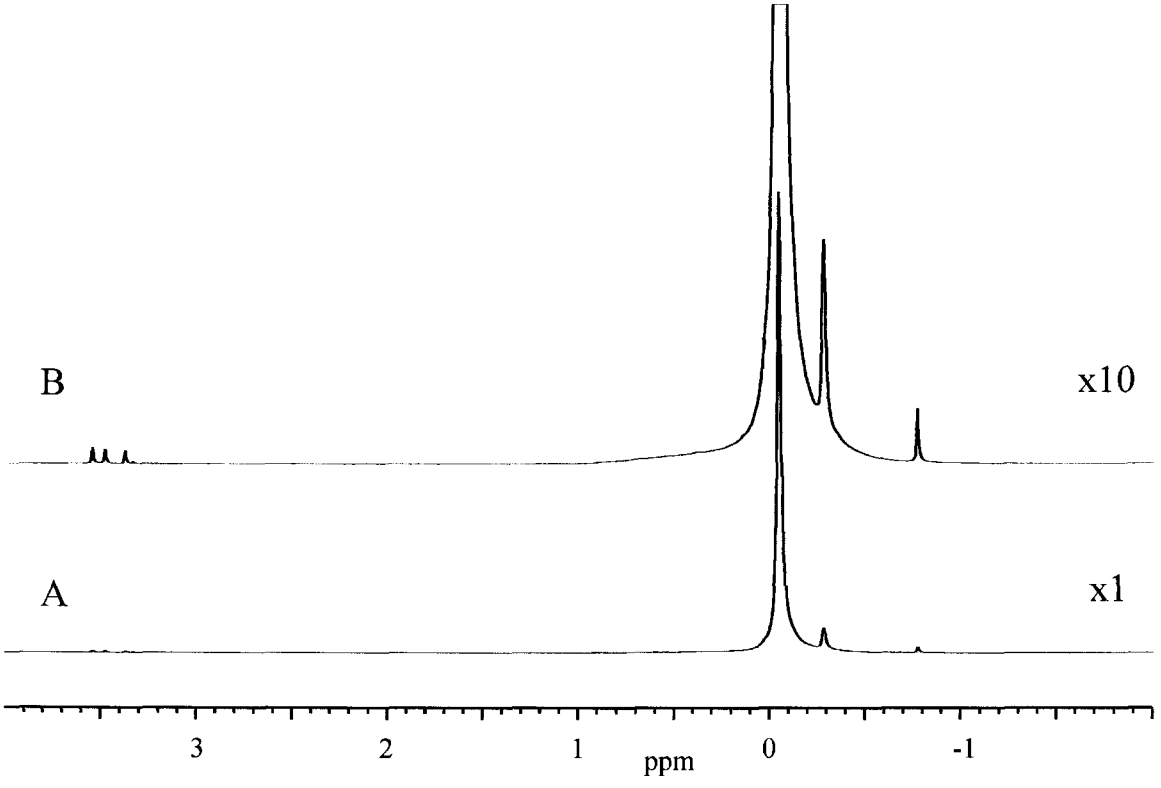

Figure 3-8 Liquid-state ^{1}H NMR spectrum of poly(ethylene-*co*-1-hexene) sample H dissolved in 1,2,4-trichlorobenzene-d_3 at 125 ^{o}C. A) x1; all peaks on scale. B) x10; most intense peaks are off scale.

Figure 3-9

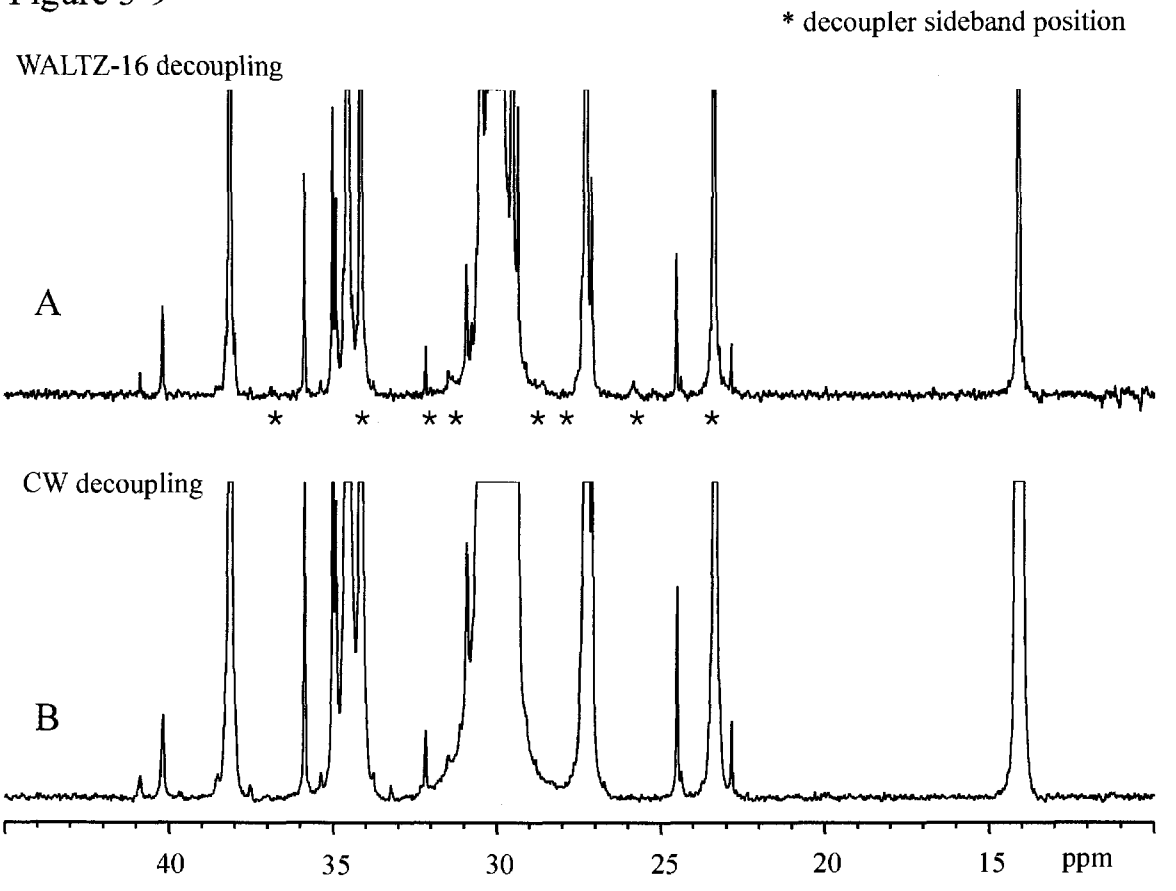

Figure 3-9. Comparison of the 126 MHz liquid-state ^{13}C NMR spectra of sample H dissolved in 1,2,4-trichlorobenzene-d_3 at 125 °C; A: with WALTZ-16 decoupling; B: with CW (continuous wave) decoupling and the same decoupler power setting. Asterisks indicate decoupler sideband positions.

Figure 3-10

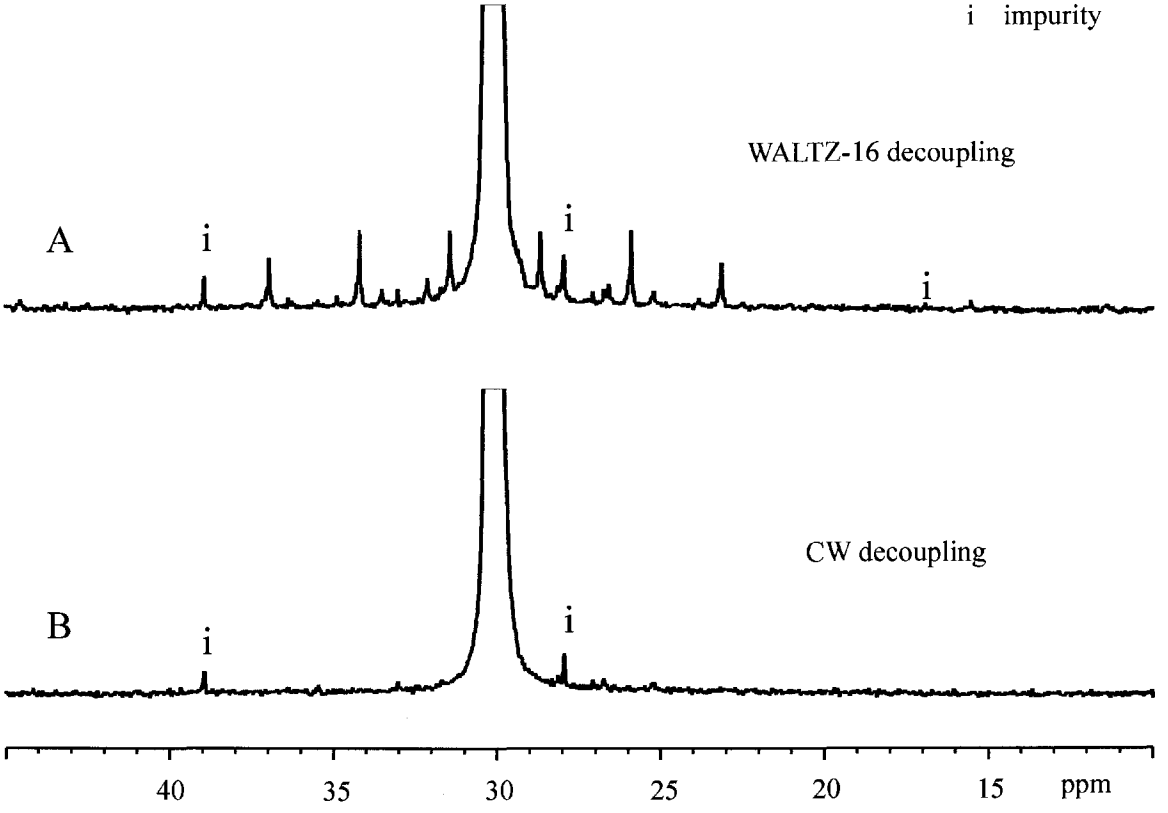

Figure 3-10. 126 MHz liquid-state ^{13}C NMR spectrum of neat DMSO at 125 °C; top: with WALTZ-16 decoupling; bottom: with CW (continuous wave) decoupling and the same decoupler power setting. Note: the ^{13}C peak of DMSO was arbitrarily set to a position of 29.98 ppm (to facilitate comparison to the copolymer spectrum).

Figure 3-11A.

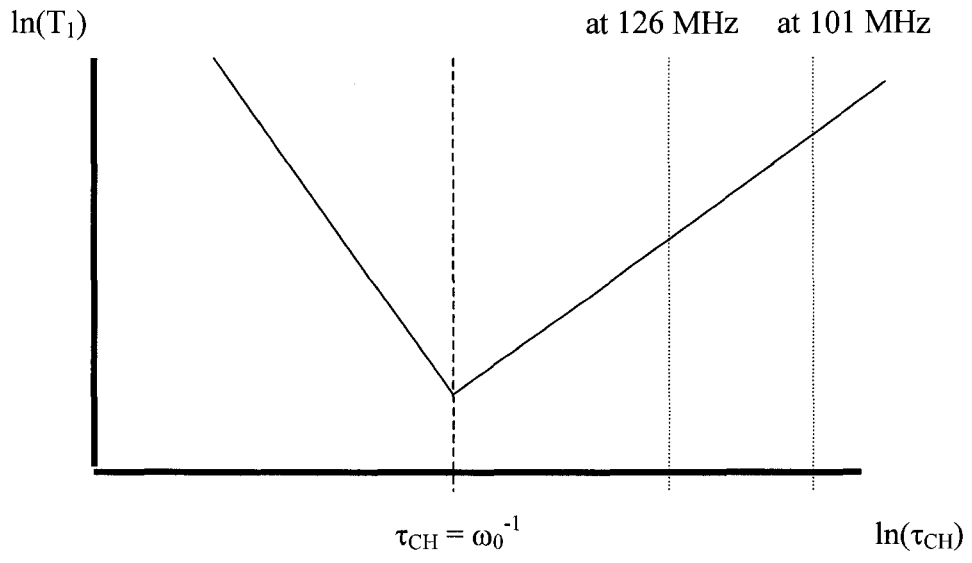

Figure 3-11B.

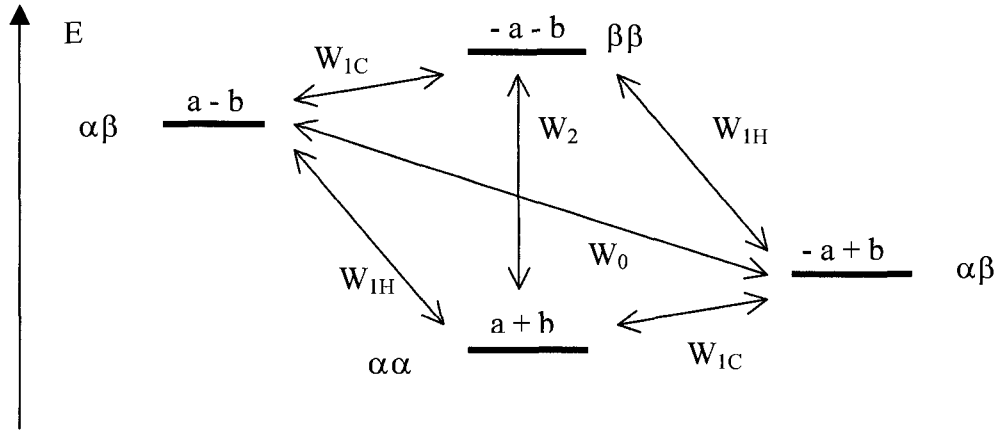

Figure 3-11. A) Plot of the spectral density function, J(ω), as a function of frequency ω, shown for three situations: short, medium and long correlation times (τ). B) Variation of $\ln(T_1)$ with the natural log of the correlation time, $\ln(\tau_{CH})$. C) Energy level diagram for the ^{13}C / ^{1}H spin system, showing the zero-, single- and double-quantum transitions. Spin states such as αβ list the spin state of the ^{13}C nucleus first and the ^{1}H spin state second.

Figure 3-12

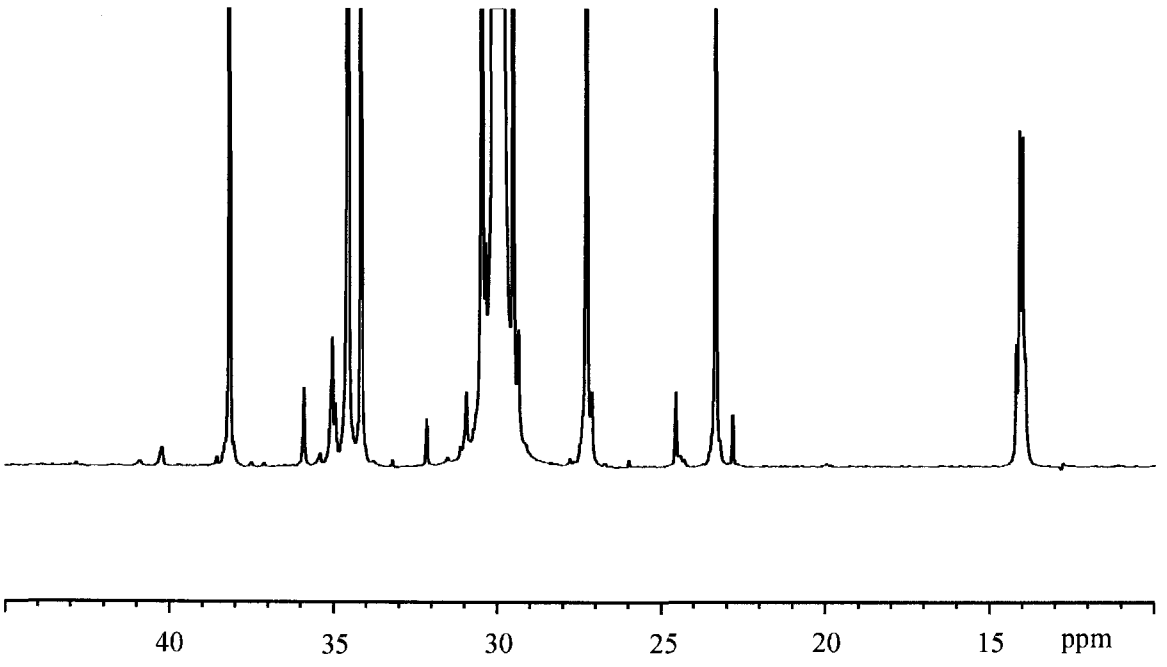

Figure 3-12. 126 MHz liquid-state ^{13}C NMR spectrum of sample L.

Appendix: ^{31}P Chemical Shift Assignments and Species Identification in the NMR Investigation of Chlorpyrifos or Methyl Parathion Sorbed on Clay Minerals

INTRODUCTION – Overview of Issues in ^{31}P Chemical Shift Assignments

Scheme A-1

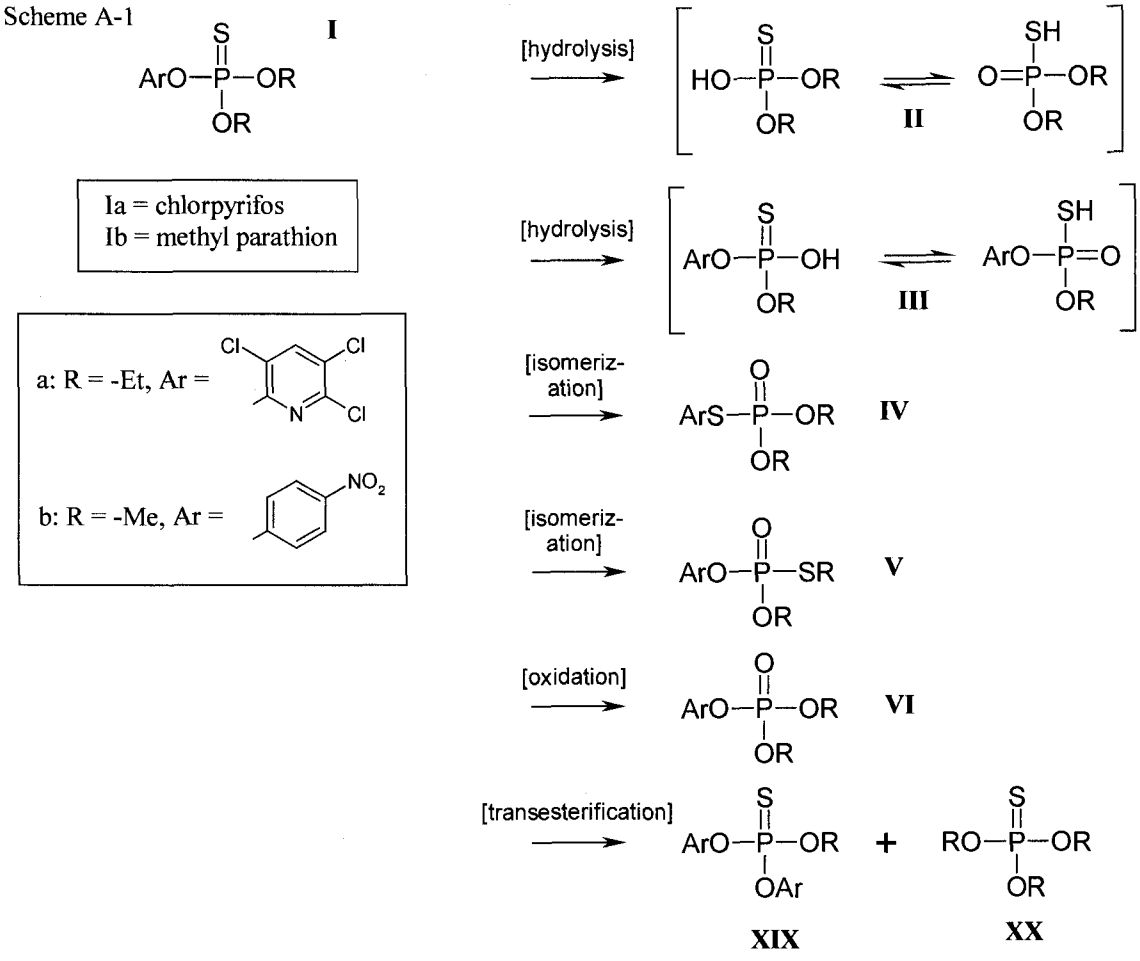

This appendix describes efforts to further investigate the identity of solvent-extractable species from the decomposition of chlorpyrifos or methyl parathion sorbed on hydrated clay minerals, as discussed in Chapters 1 and 2. These experiments include

solid-state and liquid solution ^{31}P NMR, solvent extractions, preparative thin-layer chromatography (TLC), sample synthesis, and two methods of mass spectrometry (MS).

Scheme A-1 represents the *initial* decomposition products suspected for both chlorpyrifos and methyl parathion in the presence of hydrated clay minerals. This generic representation incorporates the reaction schemes shown in Chapter 1 for chlorpyrifos and Chapter 2 for methyl parathion, plus the transesterification reaction previously noted when chlorpyrifos was refluxed in toluene for 3 days (Figure 1-8D) and when methyl parathion was synthesized (Figure 2-1B and Table 2-3). The rate of transesterification, and thus the possible importance of this reaction in the catalytic degradation of chlorpyrifos and methyl parathion on clay minerals, is likely much greater at the very high loading levels used in this study (typically about 10% pesticide by weight) than at the lower concentrations typically encountered in the environment (often in the ppm range).

Clearly, additional reactions are possible beyond those shown above in Scheme A-1; as in Chapters 1 and 2, we are not considering biotic or photochemical degradation pathways, although some of the reaction products may be the same. Scheme A-1 does not include any of the pesticide residues obtained by subsequent hydrolysis of the initial products (**II** – **VI**); these are included in Tables 1-1 and 2-1 as structures **VII** – **XVIII**. While these species represent intermediates in the step-wise degradation of these organothiophosphates to (ultimately) either phosphate ion or mineralization, the thrust of this NMR study is the detection and identification of the *initial* clay-catalyzed decomposition products.

Note also that Scheme A-1 above does not explicitly include various possible chemisorbed pesticide-derived species, in which the pesticide or one of its residues is

bound to the clay mineral sheets or strongly complexed to a metal cation such as Zn^{2+} or Al^{3+}. The presence of strongly-bound chemisorbed phosphorus-containing species was mentioned several times in Chapters 1 and 2, since solvent extraction during clay-catalyzed pesticide decomposition could desorb only some of the phosphorus-containing species (as determined by solid-state ^{31}P NMR of the washed clay samples; see for example Figure 1-11). Various reports in the literature also report an inability to extract all the phosphorus after pesticides are sorbed onto clay minerals and given time to react (*A-1,2*).

A typical result for the attempted extraction of pesticide residues from a clay mineral is shown in Figures A-1 through A-3. Figures A-1 and A-2 compare the 81 MHz ^{31}P solid state DP/MAS spectrum of chlorpyrifos sorbed on Cu(II)-montmorillonite (9.7% chlorpyrifos and 5.0% water, by weight), before and after extraction of pesticide residues using anhydrous acetonitrile; solvent extraction was performed after 11 hours of adsorption at room temperature (in the dark). Note that although several ^{31}P signals have been greatly reduced by acetonitrile extraction (especially the signal intensity near 60, 20 and zero ppm), there still remains in Figure A-2 significant ^{31}P signals. (Note that Figure A-2 entailed about 8 times as many scans as the spectrum shown in Figure A-1.) Clearly, not all phosphorus-containing species were extractable in this system. Other extraction solvents (such as ethanol, DMSO or acetone) were not any more successful than acetonitrile, in terms of the extraction of all detected phosphorus-containing species.

Figure A-3 is the 242.9 MHz ^{31}P liquid state NMR spectrum of the deutero-acetonitrile phase after the extraction process. Only two ^{31}P peaks are observed (61.0

ppm and 20.5 ppm). Note the deceptive simplicity of Figure A-3 compared to the more complex patterns observed in Figures A-1 and A-2.

It should be noted that the ^{31}P chemical shifts of the species shown in Scheme A-1 typically vary by as much as 5 ppm, depending on solvent effects and metal complexation. The ^{31}P chemical shifts of alkyl thiophosphoric acids and alkyl phosphoric acids (such as structures **II** and **III**) appear in the literature to be more solvent dependent than are those of thiophosphate (or phosphate) triesters such as structures **I**, **IV**, **V** and **VI** (*A-3*). For example, the ^{31}P chemical shift of $S{=}P(OEt)_2(OPh)$, similar to structure **I**, reportedly varied only 0.2 ppm when dissolved in $CDCl_3$ *vs.* acetone-d_6 (60.88 *vs.* 60.68 ppm), whereas the ^{31}P chemical shift of $S{=}P(OEt)(OPh)(OH)$, similar to structure **III**, varied about 2.1 ppm for the same solvents (56.63 *vs.* 58.71 ppm). The corresponding S-aryl isomerized structure similar to structure **IV** in Scheme A-1, $O{=}P(OEt)_2(SPh)$, varied about 1.4 ppm for the same solvents (20.31 *vs.* 18.92 ppm) (*A-3*).

The ^{31}P chemical shift of organophosphoric acids has been reported to *increase* about 5 ppm when deprotonated to the Na^+ salt, whereas the shift of p-nitrophenylthiophosphoric acid is reported to *decrease* about 6 ppm upon deprotonation (*A-4*).

Metal cation coordination has also been reported to significantly affect ^{31}P chemical shifts of compounds similar to the species in Scheme A-1. For example, the monoester p-nitrophenyl phosphorothioate dianion, $S{=}P(OC_6H_4NO_2)O_2^{2-}$, the dianion of structure **XVIIIb** in Scheme A-1, exhibits decreases in the ^{31}P chemical shift of more than 6 ppm when coordinated to large excesses of either aqueous Cd^{2+} or Zn^{2+} cations. In the presence of aqueous Cd^{2+}, the metal cation is reported to be coordinated to the sulfur

atom, but in the presence of aqueous Zn^{2+} the coordination occurs to either sulfur or oxygen (*A-4,5*).

Taking into account these examples of the sensitivity of ^{31}P chemical shifts of the compounds in Scheme A-1, the ^{31}P chemical shifts observed for pesticide decomposition products extracted from clay minerals may be affected by the presence of any extractable metal cations (in addition to the relative acidity of the intercalated environment); this is especially true for organothiophosphoric acids such as structures **II** and **III**. Ideally, one would synthesize and purify substantial quantities of all the compounds shown in Scheme A-1 and measure the corresponding ^{31}P chemical shifts in a wide variety of solvent environments, including examining the effect of the exchangeable metal cations involved in this study (Ca^{2+}, Zn^{2+}, Al^{3+}, and Cu^{2+}). One could then sorb these synthesized and purified standards onto various clay minerals, to confirm the assignments made for solid-state ^{31}P NMR spectra (ideally obtained at low temperature to slow decomposition reactions, when sorbed on the more catalytically active clay minerals). For both liquid-solution and solid-state ^{31}P NMR experiments, these authentic compounds could be used to 'spike' the NMR samples, providing confirmation of assignments 'in situ', which is more reliable when chemical shifts are quite matrix-dependent as they are here.

Large-scale synthetic efforts were avoided for several reasons: (1) difficulty of purification, (2) safety concerns, and (3) lack of published syntheses for most compounds of interest. Most of the decomposition products shown in Scheme A-1 are reportedly more reactive, especially to hydrolysis, than are the starting pesticides. (*A-4*) During the synthesis of methyl parathion (Experimental section in Chapter 2), product purification was difficult, although repeated liquid-solid column chromatography provided a small

amount of about 99% pure material. Better purification procedures would be required for the more reactive decomposition products.

Safety must be the prime concern when working with these highly toxic compounds, which are easily absorbed dermally. Many of the compounds are hundreds of times more toxic than the starting pesticides, especially the oxon products (structure **VI**); the isomerized structures **IV** and **V** are reportedly also quite toxic. (*A-6, 7*) Any extensive synthetic efforts may require specialized equipment and procedures, such as quick access to emergency doses of acetycholinesterase inhibitor antidote.

Published syntheses were not found for some of the compounds in Scheme A-1, especially for the chlorpyrifos-derived structures. Methyl parathion is one of the most studied of the organophosphorothioate pesticides, including more published ^{31}P NMR chemical shift data for its decomposition products than is the case for most organothiophosphate pesticides. Several synthetic methods (*A-7,8*) have been published for producing the S-methyl isomerized version of methyl parathion (structure **IIIb**), including a non-aqueous purification procedure (*A-6*); some of these methods may be extended to produce the S-ethyl isomer of chlorpyrifos, for example by substituting ethyl iodide for methyl iodide as the alkylating agent.

Synthesis of the S-aryl isomer (structures **IVa** and **IVb**) is more problematic. Structures **II** and **III** may be synthesized by selective hydrolysis of the starting pesticides, but it is difficult to selectively hydrolyze the ethyl or methyl moiety while leaving the aryl ester functionality untouched. (*A-4,6*) Furthermore, organothiophosphoric acids such as **II** and **III** are notoriously difficult to purify as they easily undergo further hydrolysis. (*A-6,7*) For example, in this study, synthesis and purification of compound **IIa** (desaryl

chlorpyrifos, also known as diethyl thiophosphoric acid) by hydrolysis of chlorpyrifos using ethanolic KOH was successful, as described in Chapter 2, but no success was achieved in the production and purification of **IIIa**, desethyl chlorpyrifos, by alkaline hydrolysis of chlorpyrifos. On the other hand, a simple synthetic method has been published (*A-9*) for the oxidation of organophosphorothioates to their oxon form (structure **VI**) using elemental bromine, and was successfully utilized in this study, as will be described later in this appendix.

Since authentic samples of many of the compounds in Scheme A-1 were not available, the utility of preparative thin-layer chromatography (TLC) combined with mass spectral (MS) analysis was investigated as part of this study. Both of these techniques have been reported to be useful for the detection of certain organophosphorothioate decomposition products. (*A-10 through A-14*) During the synthesis of methyl parathion, it was determined that silica TLC plates (developed with a 75% n-hexane/25% ethyl acetate by-volume solvent mix), were able to separate some of the reaction byproducts, including apparently the S,O-isomerized structures (**IVb** and **Vb**), from the unreacted pesticide. The organothiophosphoric acids (structures (**IIb** and **IIIb**) are strongly sorbed by the stationary silica phase, and thus remain at the origin during elution in this solvent system. R_f values measured for this system are shown in Table A-1.

It was determined in this study that solvent extraction (typically using DMSO-d_6, acetonitrile-d_3, methanol or ethanol) of some of the spots observed on the TLC plate produced detectable ^{31}P NMR signals that could be obtained with overnight signal averaging (using the Chemagnetics 600 MHz NMR spectrometer setup described earlier). These same samples could then be analyzed by MS, an advantage utilizing the non-

destructive nature of NMR analysis. Not all of the TLC spots, however, produced detectable ^{31}P NMR signals when a variety of extraction solvents were tested; unreacted chlorpyrifos could be detected (by ^{31}P NMR) in some extract solutions, but other species were not usually detected by ^{31}P NMR.

Published studies of the mass spectral analysis of organothiophosphate pesticides show that extensive fragmentation of the molecular ion occurs, with molecular ion intensities typically 5% or less than the largest MS peak. (*A-13*) Apparently, the undecomposed pesticides typically survive liquid-chromatography (LC) separation during LC-MS analysis, but easily fragment upon ionization. Published reports (*A-11,13,14*) describe a variety of ionization techniques, including electron ionization (EI), chemical ionization (CI) and Fast Atom Bombardment (FAB); in each case, the molecular ion (typically designated M^+) intensity was quite small relative to the fragmentation pattern. In this study electrospray and FAB were attempted, as they are lower energy ionization techniques than is EI (and thus may provide a somewhat more intense molecular ion peak), and instrument time was available.

There are very few reports of MS analysis of the pesticide decomposition products shown in Scheme A-1. These residues are typically more reactive than the parent pesticide, and are more difficult to purify. (*A-6,10*) Published MS analyses (*A-11,12*) of purified methyl parathion oxon and chlorpyrifos oxon samples also exhibit very facile fragmentation, with very small molecular ion peaks. MS analysis has been performed (*A-11*) for the S-methyl isomer of methyl parathion (structure **Vb**), but no reports were found for the MS analysis of the other S,O-isomerized structures shown in Scheme A-1 (structures **IVa**, **IVb** and **Va**).

The very efficient fragmentation of the pesticides and their residues complicates the use of MS analysis for the confirmation of the ^{31}P NMR assignments. Tables A-2 through A-7 list the MS peaks observed for pure chlorpyrifos and purified methyl parathion, obtained by both positive-ion and negative-ion electrospray-ionization ion-trap mass spectrometry; additionally, positive-ion FAB results are shown in Table A-8.

EXPERIMENTAL

Synthesis. The synthesis of methyl parathion is described in the Experimental portion of Chapter 2; the synthesis of the potassium salt of structure **IIa**, desaryl chlorpyrifos (also known as diethylthiophosphoric acid or diethyl phosphorothioate), is described in Chapter 1.

Synthesis of chlorpyrifos oxon and methyl parathion oxon (structure **VI**) was derived from the procedure described by Kim et al. (*A-9*) In this method, the starting pesticide can be oxidized directly in the NMR tube, using an excess of elemental bromine (as an 8M solution in acetonitrile). The authors report rapid and clean reaction at RT, when the pesticide is at low concentrations (in the mM range). They claim to have used HPLC grade acetonitrile, but consideration of the oxon structure suggests that the oxygen atom that replaces S in the pesticide may originate from traces of water in the acetonitrile.

Several reports (*A-6,7,10*) indicate that thermal isomerization of neat methyl parathion in a sealed container results in the production of the S-methyl isomer of methyl parathion.

Synthesis of the S-ethyl isomer of chlorpyrifos was attempted by sealing 260.4 mg (742.7 μmol) in a 0.5 mL glass ampoule and heated at 140 (± 3) °C for 15 hours. The product mixture was a light yellow-brown viscous liquid at room temperature. Most of the product was split and dissolved in acetonitrile-d_3 and acetone-d_6 for NMR analysis; small amounts of the product were dissolved in ethanol and methanol for MS analysis.

NMR. All hardware and conditions used for liquid-solution and solid-state ^{31}P NMR are described in the Experimental sections of Chapters 1 and 2, except that a Varian Inova-300 liquids NMR spectrometer (with a quad-tuned 5mm probe) was also used to obtain some ^{31}P NMR spectra (at a resonance frequency of 121.5 MHz).

TLC. All thin-layer chromatography was performed using Merck brand Silica Gel 60F-254 silica on glass TLC plates, developed (mostly) with a 75% n-hexane/25% ethyl acetate (by volume) solvent mix. When performing preparative TLC, the clay-mineral extracts or reaction mixtures were sorbed onto the TLC plate as a band at the origin, not a single spot. The resolved component bands after developing were visualized by UV, and scraped from the glass using a razor blade. The extractable constituents of each resolved band were then extracted (10 minutes at RT) from the silica-gel using 1.0 mL of anhydrous solvent, typically DMSO-d_6 or acetonitrile-d_3. The extracts were filtered through glass wool or disposable micropore filters before ^{31}P NMR or MS analysis.

Mass Spectrometry. Positive and negative ion MS were obtained via electrospray ionization into an ion-trap, with MS/MS identification of fragmentation patterns, using a Finnegan LCQ Duo LC/MS instrument (the LC hardware was not used; instead a syringe pump was utilized to introduce the samples into the electrospray). Pesticides and residue samples were dissolved (10 to 100 μM) in either methanol or ethanol, each with 1%

formic acid added as a proton source to facilitate positive ion MS, resulting in more intense protonated molecular ion signals ($M + H^+$). Although no sodium or lithium salts were intentionally added to any sample, $M + Na^+$ signals were frequently seen, especially for samples heated in glass; glassware is frequently the source of sodium ions. (*A-15*) If acetonitrile had been used previously in the sample preparation, or was present in the analyte mixture, $M + Li^+$ signals were often detected. Note that double peaks are seen by MS for $M + Li^+$ species because of the mixture of Li-6 and Li-7 isotopes found in nature (percent abundances of 7.4% and 92.6 %, respectively).

Some additional samples were analyzed in a m-nitrobenzyl alcohol matrix using FAB/MS (*A-15*) on a VG Autospec LSIMS instrument.

RESULTS AND DISCUSSION

The ^{31}P chemical shifts observed for the unreacted pesticides (structure **Ia** and **IIb** in Scheme A-1) are in excellent agreement with values reported in the literature. In this study, the ^{31}P chemical shifts were reproducible to within about 1 ppm (of 60.6 ppm for chlorpyrifos, and of 66.8 ppm for methyl parathion) as the solvent was varied (including ethanol, DMSO, acetonitrile, acetone and toluene), also in agreement with values reported in the literature. (*A-6,16,17*) Chlorpyrifos and methyl parathion extracted after being sorbed on Zn-montmorillonite also exhibited ^{31}P chemical shifts within about 1 ppm of these values. Spiking the sample of extracted chlorpyrifos with some additional authentic chlorpyrifos did not change the chemical shift or add a new resonance to the spectrum. This suggests that the extracted chlorpyrifos is not complexed with zinc(II) cations.

Structures **IIa** and **IIb** in Scheme A-1 represent the result of aryl hydrolysis:

diethyl thiophosphate (**IIa**) and dimethyl thiophosphate (**IIb**). The ^{31}P chemical shifts (in D_2O) of these are reported to be 55.3 ppm and 57.7 ppm, respectively. (*A-4,16,18*) In this study they were observed in DMSO at 55.2 and 57.2 ppm, respectively. **IIa** was synthesized in this study by the hydrolysis of chlorpyrifos by ethanolic KOH, as discussed in Chapter 1. It has been reported that coordination to aqueous Cd^{2+} causes a 1.7 ppm decrease in the ^{31}P chemical shift (i.e., increased shielding) when **IIa** is observed at saturating Cd^{2+} concentrations. (*A-19*)

Structures **IIIa** and **IIIb** in Scheme A-1 represent the result of alkyl hydrolysis: desethyl chlorpyrifos (**IIIa**) and desmethyl methyl parathion (**IIIb**). The ^{31}P chemical shift of the latter has been reported in the literature, including in one report a value of 56.1 ppm in deuterochloroform. (*A-19*) Desethyl chlorpyrifos (**IIIa**), however, has apparently not been reported in the literature. Desethyl ethyl parathion is at 55.1 ppm (in $CDCl_3$; *A-20*) and O-methyl-O-phenyl-phosphorothioate (similar to **IIIa**, but Ar = Ph) is reported at 56.6 ppm in $CDCl_3$ (and 58.7 ppm in acetone-d_6). (*A-3*). There is apparently no published information on the effect of deprotonation or metal cation complexation on the ^{31}P chemical shifts of **IIIa** and **IIIb**, but as discussed in the Introduction to this appendix, O-p-nitrophenyl phosphorothioate (p-nitrophenylthiophosphoric acid) shows decreases of up to 6 ppm in the ^{31}P chemical shift upon deprotonation or Zn^{2+} complexation (*A-4*).

The literature shifts discussed above indicate that, although the hydrolysis products (**II** and **III** in Scheme A-1) are well separated in chemical shift from the unreacted pesticides, at present one cannot reliably distinguish the ^{31}P NMR peaks due to alkyl vs. aryl hydrolysis using ^{31}P chemical shift alone. Variations in solvent

environment, including possible metal cation complexation, are expected to cause larger variations in the ^{31}P chemical shift than due to the structural difference between the desaryl vs. desalkyl species.

Structures **IV** and **V** represent the possible S,O-isomerized pesticides, in which the sulfur atom is present as either an S-aryl (structure **IV**) or S-alkyl group (structure **V**). The latter situation is apparently recognized as being much more common (*A-21*); there are several reports of the ^{31}P chemical shifts of S-methyl and S-ethyl organothiophosphates pesticides isomers, but very little information regarding the shifts for similar S-aryl compounds. For example, the S-methyl isomer of methyl parathion (**Vb**) has a ^{31}P chemical shifts of 27.9 to 27.5 ppm, depending on solvent. (*A-6,16,21*) No value for the ^{31}P chemical shift of structure **Va** was found in the literature, although values were found for the S-ethyl isomers of various pesticides with structures similar to that of chlorpyrifos (varying only in the aryl group), ranging from 28 to 24 ppm. (*A-16*)

Apparently, when organothiophosphates are thermally, chemically or photochemically isomerized, only the S-alkyl isomer is formed, as no report of the detection of the S-aryl isomer is mentioned in any literature reports. This possibility (of the S-aryl isomer of chlorpyrifos or methyl parathion) was included in Scheme A-1 to be as complete as possible, as this isomerization is (in principle) possible, although thought to be less likely than isomerization to the S-alkyl structures reported in the literature. (*A-6,7,22*) A few ^{31}P chemical shift values of a similar S-aryl structure have been reported for S-phenyl O,O-diethylphosphorothioate (same as **IVa** except Ar = Ph): one older reference gives a value of 22 ppm (*A-23*), while a more recent paper reports shifts of 20.3 ppm in $CDCl_3$ and 18.9 ppm in acetone-d_6 (*A-3*). This suggests that S-aryl isomers of

organophosphorothioate pesticides exhibit ^{31}P chemical shifts that are about 7 ppm smaller (higher shielding) than for the corresponding S-alkyl isomer.

Synthesis of the S-aryl isomer of chlorpyrifos might be achieved by reaction of the corresponding aryl thiol (ArSH, where Ar = 3,5,6-trichloropyridyl) with diethylphosphorochloridate, although this thiol does not appear to be

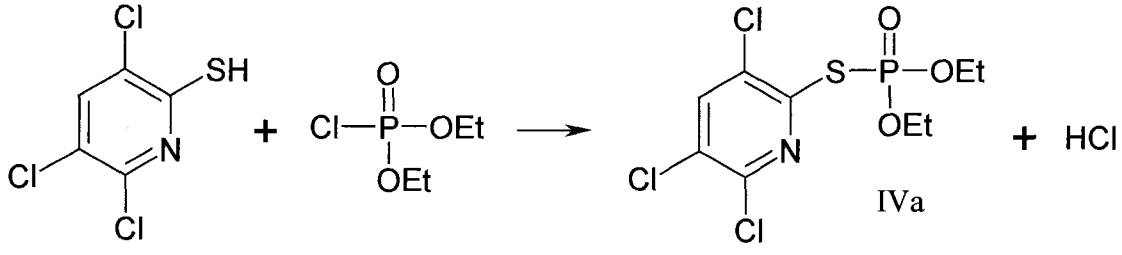

IVa

commercially available and would also require synthesis.

The oxon form of organothiophosphate pesticides are of particular concern in the literature because of their high mammalian toxicity. (*A-6,9,22*) Methyl parathion oxon (structure **VIb**) is reported to have a ^{31}P chemical shift of – 4.8 ppm in toluene. (*A-16*) Other dimethyl aryl phosphates (i.e., other similar pesticide oxons with R = Me) also have ^{31}P chemical shifts reportedly between – 4 and – 5 ppm, whereas diethyl aryl phosphates (i.e., other similar pesticide oxons with R = Et) have ^{31}P chemical shifts reportedly around – 6 and – 7 ppm. (*A-16,24*) Thus, we may predict a ^{31}P chemical shift of – 6 to – 7 ppm for chlorpyrifos oxon (VIa). Although proton NMR chemical shifts are reported for chlorpyrifos oxon (structure **VIa**; *A-9*), no ^{31}P chemical shift values have been found in the literature.

Figure A-4 shows ^{31}P NMR evidence of oxidation of chlorpyrifos and methyl parathion to the oxon forms (structure **VI**) using elemental bromine in acetonitrile, as was reported by Kim, Lee, Park and Lee (*A-9*). They report rapid and efficient oxidation

(89% yield) when a 2 mM solution of chlorpyrifos in HPLC grade acetonitrile was mixed (for a few minutes) with an equal volume of 20 mM Br_2 in acetonitrile. In this study, 0.028 mmol chlorpyrifos was dissolved in 1.0 mL HPLC grade acetonitrile (in a 5mm NMR tube), to which was added 0.10 mL (0.82 mmol) elemental bromine. The NMR tubes were stirred with a clean quartz rod for two minutes (to allow excess bromine to evaporate), and then covered with a polyethylene cap. Figure A-4A shows the 242.9 MHz ^{31}P NMR spectrum of this bromine-oxidized chlorpyrifos sample in HPLC grade acetonitrile. In addition to unreacted chlorpyrifos at 62.1 ppm, the large product peak at – 7.5 ppm is chlorpyrifos oxon (structure **VIa**). (This assignment was confirmed by comparing the proton NMR spectrum of this sample to the chemical shifts and coupling constants reported for chlorpyrifos oxon in ref. *A-9*). The smaller byproduct peaks at + 0.4 ppm and – 0.7 ppm are unidentified, but may be diethyl or monoethyl phosphoric acid, or even inorganic phosphoric acid. (*A-3*) The oxon is reported to be hydrolytically less stable than the starting pesticide, as are the S-alkyl isomers, structure **V**, and the desalkyl or desaryl hydrolysis products, structures **II** and **III**. (*A-1,4,6*) Thus, if any water is present in the acetonitrile solvent (for example, water adsorbed from the air), it may react very quickly with the oxon. The overall yield of chlorpyrifos oxon is 76% (as determined by spectrum integration), while byproduct formation (near zero ppm) represents 6% of the total ^{31}P NMR signal integral.

Note that water appears to be the source of the oxygen atom in the P=O moiety of the oxon; no special care was taken in this study (or apparently by Lee et al. in ref. *A-9*) to dehydrate the HPLC grade acetonitrile. This conclusion is confirmed in Figures A-4B, which show the effect of added excess elemental bromine to technical grade methyl

parathion (about 92% pure) dissolved in 1.0 mL anhydrous acetonitrile-d_3 (from a sealed ampoule); the solvent was exposed to atmospheric humidity for less than 2 minutes. Only a small peak is observed in Figure A-4B for methyl parathion oxon (– 4.1 ppm), representing only 4% yield. The large product peak at 16.1 ppm is unidentified (perhaps a phosphorothiobromidate?) and accounts for 68% of the total ^{31}P integral.

The sample shown in Figure A-4C was prepared identically to that shown in Figure A-1B, except for the addition of 0.10 mL deionized water to the 1.0 mL acetonitrile-d_3 solvent (containing 10 mg technical grade methyl parathion), prior to the addition of the 0.20 mL bromine. In this case, the oxon of methyl parathion (– 4.2 ppm) is the largest product, representing a 27 % yield by ^{31}P NMR. Note that, in the presence of excess water, the unidentified 16.1 ppm seen in Figure A-1B is no longer visible. The peaks at 74.2 ppm and 28.2 ppm are impurities present (structures **XX** and **V**, respectively) in the technical grade methyl parathion used for this experiment, and appear unchanged by the elemental bromine oxidation.

Several researchers have reported that heating sealed samples of neat organothiophosphate pesticides can result in isomerization to the S-alkyl structure. For example, Fukuto *et al.* (*A-10*) showed that heating purified methyl parathion in a sealed ampoule at 125 °C for 7 hours produced a mixture of S-methyl parathion (the major product; structure **Vb**), the methyl paraoxon (**VIb**), unreacted methyl parathion (**Ib**) and at least one unknown substance. These were identified using gas-liquid chromatography by comparison to authentic samples, in addition to confirmation by TLC and ^{1}H NMR. Methyl parathion is known to be especially prone to thermal decomposition and rearrangement; other organothiophosphate pesticides such as chlorpyrifos are reported to

be more thermally stable than methyl parathion, especially when they contain O-ethyl groups instead of O-methyl. Likewise, Rengasamy and Parmar produced isomalathion in about 50% yield by refluxing malathion in N,N-dimethylformamide at 110 °C in the presence of silica gel. (*A-22*)

Figure 1-8D shows the effects of heating chlorpyrifos in refluxing toluene (105 °C) for three days. As discussed in Chapter 1, most of the chlorpyrifos remained unreacted, although small peaks at 69.3 and 53.7 showed that some trans-esterification reaction had occurred to form structures **XX** and **XIX**:

$$2\ (EtO)_2(ArO)P(=S) \rightarrow (EtO)_3P(=S) + (EtO)(ArO)_2P(=S)$$

Additional small peaks are seen in Figure 1-8D, including chlorpyrifos oxon (-6.7 ppm) and three peaks near the expected shift for S-ethyl chlorpyrifos (26.4, 24.9 and 23.7 ppm). These peaks were not identified, although it is thought to be likely that one represents the desired S-ethyl chlorpyrifos (**Va**).

Liquid-solution ^{31}P NMR of heated neat chlorpyrifos.

In an attempt to produce S-ethyl chlorpyrifos (structure **Va**), which has not been reported in the literature, pure chlorpyrifos was heated as a neat substance in a sealed ampoule, and also refluxed in N,N-dimethylacetamide; the latter situation will be discussed in a later section. Figure A-5 shows the 121.5 MHz ^{31}P NMR spectrum of neat chlorpyrifos heated at 140 °C for 15 hours in a sealed glass ampoule; after cooling, the sample was dissolved in acetone-d_6 as the NMR solvent. Semi-quantitative NMR parameters (gated decoupling to eliminate nOe enhancements, and using 90° ^{31}P pulses every 9.6 seconds) were utilized to obtain spectrum integrals for estimating the relative amounts of products formed. (These parameters gave good quantitation in previous

experiments, and using longer relaxation delays had no significant effect on the relative integrals.)

The largest peak seen in Figure A-5, at 62.0 ppm, is unreacted chlorpyrifos; its relative integration of 93.1 % shows that most of the starting chlorpyrifos remained unchanged when neat chlorpyrifos was heated at 140 °C for 15 hours . The peak at – 7.1 ppm represents chlorpyrifos oxon (as discussed above), with a relative integral of 3.9% of the detected phosphorus. The peak at 24.9 ppm is assigned as the desired S-ethyl isomer of chlorpyrifos, but has a relative integral of only about 0.3 %. A peak at 94.8 ppm was also seen with a relative integral of 2.4 %; a smaller nearby peak at about 95.4 ppm represented only about 0.3 % of the total ^{31}P detected by NMR. Features at about 35.5 ppm and – 10.5 ppm were identified as instrumental artifacts.

Based on Figure A-5, it is clear that only a small amount of chlorpyrifos was thermally isomerized to S-ethyl chlorpyrifos (structure **Va**), in contrast to the rapid and facile isomerization reported for the methyl parathion (*A-7,10*); note the S-methyl methyl parathion peak at 26.8 ppm seen in Figure A-6, which shows the 242.9 MHz liquid-solution ^{31}P NMR spectrum of technical grade methyl parathion (synthesis of methyl parathion described in Chapter 2). Instead, Figure A-5 shows that when heating neat chlorpyrifos at 140 °C, oxidation of chlorpyrifos to its oxon form (**VIa**, - 7.1 ppm) predominated, plus the production of the previously unseen peak at 94.8 ppm. Investigation of the literature shows that phosphorodithioate esters, containing both P=S and –SR moieties, exhibit ^{31}P resonances between 90 and 100 ppm (*A-16*). Thus, the peak at 94.8 ppm could represent either structure **XXI** or **XXII**, the S-alkyl or S-aryl dithio derivatives of chlorpyrifos:

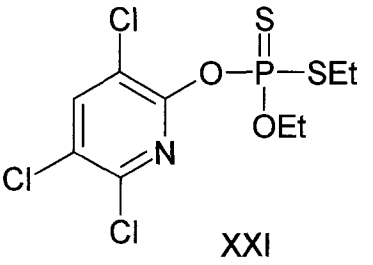

XXI

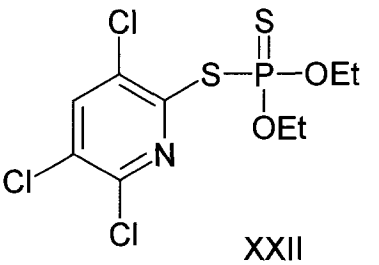

XXII

The amount of oxygen gas present in the 0.3 mL air included in the sealed glass ampoule is estimated to be less than 3 μmoles. Considering that 743 μmoles chlorpyrifos was initially in the sealed ampoule, the amount of oxygen gas also present was clearly insufficient to produce the amount of chlorpyrifos oxon detected (about 29 μmoles oxon). Thus, direct oxidation of chlorpyrifos by oxygen gas could have only contributed a small fraction of the oxon product observed. Instead, it is proposed that the chlorpyrifos oxon was mostly produced by a type of disproportionation reaction between two chlorpyrifos molecules:

$$2\ (EtO)_2(ArO)P(=S) \rightarrow (EtO)_2(ArO)P(=O) + (EtO)(EtS)(ArO)P(=S)$$

or, $$2\ (EtO)_2(ArO)P(=S) \rightarrow (EtO)_2(ArO)P(=O) + (EtO)_2(ArS)P(=S)$$

The first product shown in both reactions is chlorpyrifos oxon (structure **VI**), whereas the latter is the S-ethyl dithioate derivative of chlorpyrifos (in the first reaction) or the S-aryl dithioate derivative of chlorpyrifos (in the second reaction).

Scheme A-2 shows possible reaction mechanisms involved to produce the assigned products: Mechanism 1 is the possible bimolecular isomerization reaction of chlorpyrifos to S-ethyl chlorpyrifos, and Mechanism 2 is a possible two-step reaction of two chlorpyrifos molecules to produce both oxon and the S-ethyl dithioate derivative of chlorpyrifos.

Scheme 2 -- possible reaction mechanisms for thermal modification of neat chlorpyrifos

Mechanism 1

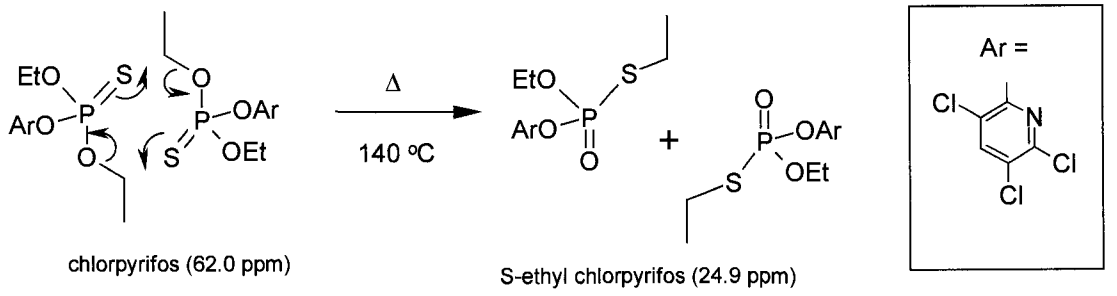

Mechanism 2

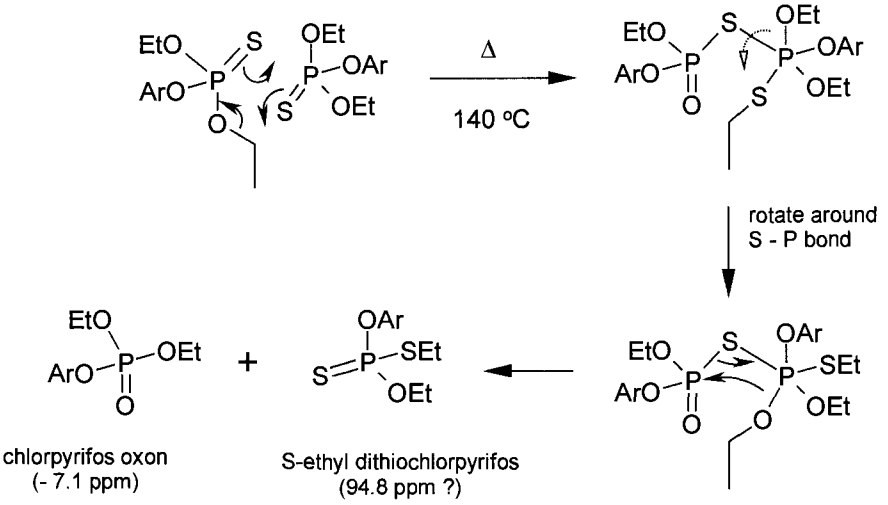

Mechanism 3

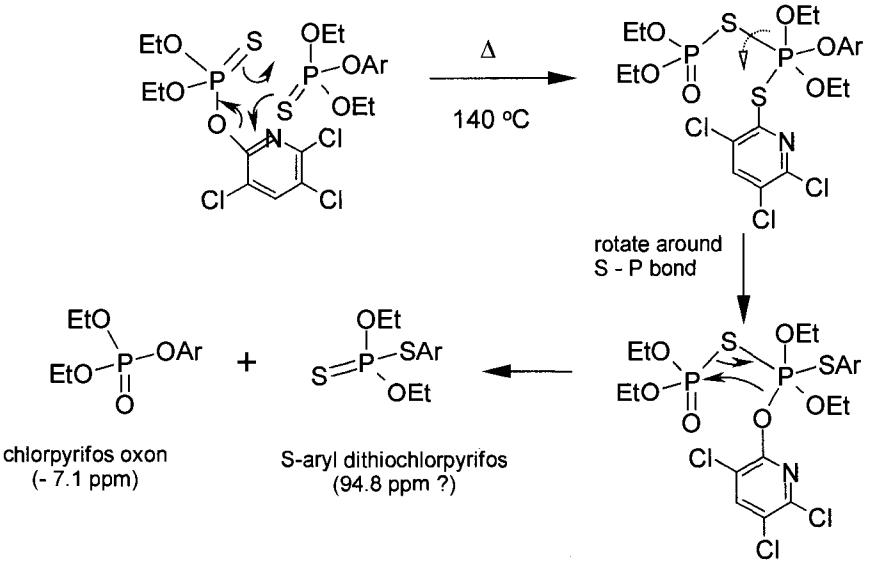

Note that although the mechanisms in Scheme A-2 are shown as involving

concerted steps (a single step in Mechanism 1, but two concerted steps in Mechanism 2), it is quite possible that each concerted step shown is in actuality a series of steps involving ionic intermediates. Mechanism 3 is similar to Mechanism 2, but involves nucleophilic attack on the oxygen-bonded aryl carbon instead of nucleophilic attack on the secondary carbon of an ethoxy group, to produce the S-aryl dithioate derivative of chlorpyrifos (along with oxon).

The bimolecular mechanisms shown in Scheme A-2 could explain why no dithioate derivatives of chlorpyrifos were detected (between 90 and 100 ppm in the ^{31}P spectrum, Figure 1-8D) when pure chlorpyrifos was refluxed in toluene for three days. Heating neat chlorpyrifos (m.p. = 42 °C) produced a much higher concentration of chlorpyrifos reactant, favoring bimolecular reactions such as those shown in Scheme A-2.

Note also in Figure A-5 the absence of ^{31}P peaks near 54 ppm and 69 ppm, indicating that no significant amount of trans-esterification reaction occurred when neat chlorpyrifos was heated in the sealed ampoule:

$$2\ (EtO)_2(ArO)P(=S) \rightarrow (EtO)_3P(=S) + (EtO)(ArO)_2P(=S)$$

Both of these products (O,O,O-triethyl phosphorothioate, structure **XX**, and the bis aryl derivative of chlorpyrifos, **XXI**) were previously detected in the ^{31}P NMR spectrum of chlorpyrifos refluxed in toluene (Figure 1-8D) at chemical shift values of 69.3 ppm and 53.7 ppm, in good agreement with a reported value of 68.6 ppm for structure **XX** and values of 56.3 and 56.2 ppm for similar bis aryl organothiophosphate pesticides (diazinon and ethyl parathion, *A-16*).

MS analysis of heated neat chlorpyrifos.

In order to confirm the assignments of the oxon and dithioate structures assigned

to Figure A-5, some of this NMR sample (roughly 10 μL) was diluted to about 100 μM in ethanol (with 1% added formic acid) and immediately analyzed using the electrospray ion-trap MS instrument previously described. Mass spectral analysis of the reaction products was pursued because the isotopic patterns present in chlorpyrifos and its aryl-containing derivatives make it easy to detect and distinguish even small MS signals, even in the presence of the frequently large background signals observed during electrospray MS analysis.

Figure A-7A shows the simulated mass spectrum (using Xcalibur software) expected for the molecular ion of chlorpyrifos, with the distinctive isotopic distribution pattern arising from the presence of three Cl atoms; chlorine occurs as a pair of isotopes, ^{35}Cl and ^{37}Cl, in a 75.53% / 24.47% abundance ratio, giving rise to two larger (and almost equally intense) peaks at [M] and [M+2], where M refers to the molecular ion containing three ^{35}Cl atoms (also known as the exact mass), and M+2 contains two ^{35}Cl and one ^{37}Cl atom. Also present are much smaller MS peaks at M+1 (11%), M+3 (12%), M+4 (36%), M+5 (4%) and M+6 (5%), which reflect the isotopic distributions of all the elements in chlorpyrifos, such as hydrogen, carbon and sulfur, in addition to chlorine isotopes.

Also shown in Figure A-7 (as Figure A-7B) is the simulated isotopic distribution pattern arising from the presence of *six* Cl atoms, as may occur if clustering happens during MS analysis, as is reportedly (*A-13,14*) quite common during ion-trap or FAB mass spectrometry. Such clustering is apparent in many of the mass spectra obtained in this study, obtained both by electrospray and FAB, observed as strong MS peaks ranging from about 400 daltons to over 1000 daltons. Unreacted chlorpyrifos has an exact mass (i.e., all atoms present as their most abundant isotope, so chlorines are present as

chlorine-35) of 348.9263 daltons. Thus, detection of MS species with much greater m/Z values reflects the formation of clusters, a phenomenon quite common in electrospray MS. In practice, the high molecular-weight MS peaks are frequently more intense than seen for the low molecular-weight un-clustered fragments.

The distinctive isotope distribution pattern expected for MS species containing either 3 or 6 chlorine atoms makes it easy to distinguish MS fragments containing either one or two trichloropyridyl groups (the aryl functionality in chlorpyrifos); we shall refer to these as the Cl_3 or Cl_6 isotope patterns. These patterns make it easy to locate even small MS peaks of interest in the presence of background signals.

Figure A-8 shows the positive-ion electrospray MS spectrum of chlorpyrifos heated at 140 °C for 15 hours (^{31}P liquid-solution NMR shown in Figure A-5) as an approximately 100 μM solution in ethanol with 1% formic acid added as a protonation source. Figure A-8A shows a scan from m/Z = 50 to 1200; Figure A-8B shows a subsequent narrower scan (from m/Z = 50 to 500). The assignment of some of the MS signals of chlorpyrifos and thermally-treated chlorpyrifos are shown in Tables A-2 and A-3. Cl_3 isotope patterns are seen for [oxon + H^+] (m/Z = 334,336), [oxon + Na^+] (356,358), [chlorpyrifos + H^+] (350,352) and [chlorpyrifos + Na^+] (372,374), confirming the presence of both the oxon species and unreacted chlorpyrifos. Fragments corresponding to the loss of either one or two neutral C_2H_4 molecules from [oxon + H^+] are seen at m/Z = 306,308 and 278,280 respectively. This loss of neutral ethylene is a very commonly seen fragmentation in the MS of ethoxy-containing phosphorothioate triester pesticides (*A-13,14*); similar fragments representing the loss of one or two neutral ethylene molecules were seen (at m/Z = 306,308 and 278,280) in the positive-ion

electrospray MS spectra of pure chlorpyrifos obtained in this study (Figure A-9, and subsequent MS/MS analyses (not shown)).

Note that although much more unreacted chlorpyrifos is present in the sample represented in Figure A-8, the MS signals due to the oxon are much more intense. (In fact, in the three minutes between acquiring the mass spectra shown in Figures 8B and 8A, the [chlorpyrifos + H^+] signal decreased significantly.) This appears to reflect a greater ability of the oxon to form positive ions (by either protonation from the added formic acid, or the formation of the complex with a sodium ion) in this solvent system (and under the MS conditions utilized) than for unreacted chlorpyrifos.

The two Cl_6 isotope patterns seen in Figure A-8 near m/Z = 700 are assigned as [oxon + oxon + Na^+] for the pattern from 689 to 695, and [oxon + chlorpyrifos + H^+] at 705 to 711; see Figure A-8C for an expansion of this region of the mass spectrum. Note that no obvious Cl_6 isotope pattern is detected in Figure A-8A for the bis aryl derivative of chlorpyrifos (structure **XIX**) at m/Z = 501 to 507 (if protonated), nor at 523 to 529 (if complexed with Na^+), in agreement with the lack of a ^{31}P NMR signal near 54 ppm in Figure A-5. Likewise, no signal due to the other product of chlorpyrifos trans-esterification, $(EtO)_3P(=S)$ (structure **XX**), which would give rise to a single peak at m/Z = 199 (if protonated) or m/Z = 221 (if complexed to Na^+), is seen. Therefore, in agreement with the ^{31}P NMR results shown in Figure A-5, we may conclude that no significant trans-esterification occurred when neat chlorpyrifos was heated in the sealed ampoule at 140 °C for 15 hours.

The assignments of the Cl_3 or Cl_6 isotope patterns given above (and shown in Tables A-2 and A-3) were confirmed by MS/MS analysis. For example, Figure A-10

shows the MS/MS fragmentation spectrum of the Cl_6 isotope pattern centered at about m/Z = 691, assigned as [oxon + oxon + Na^+]. The fragmentation observed is almost entirely due to the loss of a neutral oxon molecule to leave the Cl_3 isotope pattern due to [oxon + Na^+], observed at m/Z = 356,358. A small amount of neutral ethylene loss also occurred during the loss of neutral oxon, to give the small Cl_3 isotope pattern due to [oxon – C_2H_4 + Na^+], observed at m/Z = 356,358.

Likewise, the MS/MS spectrum observed for the fragmentation of the MS peak due to the [oxon + H^+] at m/Z = 334,336 shows the loss of one or two neutral ethylene molecules, as shown by the peaks at m/Z = 306,308 and m/Z = 278,280 in Figure A-11. Figure A-12 shows even simpler fragmentation is observed for the [chlorpyrifos + Na^+] MS signal at m/Z =372,374 with only the loss of a single neutral ethylene molecule (yielding the peaks at m/Z = 344,346) under the experimental conditions used.

The MS/MS fragmentation of the [chlorpyrifos + H^+] MS signal at m/Z = 350,352 is more complex, as shown in Figure A-13. In addition to the loss of either one or two ethylene molecules (m/Z = 322,324 and 294,296 respectively), a Cl_3 isotope pattern is seen at m/Z = 198,200 which is assigned as [ArOH + H^+]; this type of fragmentation has been reported in the literature for CI/MS analyses of similar organothiophosphate triester pesticides. (*A-13,14*) Also seen in Figure A-13 is a 'singlet' MS/MS peak at m/Z = 153 which is assigned as $[(EtO)_2P{=}S]^+$, a fragment also previously reported for CI/MS analyses of similar compounds. (*A-13,14*) A tentative assignment for Figure A-13 is that the Cl_3 isotope pattern at m/Z = 304,306 represents the loss of neutral ethanol: [chlorpyrifos – C_2H_5OH + H^+], giving the fragment structure $[(EtO)(ArO)P{=}S]^+$. A MS/MS signal seen in Figure A-13 near m/Z = 334 is not assigned, as it is not clear

whether this is possibly a distorted Cl_3 isotope pattern at either 332,334 or 334,336; a Cl_3 isotope pattern at 332,334 could represent the loss of neutral water from the starting [chlorpyrifos + H^+] structure.

Returning to Figure A-8A, the positive-ion electrospray MS spectrum for neat chlorpyrifos heated at 140 °C for 15 hours, at least three Cl_3 isotope patterns are observed in the range m/Z = 420 to 560; this region is expanded in Figure A-8D . Comparison to the background spectrum shown in Figure A-14, obtained by injecting only the ethanol/ 1% formic acid solvent into the electrospray unit just prior to analyzing the thermally-treated chlorpyrifos sample, shows that although many background signals were detected, there are no obvious Cl_3 isotope patterns in the range m/Z = 420 to 560 of this background mass spectrum. Thus, those signals observed in Figure A-8D must arise from the thermally-treated chlorpyrifos sample in some manner. Considering that they appear to be Cl_3 isotope patterns with masses 114, 130, 146 and 156 daltons greater than the molecular mass of [chlorpyrifos + H^+], these probably represent clustering of protonated (or possibility sodiated) chlorpyrifos with neutral solvent molecules such as ethanol or formic acid (both of which have a molar mass of 46 daltons) and possibly traces of water (note that the first three Cl_3 isotope patterns in this range appear to be separated by 18 daltons, the molecular mass of neutral water). No MS/MS analysis was performed on the apparent Cl_3 isotope patterns in the range m/Z = 440 to 540.

The MS results shown thus far confirm the presence of chlorpyrifos oxon (structure **VIa**) in the thermally-treated chlorpyrifos material, in agreement with the observed ^{31}P NMR peak for chlorpyrifos oxon seen in Figure A-5. What then about the possible presence of either the S-ethyl or S-aryl dithio derivatives of chlorpyrifos, as

discussed above for the ^{31}P NMR peak at 94.8 ppm? These dithio isomers would show a Cl_3 isotope pattern at 366,368 daltons if protonated, or 388,390 if complexed to Na^+. Neither of these possibilities is observed in Figure A-8B, but that alone does not prove that dithio derivatives of chlorpyrifos are not present in the thermally-treated material. The electrospray MS response of various compounds appears to vary greatly depending on solvent and instrumental conditions. For example, in ethanol with 1% formic acid, the mass spectrum shows more intense signals for chlorpyrifos oxon than for unreacted chlorpyrifos, although the latter is much more abundant in the sample according to the semi-quantitative NMR analysis. It is quite possible that a dithio derivative of chlorpyrifos is not effectively ionized under these conditions.

Figure A-15 and Table A-5 show the negative ion electrospray MS analysis performed on the same sample previously analyzed by positive ion electrospray MS (shown in Figure A-8), namely neat chlorpyrifos heated in the sealed ampoule at 140 °C for 15 hours, followed by dissolving into ethanol with 1% formic acid. In general, negative ion electrospray MS is less useful than the positive ion version, since negative molecular ions are not formed or detected; only stable anion fragments are seen. For example, in Figure A-15 the Cl_3 isotope pattern at m/Z = 196,198 is assigned as $[ArO]^-$, the Cl_3 isotope pattern at m/Z = 320,322 is assigned as $[(EtO)(ArO)PSO]^-$ (i.e., deprotonated desethyl chlorpyrifos), and the 'singlet' at m/Z = 169 is assigned as $[(EtO)_2PSO]^-$ (deprotonated desaryl chlorpyrifos).

More intriguing in Figure A-15 are the 'singlet' at m/Z = 185 and the Cl_3 isotope pattern at m/Z = 212,214; the former appears to be the deprotonated desaryl dithio derivative of chlorpyrifos, namely either $[(EtO)_2PS_2]^-$ or $[(EtO)(EtS)PSO]^-$ (the other

isomer, $[(EtS)_2PO_2]^-$, is not thought to be as likely). The Cl_3 isotope pattern at m/Z = 212,214 appears to be $[ArS]^-$. Neither of these MS signals were observed in the negative ion electrospray MS spectrum of pure chlorpyrifos dissolved in methanol with 1% acetic acid, as shown in Figure A-16. Thus, the presence of these negative ion MS fragments supports the conclusion that the thermally-treated chlorpyrifos does contain a significant amount of a dithio derivative of chlorpyrifos, especially the S-aryl dithio derivative.

In this study, it was observed that chlorpyrifos appears to be more effectively protonated during electrospray when analyzed using methanol with 1% formic acid as solvent, than when ethanol was used with 1% formic acid or 1% acetic acid. Ethanol was originally used to minimize the possible exchange of an ethoxy group by a methoxy group. Figure A-17A shows the positive ion electrospray mass spectrum observed for the previously discussed thermally-treated chlorpyrifos (15 hours at 140 °C in a sealed glass ampoule), but now using methanol with 1% formic acid as solvent. (The corresponding background electrospray spectrum using the methanol/1% formic acid solvent is shown in Figure A-18, for comparison purposes.)

Figure A-17A shows two Cl_3 isotope patterns below m/Z = 500, at 350,352 daltons and at 366.6,368.6 daltons. The assignment of the first Cl_3 isotope pattern is clearly [chlorpyrifos + H^+], but the assignment of the Cl_3 isotope pattern at 366.6,368.6 daltons is more problematic. (See Figure A-17B for an expansion of the region m/Z = 330 to 410). If present, the protonated dithio isomers would appear at m/Z = 366.0,368.0 and thus appear to almost fit the pattern seen, except for the 0.6 dalton discrepancy. To this point, m/Z values have been listed and discussed with values rounded to the nearest dalton, for convenience and improved readability of the text. That was justifiable since, to

this point, the agreement between the calculated exact masses and observed MS peaks has been to within 0.1 daltons. In the case of the Cl_3 isotope pattern at m/Z = 366.7,368.6 however, the 0.6 dalton discrepancy appears to be significant. One possible explanation for the discrepancy might be that overlap of the Cl_3 isotope pattern with background signals shifts the apparent peak maxima up about 0.6 daltons (or even perhaps down 0.4 daltons from m/Z = 367.0,369.0), although this m/Z region does not seem to have significantly more intense background signals than other regions of interest (see Figure A-18 for background spectrum).

A more serious concern involved in the assignment of the Cl_3 isotope pattern at m/Z = 366.7,368.6 is the MS/MS fragmentation results seen for this peak pattern. Figure 19 shows that the largest fragmentation product occurs at m/Z = 350,352 , which appears to be simply [chlorpyrifos + H^+]. Smaller fragments seen by MS/MS in Figure A-19 include a Cl_3 isotope pattern at m/Z = 304,306, and a 'singlet' at m/Z = 169. The former represents the loss of 46 daltons from [chlorpyrifos + H^+], probably due to the loss of neutral ethanol. The latter fragment (m/Z = 169) represents the loss of neutral ArH from protonated chlorpyrifos, leaving the positive ion fragment $[(EtO)_2PSO]^+$.

A better possibility is that the Cl_3 isotope pattern observed at m/Z = 366.6,368.6 is due to [chlorpyrifos + NH_4^+], which has a calculated exact mass of 366.96, giving a Cl_3 isotope pattern of 367.0,369.0 (to the nearest 0.1 dalton). Loss of neutral NH_3 would then create the fragment [chlorpyrifos + H^+], which dominates the MS/MS fragmentation results seen in Figure A-19. Although no ammonia or ammonium salts were added (or expected) in the thermally-treated chlorpyrifos, ammonia is a deprotonating agent commonly utilized by other users of the LCQ-MS instrument, and is thus is a quite likely

contaminant. Indeed, other positive ion electrospray mass spectra for pure chlorpyrifos (obtained in this study), when using methanol with 1% formic acid (or 1% acetic acid) as the solvent system, frequently showed a Cl_3 isotope pattern at m/Z = 367,369.

In conclusion, it is likely that [chlorpyrifos + NH_4^+] is being observed in Figures A-17A and A-17B, and no molecular ions are detected for the dithio derivatives of chlorpyrifos. The apparent absence of molecular ions for either the S-ethyl or S-aryl dithio derivatives does not prove they are not present, since they may not form positive ions as easily as either chlorpyrifos oxon or unreacted chlorpyrifos. Indeed, as discussed above, there is indirect MS evidence for the presence of at least one of the dithio derivatives (such as the detection of ArS^- and either $[(EtO)_2PS_2]^-$ or $[(EtO)(EtS)PSO]^-$).

Thus, it may be concluded that the MS analyses discussed above confirm the presence of chlorpyrifos oxon in the thermally-treated chlorpyrifos, but merely suggest the presence of a dithio derivative. MS detection of the presence of the S-ethyl or S-aryl isomers of chlorpyrifos (structures **Va** and **IVa**, respectively) is more problematic, since these isomers have exactly the same mass and isotopic distribution as unreacted chlorpyrifos; thus, there is not a distinguishable molecular ion to detect. Nothing was found in the MS analyses that identifies a fragment unique to either structure **Va** or **IVa**, although the detection of ArS^- may be (in part?) due to fragmentation of **IVa**, the S-aryl isomer of chlorpyrifos.

Liquid-solution ^1H and ^{13}C NMR of heated neat chlorpyrifos.

Liquid-solution ^1H NMR is another tool that may identify the presence of structure **Va**, the S-ethyl isomer of chlorpyrifos, or at least the presence of $-SCH_2CH_3$ groups within the sample. The methylene protons of the –OEt group in chlorpyrifos (**Ia**)

appear as a complex multiplet centered at 4.41 ppm (in acetone-d_6), while the ethyl methylene protons in chlorpyrifos oxon (**VIa**) were observed at 4.36 ppm. (*A-9*) No reference was found in the literature that even mentioned the S-ethyl isomer of chlorpyrifos, much less a value for its proton chemical shifts. A few proton chemical shift values were found (*A-25*) for methylenes in molecules of the general structure $(R'X)_2P(=X)\text{-}SCH_2R$, where X = O or S; these values are all in the range 3.0 to 3.2 ppm.

Figure A-20A shows the 300 MHz ^1H NMR spectrum, including chemical shifts, of the previously-mentioned heat-treated chlorpyrifos (140 °C neat for 15 hours) dissolved in acetone-d_6. The spectrum is dominated by the 93% of the sample that is unreacted chlorpyrifos. The four largest peaks (from left-to-right) are the aryl proton, CH_2 protons of the ethyl groups, residual hydrogen in the perdeuteroacetone solvent, and the CH_3 protons of the ethyl groups. Figure A-20B shows only the region from 4.6 to 1.4 ppm; note the complexity of the methylene signal at 4.41 ppm, which includes about 10 Hz scalar coupling to the ^{31}P nucleus. Kim et al describe the methylene multiplet as a doublet of quartets of doublets. (*A-9*) Also note that the methylene protons of chlorpyrifos oxon (3.9 mol %) are entirely obscured by the much more intense signal due to the methylenes of unreacted chlorpyrifos (chemical shifts of 4.41 and 4.36 ppm, respectively).

Figure A-20C is the same as A-20B, except the vertical scale is expanded by a factor of about 64. The satellites about each of the off scale peaks are ^{13}C satellites, and are 0.55% the intensity of their centerbands. New peaks are now clearly visible, only somewhat larger than the ^{13}C satellites of the methylene proton signal: a broad singlet at 2.85 ppm, which is a trace of water in the solvent, and a complex multiplet centered at

3.21 ppm that has the same splitting pattern as in the methylene peak of chlorpyrifos. Considering the chemical shift range reported in the literature (*A-25*) for similar compounds (3.0 to 3.2 ppm), this peak can be assigned as the methylene protons of an S-ethyl group ($-SCH_2CH_3$). The intensity of the S-ethyl methylene relative to that of the O-ethyl methylene is about 1.1 %. The S-ethyl intensity cannot be entirely due to structure **Va**, the S-ethyl isomer of chlorpyrifos, since semi-quantitative ^{31}P NMR of the same sample indicated 0.3 mol % of structure **Va** in the thermally-treated chlorpyrifos. On the other hand, the 2.4 mol % dithio derivative estimated by ^{31}P NMR is roughly consistent with these proton results if the dithio derivative is mostly S-ethyl, not S-aryl.

In Figure A-20C there appears to be a very small complex multiplet (centered near 3.00 ppm) that is partially obscured by the previously-mentioned water singlet and S-ethyl methylene multiplet. Assuming this partially-obscured multiplet actually has the correct splitting pattern to be another type of S-ethyl methylene, this may represent the S-ethyl methylene of structure **Va**, the S-ethyl isomer of chlorpyrifos (0.3 mol %).

Liquid-solution ^{13}C NMR was also briefly considered for the detection of structure **Va**, the S-ethyl isomer of chlorpyrifos, or at least the presence of $-SCH_2CH_3$ groups. Figure A-21 shows the 75.5 MHz ^{13}C NMR spectrum of the same sample analyzed by ^{1}H NMR (and discussed in the preceding paragraphs), obtained using non-quantitative experimental conditions. Other than the acetone-d_6 solvent peaks near 205.5 ppm and 30 ppm, the three largest peaks are the protonated aryl carbon (142.2 ppm), and the methylene (65.9 ppm) and methyl (15.6 ppm) peaks of unreacted chlorpyrifos. The unprotonated aryl carbons of chlorpyrifos are the four significantly smaller peaks seen between 152 and 120 ppm. Considering the signal-to-noise represented in Figure A-21,

obtained after 35 minutes of ^{13}C signal averaging (using a 2.3 seconds repetition period), it was decided not to further pursue liquid-solution ^{13}C NMR as a method to detect the trace amounts of S-ethyl groups indicated by the liquid-solution ^{31}P NMR integration. Note, however, that in Figure A-21 another type of O-ethyl methylene carbon may be present near 65 ppm, perhaps due to the O-ethyl methylenes of chlorpyrifos oxon (**VIa**).

Refluxing chlorpyrifos in N,N-dimethylacetamide.

In Chapter 1, Figure 1-8D, it was shown that refluxing chlorpyrifos in toluene (105 °C) for three days produced three small ^{31}P NMR peaks at 26.4, 24.9 and 23.7 ppm (in addition to ^{31}P NMR intensity of some trans-esterification reaction products), any of which may represent the S-ethyl isomer of chlorpyrifos (structure **Va**). After consulting the literature (*A-7*), it was decided to utilize a much more polar solvent with a higher boiling point, as these conditions were judged to be more favorable for the thermal isomerization of chlorpyrifos to its S-ethyl isomer (or even potentially, isomerization to the S-aryl form, structure **IVa**). The solvent chosen was N,N-dimethylacetamide, which has a boiling point of 165 °C at 1 atm pressure.

Figure A-22 shows the 242.9 MHz ^{31}P NMR spectrum of chlorpyrifos refluxed in N,N-dimethylacetamide for three hours (run without the addition of any NMR solvent, and thus acquired without locking on a ^{2}H NMR signal). Note that after only three hours, most of the chlorpyrifos (60.5 ppm) has been transformed into many other substances, considering the 8 non-chlorpyrifos ^{31}P peaks seen in Figure A-22. Most of these peaks are only tentatively identifiable; for example, the peak at 26.8 ppm probably represents the S-ethyl isomer of chlorpyrifos, structure **Va**. The peak at 16.3 ppm may represent the S-aryl isomer of chlorpyrifos, structure **IVa**, considering the chemical shift involved, but

any such assignment would be only supposition at present. Likewise, the bis aryl derivative of chlorpyrifos (67.0 ppm; structure **XIXa**) and desaryl chlorpyrifos (51.2 ppm; structure **IIA**) also appear to be present. Clearly not present are any ^{31}P NMR peaks between 90 and 100 ppm, the region expected for a dithio derivative of chlorpyrifos (*A-3*), the region seen in Figure A-5 when neat chlorpyrifos was heated.

Mass spectral analysis of the sample shown in Figure A-22 was attempted by both electrospray ion-trap MS and FAB MS, neither of which ultimately provided any definitive information about the various species present, other than to confirm the presence of some unreacted chlorpyrifos in the mixture. Figures A-23A and A-23B (plus Table A-8, show an example of FAB/MS analysis of the sample shown in Figure A-22. Figures A-24A and A-24B show the positive-ion and negative-ion electrospray of the same sample, dissolved in methanol with 1% acetic acid (as a protonation source). Both MS techniques show results similar to those obtained for unreacted chlorpyrifos.

Thin layer chromatography (TLC) of the sample shown in Figure A-22 gave rise to at most 5 spots (when developed using a 3:1 n-hexane : ethyl acetate mixture; other TLC development solvent mixtures tried often did worse, and none did better). Observed R_f values for the five spots (bands) are given in Table A-1; band assignments included are based on literature R_f values (including related compounds; *A-9,10,11*). Attempts to perform preparative TLC for separating the compounds present were almost uniformly unsuccessful, since usually only unreacted chlorpyrifos was extracted from the silica gel of the TLC plates (band A, with the largest R_f value) and subsequently detected by liquid-solution ^{31}P NMR and MS. A number of extracting solvents were tried (including acetone, acetonitrile, ethanol and DMSO), but no success was usually achieved in

extracting compounds other than unreacted chlorpyrifos from a TLC band, as determined by both liquid-solution ^{31}P NMR and MS analyses.

The 300 MHz liquid-solution ^{1}H NMR of the sample represented in Figure A-22 (with the addition of some acetone-d_6 to provide a lock solvent) is shown in Figures A-25A through A-25D. The largest proton peaks observed are the three methyl singlets from the N,N-dimethylacetamide solvent (see Figure A-25A; the two amide methyl groups show separate signals because the hindered rotation about the C(=O)-N bond makes them non-equivalent). When the spectra are vertically expanded (Figures A-25B and A-25C), it is clear that the sample is a complex mixture of many compounds, including apparently compounds with O-ethyl groups not bonded to phosphorus (such as ethanol resulting from chlorpyrifos hydrolysis). Note the absence of any definitive S-ethyl methylene near 3.2 ppm, as was seen in Figure A-20C (for neat chlorpyrifos heated at 140 °C for 15 hours). Note also that the O-ethyl methylene peak of unreacted chlorpyrifos (4.4 ppm in Figure A-20C) is also not present in any significant amount in Figure A-25C. In an expansion of the aromatic region of the proton spectrum, Figure A-25D, there are several peaks between 7.9 and 8.2 ppm, indicative of several aryl-containing compounds (the leftmost peak, at 8.17 ppm, has a shift identical to that of the aryl proton of unreacted chlorpyrifos shown in Figure A-20A). The complexity of this proton spectrum for chlorpyrifos refluxed three hours in N,N-dimethylacetamide hindered further analysis.

Chlorpyrifos extracted from partially-hydrated Cu(II)-montmorillonite.

As discussed in the Introduction to this appendix, Figures A-1 and A-2 compared the 81 MHz ^{31}P solid state DP/MAS spectrum of chlorpyrifos sorbed on Cu(II)-

montmorillonite (9.7% chlorpyrifos and 5.0% water, by weight), before and after extraction of pesticide residues. Solvent extraction was performed after 11 hours of reaction at room temperature (in the dark) using anhydrous deuteroacetonitrile. Figure A-3 showed that only two ^{31}P NMR peaks were detected in the extract: unreacted chlorpyrifos at 61.0 ppm and a peak at 20.5 ppm (in roughly a two-to-one intensity ratio). The 20.5 ppm ^{31}P peak could be either the S-ethyl isomer of chlorpyrifos (structure **Va**) or the S-aryl isomer of chlorpyrifos (structure **IVa**); the chemical shift involved is closer to the value expected for the S-aryl isomer, based on literature chemical shifts of related compounds (as discussed in the Introduction of this appendix). Electrospray MS analysis (Figures A-26A and A-26B show the positive- and negative-ion mass spectra obtained, respectively), and subsequent MS/MS studies (not shown), were not successful to identify which isomer is responsible for the 20.5 ppm ^{31}P peak in Figure A-3.

Liquid-solution ^{1}H NMR analysis of the same perdeuteroacetonitrile extract was more informative. Figures A-27A through 27C show the ^{1}H NMR spectra of the acetonitrile extract (with added perdeuteroacetonitrile to provide a lock signal). The very large (off scale) peak seen at about 2.0 ppm is due to the acetonitrile solvent. Two distinct O-ethyl methylene signals are observed: the multiplet at 4.41 ppm is due to unreacted chlorpyrifos, but there is another multiplet at 4.27 ppm. Likewise, the aryl proton signal at 8.18 is due to unreacted chlorpyrifos, but there is another aryl singlet at 7.95 ppm. In both cases, the 'new' signals are about half as intense as the corresponding signals from unreacted chlorpyrifos (see Figures A-27B and A-27C for the integrals), roughly reflecting the approximately two-to-one intensity ratio observed in the ^{31}P NMR spectrum (Figure A-3). Finally, note the absence of any detectable S-ethyl methylene

signals near 3.2 ppm. Taken all together, these NMR results strongly indicate that the 20.5 ppm ^{31}P peak in Figure A-3 is due to the S-aryl isomer of chlorpyrifos (structure **IVa**), not the S-ethyl isomer (structure **Va**).

Liquid State ^{31}P NMR assignments.

Table A-9 summarizes the confirming evidence for the ^{31}P liquids NMR assignments of solvent-extractable species detected in this study. Note that the identity of the decomposition products **IIa** and **IIb**, and **VIa** and **VIb** have been confirmed by multiple techniques. On the other hand, the assignment of ^{31}P liquids NMR peaks to structures **IIIa** and **IVa** should be labeled as tentative, at present. No ^{31}P chemical shifts have been reported in the literature for structures **IIIa**, **IVa** and **Va**, possibly in part because the decomposition of chlorpyrifos has been much less studied (or reported) than other pesticides, such as methyl parathion. Judging by published reports on the decomposition of similar organothiophosphate pesticides, hydrolysis appears to preferentially replace the aryl ester moiety, while thermal and photochemical isomerization reactions have previously been reported to produce only the S-alkyl isomer, but not the S-aryl isomer. Thus, unlike the other structures, the assignment of structures **III** and **IV** are only tentative, albeit consistent with previous literature reports on similar compounds.

The ^{31}P chemical shift of structure **IIIb** has been previously reported, and is consistent with the value observed for those peaks assigned in previous chapters as **IIIb**, but confirmation by an independent analytical technique is lacking in this study. The desaryl (and presumably, also the desalkyl) pesticide residues could not be isolated by preparative TLC, since these disubstituted thiophosphoric acids could not be effectively

extracted from the developed TLC plate.

Tables A-10 and A-11 summarize the assignments of solid state ^{31}P NMR signals observed in this study for structures **I** through **VI**, as seen in Scheme A-1, along with the assignment methods used. Tables A-12 and A-13 summarize literature chemical shift values for possible chlorpyrifos and methyl parathion decomposition products; Table A-14 summarizes liquid solution ^{31}P NMR chemical shifts observed for various samples and extracts discussed in this appendix for chlorpyrifos decomposition.

Appendix References:

(A-1) Racke, K. D.; Steele, K. P.; Yoder, R. N.; Dick, W. A.; Avidov, E., *J. Agric. Food Chem.*, **1996**, *44*, 1582-1592.

(A-2) Krolski, M. E.; Bosnak, L. L.; Murphy, J. J. *J. Agric. Food Chem.* **1992**, *40*, 458-461.

(A-3) Bielawski, J.; Casida, J. E. *J. Agric. Food Chem.* **1988**, *36*, 610-615.

(A-4) Catrina, I.; Hengge, A., *J. Am. Chem. Soc.*, **2003**, *125*, 7546-7552.

(A-5) Suzumura, K.; Yoshinara, K.; Tanaka, Y.; Takagi, Y.; Kasai, Y.; Warashina, M.; Kuwabara, T.; Orita, M.; Taira, K. *J. Am. Chem. Soc.*, **2002**, *124*, 8230-8236.

(A-6) Thompson, C.; Frick, J.; Natke, B.; Hansen, L., *Chem. Res. Toxicol.*, **1989**, *2*, 386-391.

(A-7) Metcalf, R. L.; March, R. B. *J. Econ. Entomology*, **1953**, *46*, 288-294.

(A-8) Burn, A. J.; Cadogan, J. I. G. *J. Chem. Soc.*, **1961**, 5532-5541.

(A-9) Kim, Y. A.; Lee, S. L.; Park, Y. C.; Lee, Y. T. *Environ. Research*, **2000**, *84*, 303-309.

(A-10) Jaglan, P.; March, R.; Fukuto, T.; Gunther, F., *J. Agr. Food Chem.*, **1970**, *18*, 809-813.

(A-11) Chukwudebe, A.; March, R.; Othman, M.; Fukuto, T., *J. Agr. Food Chem.*, **1989**, *37*, 539-545.

(A-12) Hernandez, J.; Robledo, N.; Velasco, L.; Quintero, R.; Pickard, M.; Vazquez-Duhalt, R. Pest., *Biochem. and Physiol.*, **1998**, *61*, 87-94.

(A-13) Holmstead, R.; Casida, J. *Journal of the AOAC*, **1974**, *57*, 1050-1055.

(A-14) Lores, E.; Sovocool, G.; Harless, R.; Wilson, N.; Moseman, R. *J. Agr. Food Chem.*, **1978**, *26*, 118-122.

(A-15) Private communication, Dr. Donald Dick, Colorado State University.

(A-16) Greenhalgh, R.; Blackwell, B. A.; Preston, C. M.; Murray, W. J. *J. Agric. Food Chem.* **1983**, *31*, 710-713.

(A-17) Mortimer, R. D.; Dawson, B. A. *J. Agric. Food Chem.*, **1991**, *39*, 911-916.
(A-18) Stec, W. J.; Zon, G.; Egan, W.; Stec, B., *J. Am. Chem. Soc.*, **1984**, *106*, 6077-6079.
(A-19) Maderia, M.; Hunsicker, L. M.; DeRose, V. J., *Biochemistry*, **2000**, *39*, 12113-12120.
(A-20) Li, W.; Li, Y.; Hill, C.; Lum, K.; Raushel, F., *J. Amer. Chem. Soc.*, **2002**, *124*, 3498-3499.
(A-21) Thompson, C.; Ryu, S,; Berkman, C., *J. Amer. Chem. Soc.*, **1992**, *114*, 10710-10715.
(A-22) Rengasamy, S.; Parmar, B. S., *J. Agric. Food Chem.*, **1988**, *36*, 1025-1030.
(A-23) Van Wazer J. R.; Callis C. F.; Shoolery J. N.; Jones R. C., *J. Am. Chem. Soc.* **1956**, *78*, 5715-5726.
(A-24) Greenhalgh, R.; Shoolery, J. N., *Anal. Chem.*, **1978**, *50*, 2039-2042.
(A-25) Keith, L. H.; Alford, A. L., *Journal of the AOAC*, **1970**, *53*, 1018-1035.
(A-26) Turner, B. L.; Mahieu, N.; Condron, L. M., *Soil Sci. Soc. Am. J.*, **2003**, *67*, 497-510.
(A-27) Knight, W. B.; Weiss, P. M.; Cleland W. W., *J. Amer. Chem. Soc.*, **1986**, *108*, 2759-2761.
(A-28) Kuivalainen T.; El-Bahraoui J.; Uggla R.; Kostiainen R.; Sundberg M. R., *J. Am. Chem. Soc.* **2000**, *122*, 8073-8074.
(A-29) Almer, H.; Stawinski, J.; Strömberg, R.; Thelin, M., *J. Org. Chem.*, **1992**, *57*, 6163-6169.
(A-30) Gurley T. W.; Ritchey W. M., *Anal. Chem.*, **1976**, *48*, 1137-1140.
(A-31) Olah, G. A.; McFarland, C. W., *J. Org. Chem.*, **1975**, *40*, 2582-2587.
(A-32) Maniara, G.; Rajamoorthi, K.; Srinivasan, R.; Stockton, G., *Anal. Chem.*, **1998**, *70*, 4921-4928.

Table A-1. Typical observed R_f Values on 60-F256 using 75% n-hexane/25% ethyl acetate by-volume solvent mix.

	species	R_f value for chlorpyrifos residues	R_f value for methyl parathion residues
band A	I	0.95	0.87
band B	V (and/or IV?)	0.86	0.76
band C	VI ?	0.44	0.53
band D	II (and/or III?) ?	0.20	0.29
band E	II (and/or III?) ?	0	0

Table A-2. Electrospray Positive Ion MS assignments for Pure Chlorpyrifos

m/z	abundance	assignment
372, 374 – Cl_3 pattern	38 %	$M + Na^+$
350, 352 – Cl_3 pattern	100 %	$M + H^+$
324, 326 – Cl_3 pattern	6 %	$M - C_2H_4 + H^+$

Table A-3. Electrospray Positive Ion MS assignments for Thermally-isomerized Chlorpyrifos

m/z	abundance in EtOH/FA	abundance in MeOH/FA	assignment
705, 707, 709, 711 – Cl_6 pattern	10 %		M + oxon + Na^+
689, 691, 693, 695 – Cl_6 pattern	100 %		oxon + oxon + Na^+
388, 390 – Cl_3 pattern			dithio + Na^+
372, 364 – Cl_3 pattern	7 %		M + Na^+
366, 368 – Cl_3 pattern		49 %	dithio + H^+
356, 358 – Cl_3 pattern	97 %		oxon + Na^+
350, 352 – Cl_3 pattern	2 %	100 %	M + H^+
334, 336 – Cl_3 pattern	10 %		oxon + H^+
306, 308 – Cl_3 pattern	3 %		oxon – C_2H_4 + H^+

Table A-4. Electrospray Negative Ion MS assignments for Pure Chlorpyrifos

m/z	abundance	assignment
196, 198 – Cl_3 pattern	100 %	ArO^-
281, 283 – Cl_3 pattern		?
320, 322 – Cl_3 pattern		$(EtO)(ArO)P(S)O^-$

Table A-5. Electrospray Negative Ion MS assignments for Thermally-isomerized Chlorpyrifos.

m/z	abundance in EtOH/FA	assignment
320, 322 – Cl_3 pattern	45 %	$(EtO)(ArO)P(S)O^-$
212, 214 – Cl_3 pattern	73 %	ArS^-
196, 198 – Cl_3 pattern	100 %	ArO^-
185	94 %	$(EtO)_2PS_2^-$
169	60 %	$(EtO)_2P(S)O^-$

Table A-6. Electrospray Positive Ion MS assignments for Pure Methyl Parathion

m/z	assignment
264	$M + H^+$
234	$M - C_2H_6$ or $M - CH_2O$?
216	?
170	?
143	$M - Ar + H^+$ (i.e., $(MeO)_2(OH)P{=}S + H^+$) (i.e., IIb + H^+)
125	$[(MeO)_2P{=}S]^+$
123	$Ar + H^+$?

Table A-7. Electrospray Negative Ion MS assignments for Pure Methyl Parathion

m/z	abundance	assignment
519	26 %	?
412	6 %	?
358	8 %	?
339	18 %	?
248	100 %	IIIb $- H^+$ (desmethyl anion)
141	7 %	IIb $- H^+$ (desaryl anion)
138	52 %	p-nitrophenoxide anion

Table A-8. FAB Positive Ion MS assignments for Pure Chlorpyrifos

m/z	abundance	assignment
350, 352 – Cl_3 pattern	100%	$M + H^+$
322, 324 – Cl_3 pattern	4 %	$M - C_2H_4 + H^+$
314, 316 – Cl_3 pattern	25 %	$M - Cl^-$
208, 210 – Cl_3 pattern	6 %	
198, 200 – Cl_3 pattern	32 %	$ArOH + H^+$
153	21 %	$[(EtO)_2P{=}S]^+$
139	7 %	$[(EtO)_2P{=}O]^+$?
125		$[(EtO)(HO)P{=}S]^+$
97		$[(HO)_2P{=}S]^+$
485, 487 – Cl_3 pattern		?
503, 505 – Cl_3 pattern		?

Table A-9. Summary of confirming evidence for the ^{31}P liquids NMR assignments of solvent-extractable species.

structure no.	structure	chlorpyrifos	ref.	methyl parathion	ref.
I (pesticide)	$(ArO)(RO)_2P=S$	1, 2, 3, 4, 5	*A-17* *A-3*	1, 2, 3, 4, 5	*A-28* *A-17*
II (desaryl)	$(HO)(RO)_2P=S$	1, 3, 4, 5, 6	*A-19* *A-3* *A-31*	3, 4, 5, 6	*A-23* *A-29*
III (desalkyl)	(ArO)(RO)(HO)P=S	5, 6	*A-3*	4, 5, 6	*A-20*
IV (S-aryl)	$(ArS)(RO)_2P=O$	3, 5	*A-23* *A-3*	4, 5	*A-24*
V (S-alkyl)	(ArO)(RO)(RS)P=O	5	*A-2*	4, 5	*A-6* *A-16* *A-21*
VI (oxon)	$(ArO)(RO)_2P=O$	1, 2, 3, 5	*A-3*	1, 3, 4, 5	*A-16* *A-3*

Key:

1. ^{31}P liquids NMR assignment confirmed by 'spiking' with (or comparison to) an authentic sample.
2. ^{31}P liquids NMR assignment confirmed by MS detection of the molecular ion.
3. ^{31}P liquids NMR assignment is consistent with assignments made by ^{1}H liquids NMR.
4. ^{31}P liquids NMR chemical shift is in agreement with literature values for that compound.
5. ^{31}P liquids NMR chemical shift is consistent with literature values for similar compounds.
6. ^{31}P liquids NMR assignment is consistent with MS results, but not confirmed.

Table A-10. Solid State ^{31}P NMR assignments for chlorpyrifos adsorbed on clay minerals.

structure no.	structure	observed shifts (clay sorbed)	observed shifts (solvent extract)	assignment methods
Ia (chlorpyrifos)	$(ArO)(EtO)_2P=S$	62 to 59 ppm	62 to 60 ppm	A, B, C, D
IIa (desaryl chlorpyrifos)	$(HO)(EtO)_2P=S$	55 to 45 ppm	56.6, 55.2, 53.7 ppm	A, B, C, D
IIIa (desethyl chlorpyrifos)	$(ArO)(EtO)(HO)P=S$	about 48 ppm *	49 ppm *	E
IVa (S-aryl chlorpyrifos)	$(ArS)(EtO)_2P=O$	24 to 15 ppm	20.1 ppm	C, E
Va (S-ethyl chlorpyrifos)	$(ArO)(EtO)(EtS)P=O$	32 to 25 ppm	28 to 23 ppm	C, E
VIa (chlorpyrifos oxon)	$(ArO)(EtO)_2P=O$	-4 to -9 ppm	-6.7, -7.2 ppm	B, C, E

Assignment Key:
A. Solid state ^{31}P NMR assignment confirmed by 'spiking' with an authentic sample.
B. Solid state ^{31}P NMR assignment confirmed by solvent extraction, liquid-solution ^{31}P NMR and MS identification.
C. Solid state ^{31}P NMR assignment confirmed by solvent extraction, followed by liquid state ^{31}P or ^{1}H NMR assignment (see table below for ^{31}P NMR details).
D. Solid state ^{31}P NMR chemical shift is in agreement to the literature-reported value for the compound by liquid state ^{31}P NMR.
E. Solid state ^{31}P NMR chemical shift is in agreement to the literature-reported value for *similar* compounds by liquid state ^{31}P NMR.
* Value reported is based on tentative assignments of solid state and liquid-solution state ^{31}P NMR peaks observed in this study.

Table A-11. Solid State ^{31}P NMR assignments for methyl parathion adsorbed on clay minerals.

structure no.	structure	observed shifts (clay sorbed)	observed shifts (solvent extract)	assignment methods
Ib (methyl parathion)	$(ArO)(MeO)_2P=S$	68 to 65 ppm	68 to 66 ppm	A, B, C, D
IIb (desaryl methyl parathion)	$(HO)(MeO)_2P=S$	60 to 45 ppm	57 to 52 ppm	A, B, C, D
IIIb (desmethyl methyl parathion)	(ArO)(MeO)(HO)P=S	60 to 45 ppm *	56 ppm **	D
IVb (S-aryl methyl parathion)	$(ArS)(MeO)_2P=O$	27 to 20 ppm *	27 ppm	C, E
Vb (S-methyl methyl parathion)	(ArO)(MeO)(MeS)P=O	35 to 27 ppm	31 to 27 ppm	C, D
VIb (methyl paraoxon)	$(ArO)(MeO)_2P=O$	0 to -11 ppm	-3 to -5 ppm	B, C, D

Assignment Key:

A. Solid state ^{31}P NMR assignment confirmed by 'spiking' with (or comparison to) an authentic sample.

B. Solid state ^{31}P NMR assignment confirmed by solvent extraction, TLC separation and MS identification.

C. Solid state ^{31}P NMR assignment confirmed by solvent extraction, followed by liquid state ^{31}P NMR assignment (see table below for details).

D. Solid state ^{31}P NMR chemical shift is in agreement to the literature-reported value for the compound by liquid state ^{31}P NMR.

E. Solid state ^{31}P NMR chemical shift is in agreement to the literature-reported value for *similar* compounds by liquid state ^{31}P NMR.

* Range reported is based on tentative assignments of solid state and liquid-solution state ^{31}P NMR peaks observed in this study.

** Not detected in this study; value given is a literature-reported chemical shift for **IIIb** by liquid-solution state ^{31}P NMR (*A-11*).

Table A-12. Some possible chlorpyrifos decomposition products and relevant ^{13}P chemical shifts from the literature.

	structure	^{13}P chemical shifts	exact mass	ref.
I chlorpyrifos	$S=P(OR)_2(OAr)$	60.8 ppm ($DMSO-d_6$) 61.5 ppm ($CDCl_3$) 60.9 ppm ($CDCl_3$, if Ar=Ph) 60.7 ppm ($(CD_3)_2CO$, if Ar=Ph)	348.93	this study *A-17* *A-3*
II	$S=P(OR)_2(OH) \leftrightarrows O=P(OR)_2(SH)$	55.2 ($DMSO-d_6$, as K^+ salt) 57 ppm (ref.; as Na^+ salt) 55.3 ppm (D_2O) 58.3 ppm (neat liquid) 61.3 ppm ($CDCl_3$) 63.4 ppm ($(CD_3)_2CO$)	170.02	this study *A-19* *A-31* *A-3* *A-3*
III	$S=P(OR)(OAr)(OH) \leftrightarrows O=P(OR)(OAr)(SH)$	50 ppm, estimate 56.6 ppm ($CDCl_3$, if Ar=Ph) 58.7 ppm ($(CD_3)_2CO$, if Ar=Ph)	320.90	this study *A-3* *A-3*
IV	$O=P(OR)_2(SAr)$	22 ppm (if Ar = phenyl) 22 ppm (if SEt vs. SAr) 21 ppm (if Ar = C_6H_4Cl) 20.3 ppm ($CDCl_3$, if Ar=Ph) 18.9 ppm ($(CD_3)_2CO$, if Ar=Ph)	348.93	*A-23* *A-23* *A-23* *A-3* *A-3*
V	$O=P(OR)(SR)(OAr)$	26.8 ppm (CH_3CONMe_2) 24.6 ppm (if Ar = 4-nitrophenyl) 24.0 ppm (if Ar = 4-nitrophenyl) 31.4 ppm (if SR = S-n-propyl and Ar = $-C_6H_4SMe$) 25.9 ppm (if SR = S-n-propyl and Ar = $-C_6H_4S(=O)Me$)	348.93	this study *A-16* *A-16* *A-3* *A-3*
VI oxon	$O=P(OR)_2(OAr)$	-7.6 ppm (CH_3CN) -8.7 ppm ($CDCl_3$, if Ar=Ph) -8.7 ppm ($(CD_3)_2CO$, if Ar=Ph)	332.95	this study *A-3* *A-3*
VII	$S=P(OR)(OH)_2 \leftrightarrows O=P(OR)(OH)(SH)$		141.99	
VIII	$S=P(OH)_3 \leftrightarrows O=P(OH)_2(SH)$	32 to 34 ppm	113.95	
IX	$O=P(OR)_2(OH)$	1.3 ppm (+3.8 ppm as Na^+ salt) -1.8 ppm ($CDCl_3$, if Ar=Ph) -3.3 ppm ($(CD_3)_2CO$, if Ar=Ph)	154.04	*A-19* *A-3* *A-3*
X	$O=P(OR)(OH)_2$	4.3 to 0.6 ppm (D_2O, if R = 3-glycerol, depends on pH)	126.01	*A-27*
XI	$O=P(OH)_3$	0 ppm (85% H_3PO_4) 6.1 ppm (D_2O w/ 1M NaOH) +6 to -3 ppm (H_2O; various pH)	97.98	 *A-26* *A-23*
XII	$O=P(OR)(SAr)(OH)$		320.90	
XIII	$O=P(SAr)(OH)_2$		292.86	
XIV	$O=P(OR)(OAr)(OH)$	-7.4 ppm ($CDCl_3$, if Ar=Ph) -8.1 ppm ($(CD_3)_2CO$, if Ar=Ph)	304.92	*A-3* *A-3*
XV	$O=P(OAr)(OH)_2$	- 5 ppm (if Ar = phenyl; 0 ppm if	276.89	

		Na^+ salt and Ar = phenyl)		
XVI	O=P(SR)(OAr)(OH)	24.9 ppm (if R = n-Pr and Ar = -C_6H_4SMe)	320.90	*A-2*
XVII	O=P(SR)$(OH)_2$		170.02	
XVIII	S=P(OAr)$(OH)_2$ ⇆ O=P(OAr)(OH)(SH)		292.86	
XIX bis	S=P(OR)$(OAr)_2$	56.2 ppm (for ethyl parathion) 56.3 ppm (for diazinon)	499.80	
XX	S=P$(OR)_3$	68.6 ppm 67 ppm ($CDCl_3$?)	198.05	*A-16* *A-30*
XXI	(ArS)$(RO)_2$P=S	85.7 ppm ($CDCl_3$, if Ar=Ph) 84.6 ppm ($(CD_3)_2CO$, if Ar=Ph)	364.90	*A-3* *A-3*
XXII	(ArO)(RS)(RO)P=S		364.90	

Table A-13. Some possible methyl parathion decomposition products and relevant ^{13}P chemical shifts from the literature.

	structure	^{13}P chemical shifts	exact mass	ref.
I methyl parathion	$S=P(OR)_2(OAr)$	66.3 ppm (C_6D_6) 65.6 ppm ($CDCl_3$) 66.3 ppm (C_6D_6)	263.00	this study *A-28* *A-17*
II	$S=P(OR)_2(OH) \leftrightarrows O=P(OR)_2(SH)$	57.7 ppm 57 ppm (Na^+ salt in EtOH) 55.8 to 57.0 ppm (D_2O, as anion, R = various ribonucleotides)	141.99	this study *A-23* *A-29*
III	$S=P(OR)(OAr)(OH) \leftrightarrows O=P(OR)(OAr)(SH)$	56.1 ppm (as strychnine salt in $CDCl_3$) 56.6 ppm (if Ar = Ph)	248.99	*A-20* *A-3*
IV	$O=P(OR)_2(SAr)$	31 ppm (if SC_3H_7 vs. SAr) 32.1 ppm (if SMe vs. SAr)	263.00	*A-24*
V	O=P(OR)(SR)(OAr)	27.5 ppm (C_6D_6) 27.8 ppm ($CDCl_3$) 27.9 ppm ($CDCl_3$)	263.00	*A-16* *A-6* *A-21*
VI oxon	$O=P(OR)_2(OAr)$	-4.8 ppm (C_6D_6) -4.2 ppm (CD_3CN) -6.3 ppm (if Ar = Ph)	247.02	*A-16* this study *A-3*
VII	$S=P(OR)(OH)_2 \leftrightarrows O=P(OR)(OH)(SH)$		127.97	
VIII	$S=P(OH)_3 \leftrightarrows O=P(OH)_2(SH)$	32 to 34 ppm	113.95	*A-3*
IX	$O=P(OR)_2(OH)$	-1.3 ppm (+3.8 ppm as Na^+ salt) -12.7 ppm	126.01	*A-3* *A-16*
X	$O=P(OR)(OH)_2$	0.4 ppm (D_2O w/ 1M NaOH) 4.3 to 0.6 ppm (D_2O, if R = 3-glycerol, depends on pH)	111.99	*A-26* *A-27*
XI	$O=P(OH)_3$	0 ppm (85% H_3PO_4) 6.1 ppm (D_2O w/ 1M NaOH) +6 to -3 ppm (H_2O; various pH)	97.98	*A-3* *A-26* *A-23*
XII	O=P(OR)(SAr)(OH)		248.99	
XIII	$O=P(SAr)(OH)_2$		234.97	
XIV	O=P(OR)(OAr)(OH)	-4.5 ppm	233.01	*A-3*
XV	$O=P(OAr)(OH)_2$	-5 ppm (Ar = Ph, R = Et) 0 ppm (if Na^+ salt and Ar = Ph, R = Et)	218.99	*A-3* *A-28*
XVI	O=P(SR)(OAr)(OH)		248.99	
XVII	$O=P(SR)(OH)_2$		127.97	
XVIII	$S=P(OAr)(OH)_2 \leftrightarrows O=P(OAr)(OH)(SH)$	41.2 ppm (mono-anion) 32.5 ppm (as Zn^{2+} complex)	234.97	*A-4* *A-4*
XIX bis	$S=P(OR)(OAr)_2$	58.3 ppm (C_6D_6)	370.00	*A-19*

XX	$S=P(OR)_3$	74.0 ppm 73.9 ppm (C_6D_6) 73.7 ppm (C_6D_6)	156.00	*A-16* *A-30* *A-19*
XXI	$(ArS)(RO)_2P=S$	91.1 ppm (C_6D_6) 99.9 ppm (C_6D_6)	278.98	this study *A-19*
XXII	(ArO)(RS)(RO)P=S		278.98	

Table A-14 . ^{31}P chemical shifts (in ppm) [a] of extracts of chlorpyrifos and its decomposition products sorbed on partially-hydrated clays. [b]

sample	age	solvent		XX	I	II or XIX	III	IV or VIII	V or XVI ?	VI or XV
chlorpyrifos refluxed in toluene	3 days	toluene		69.3		53.7		26.4 24.9 23.7		– 6.7
chlorpyrifos sorbed on kaolinite	108 days	DMSO-d_6			62	53 49		28		
chlorpyrifos sorbed on Ca-mont.	3.7 years	acetone-d_6			61			27 24		
chlorpyrifos sorbed on Zn-mont.	166 days	DMSO-d_6			61.6	56.6		28.1	17.1	
chlorpyrifos sorbed on Al-mont.	3 years	DMSO-d_6			none			31 27		
chlorpyrifos sorbed on Cu-mont.	13 hours	DMSO-d_6			61			20		
chlorpyrifos oxidized with Br_2 in CH_3CN	1 hour	CD_3CN			61.9					– 7.6
chlorpyrifos heated neat (140 °C)	15 hours	CD_3CN	94.8		62.0			24.9		– 7.1

[a] relative to 85 % H_3PO_4

[b] Qualitative peak intensities: vl = very large, l = large, m = medium, s = small, vs = very small.

Fig. A-1

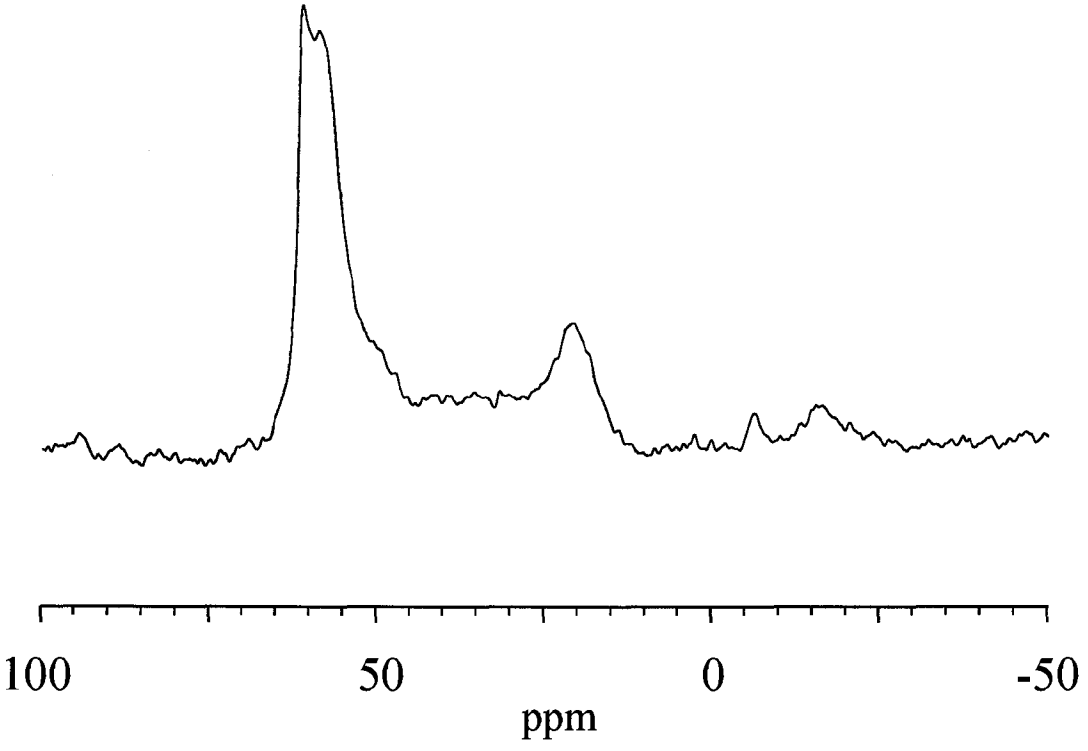

Figure A-1. 80.9 MHz DP/MAS ^{31}P NMR spectrum of chlorpyrifos (9.7% by wt.) sorbed on partially-hydrated Cu(II)-montmorillonite (5.0% H_2O by wt.), allowed to react for 11 hours at RT (in the dark), *before* solvent extraction (6.1 kHz MAS; 1068 scans).

Fig. A-2

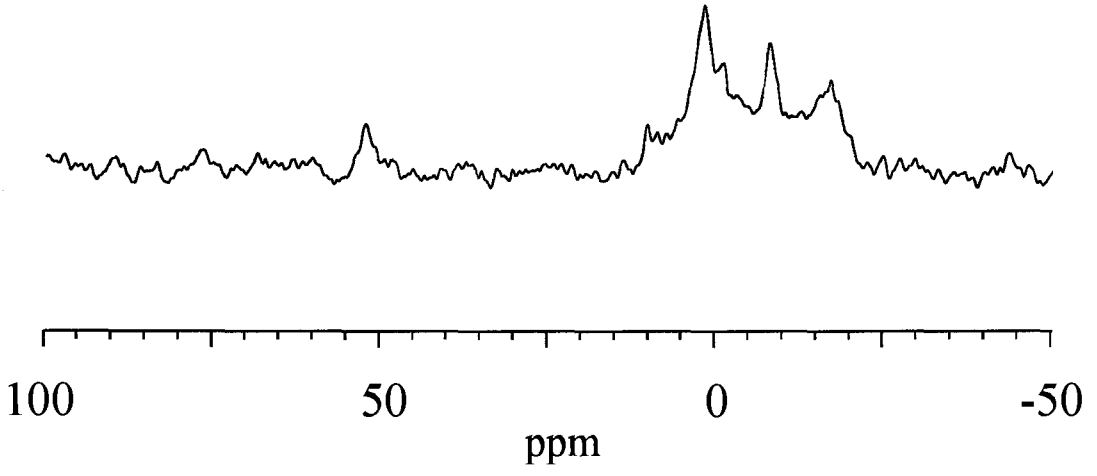

Figure A-2. 80.9 MHz DP/MAS ^{31}P NMR spectrum of chlorpyrifos (9.7% by wt.) sorbed on partially-hydrated Cu(II)-montmorillonite (5.0% H_2O by wt.), allowed to react for 11 hours at RT (in the dark), *after* acetonitrile extraction (6.1 kHz MAS; 8000 scans).

Fig. A-3

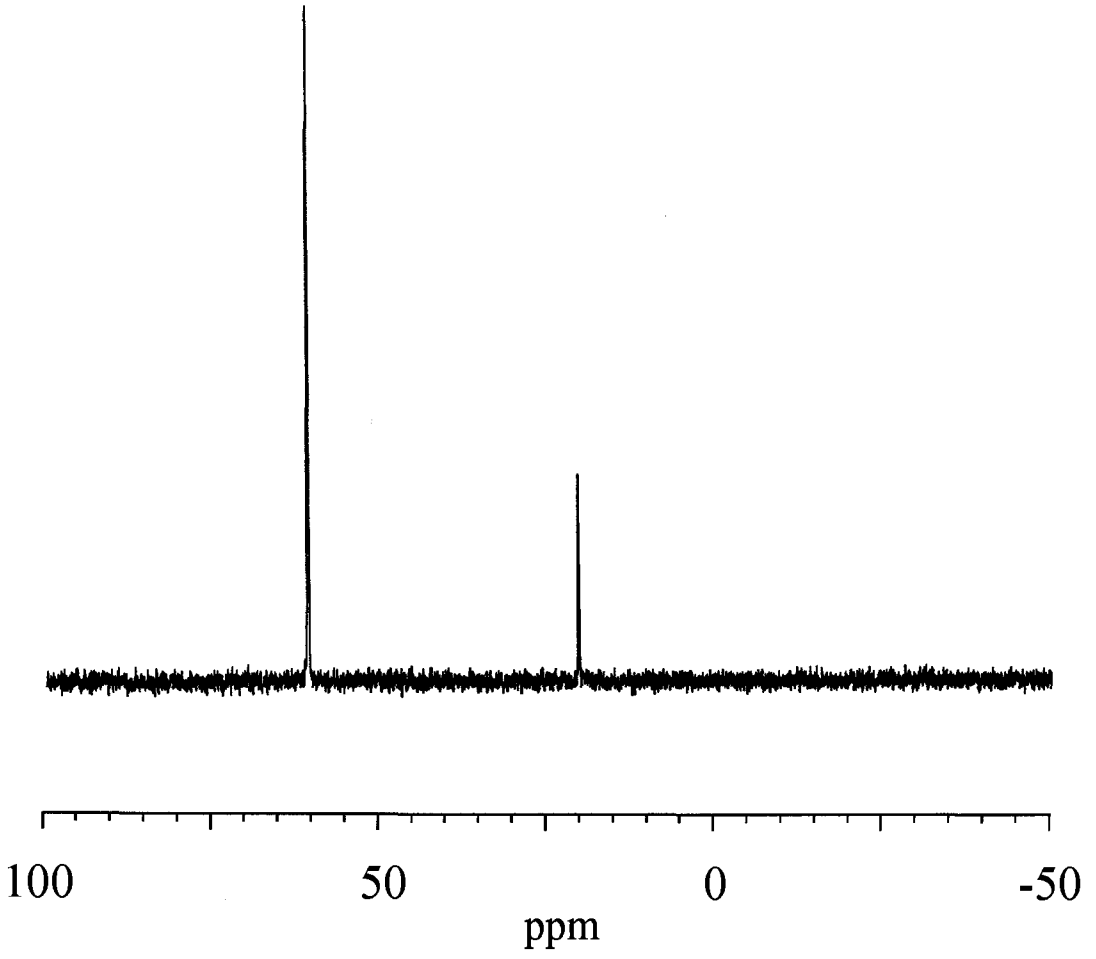

Figure A-3. 242.9 MHz liquid-solution ^{31}P NMR spectrum of the acetonitrile extract of the sample shown in Figure A-1, chlorpyrifos (9.7% by wt.) sorbed on partially-hydrated Cu(II)-montmorillonite (5.0% H_2O by wt.), allowed to react for 11 hours at RT (in the dark) (28820 scans).

Fig. A-4

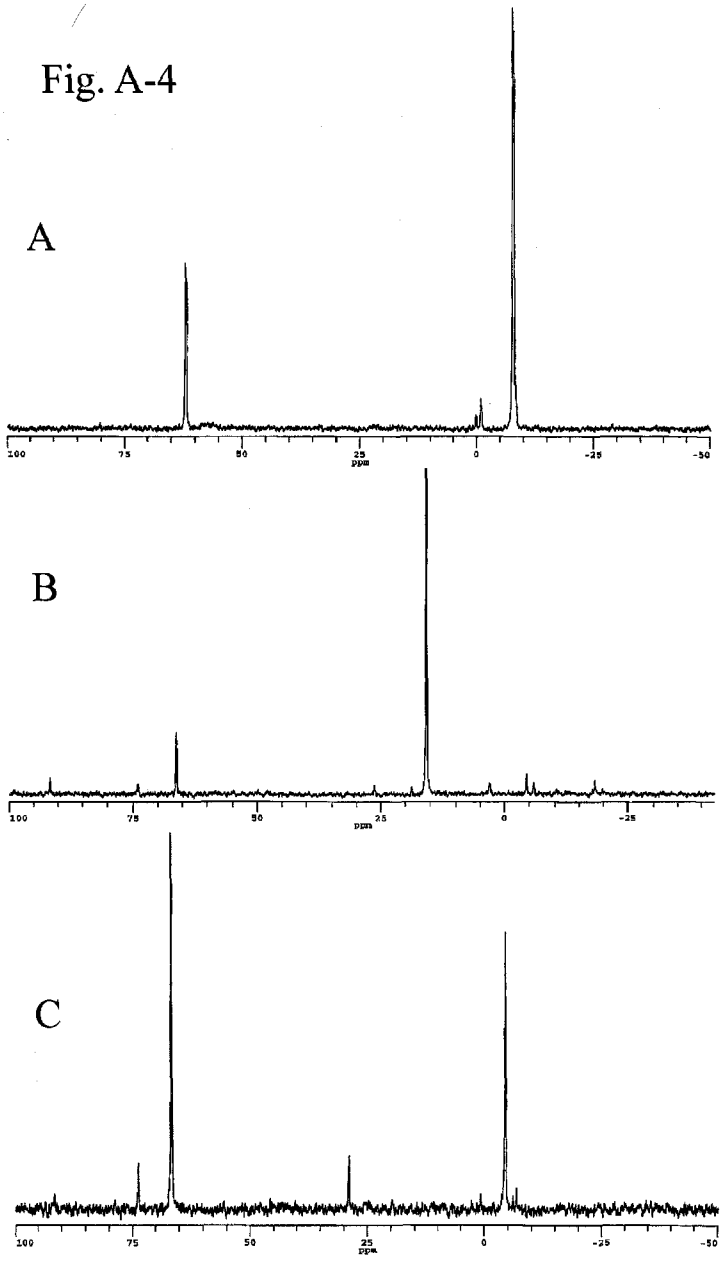

Figure A-4A. 242.9 MHz liquid-solution ^{31}P NMR spectrum of chlorpyrifos in deuteroacetonitrile, after reaction with excess elemental bromine (25932 scans).
Figure A-4B. 242.9 MHz liquid-solution ^{31}P NMR spectrum of technical grade methyl parathion in anhydrous deuteroacetonitrile, after reaction with excess elemental bromine (3904 scans).
Figure A-4C. 242.9 MHz liquid-solution ^{31}P NMR spectrum of technical grade methyl parathion in deuteroacetonitrile with added water, after reaction with excess elemental bromine (244 scans).

Fig. A-5

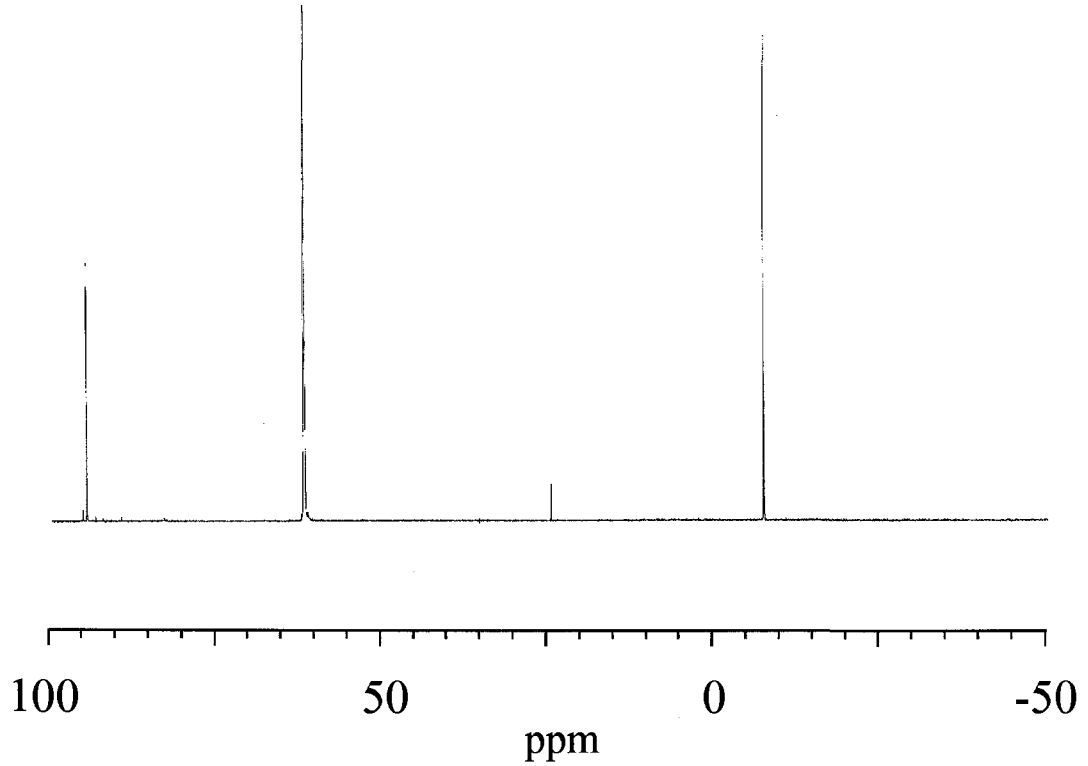

Figure A-5. 121.5 MHz liquid-solution ^{31}P NMR spectrum of neat chlorpyrifos (sealed in glass) heated to 140 °C for 15 hours, followed by dissolving in CD_3CN (336 scans).

Fig. A-6

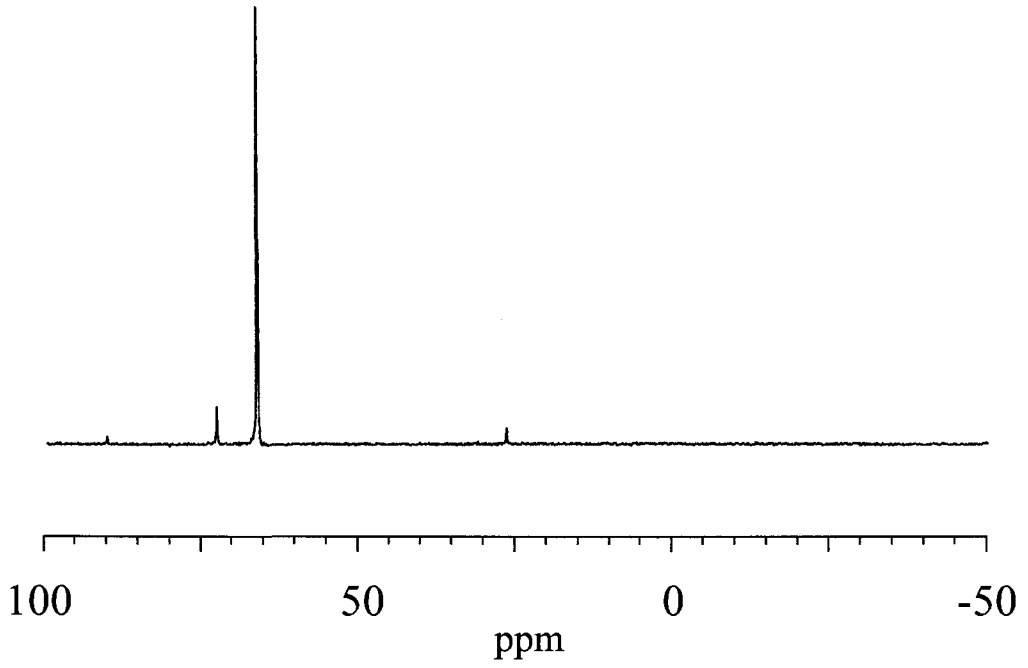

Figure A-6. 242.9 MHz liquid-solution ^{31}P NMR spectrum of technical grade methyl parathion in toluene (320 scans).

Fig. A-7

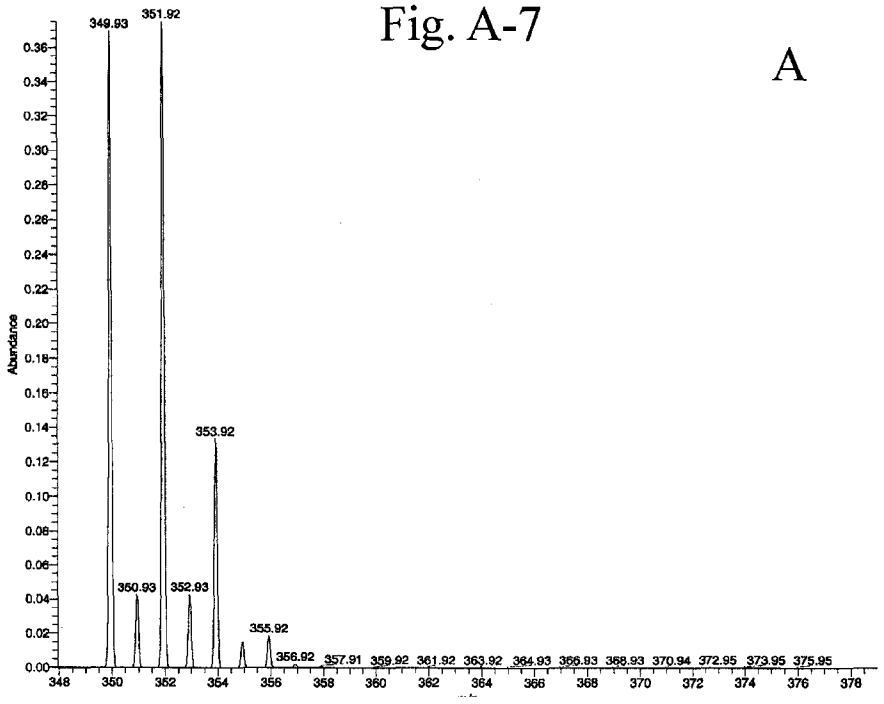

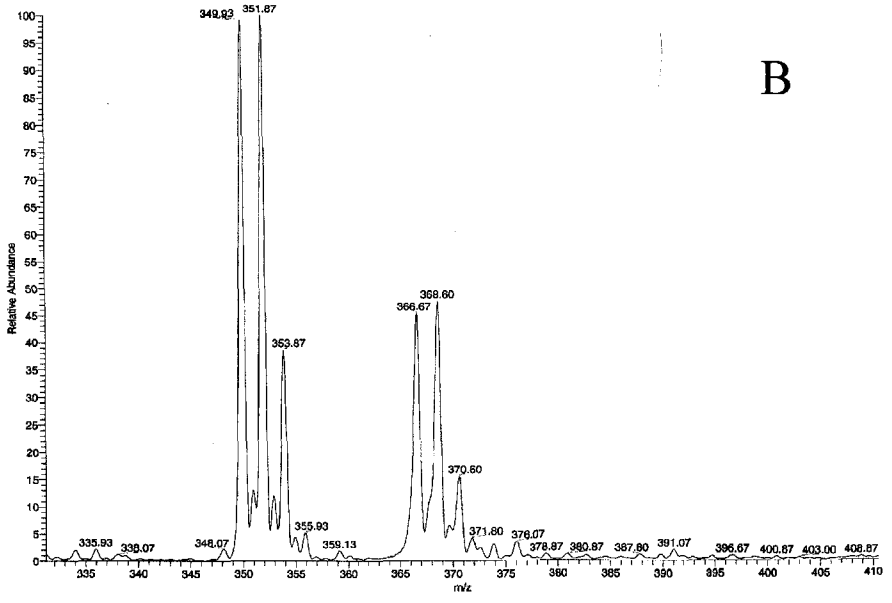

Figure A-7A. Simulated mass spectrum (using Xcalibur software) of protonated chlorpyrifos, illustrating the isotopic distribution typical of molecules containing three chlorine atoms.

Figure A-7B. Simulated mass spectrum (using Xcalibur software) of a protonated complex containing a single chlorpyrifos molecule and a single oxon molecule, illustrating the isotopic distribution typical of molecules containing six chlorine atoms.

Fig. A-8

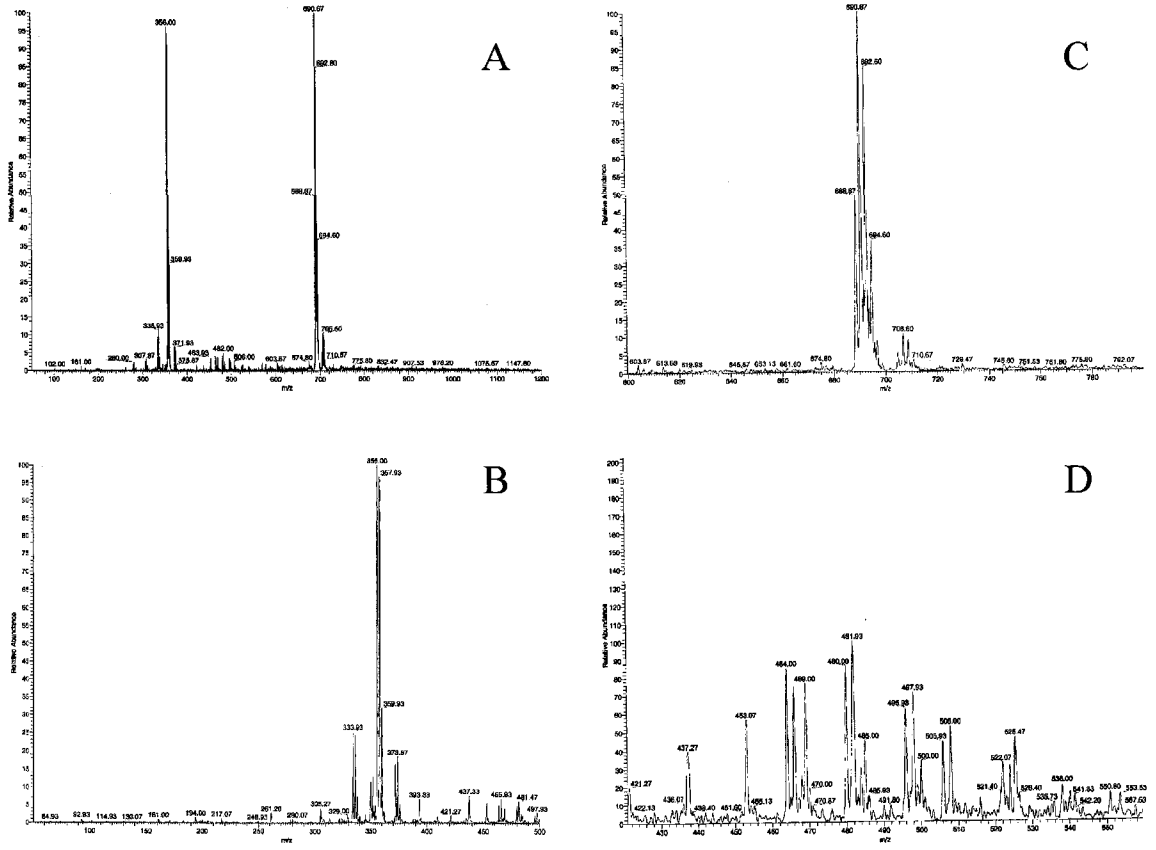

Figure A-8A. Positive-ion electrospray mass spectrum of neat chlorpyrifos (sealed in glass) heated to 140 °C for 15 hours (followed by dissolving in CD_3CN, then dilution into ethanol containing 1% formic acid), scanning the range m/Z = 50 to 1200. The mass spectrum shown is the average of 25 repeated scans.

Figure A-8B. Same as Figure A-8A, except the scanned range is m/Z = 50 to 500.

Figure A-8C. Same as Figure A-8A, except the displayed range is m/Z = 600 to 800.

Figure A-8D. Same as Figure A-8A, except the scanned range is m/Z = 50 to 1000, and the displayed range is m/Z = 420 to 560.

Fig. A-9

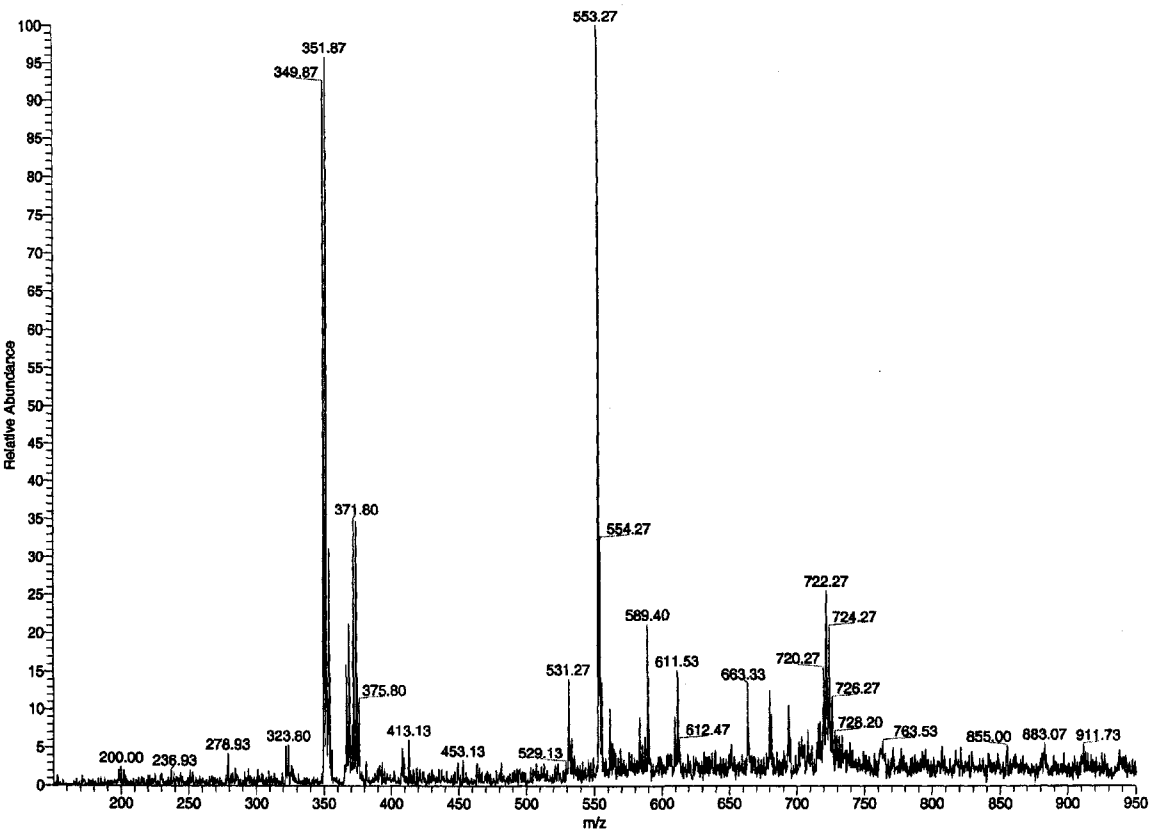

Figure A-9. Positive-ion electrospray mass spectrum of pure chlorpyrifos dissolved in ethanol containing 1% formic acid), scanning the range m/Z = 150 to 950. The mass spectrum shown is the average of 25 repeated scans.

Fig. A-10

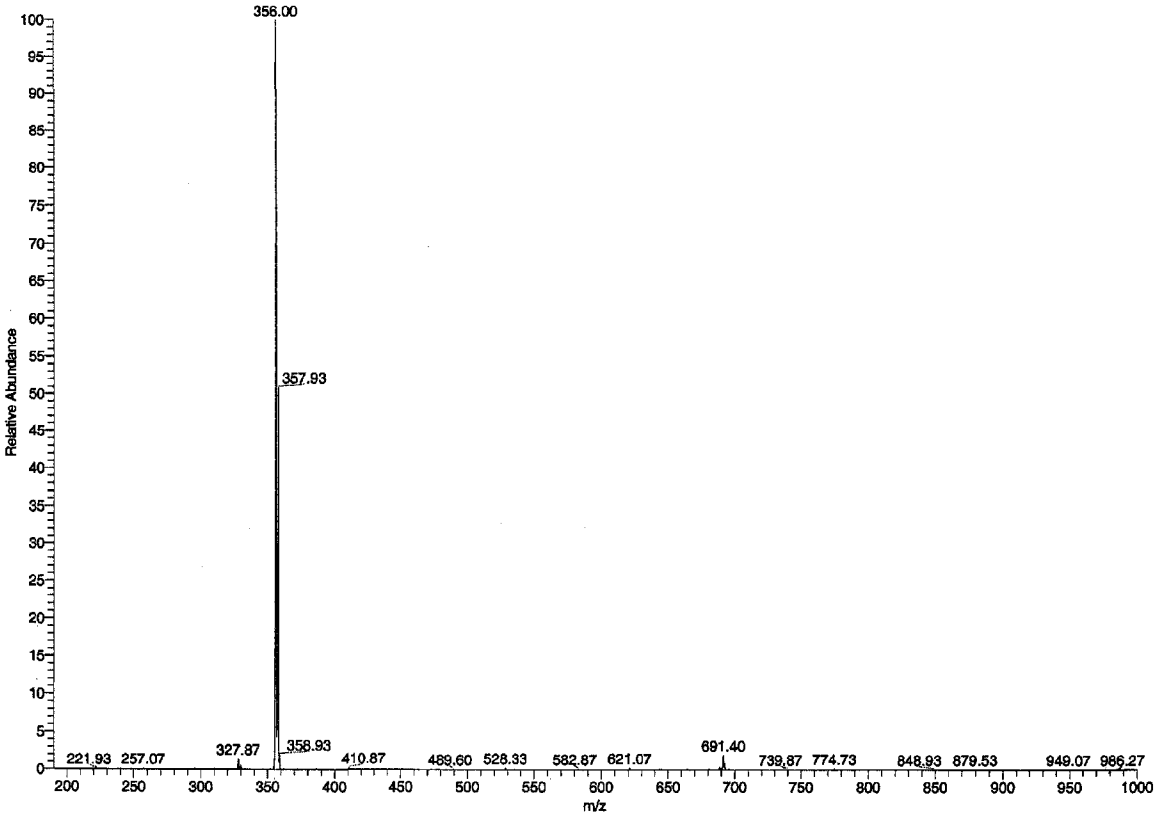

Figure A-10. Positive-ion electrospray MS/MS of the peak at m/Z= 691 for the sample represented in Figure A-8A (neat chlorpyrifos, sealed in glass and heated to 140 °C for 15 hours, followed by dissolving in CD_3CN and dilution into ethanol containing 1% formic acid), scanning the range m/Z = 190 to 1000. The mass spectrum shown is the average of 25 repeated scans.

Fig. A-11

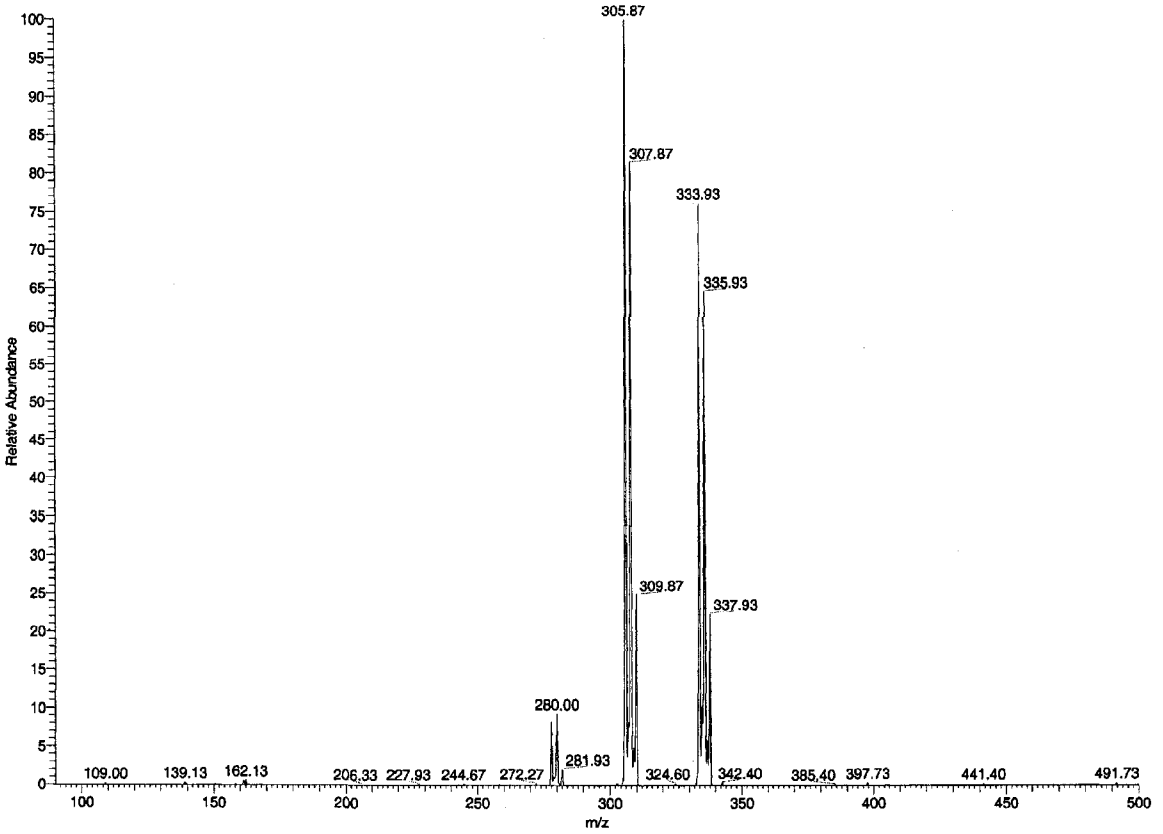

Figure A-11. Positive-ion electrospray MS/MS of the peak at m/Z= 336 for the sample represented in Figure A-8A (neat chlorpyrifos, sealed in glass and heated to 140 °C for 15 hours, followed by dissolving in CD_3CN and dilution into ethanol containing 1% formic acid), scanning the range m/Z = 90 to 500. The mass spectrum shown is the average of 25 repeated scans.

Fig. A-12

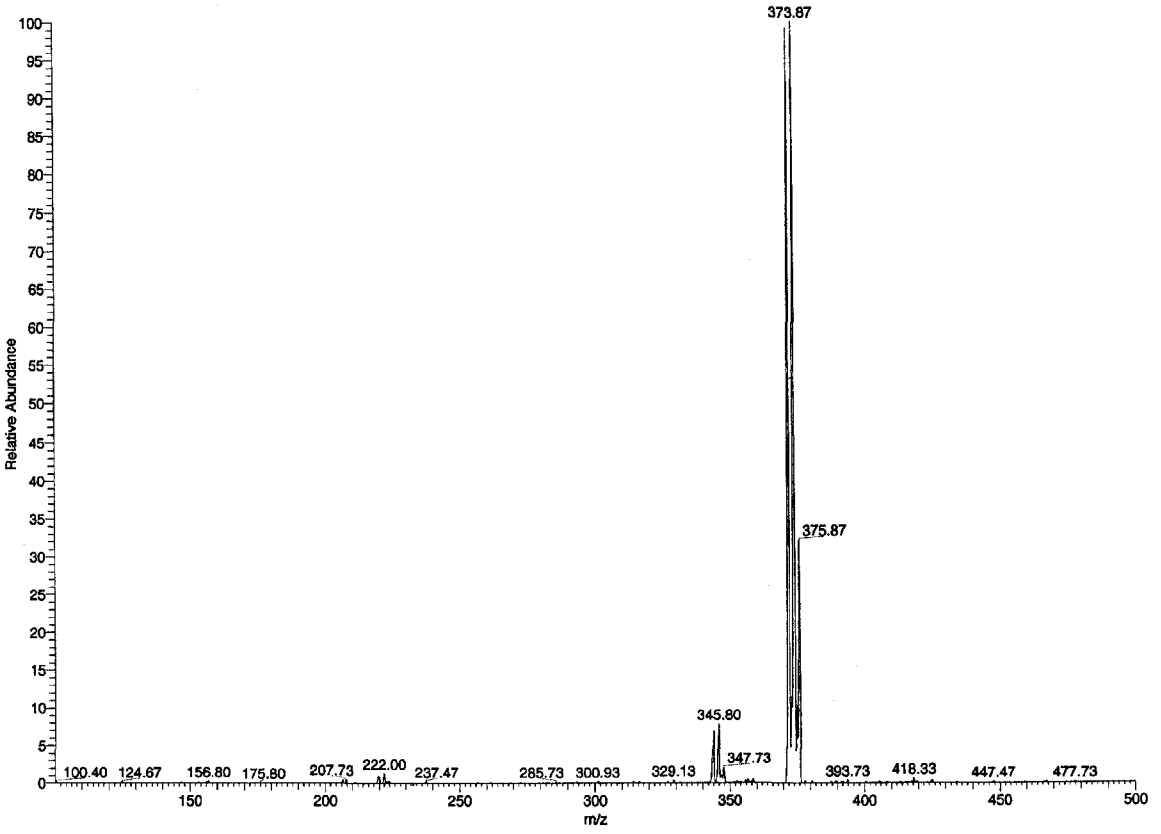

Figure A-12. Positive-ion electrospray MS/MS of the peak at m/Z= 374 for the sample represented in Figure A-8A (neat chlorpyrifos, sealed in glass and heated to 140 °C for 15 hours, followed by dissolving in CD_3CN and dilution into ethanol containing 1% formic acid), scanning the range m/Z = 100 to 500. The mass spectrum shown is the average of 25 repeated scans.

Fig. A-13

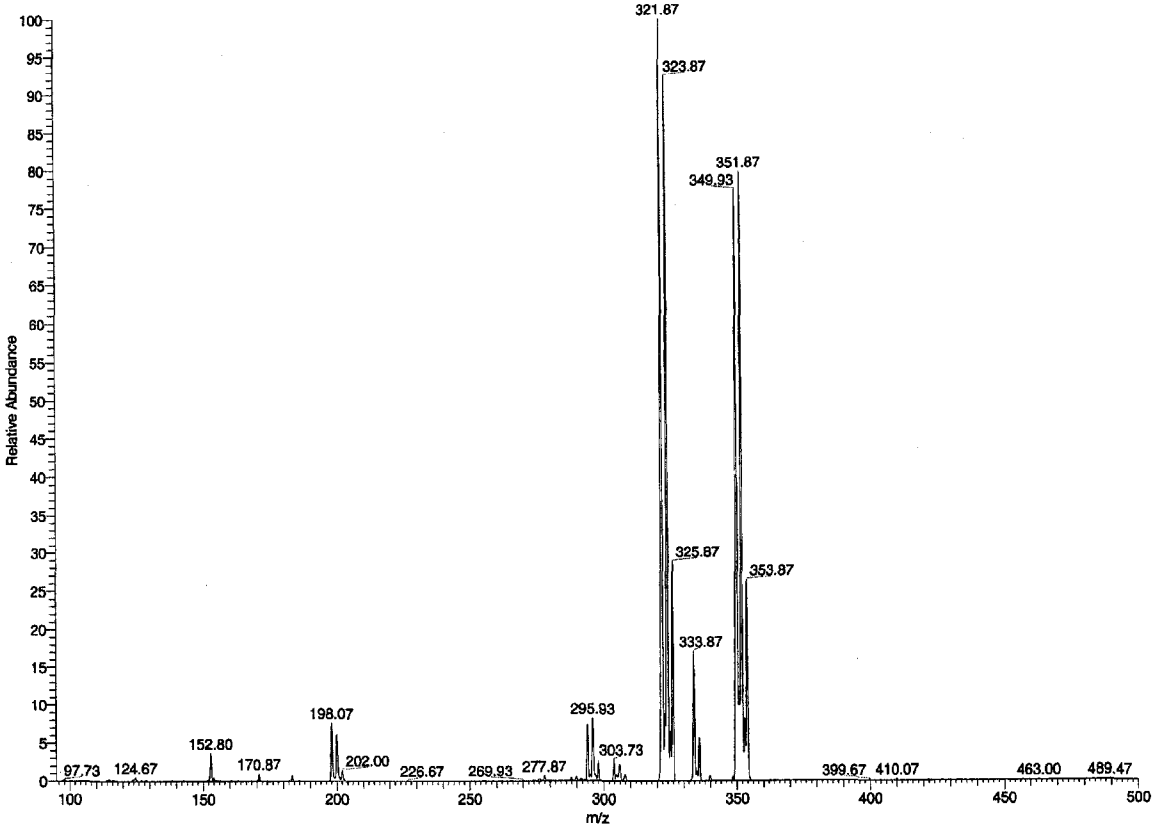

Figure A-13. Positive-ion electrospray MS/MS of the peak at m/Z= 352 for the sample represented in Figure A-8A (neat chlorpyrifos, sealed in glass and heated to 140 °C for 15 hours, followed by dissolving in CD_3CN and dilution into ethanol containing 1% formic acid), scanning the range m/Z = 95 to 500. The mass spectrum shown is the average of 25 repeated scans.

Fig. A-14

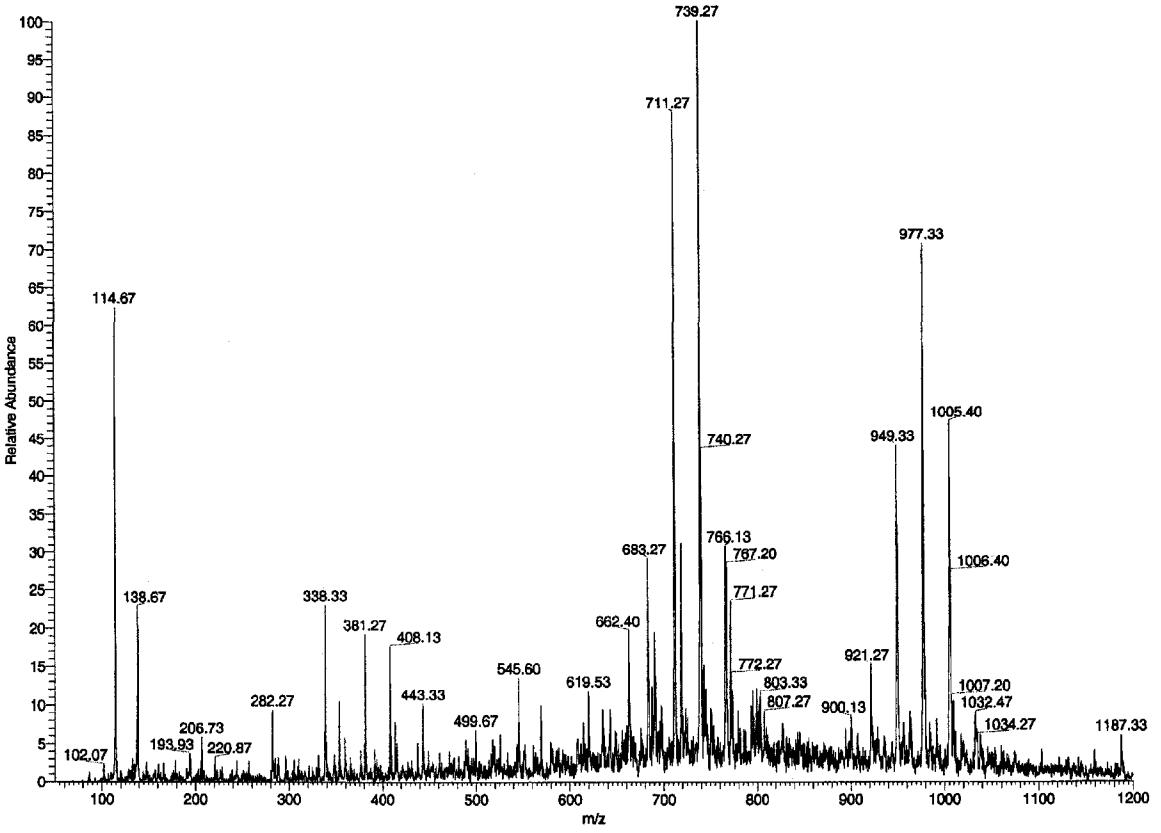

Figure A-14. Background positive-ion electrospray mass spectrum of ethanol containing 1% formic acid, scanning the range m/Z = 50 to 1200. The mass spectrum shown is the average of 25 repeated scans.

Fig. A-15

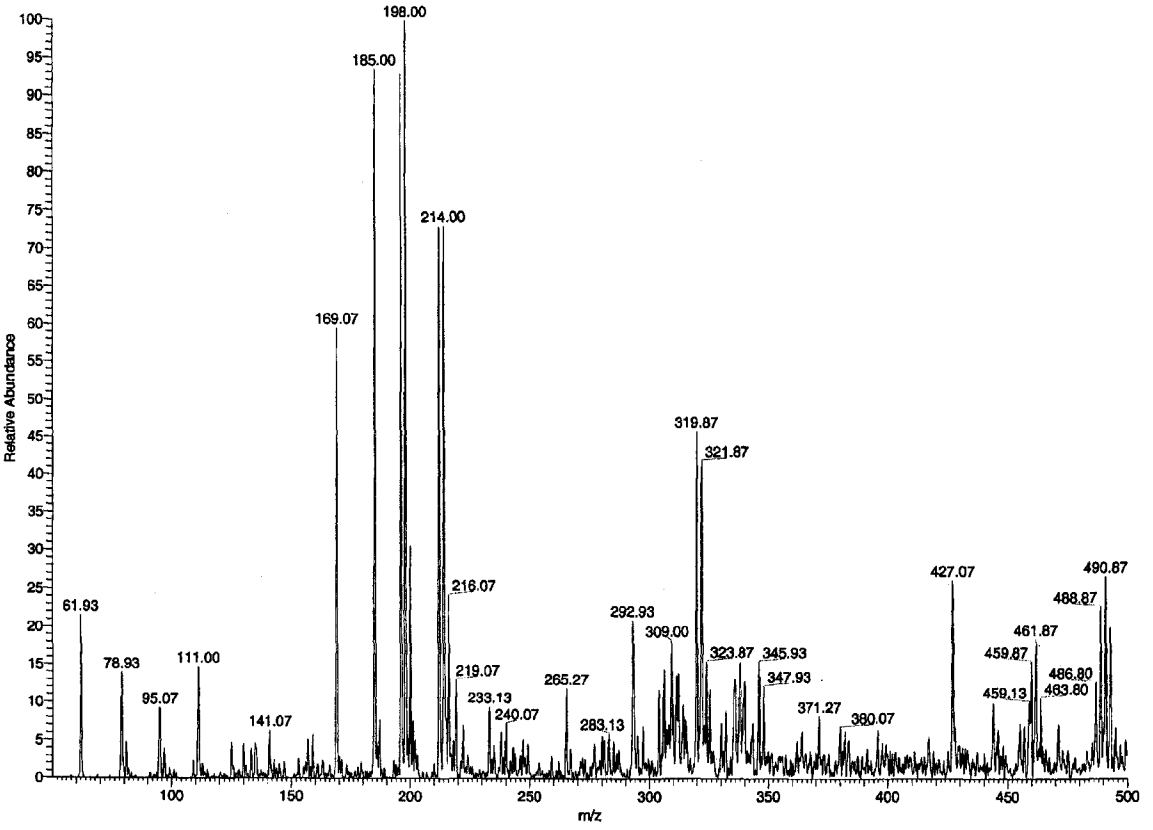

Figure A-15. Negative-ion electrospray mass spectrum of neat chlorpyrifos (sealed in glass) heated to 140 °C for 15 hours (followed by dissolving in CD_3CN, then dilution into ethanol containing 1% formic acid), scanning the range m/Z = 50 to 500. The mass spectrum shown is the average of 25 repeated scans.

Fig. A-16

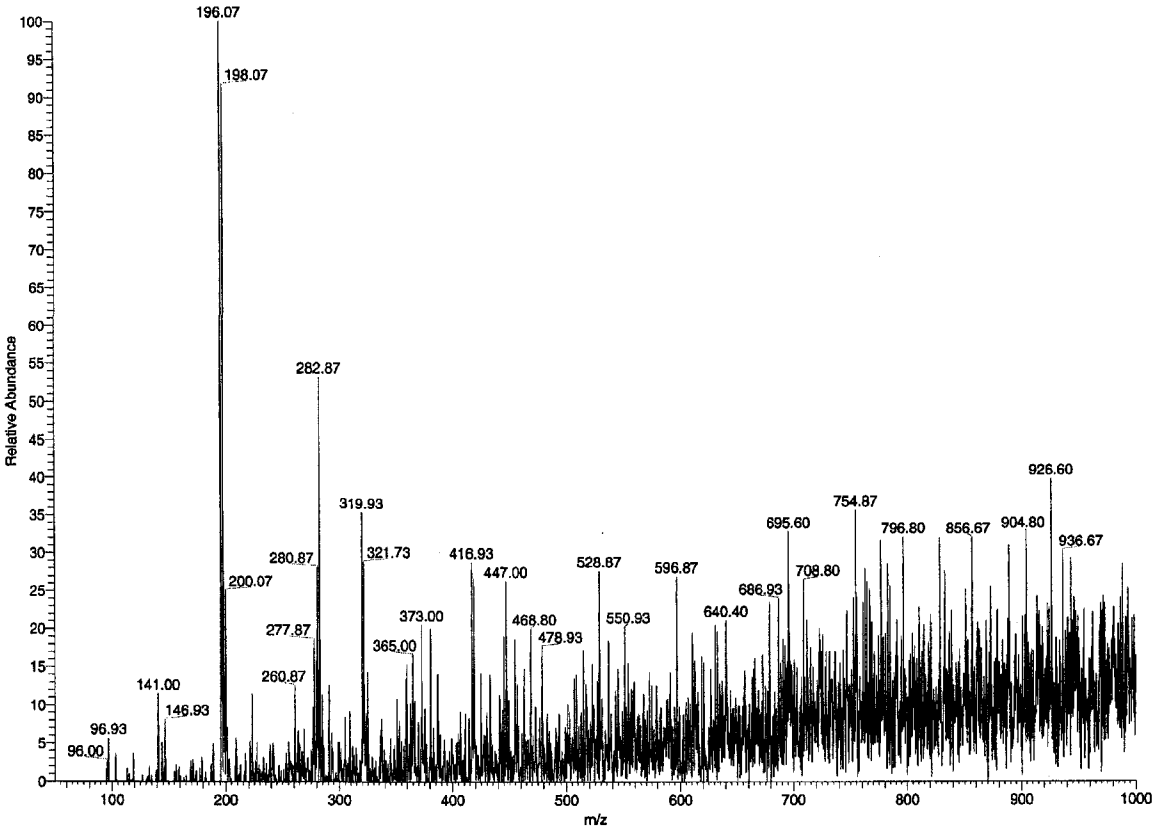

Figure A-16. Background negative-ion electrospray mass spectrum of methanol containing 1% acetic acid, scanning the range m/Z = 50 to 1000. The mass spectrum shown is the average of 25 repeated scans.

Fig. A-17

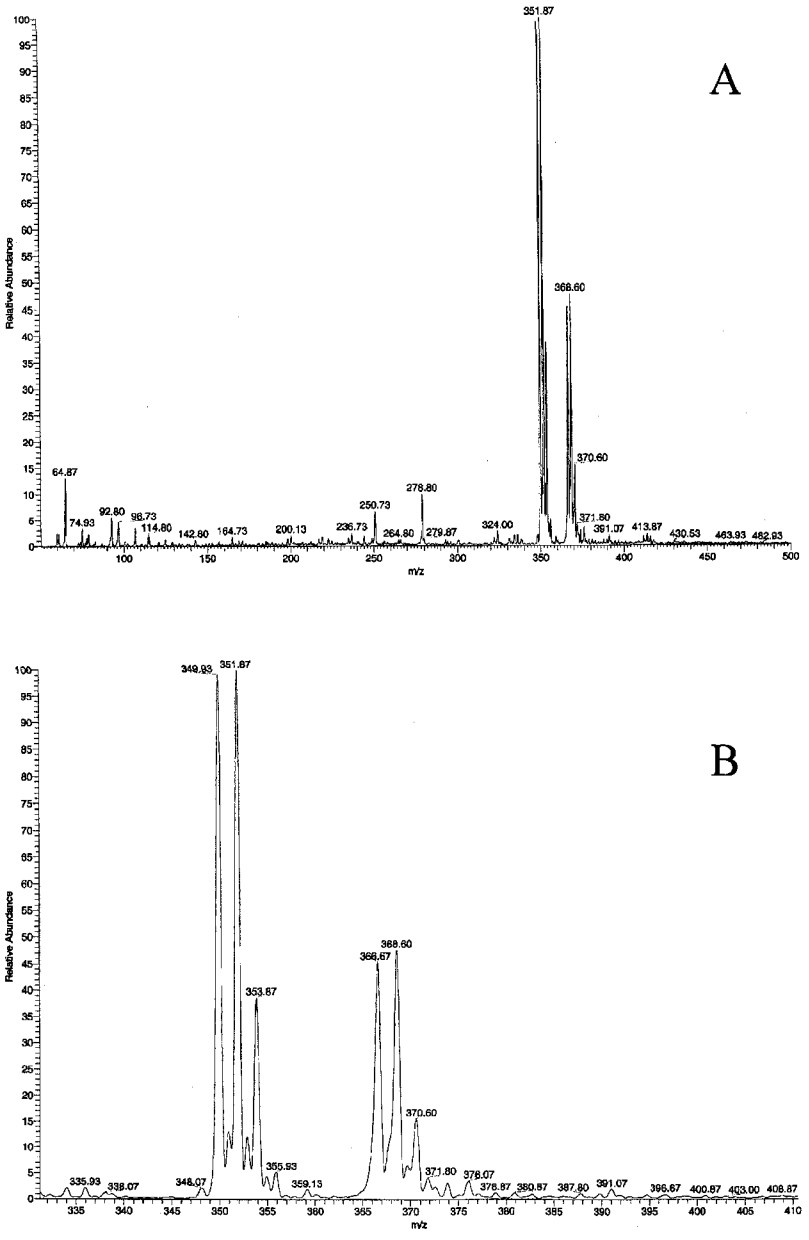

Figure A-17A. Positive-ion electrospray mass spectrum of neat chlorpyrifos (sealed in glass) heated to 140 °C for 15 hours (followed by dissolving in CD_3CN, then dilution into methanol containing 1% formic acid), scanning the range m/Z = 50 to 500. The mass spectrum shown is the average of 25 repeated scans.
Figure A-17B. Same as Figure A-17A, but displaying the region m/Z = 330 to 410.

Fig. A-18

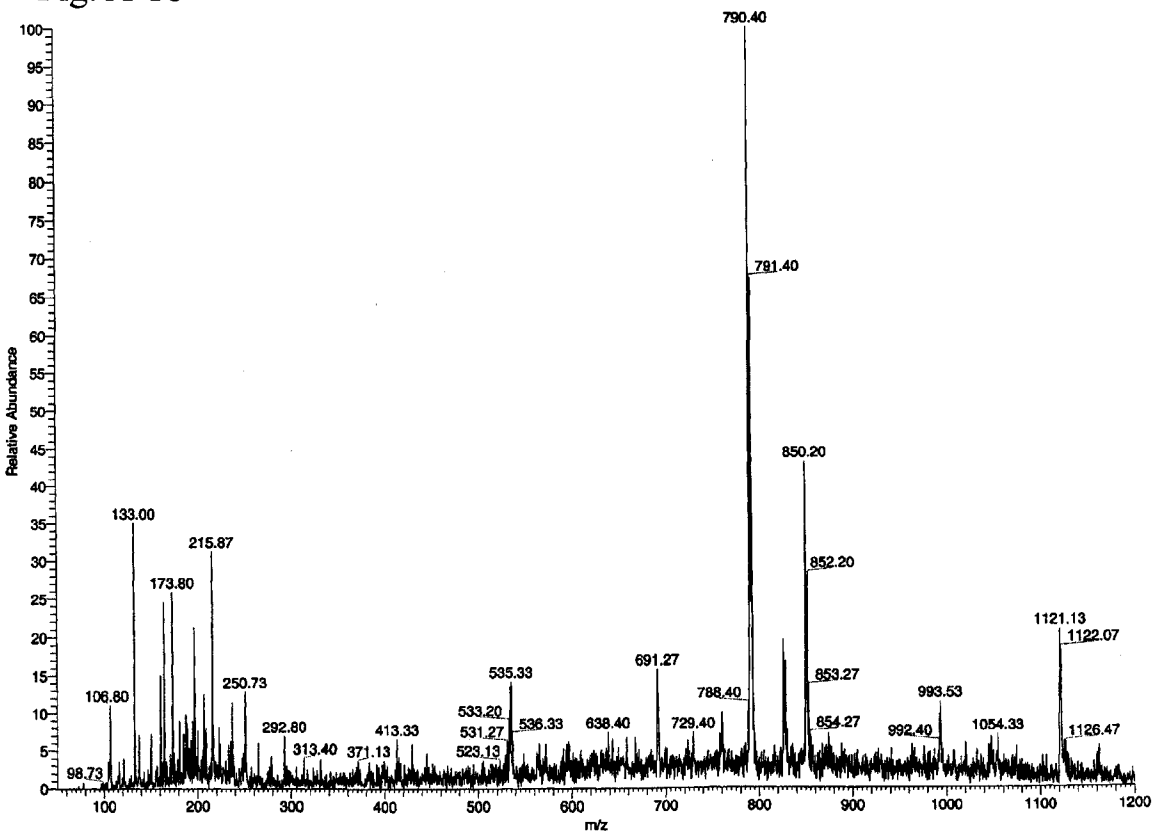

Figure A-18. Background positive-ion electrospray mass spectrum of methanol containing 1% formic acid, scanning the range m/Z = 50 to 1200. The mass spectrum shown is the average of 25 repeated scans.

Fig. A-19

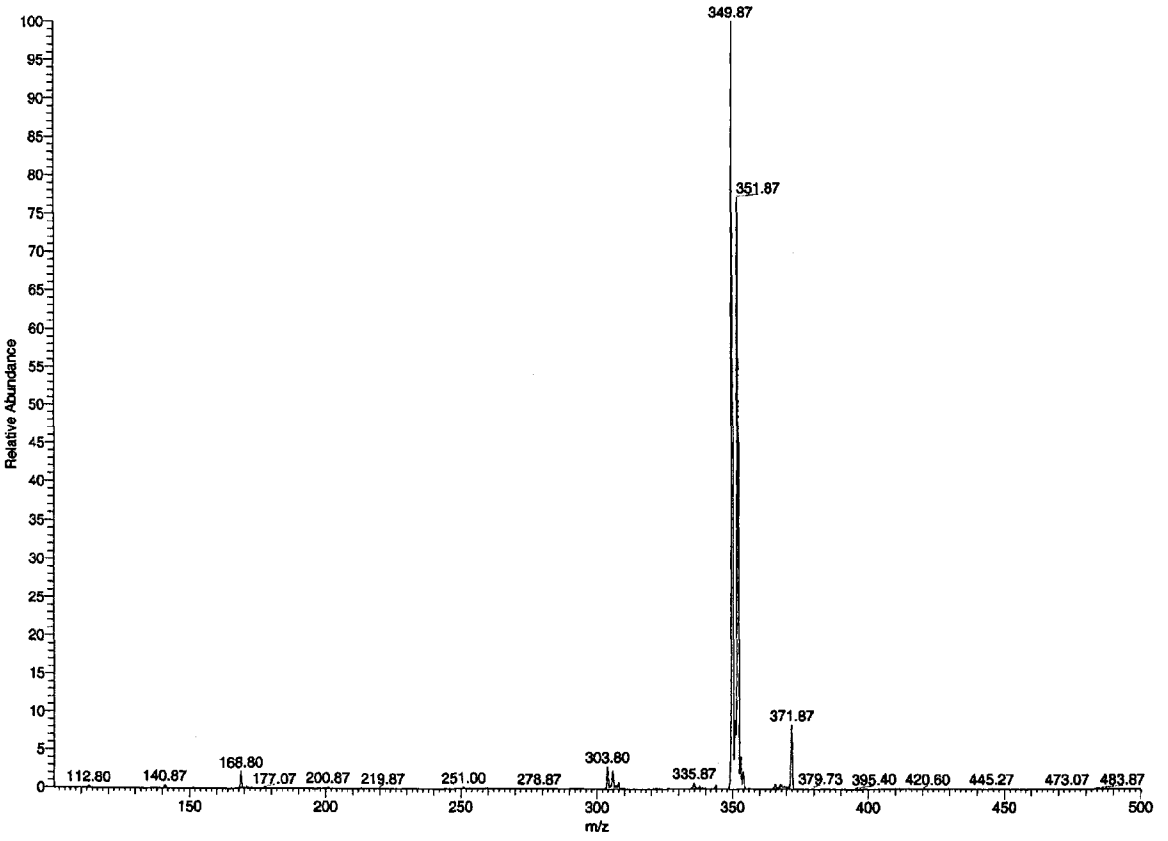

Figure A-19. Positive-ion electrospray MS/MS of the peak at m/Z= 369 for the sample represented in Figure A-17A (neat chlorpyrifos, sealed in glass and heated to 140 °C for 15 hours, followed by dissolving in CD_3CN and dilution into methanol containing 1% formic acid), scanning the range m/Z = 100 to 500. The mass spectrum shown is the average of 25 repeated scans.

Fig. A-20

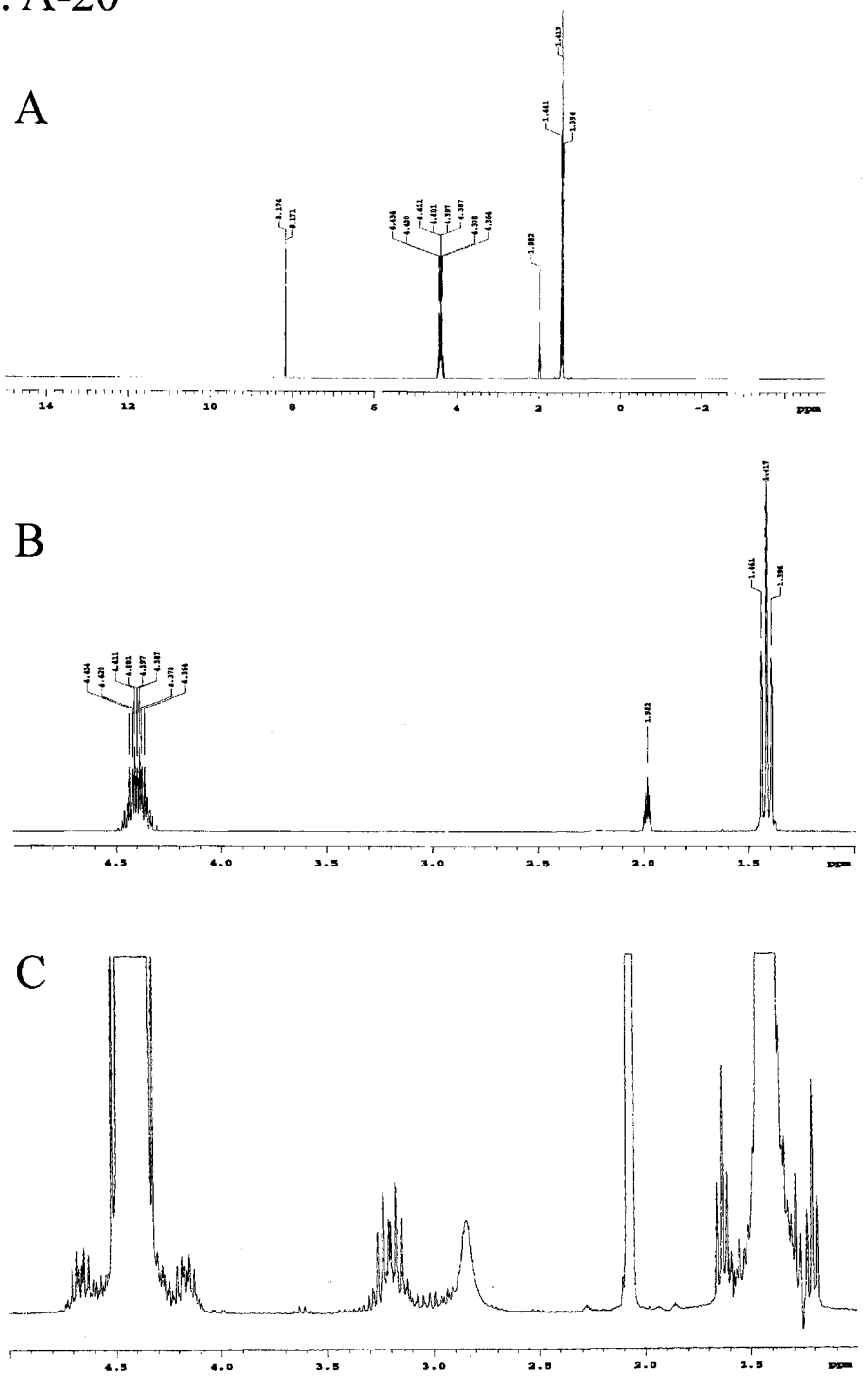

Figure A-20A. 300.1 MHz liquid-solution ^{1}H NMR spectrum of neat chlorpyrifos (sealed in glass) heated to 140 °C for 15 hours, followed by dissolving in CD_3CN (32 scans).
Figure A-20B. Same as Figure A-20A, except that region 5.0 to 1.0 ppm is displayed.
Figure A-20C. Same as Figure A-20B, except that the vertical scale is expanded by a factor of 64.

Fig. A-21

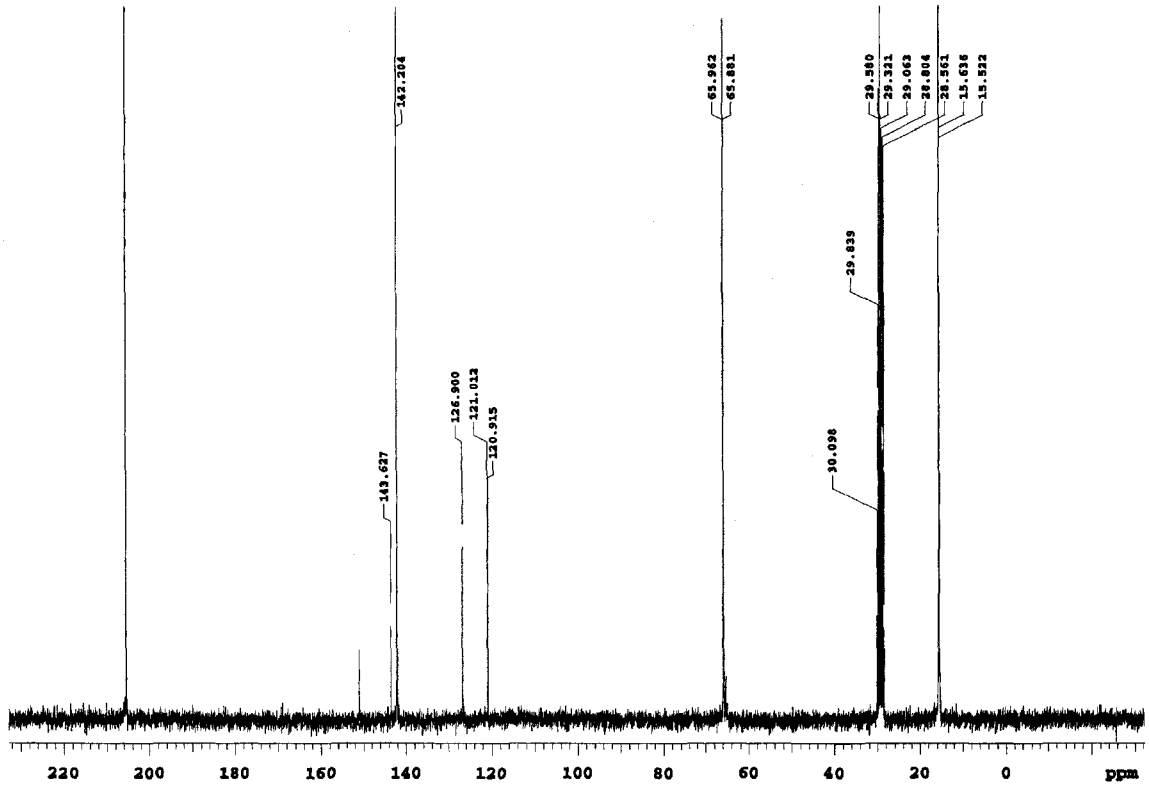

Figure A-21. 75.5 MHz liquid-solution ^{13}C NMR spectrum of neat chlorpyrifos (sealed in glass) heated to 140 °C for 15 hours, followed by dissolving in CD_3CN (32 scans).

Fig. A-22

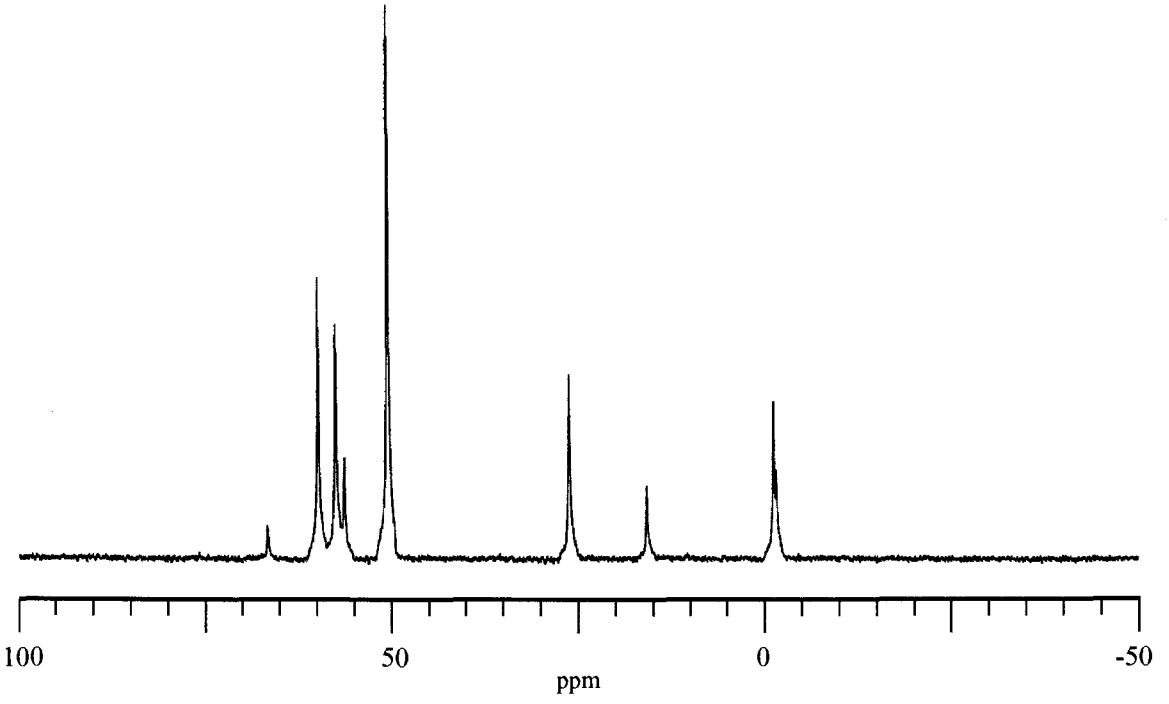

Figure A-22. 242.9 MHz ^{31}P NMR spectrum of chlorpyrifos refluxed in N,N-dimethylacetamide for three hours (without the addition of any NMR solvent, 15760 scans unlocked).

Fig. A-23

A

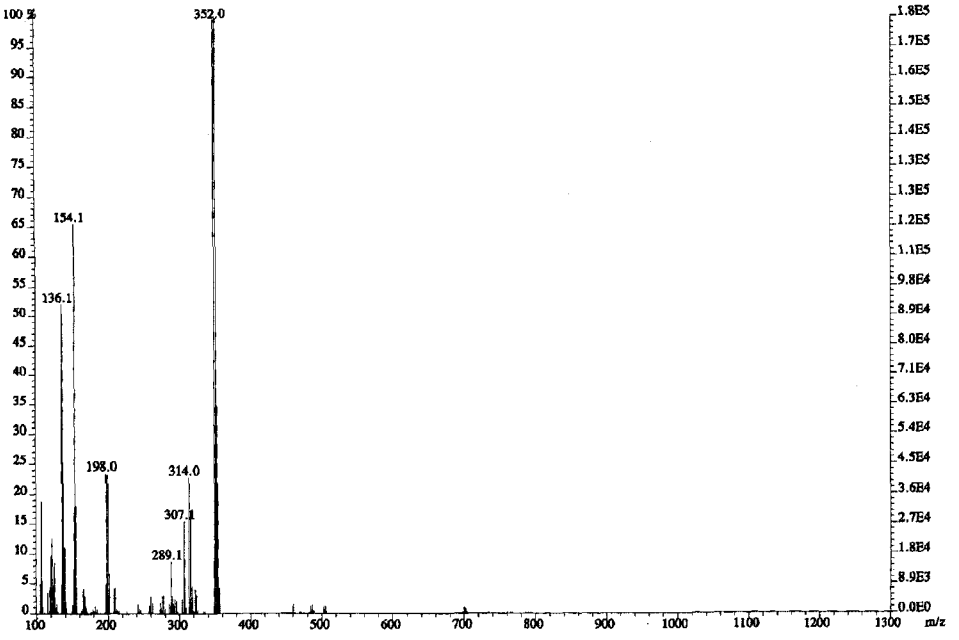

B

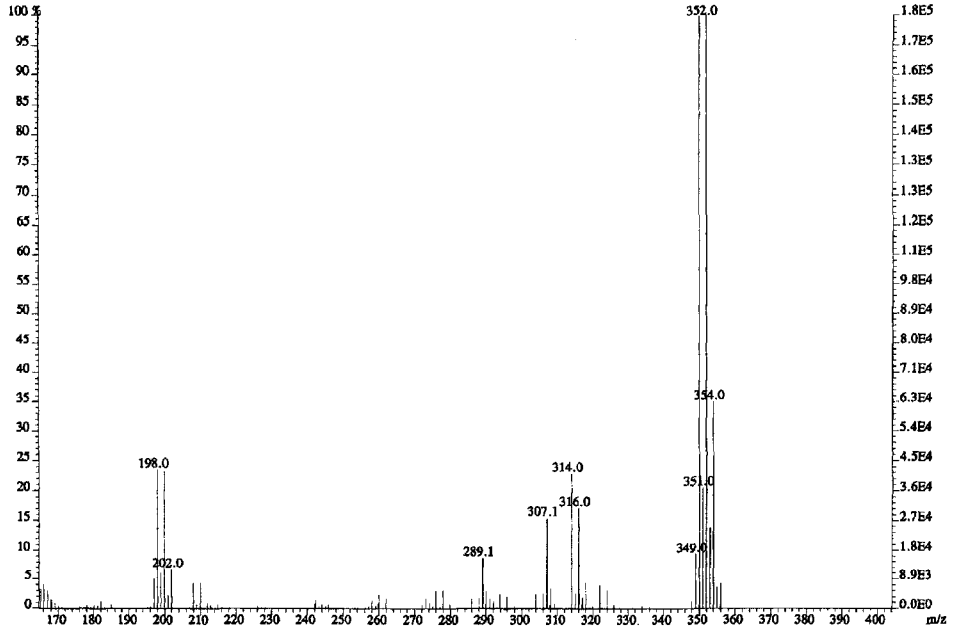

Figure A-23A. Positive-ion FAB/MS analysis (in a m-nitrobenzyl alcohol matrix) of chlorpyrifos refluxed in N,N-dimethylacetamide for three hours (^{31}P NMR shown in Figure A-22), scanning from m/Z = 100 to 1300.
Figure A-23B. Same as Figure A-23A, except the displayed region is m/Z = 165 to 404.

Fig. A-24

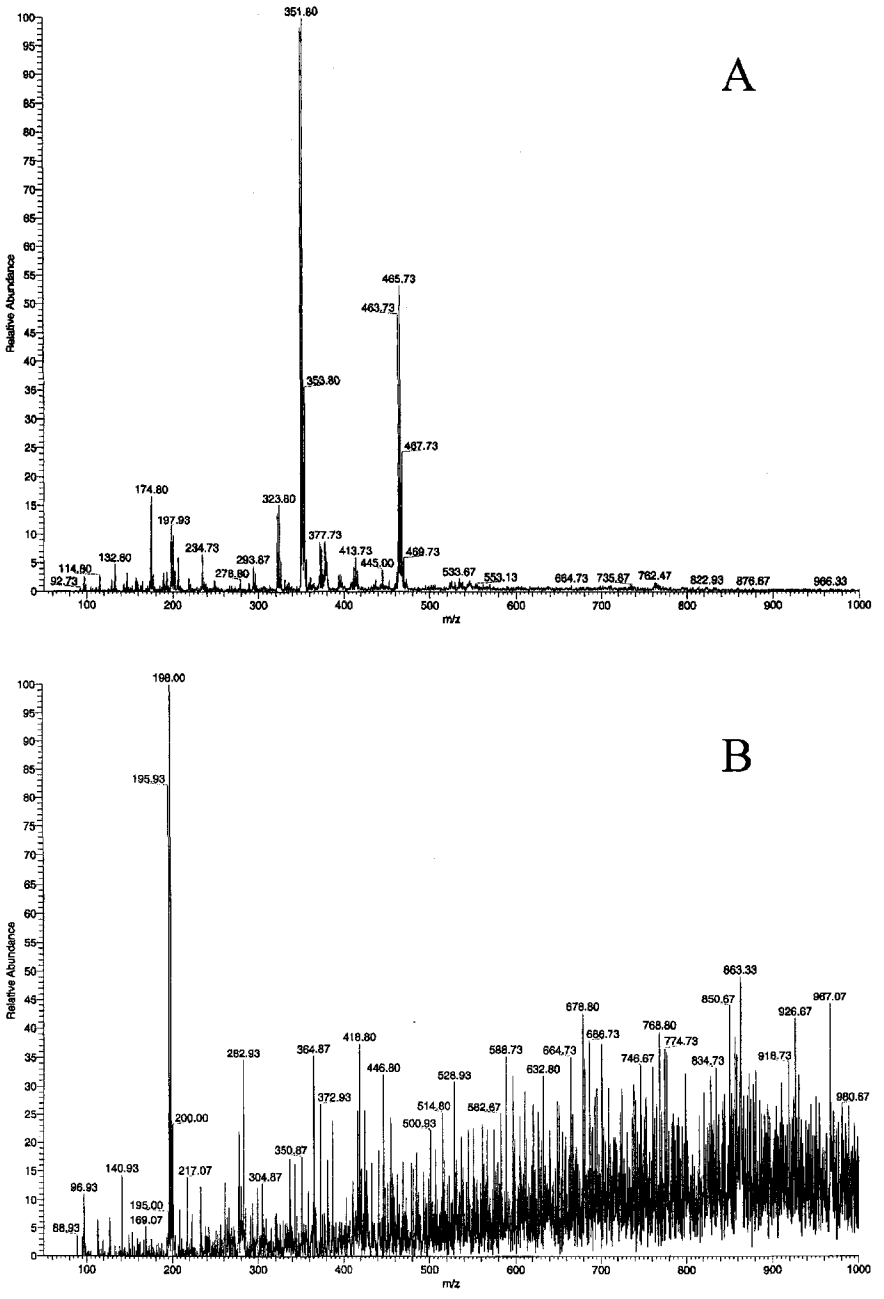

Figure A-24A. Positive-ion electrospray of chlorpyrifos refluxed in N,N-dimethylacetamide for three hours, dissolved in methanol with 1% acetic acid (as a protonation source), scanning from m/Z = 50 to 1000. The mass spectrum shown is the average of 30 repeated scans.

Figure A-24B. Same as Figure A-24A, but negative-ion electrospray.

Fig. A-25

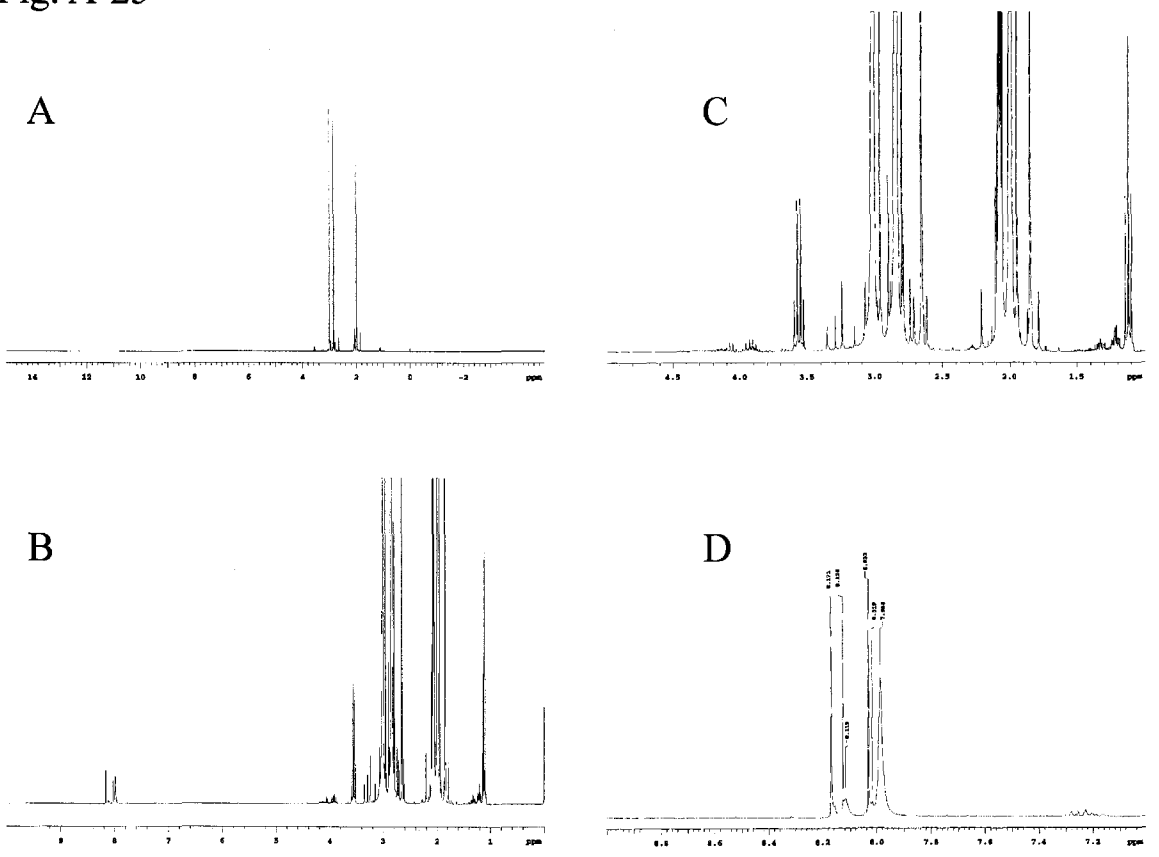

Figure A-25A. 300.1 MHz liquid-solution ^{1}H NMR spectrum of chlorpyrifos refluxed in N,N-dimethylacetamide for three hours, with the addition of some acetone-d_6 to provide a lock solvent, displaying the entire proton NMR spectrum (15 to -5 ppm; 64 scans).
Figure A-25B. Same as Figure A-25A, except the region 10 to 0 ppm is displayed with a vertical expansion factor of 32; offscale peaks arise from the solvents.
Figure A-25C. Same as Figure A-25A, except the region 5 to 1 ppm is displayed with a vertical expansion factor of 40; offscale peaks arise from the solvents.
Figure A-25D. Same as Figure A-25A, except the region 9 to 7 ppm is displayed with a vertical expansion factor of about 640; offscale peaks arise from the solvents.

Fig. A-26

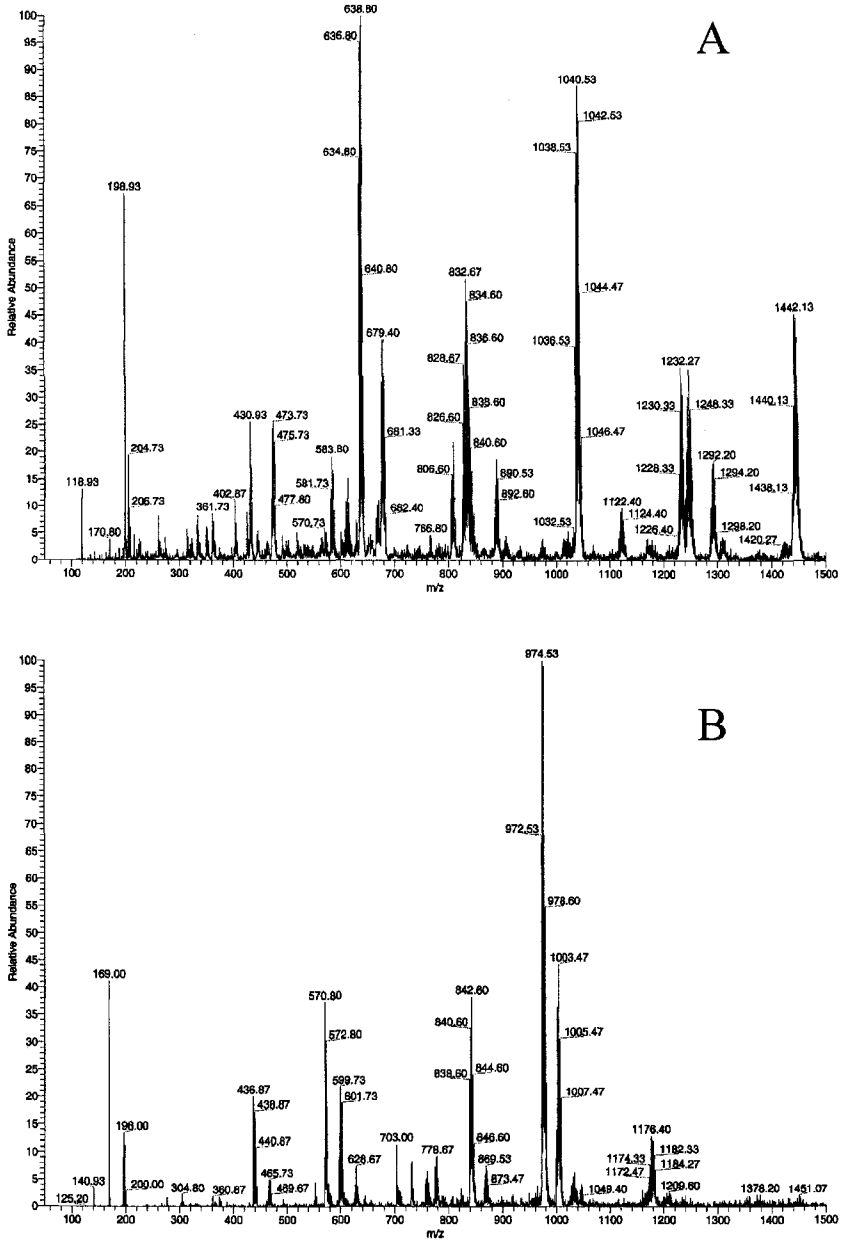

Figure A-26A. Positive-ion electrospray mass spectrum of acetonitrile-d_3 extract of chlorpyrifos sorbed on Cu(II)-montmorillonite (9.7% chlorpyrifos and 5.0% water, by weight; CD_3CN extraction after 11 hours of reaction at room temperature in the dark, followed by dissolution into methanol with 1% acetic acid), scanning from m/Z = 50 to 1500. The mass spectrum shown is the average of 25 repeated scans.
Figure A-26B. Same as Figure A-26A, but negative-ion.

Fig. A-27

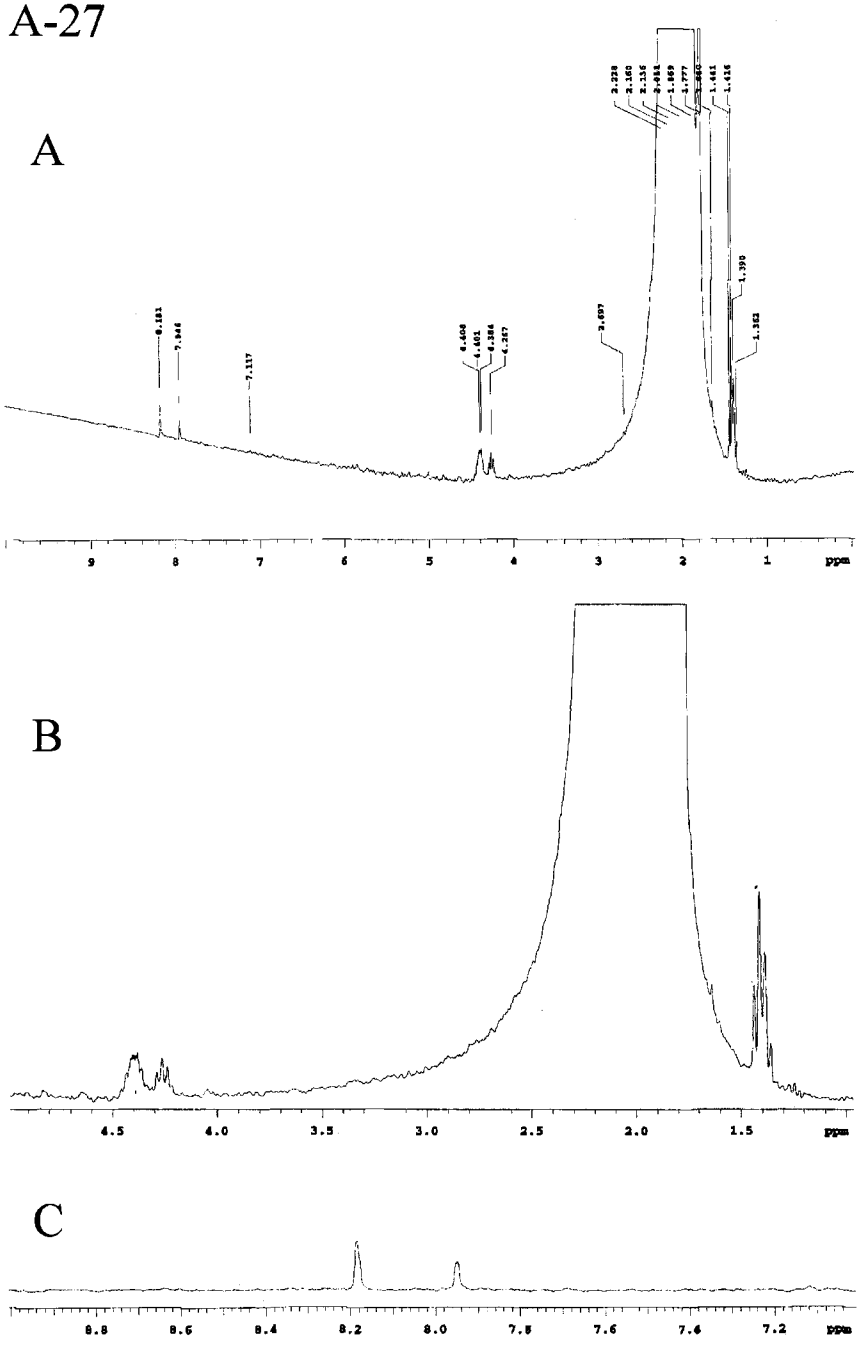

Figure A-27A. 300.1 MHz liquid-solution ^1H NMR spectrum of acetonitrile-d_3 extract of chlorpyrifos sorbed on Cu(II)-montmorillonite (9.7% chlorpyrifos and 5.0% water, by weight; CD_3CN extraction after 11 hours of reaction at room temperature in the dark; 64 scans). Offscale peaks arise from the solvent.

Figure A-27B. Same as Figure A-27A, except the region 5 to 1 ppm is displayed with additional vertical expansion; offscale peaks arise from the solvents.

Figure A-27C. Same as Figure A-27A, except the region 9 to 7 ppm is displayed with additional vertical expansion.